

**THE ROLE OF THREE-DIMENSIONAL GEOMETRY
ON TURBULENCE IN QUASI-HELICALLY SYMMETRIC
STELLARATORS**

by

Benjamin J. Faber

A dissertation submitted in partial fulfillment of
the requirements for the degree of

Doctor of Philosophy

(Physics)

at the

UNIVERSITY OF WISCONSIN–MADISON

2018

Date of final oral examination: 07/27/2018

The dissertation is approved by the following members of the Final Oral Committee:

Chris C. Hegna, Professor, Engineering Physics

Paul W. Terry, Professor, Physics

John S. Sarff, Professor, Physics

Cary B. Forest, Professor, Physics

David T. Anderson, Professor, Electrical and Computer Engineering

© Copyright by Benjamin J. Faber 2018
All Rights Reserved

To my parents, Jacinta and Paul.

ACKNOWLEDGMENTS

First and foremost, this thesis would not be possible without the guidance and support of my advisors, Profs. Chris Hegna and Paul Terry. Their patience with my many questions and willingness to let me explore has helped me develop into the physicist I am today. I am also indebted to the guidance of Dr. M.J. Pueschel, who provided not only expert advice on the inner workings of GENE, but also many enlightening conversations on a diversity of subjects that greatly enriched my graduate education.

It goes without saying that my time in Madison would have been worse if not for the members of the Cascade: Zach, Garth, Adrian, Ian, Jason, and Justin. I am forever grateful to you all for helping alleviate the stress of graduate school and making each day not feel like work. The lively conversations we have had, whether it be the details of plasma turbulence to the details of Star Wars, has been an essential part of my education. I must also thank the HSX crew, and in particular Jason, Alice, Laurie, Brandon, and Fernando, for making sure I had plenty of opportunities to relax. Our long evenings at the Terrace were always the highlights of the summer.

To Michael, Chris, Emma, Sean, Fady, Ana, and Will, who were there when it started all those years ago at Caltech, the constant reminder that I was the last to finish was the major motivation for finally authoring this thesis. Now I can sit at the big kids table again.

I do not think I would even be a physicist, if not for the graciousness of Prof. Gavin Buffington, who took seriously the desires of a fourteen-year-old high-schooler with an enthusiasm for physics and encouraged me to achieve more than I thought possible. I will forever be thankful for introducing me to my greatest passion and for fostering a love of everything cycling.

And finally, to my family. Your love, support, and encouragement through thick and thin has meant the world.

CONTENTS

Contents iii

List of Tables vi

List of Figures vii

Abstract xvii

1 Introduction 1

- 1.1 *Fusion Energy and Plasma Physics* 1
 - 1.1.1 Basic plasma theory 4
- 1.2 *Magnetic Confinement Fusion* 7
 - 1.2.1 Single particle drifts 9
 - 1.2.2 Particle trapping 10
 - 1.2.3 Magnetohydrodynamic equilibrium 11
 - 1.2.4 Toroidal configurations 13
 - 1.2.5 Plasma dynamics at multiple scales 15
- 1.3 *Drift Waves* 18
 - 1.3.1 Trapped particle modes 22
 - 1.3.2 Temperature gradient modes 23
- 1.4 *Plasma turbulence* 24
- 1.5 *Thesis Outline* 28

2 Toroidal Magnetic Fields and Stellarators 29

- 2.1 *Magnetic Coordinates* 29
 - 2.1.1 General magnetic coordinates 31
 - 2.1.2 Boozer coordinates 33
- 2.2 *Collisionless Orbit Confinement* 35
 - 2.2.1 Quasi-symmetry 37

2.2.2	Quasi-omnigeneity	40
2.3	<i>Stellarator Experiments</i>	43
2.4	<i>Chapter Summary</i>	44
3	Gyrokinetic Simulation of Plasma Turbulence	45
3.1	<i>Gyrokinetic Theory</i>	45
3.1.1	Phase space transformations	47
3.1.2	Gyrokinetic Vlasov-Maxwell equations	54
3.2	<i>Flux Tube Geometry</i>	62
3.3	<i>The GENE Code</i>	70
3.3.1	GENE Normalizations	70
3.3.2	Vlasov-Maxwell equations in GENE	72
3.4	<i>Stellarator Turbulence Simulations</i>	74
3.5	<i>Chapter Summary</i>	76
4	Trapped Electron Mode Turbulence in HSX	77
4.1	<i>TEM Instability in HSX</i>	77
4.2	<i>Linear Instability Analysis</i>	80
4.2.1	Linear dispersion relation	81
4.2.2	Linear eigenmode structure	85
4.2.3	Linear eigenmode classification	88
4.3	<i>Nonlinear Simulations of Turbulence in HSX</i>	91
4.3.1	Standard TEM	92
4.3.2	Impact of the density gradient	99
4.4	<i>Chapter Summary</i>	105
5	Microinstabilities and Turbulence at Low Magnetic Shear	106
5.1	<i>Gyrokinetic Simulations at Low Magnetic Shear</i>	106
5.1.1	Parallel correlations	107
5.1.2	Impact of small global magnetic shear	112
5.2	<i>Linear Mode Calculations</i>	113

5.2.1	Trapped electron modes	114
5.2.2	Ion temperature gradient modes	118
5.2.3	Zero-magnetic-shear approximation	121
5.2.4	Flux-tube equivalence	127
5.3	<i>Nonlinear Effects</i>	128
5.4	<i>Chapter Summary</i>	136
6	Role of Geometry in Turbulence Saturation	138
6.1	<i>Fluid Modeling of Turbulence Saturation</i>	140
6.1.1	Three-Field Fluid Model	141
6.1.2	Numerical Implementation	148
6.2	<i>Turbulence Saturation in Quasi-Symmetric Stellarators</i>	151
6.2.1	Turbulence Saturation in HSX	151
6.2.2	Turbulence Saturation in NCSX	156
6.3	<i>HSX Hill/Well Calculations</i>	160
6.4	<i>Chapter Summary</i>	167
7	Conclusions	169
7.1	<i>Summary</i>	169
7.1.1	First TEM turbulence simulations in HSX	169
7.1.2	Effect of low magnetic shear on turbulence	170
7.1.3	Turbulence saturation in stellarators	171
7.2	<i>Future Research</i>	172
7.2.1	Experimental comparisons	172
7.2.2	Nonlinear energy transfer in stellarators	173
7.2.3	Turbulence optimization	173
	References	174

LIST OF TABLES

1.1	Intrinsic time scales for a uniform plasma with $T_{i,e} = 2keV$, $n_{i,e} = 10^{20}m^{-3}$ in a background magnetic field of 1 T. The ion species is hydrogen, with an ion-to-electron mass ratio $m_i/m_e = 1837$. Time scales are identified by species in parentheses, with interspecies interactions denoted by letter combinations.	16
1.2	Intrinsic length scales for a uniform plasma of size 1m with $T_{i,e} = 2keV$, $n_{i,e} = 10^{20}m^{-3}$ in a background magnetic field of 1 T. The ion species is hydrogen, with an ion-to-electron mass ratio $m_i/m_e = 1837$. Length scales are identified by species in parentheses, with interspecies interactions denoted by letter combinations.	17
4.1	Classification of the different linear modes in HSX-b and HSX-t based on $\Delta\gamma/\gamma_0$ change in growth rate for 10% increases in driving density and temperature gradient, stabilization due to β , negative (positive) sign denotes propagation in electron (ion) drift direction, and mode parity (ballooning or tearing). The acronyms are explained in the text.	89

LIST OF FIGURES

1.1	Annual energy consumption by source in the United States. Source: U.S. Energy Information Agency, Monthly Energy Review, June 2018.	1
1.2	Example of a tokamak (top) and a stellarator (bottom). The magnetic surface is in yellow, with a field line overlaid. Source: Xu (2016)	14
1.3	Schematic of a curvature-driven drift wave (left) and a slab drift wave (right). The pressure gradient is in the $-x$ direction, the magnetic field is out of the page in the z direction. Source: Grulke and Klingner (2002)	19
2.1	Simple toroidal coordinate system. Source: FusionWiki.	30
4.1	Normalized normal curvature (red dotted line) and normalized magnetic field strength (blue dashed line) in the parallel direction in HSX-b. Negative curvature indicates bad curvature. Source: Faber et al. (2015).	79
4.2	Normalized normal curvature (red dotted line) and normalized magnetic field strength (blue dashed line) in the parallel direction in HSX-t. Negative curvature indicates bad curvature. Source: Faber et al. (2015).	80

- 4.3 Linear growth rates (top) and real frequencies (bottom) in HSX flux tubes for canonical TEM parameter set: $a/L_n = 2$, $a/L_{Te} = 1$. The different dominant mode regions are identified as the B modes for HSX-b and the T modes for HSX-t. The red dashed lines indicate the approximate boundaries between different dominant B modes and the blue solid line is the approximate boundary between T modes. Negative real frequencies indicate modes with electron-direction drift frequencies. Source: Faber et al. (2015). 82
- 4.4 Linear growth rates (top) and real frequencies (bottom) in HSX-b for the density gradient scan: $a/L_n = 1 - 4$, $a/L_{Te} = 0$. Approximate mode boundaries are indicated by the dashed vertical lines. The mode types are determined by the analysis in Secs. 4.2.2 and 4.2.3. Source: Faber et al. (2015). 84
- 4.5 The normalized real and imaginary parts of the extended mode structure in the electrostatic potential Φ for the four different dominant modes in Fig. 4.3 for HSX-b for standard TEM parameters: $a/L_n = 2$, $a/L_{Te} = 1$. Source: Faber et al. (2015). 86
- 4.6 The normalized real and imaginary parts of the extended mode structure in the electrostatic potential Φ for the two different dominant modes in Fig. 4.3 in HSX-t for standard TEM parameters: $a/L_n = 2$, $a/L_{Te} = 1$. Source: Faber et al. (2015). 87
- 4.7 First 5 largest eigenmodes for the standard TEM parameter set in HSX-b. The eigenvalues at each k_y are ordered from largest to smallest linear growth rate. Continuity in real frequencies (bottom) shows the existence of at least 5 distinct mode branches for $k_y \geq 0.7$. The different dominant modes (red \square) identified by the designations in Table 4.1. Source: Faber et al. (2015). . . 90

- 4.8 Time trace of the electron heat flux in HSX-bean (solid red) and HSX-triangle (dashed blue) flux tubes for standard TEM parameters: $a/L_n = 2$, $a/L_{Te} = 1$. Also shown is the time trace of the heat flux in a simulation for HSX-b where k_y^{\min} was halved (dotted green), showing that the simulations are converged. Source: Faber et al. (2015). 92
- 4.9 Heat flux spectrum in HSX-b with $k_y^{\min} = 0.1$ (red solid), $k_y^{\min} = 0.05$ (green dotted) and HSX-t with $k_y^{\min} = 0.1$ (blue dashed) for standard TEM parameters: $a/L_n = 2$, $a/L_{Te} = 1$. The simulation with $k_y^{\min} = 0.05$ has been scaled by a factor of 2 to illustrate more clearly its near-identical integrated flux level. Source: Faber et al. (2015). 93
- 4.10 Nonlinear frequencies ω in HSX-b for standard TEM parameters. The frequencies are obtained by performing a Fourier transform in time over the quasi-stationary state. The color scale is linear and independent for each k_y . Linear frequencies from Fig. 4.3 are overlaid with the white and black dash line. Source: Faber et al. (2015). 94
- 4.11 Contours of Φ (normalized by $T_{e0}\rho_s^*/e$) and n_e (normalized by $n_{e0}\rho_s^*$) fluctuations at zero poloidal angle in (a) HSX-b and (b) HSX-t. The x direction is radial and the y direction is poloidal. Zonal flows are present in both flux tubes, however a coherent structure centered at $x = 0$ is only observed in HSX-b. Source: Faber et al. (2015). 96
- 4.12 k_y resolved electron heat flux spectrum for standard TEM parameters in HSX-b for $\beta = 5 \times 10^{-4}$ (solid red) and $\beta = 5 \times 10^{-5}$ (dashed blue). While these values appear to be rather low, when normalizing to the ballooning threshold, they become more sizeable. Source: Faber et al. (2015). 98

- 4.13 Nonlinear cross phases between Φ and n_e , Φ and $T_{e\parallel}$, and Φ and $T_{e\perp}$ for the standard parameters in HSX-b. Overlaid are the linear cross phases (black line) for each quantity. The color scale for the nonlinear cross phases is logarithmic. The linear and nonlinear phases differ for $k_y \leq 0.2$ where the coherent structure lies, but generally agree for $k_y > 0.3$, where linearly the TEM is dominant. Source: Faber et al. (2015). 100
- 4.14 Time trace of the electron electrostatic heat fluxes in HSX-bean for density gradient scan: $a/L_n = 1 - 4$, $a/L_{Te} = 0$. Larger variability in the flux corresponds with the growth of the central coherent structure, much like in Fig. 4.11a. Source: Faber et al. (2015). 101
- 4.15 Density gradient scaling of the linear growth rates at $k_y = 0.7$ (red \square) and nonlinear electron heat flux (blue \odot) in HSX-b. A square root fit predicts a linear critical gradient at $a/L_n \approx 0.2$. A linear fit of the $a/L_n \leq 3$ range of the nonlinear fluxes produces an upshift with a nonlinear critical gradient predicted at $a/L_n \approx 0.8$. Source: Faber et al. (2015). 102
- 4.16 Electron electrostatic heat flux spectrum for HSX-b for the density gradient scan: $a/L_n = 1 - 4$, $a/L_{Te} = 0$. The flux at low- k_y increases steadily with increasing a/L_n , however the TEM peak at $k_y = 0.7-0.8$ still determines the overall flux level. Source: Faber et al. (2015). 103
- 4.17 Contours of Φ fluctuations at zero poloidal angle in HSX-bean tube with $a/L_{Te} = 0$ in all simulations. Zonal flows are present in all simulations and the coherent structure develops as a/L_n is increased. Source: Faber et al. (2015). 104

- 5.1 Comparison of HSX geometry terms for a flux tube constructed from one poloidal turn (black) and four poloidal turns (red solid lines). The FLR term, defined by Eq. (5.1), is shown on top, while the curvature drive, defined by Eq. (5.2), is on bottom. Both quantities are plotted as functions of the parallel coordinate. Source: Faber et al. (2018). 110
- 5.2 Eigenspectrum for the strongly driven ∇n TEM in HSX. The horizontal axis is the growth rate γ and the vertical axis is the real frequency ω . Different k_y are indicated different symbols and colors. Examples of different types of modes are given by the labels “A”, “B”, “C”, and “D”, and the mode structure is shown in Fig. 5.3. Source: Faber et al. (2018). 115
- 5.3 Electrostatic potential eigenmode structures for the TEM branches labeled “A”, “B”, “C”, and “D” from Fig. 5.2. The modes show conventional ballooning behavior (A), finite k_x dependence (B), extended structure along the field line (C), and two-scale structure with an extended envelope along the field line (D). Source: Faber et al. (2018). 116
- 5.4 TEM eigenspectrum at $k_y = 0.2$ for different poloidal turn values. Modes from one poloidal turn are the solid red diamonds and from four poloidal turns are the hollow blue diamonds. Generally, the modes at four poloidal turns are more stable, and there are fewer unstable modes than for one poloidal turn. Importantly, the extended ion mode branch (mode “D” in Fig. 5.3), transitions from unstable to stable at four poloidal turns. Source: Faber et al. (2018). 117
- 5.5 ITG eigenmode spectrum for different k_y values, denoted by different symbols and colors. The modes labeled “A”, “B”, and “C” are modes with two-scale behavior, and the mode structures are shown in Fig. 5.6. Source: Faber et al. (2018). 119

- 5.6 Electrostatic potential for eigenmodes “A”, “B”, and “C” from Fig. 5.5. The real part is the solid line and the imaginary part is the dotted black line. Similar to the mode “D” in Fig. 5.3, the ITG eigenmodes display two-scale structure, with an outer scale envelope and inner-scale structure set by the helical magnetic structure. Source: Faber et al. (2018). 120
- 5.7 Comparison of the ITG eigenmode spectrum at $k_y = 0.9$ for kinetic electrons (red) and adiabatic electrons (blue). Adding kinetic electron effects primarily the real frequency and reduces the number of unstable modes. However the extended ion modes that are unstable for kinetic electrons are absent from adiabatic electron calculations. Source: Faber et al. (2018). 121
- 5.8 Linear growth rate spectrum of TEMs for one poloidal turn for the finite-shear approach (red) and the zero-shear approach (black and blue). The blue points are from calculations where the k_x value was varied to find the maximum growth rate, while the black points are the $k_x = 0$ streamer instability. The non-zero k_x effects are required to reproduce the finite-shear spectrum for $0.3 \leq k_y \leq 0.7$. Source: Faber et al. (2018). 124
- 5.9 Eigenspectrum of the artificially enhanced mode (red diamonds) of Fig. 5.8 for a range of wavenumbers k_y . Select k_y modes are identified by the outlined symbols and compared with the finite-shear counterpart for one poloidal turn (black diamonds). All finite-shear eigenvalues are clustered near marginal stability, whereas zero-shear modes are artificially enhanced at one poloidal turn. Source: Faber et al. (2018). 125

- 5.10 Comparison of the finite-shear (hollow red diamonds) and zero-shear (solid black diamonds) eigenspectrum at $k_y = 0.7$ for the ∇n -driven TEM. Sufficient agreement is observed between the two computational approaches when multiple poloidal turns are used. In particular, the zero-shear technique recovers the appropriate clustering of eigenmodes, including the marginally stable ion mode branch (branch “D” of Fig. 5.2). Source: Faber et al. (2018). 126
- 5.11 Dominant linear growth rates for the HSX-bean flux and HSX-triangle flux tube with $n_{\text{pol}} = 4$. This figure should be compared with Fig. 4.3. 127
- 5.12 Nonlinear TEM heat fluxes for HSX as function of poloidal turns. In red and blue are finite shear simulations with $k_y^{\text{min}} = 0.1$ and 0.05 respectively, while zero-shear simulations are shown in black. Simulations agree for $n_{\text{pol}} \geq 4$. Source: Faber et al. (2018). . . . 129
- 5.13 Flux spectrum from nonlinear TEM simulations for HSX. The different curves represent different combinations of poloidal turns used for the geometry and k_y^{min} values. All curves, except for the black curve, were simulations with non-zero shear. The blue and teal dashed curves have been scaled by a factor of two due to having twice the k_y resolution as the solid curves. Source: Faber et al. (2018). 130
- 5.14 Spectrum of non-conservative energy terms in the high- ∇n TEM simulation for HSX. A positive (red) dE/dt value at a (k_x, k_y) indicates energy is being input into the system. The modes at $k_y = 0.2$ have the largest dE/dt values, coinciding with the heat flux peak at $k_y = 0.2$ in Fig. 5.13. Source: Faber et al. (2018). . . 132

5.15	Instantaneous contours of fluctuating electrostatic potential Φ (top) and density n (bottom) from a zero-shear simulation with one poloidal turn (black curve of Fig. 5.12). Both Φ and n display dominant zonal components, and the density shows a clear coherent mode. Source: Faber et al. (2018).	134
5.16	Projection of TEM turbulence onto eigenmodes at $k_y = 0.2$ using geometry with four poloidal turns. The colorbar gives the projection value. The projection shows subdominant and stable modes have higher projection values than the most unstable modes. The inset figures show the potential mode structure of the high-projection modes, emphasizing that at $k_y = 0.2$, modes with extended structure along the field line play a large role in the nonlinear state. Source: Faber et al. (2018).	135
6.1	Growth rate spectrum for the HSX QHS configuration (red diamonds) and the HSX Mirror configuration (blue squares) for ∇n TEMs with $a/L_n = 4$. Courtesy J. Smoniewski.	139
6.2	Nonlinear heat fluxes HSX QHS configuration (red diamonds) and the HSX Mirror configuration (blue squares) for ∇n -driven TEM turbulence as a function of a/L_n . Courtesy J. Smoniewski.	139
6.3	Example of an eigenmode (dashed line) compared with B_k (Eq. (6.17)) along a field line for a particular point in the \mathbf{k} -spectrum. The eigenmode is centered in a location where B_k is minimized and the adjacent B_k maxima are large enough to provide localization.	149
6.4	Growth rate spectrum for HSX (QHS) as computed by GENE. Source: Hegna et al. (2018).	152
6.5	Linear growth rate spectrum for HSX (QHS) as computed by PTSM3D. Source: Hegna et al. (2018).	153
6.6	Contours of $ \tau_{12F}C_{12F} $ for the HSX configuration as a function of k_x^z and k_y as computed by PTSM3D. Source: Hegna et al. (2018).	154

6.7	Contours of $ \tau_{qst}C_{qst} ^{\max}$ for the HSX configuration as a function of k_x and k_y as computed by PTSM3D. Source: Hegna et al. (2018).	155
6.8	Identity of the triplets involved in maximizing $ \tau_{qst}C_{qst} $. The color green indicates the triplet was comprised of an unstable mode, stable mode, and marginally stable mode. Source: Hegna et al. (2018).	156
6.9	Growth rate spectrum for NCSX (QAS) as computed by GENE. Source: Hegna et al. (2018).	157
6.10	Linear growth rate spectrum for NCSX (QAS) as computed by PTSM3D. Source: Hegna et al. (2018).	158
6.11	Contours of $ \tau_{12F}C_{12F} $ for the NCSX configuration as a function of k_x^z and k_y as computed by PTSM3D. Source: Hegna et al. (2018).	159
6.12	Contours of $ \tau_{qst}C_{qst} ^{\max}$ for the NCSX configuration as a function of k_x and k_y as computed by PTSM3D. Source: Hegna et al. (2018).	159
6.13	Identity of the triplets involved in maximizing $ \tau_{qst}C_{qst} $. The color green indicates the triplet was comprised of an unstable mode, stable mode, and marginally stable mode. Source: Hegna et al. (2018).	160
6.14	Amplitude of the 10 largest Boozer components at the half-toroidal flux surface of the 11% hill configuration, plotted as a function of plasma radius.	161
6.15	Amplitude of the 10 largest Boozer components at the half-toroidal flux surface of the 11% well configuration, plotted as a function of plasma radius.	162
6.16	Scaling of nonlinear fluxes (solid magenta diamonds), normalized $\langle \tau_{12F}C_{12F} \rangle_k$ (dotted red diamonds) and $\langle \tau_{qst}C_{qst} \rangle_k$ (dashed blue diamonds) as a function of HSX hill and well percentage. The triplets are normalized to the value at zero hill/well percentage (the QHS geometry).	163

6.17	Value of k_{\perp}^2 along a field line for 0% well (solid red) and 11% well (dashed blue) configurations.	164
6.18	Electrostatic potential eigenmode structures for 2.9% well at $(k_x = 0.28, k_y = 0.3)$ (top) and 11% well at $(k_x = 0.32, k_y = 0.3)$ (bottom).	165
6.19	Value of k_{\perp}^2 along a field line for 0% hill (solid red) and 6.2% hill (dashed blue) configurations.	167
6.20	Electrostatic eigenmode structures for 6.2% hill for $k_y = 0.3$ and $k_x = 0.5$ (solid line), $k_x = 0.6$ (dotted line) and $k_x = 0.7$ (dashed line).	168

ABSTRACT

The ability to optimize stellarator geometry to reduce transport has led to renewed interest in stellarators for magnetic confinement fusion. In this thesis, turbulence in the Helically Symmetric eXperiment (HSX), a quasi-helically symmetric stellarator, is investigated through application of the gyrokinetic code GENE and the new reduced fluid model PTSM3D. Gyrokinetics provides an efficient formalism for high-fidelity plasma turbulence simulations by averaging out the unimportant fast particle gyromotion. Both GENE and PTSM3D are capable of handling three-dimensional stellarator geometries.

The first comprehensive simulations of Trapped Electron Mode turbulence in HSX are presented. HSX geometry introduces a complex landscape of unstable eigenmodes, with strongly ballooning modes, non-symmetric modes, and extended modes all coexisting at the same wavelengths. Non-linear simulations display several characteristics unique to HSX. At long wavelengths, surprisingly large transport is observed despite the corresponding linear growth rates being small, and is attributed to nonlinear mode interactions. Zonal flows are prominent, however the velocity shear is insufficient to be solely responsible for saturation.

These linear and nonlinear features are the consequence of the low global magnetic shear of HSX, which allows modes to extend far along field lines and requires simulation domains spanning multiple poloidal turns to properly resolve. Subdominant modes with extended structures play an important role in nonlinear energy transfer at long wavelengths, removing energy from shorter wavelength modes to both drive long-wavelength transport and dissipate energy through transfer to stable modes. Calculations with PTSM3D of triplet correlation times, used to quantify turbulence saturation, support the gyrokinetic results and show geometry plays a crucial role in turbulence saturation. Energy transfer from unstable modes to stable modes through non-zonal modes is the dominant mechanism in quasi-helically symmetric

geometry, while zonal modes catalyze transfer in quasi-axisymmetric geometry. PTSM3D triplet correlation time calculations for HSX configurations with different magnetic hill and well depths accurately reproduce the nonlinear simulation trends, demonstrating the suitability of triplet correlation times as the first nonlinearly-derived metric for turbulence optimization.

1 INTRODUCTION

The purpose of this chapter is to provide motivation and background for the study of kinetic plasma turbulence in stellarators. After introducing the process of nuclear fusion energy, important plasma physics concepts needed to study plasma turbulence in toroidal plasmas are briefly covered.

1.1 Fusion Energy and Plasma Physics

Progress and growth in human civilization and society has been predicated on an increasing ability to extract usable forms of energy from fuels to drive technological advancements. Traditionally, this has been accomplished primarily with combustion of fossil fuels, as is shown in Fig. 1.1 where the annual energy consumption of the United States is dominated by fossil fuels. This is a straight-forward process as combustion releases the energy

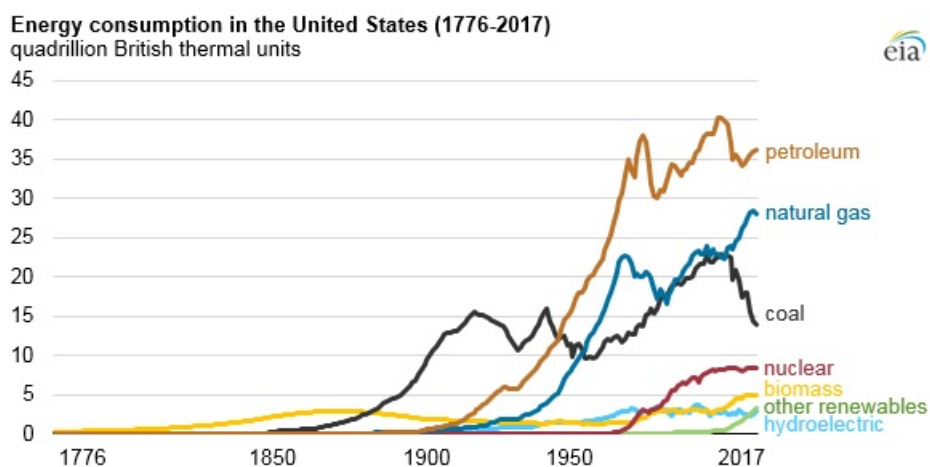


Figure 1.1: Annual energy consumption by source in the United States. Source: U.S. Energy Information Agency, Monthly Energy Review, June 2018.

stored in intermolecular bonds, however, there are several downsides. First, there is only a finite amount of consumable fossil fuel on the Earth and as society expands, the rate of energy usage and fuel consumption will only increase. Thus, there is a finite lifetime over which traditional fossil fuels can sustain society, which is estimated to be on the order of hundreds of years (Shafiee and Topal, 2009). Second, combustion of fossil fuels releases harmful byproducts, most prominent of which are carbon compounds such as carbon dioxide and methane. In sufficient quantity, these gases generate a greenhouse effect, serving to warm the entire Earth's climate similar to the processes at work in the atmosphere of Venus, an outcome one clearly wishes to avoid. Finally, combustion of fossil fuels is a rather ineffective means of extracting energy, as chemical fuels tend to have relatively low energy densities. Gasoline, for example, has an energy density of approximately 80 MJ/kg (Freidberg, 2007). Future technologies will be even more energy intensive, such as the powering of more and larger computing devices, mass deployment of electric vehicles, operation of water desalination and purification facilities, and advanced recycling plants, all of which will require energies on a scale difficult for chemical fuels to easily supply. Thus, there is a strong need for a clean way of providing energy at much higher capacity.

Chemical fuels release energy by breaking bonds associated with electromagnetic forces, which of the four fundamental forces is relatively weak, stronger only than gravity. If one can access the strong nuclear force, responsible for binding nucleons in atomic nuclei, the binding energy provides orders-of-magnitude more energy than the breaking of electromagnetic bonds. A well-known method to access the binding energy is to split an atomic nucleus into byproducts with lower binding energies and capture the excess binding energy as heat, the approach taken by nuclear fission. While this provides a fuel approximately a million times more energy dense than chemical fuels, there are still substantial drawbacks. Nuclear fission energy is optimal when the constituent atoms have high atomic number,

such as uranium. Splitting these atoms often leads to dangerous radioactive byproducts, with half-lives on the order of 10^5 years. Furthermore, for nuclear fission to make sense for power generation, a self-sustaining chain reaction is required, where a nucleus split by a neutron produces more neutrons to split more nuclei. There is the small, but real, risk of a runaway reaction, potentially leading to explosive deconfinement and the dispersal of radioactive byproducts. The need to ensure the safety of operation and waste containment adds significant expense to the fission process, calling into question its viability as a long-term energy generation solution.

Conversely, it is possible to access nuclear energy by *combining* nuclei in the process known as *nuclear fusion*, provided the resulting product has a lower binding energy than reactants. There are several advantages to pursuing this approach: fusion has an even higher energy density than fission, and fusion can more easily be accomplished effectively by light nuclei, where the by-products have little to no radioactive waste (Freidberg, 2007). However, the act of achieving fusion with net power production is a significant challenge. The strong nuclear force is an attractive but very short-range force; at larger distances there is a repulsive Coulomb barrier that nuclei must overcome to fuse, making reaction cross-sections extremely small. This requires that nuclei collide with high enough velocities to overcome the barrier. To produce enough usable energy and a self-sustaining reaction, this must be done at high densities, which is not an easy prospect. One must confine mutually repulsive charged nuclei sufficiently long to heat them to the requisite velocities necessary to overcome the Coulomb barrier, requiring temperatures on the order 100 million Kelvin, well past the temperatures corresponding to atomic ionization energies. This temperature corresponds to roughly 10 keV, while the ionization energy of atomic hydrogen is 13.6 eV. At such temperatures, gases become ionized and transition into the *plasma* state, a distinct state of matter. The behavior of plasmas is fundamentally different from a neutral gas due to the presence

of long-range electromagnetic forces. Coulomb forces exist between all constituent plasma particles and alter collisional gas dynamics. Furthermore, plasmas can be manipulated by externally imposed electromagnetic fields and have complicated interactions with self-generated fields. These properties enable a rich variety of complex collective behavior, encompassing such subjects like Landau damping (Landau, 1946) or plasma turbulence, the subject this thesis.

1.1.1 Basic plasma theory

As it is impossible to simultaneously solve for the position and velocity of every particle in a plasma, where there are often $\sim 10^{20}$ degrees of freedom, one is motivated to treat the plasma with a statistical approach. The fundamental quantity used to describe a plasma is the single-particle phase-space *distribution function* $f_\sigma(\mathbf{x}, \mathbf{v}, t)$, where σ denotes the particle species, \mathbf{x} are the configuration space coordinates, \mathbf{v} are the velocity space coordinates, and t is time (Krall and Trivelpiece, 1973; Bellan, 2006). The distribution function is the number of particles per unit volume of the six-dimensional phase space and has the property

$$\int d\mathbf{x} d\mathbf{v} f_\sigma(\mathbf{x}, \mathbf{v}, t) = N_\sigma, \quad (1.1)$$

where N_σ is the total number of particles of species σ in the plasma. The distribution function is not a readily physically-observable quantity, and has the properties of a probability distribution so that it can be interpreted as the probability of finding a particle at position \mathbf{x} with velocity \mathbf{v} in an interval $(\mathbf{x} + d\mathbf{x}, \mathbf{v} + d\mathbf{v})$. The evolution of the plasma distribution function is governed by the Fokker-Planck equation, an expression of the evolution of phase space density:

$$\frac{\partial f_\sigma}{\partial t} + \frac{\partial \mathbf{x}}{\partial t} \cdot \frac{\partial f_\sigma}{\partial \mathbf{x}} + \frac{\partial \mathbf{v}}{\partial t} \cdot \frac{\partial f_\sigma}{\partial \mathbf{v}} = \frac{\partial f_\sigma}{\partial t} \Big|_{\text{collisions}} + \mathcal{S} - \mathcal{D}. \quad (1.2)$$

On the left hand side, the first term is the change in time of f_σ at position (\mathbf{x}, \mathbf{v}) , the second term is the flux of particles in configuration space, and the third term is the flux of particles in velocity space. On the right hand side, the first term is the change in particles due to Coulomb collisions, the second term represents a source of plasma particles, such as through ionization processes, while the last term represents a particle sink, such as through atomic recombination. If the terms on the right hand side of Eq. (1.2) vanish in the collisionless, source-free limit, integrating Eq. (1.2) over phase space with the physical boundary condition that the distribution function vanish at infinite distances and velocities shows the number of particles in the plasma is conserved in time. The collision frequency between plasma particles scales inversely proportional to the particle's thermal velocity, $\nu_{\text{coll}} \propto v_{th}^{-3}$, where $v_{\sigma,th} = \sqrt{2T_\sigma/m_\sigma}$ and T_σ is the particle temperature and m_σ is the particle mass. Thus the collisionless limit is effectively reached in hot, fully ionized plasmas where scattering with neutral particles is negligible. The collisionless limit will be adopted for the remainder of this thesis and Eq. (1.2) is referred to as the Vlasov equation:

$$\frac{\partial f_\sigma}{\partial t} + \frac{\partial \mathbf{x}}{\partial t} \cdot \frac{\partial f_\sigma}{\partial \mathbf{x}} + \frac{\partial \mathbf{v}}{\partial t} \cdot \frac{\partial f_\sigma}{\partial \mathbf{v}} = 0. \quad (1.3)$$

Electric and magnetic fields enter Eq. (1.3) in the expression $\partial \mathbf{v} / \partial t$. In the absence of any external mechanical pressures or forces, such as gravity, and in the stationary, non-relativistic limit applicable for magnetic confinement fusion, the acceleration of a particle at position \mathbf{x} with velocity \mathbf{v} takes the conventional form involving Coulomb and Lorentz forces:

$$\frac{\partial \mathbf{v}}{\partial t} = \frac{q_\sigma}{m_\sigma} \left(\mathbf{E}(\mathbf{x}, t) + \frac{\mathbf{v} \times \mathbf{B}(\mathbf{x}, t)}{c} \right). \quad (1.4)$$

$\mathbf{E}(\mathbf{x}, t)$ and $\mathbf{B}(\mathbf{x}, t)$ are the *total* (external and internal) electric and magnetic fields and the mass and charge of species σ are m_σ and q_σ , respectively, and c is the speed of light in a vacuum. The internal electromagnetic fields

are generated by all the other plasma particles, which is not retained with the one-particle distribution. Rather, the internal fields are determined by an appropriate averaging over the microscopic fields from nearest neighbor particles and the resulting internal fields are not the exact fields, but only an average. The equations for the average $\mathbf{E}(\mathbf{x}, t)$ and $\mathbf{B}(\mathbf{x}, t)$ are closed by Maxwell's equations:

$$\nabla \cdot \mathbf{E}(\mathbf{x}, t) = 4\pi\rho_{\text{total}}(\mathbf{x}, t), \quad (1.5)$$

$$\nabla \times \mathbf{E}(\mathbf{x}, t) = -\frac{1}{c} \frac{\partial \mathbf{B}(\mathbf{x}, t)}{\partial t}, \quad (1.6)$$

$$\nabla \times \mathbf{B}(\mathbf{x}, t) = \frac{4\pi}{c} \mathbf{J}_{\text{total}}(\mathbf{x}, t) + \frac{1}{c} \frac{\partial \mathbf{E}(\mathbf{x}, t)}{\partial t}, \quad (1.7)$$

$$\nabla \cdot \mathbf{B}(\mathbf{x}, t) = 0. \quad (1.8)$$

ρ_{total} in Eq. (1.5) is the total charge density $\rho_{\text{total}} = \rho_{\text{external}} + \rho_{\text{plasma}}$ and $\mathbf{J}_{\text{total}}$ in Eq. (1.7) is the total current density $\mathbf{J}_{\text{total}} = \mathbf{J}_{\text{external}} + \mathbf{J}_{\text{plasma}}$. The plasma charge density is defined as

$$\rho_{\text{plasma}}(\mathbf{x}, t) = \sum_{\sigma} q_{\sigma} \int d\mathbf{v} f_{\sigma}(\mathbf{x}, \mathbf{v}, t) = \sum_{\sigma} q_{\sigma} n_{\sigma}(\mathbf{x}, t), \quad (1.9)$$

where the plasma density n_{σ} is defined as the zeroth velocity moment of the plasma distribution function, $n_{\sigma}(\mathbf{x}, t) = \int d\mathbf{v} f_{\sigma}(\mathbf{x}, \mathbf{v}, t)$. Similarly, the plasma current density is defined as the first velocity moment of the distribution function

$$\mathbf{J}_{\text{plasma}}(\mathbf{x}, t) = \sum_{\sigma} q_{\sigma} \int d\mathbf{v} \mathbf{v} f_{\sigma}(\mathbf{x}, \mathbf{v}, t). \quad (1.10)$$

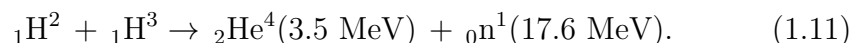
The presence of the plasma distribution function in Eq. (1.9) has serious consequences, as the second and third terms in Eq. (1.3) are now *nonlinear* in the distribution function with the form $\mathbf{E}f \sim f^2$, since \mathbf{E} is proportional to f by Eq. (1.5) and (1.9). This nonlinearity is responsible for a wealth

of interesting and complex plasma behavior, such as plasma turbulence. Only in rare, idealized circumstances may Eq. (1.3) be solved exactly, consequently a whole industry in physics and mathematics has been developed to understand the behavior of solutions to nonlinear equations like Eq. (1.3). More recently, this has entailed the use of direct numerical simulation of Eqs. (1.3), (1.5)–(1.8) and is the approach taken for the bulk of this thesis. Analytic approaches, historically accomplished through dimensional scaling analysis or with the study of reduced models, still play an important role, especially when coupled with numerical simulations, as they can more easily elucidate the complicated physics that may be obscured by the vast amount of information present in simulations.

1.2 Magnetic Confinement Fusion

Stellar fusion, which powers stars, is achieved through gravitational confinement, where enough mass is accreted to the point where core densities and temperatures are sufficiently large so that fusion occurs naturally. Obviously, this is not possible for laboratory fusion prospects. Instead, one can take advantage of the fundamental fact that charged particles follow magnetic field lines to achieve *magnetic confinement fusion*. Technological considerations on achievable plasma pressures help select which fusion process to pursue and study for a future reactor. One requirement must be met for any fusion process to be a viable candidate for use in a reactor: more energy must be released than was required to drive the reaction. Fusion in stellar cores often occurs in a complicated process, for example proton-proton fusion or the CNO-cycle in main sequence stars (Bethe, 1939), which takes advantage of the incredible core pressures to overcome smaller reaction cross sections. Terrestrial fusion favors larger reaction cross sections, the most promising of

which is the deuterium-tritium, or D-T, reaction:



This reaction produces a 3.5 MeV α particle (doubly ionized helium) and a 17.6 MeV neutron that can be captured by a thermal blanket and converted to usable heat, yielding a energy density of approximately 338×10^6 MJ/kg (Freidberg, 2007), seven orders of magnitude larger than gasoline and an order of magnitude greater than nuclear fission. Ideally, the 3.5 MeV α particle will continue to circulate in the plasma and transfer energy back to the plasma through collisions or wave-particle resonances, helping heat the plasma to create a “burning” plasma. However, unlike in a nuclear fission reaction, no new fuel particle is created in this reaction, therefore continual fueling is required.

As referenced previously, plasmas are easily manipulated by magnetic fields since they are composed of charged particles. Charged particles in a magnetic field will gyrate around field lines due to the Lorentz force, limiting motion perpendicular to field lines, the key concept behind magnetic confinement fusion research. While the Lorentz force provides confinement perpendicular to magnetic field lines, particles are still free to stream along magnetic field lines and increasing the plasma temperature can cause particles to stream ever more quickly along field lines due to increased thermal velocities. In the first attempts at magnetic confinement fusion, such as the pinch and magnetic mirror concepts, this led to unacceptable “streaming losses”. The streaming-loss problem can be solved if the plasma has no ends to stream out from, as is the case when the plasma is confined in the shape of a torus, where most progress towards a realized fusion power plant has been made. While this class of configurations solves the streaming-loss problem, but also introduces a new set of complications related to toroidal geometry. Nevertheless, toroidally-confined plasma fusion experiments have obtained plasma temperatures and densities closest to achieving a break-

even reactions and continue to provide the most promising route to a fusion reactor (Keilhacker et al., 2001; Fujita et al., 1999).

1.2.1 Single particle drifts

Shaping a magnetic field into a torus necessarily introduces non-uniformity into the magnetic field, where the magnetic field decays like $1/R$ in a toroidal solenoid, with R the major radius of the torus. When a charged particle gyrates in a non-uniform magnetic field, it does not sample the same magnetic field strength everywhere and changes in the magnetic field strength changes the instantaneous radius of the particle orbit. This means that when the particle executes one full “orbit”, the endpoint of the orbit has moved relative to the starting point, and the particle has *drifted*. For phenomena occurring on time scales slower than the inverse cyclotron frequency, given by $\Omega_{c\sigma} = q_\sigma B/m_\sigma c$, one may perform an average over the particle orbit and obtain the motion of a particle’s *guiding center*. In non-uniform magnetic fields, particle guiding centers execute “ ∇B ” drifts:

$$\mathbf{v}_{\nabla B} = \frac{v_\perp^2}{2\Omega_c B^2} \mathbf{B} \times \nabla B. \quad (1.12)$$

When a magnetic field is curved, the “curvature” guiding center drift is a manifestation of centrifugal forces due to parallel motion:

$$\mathbf{v}_c = \frac{v_\parallel^2}{\Omega_c B} \mathbf{B} \times \hat{\mathbf{b}} \cdot \nabla \hat{\mathbf{b}} = \frac{v_\parallel^2}{\Omega_c B} \mathbf{B} \times \boldsymbol{\kappa}, \quad (1.13)$$

where $\boldsymbol{\kappa} = \hat{\mathbf{b}} \cdot \nabla \hat{\mathbf{b}}$ is the magnetic field line curvature. In Eqs. (1.12) and (1.13) B is the magnetic field at the guiding center, and v_\perp and v_\parallel is the particle velocity in the direction perpendicular and parallel to the magnetic field at the guiding center, respectively. The unit vector along the magnetic field in Eq. (1.13) is denoted by $\hat{\mathbf{b}}$. In addition to the ∇B and curvature

drifts, if an electric field \mathbf{E} is present there is a drift called the “ $\mathbf{E} \times \mathbf{B}$ ” drift:

$$\mathbf{v}_E = c \frac{\mathbf{E} \times \mathbf{B}}{B^2} = c \frac{\mathbf{B} \times \nabla \Phi}{B^2}, \quad (1.14)$$

where Φ is the electrostatic potential such that $\mathbf{E} = -\nabla \Phi$. Note that this drift is independent of both charge and mass and is identical for both ions and electrons. In the event that the background electric and magnetic fields change in time, on scales much longer than the inverse cyclotron frequency, there is an additional drift called the “polarization” drift:

$$\mathbf{v}_p = -\frac{1}{\Omega_c B} \left(\frac{d}{dt} (\mathbf{v}_E + \mathbf{v}_{\nabla B} + \mathbf{v}_c) \right) \times \mathbf{B}. \quad (1.15)$$

The combination of all of the drifts lead to complicated guiding center trajectories that in general can only be integrated numerically. In a toroidal configuration where the magnetic field points only in the toroidal direction, the ∇B and curvature drifts are vertical. Due to charge dependence in Eqs. (1.12) and (1.13), electrons and ions drift in opposite directions, setting up a vertically-directed electric field. The $\mathbf{E} \times \mathbf{B}$ drift is then radially outward for both ions and electrons and can quickly transport particles out of the plasma. To order prevent this, the magnetic field must have a poloidal component so that particles drifting out of the plasma on one side of the torus can move to the other side and drift back into the plasma.

1.2.2 Particle trapping

Adding a poloidal component to the magnetic field allows particles to transit from the low-field-side to the high-field-side region of the magnetic field. In magnetic configurations where the change in the instantaneous magnetic field is slow compared to the orbit-averaged magnetic field, $(B(t) - \langle B \rangle) / \langle B \rangle \ll 1$ where $\langle B \rangle$ is the orbit-averaged magnetic field, the magnetic moment $\mu = mv_{\perp}^2 / 2B$ is conserved. The most important consequence of μ conservation

is the phenomenon of magnetic mirroring and particle trapping. The energy of a plasma particle moving in a static magnetic field is conserved:

$$\frac{mv_{\parallel}^2}{2} + q\phi(s) + \mu B(s) = H, \quad (1.16)$$

where ϕ is the electrostatic potential and s is the distance along the field line. Consider a case where $\phi(s) = 0$. The parallel velocity can then be expressed as

$$v_{\parallel}(s) = \pm \sqrt{\frac{2}{m} (H - \mu B(s))}. \quad (1.17)$$

If at some point along the field line $\mu B(s) = H$, $v_{\parallel} = 0$ and the particle will reverse direction. Thus μ conservation creates a magnetic mirror force if $H < \mu B_{\max}$, where B_{\max} is the magnetic field maximum. Since a plasma is a distribution of particles with different velocities, some fraction of the particles will always be trapped between the low-field and high-field sides of a toroidal plasma. However, local variations in the equilibrium magnetic field strength may also trap particles. The presence of trapped particles, either local or global, can alter plasma transport significantly. Classical transport in toroidal configurations is modified by particle trapping, and the resulting process is referred to as neoclassical transport. In certain situations this can lead to a dramatic increase in transport and for many years was the primary impediment to the success of stellarators (Hinton, 1976; Helander, 2014), which will be discussed further in Ch. 2. Furthermore, trapped particles can both modify existing and introduce new plasma instabilities, leading to further modification of transport properties, and is examined in more depth in Sec. 1.3.

1.2.3 Magnetohydrodynamic equilibrium

Plasmas must be confined on time scales long enough to reach sufficient temperatures for fusion, a situation best described by *magnetohydrodynamics*

(MHD), where the plasma is treated as a single magnetofluid with mass density $\rho = \sum_{\sigma} m_{\sigma} n_{\sigma}$ and velocity $\mathbf{U} = \left(\sum_{\sigma} m_{\sigma} n_{\sigma} \mathbf{u}_{\sigma} \right) / \rho$. This approach assumes the characteristic time scales are much longer than collisional times and the length scales are larger than gyroradius scales, thus neglecting kinetic effects (Bellan, 2006). The ideal MHD equations, which neglects visco-resistive effects, are given by

$$\frac{\partial \rho}{\partial t} + \nabla \cdot (\rho \mathbf{U}) = 0, \quad (1.18)$$

$$\rho \left[\frac{\partial \mathbf{U}}{\partial t} + \mathbf{U} \cdot \nabla \mathbf{U} \right] = \frac{\mathbf{J} \times \mathbf{B}}{c} - \nabla P, \quad (1.19)$$

$$\frac{\partial \mathbf{B}}{\partial t} - \nabla \times (\mathbf{U} \times \mathbf{B}) = 0, \quad (1.20)$$

$$\frac{P}{\rho^{\gamma}} = \text{const.}, \quad (1.21)$$

where $\mathbf{J} = \sum_{\sigma} n_{\sigma} q_{\sigma} \mathbf{u}_{\sigma}$ is plasma current and P is an isotropic pressure and $\gamma = (N + 2)/N$ is the adiabatic index with N the number of degrees of freedom. When the plasma is in equilibrium with no macroscopic flows, the left side of Eq. (1.19) vanishes and we have the MHD force balance equation:

$$\mathbf{J} \times \mathbf{B} = \nabla P. \quad (1.22)$$

Requiring Eq. (1.22) be satisfied means that \mathbf{B} and \mathbf{J} lie on surfaces of constant pressure, as dotting either \mathbf{B} or \mathbf{J} with Eq. (1.22) yields

$$\mathbf{B} \cdot \nabla P = 0, \quad \mathbf{J} \cdot \nabla P = 0. \quad (1.23)$$

The consequences of Eq. (1.23) are central to the methods discussed in Ch. 2, as the magnetic field and plasma current must exist on surfaces of constant pressure, allowing the pressure to be used as an independent coordinate.

1.2.4 Toroidal configurations

Different approaches may be taken to produce the poloidal magnetic field necessary to confine plasma particles. The simplest toroidal configurations are symmetric in the geometric toroidal angle (called axisymmetric) and can be fully described with a two-dimensional representation. Axisymmetric experiments comprise the bulk of fusion experiments, the most prevalent design is that of the *tokamak* (Wesson, 2003), an example of which is shown in Fig. 1.2a. Tokamak plasmas are confined by a magnetic field produced by magnetic coils that close poloidally so as to generate only a toroidal field. The poloidal magnetic field is generated by the plasma itself through a toroidal plasma current. This is a simple, but relatively delicate scheme. The plasma current must be driven externally, either through ohmic current drive or radio-frequency current drive, or internally through bootstrap currents (Helander and Sigmar, 2002). Ohmic-driven plasmas are limited to producing plasmas in pulses due to engineering constraints on the transformers required to drive the plasma current. Furthermore, large plasma currents make free energy available to drive MHD instabilities (White, 2001; Wesson, 2003; Bellan, 2006), which can degrade heat and particle confinement, as well as disrupt the plasma entirely. The susceptibility to MHD instabilities places constraints on achievable plasma pressures and currents, limiting the prospective fusion gain. Careful control must be exercised during tokamak operation to avoid these instabilities, further complicating the path to a reactor.

The *stellarator* concept, on the other hand, produces the poloidal magnetic field without relying on a large plasma current. This is accomplished by twisting magnetic flux surfaces through specifically constructed magnetic coils designed to produce the proper field line pitch. An example of a stellarator with the corresponding set of complicated three-dimensional magnetic field coils is shown in Fig. 1.2b, where a field line on the stellarator flux surface is shown in green. Stellarators are not free of plasma

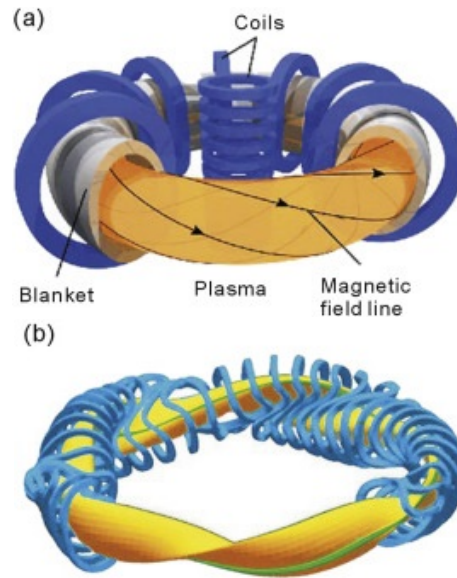


Figure 1.2: Example of a tokamak (top) and a stellarator (bottom). The magnetic surface is in yellow, with a field line overlaid. Source: Xu (2016)

current, satisfying Eq. (1.22) and $\nabla \cdot \mathbf{J} = 0$ always gives rise to parallel Pfirsch-Schlüter currents, but the magnitude of the current can be reduced such that the plasma is stable against current-driven MHD instabilities. A major benefit of this approach is that eliminating both MHD instabilities and ohmic current drive enables continuous, steady-state operation, a highly desirable quality. The major drawback to the stellarator approach is that by providing the necessary field twist externally, the magnetic field necessarily becomes three-dimensional, introducing significant complexity to both the theory and experiment. However, this is not necessarily a detriment. Stellarators can explore a vast space of possible three-dimensional configurations to *optimize* the magnetic geometry to target certain physics properties, such as neoclassical transport, or in the case of this thesis, turbulence. Optimization is a key component to modern stellarator research and turbulence

optimization has been identified as one of the key frontiers for the next generation of stellarators (Gates et al., 2018).

1.2.5 Plasma dynamics at multiple scales

A hallmark of fusion plasmas is a hierarchy of intrinsic length and time scales. These scales are dependent on plasma parameters, such as plasma temperature, density and degree of magnetization. By confining plasmas in strong magnetic fields, several distinct time scales exist. Microscopic processes, such as Debye shielding (Bellan, 2006) and cyclotron motion, occur on short time and length scales, while processes that affect the plasma equilibrium occur on long time and length scales. For illustrative purposes, typical time and length scales for a fusion-experiment-relevant plasma will be given, with ion and electron temperatures $T_{i,e} = 2keV$, densities $n_{i,e} = 10^{20}m^{-3}$ and with a 1 T magnetic field embedded in the plasma. Additionally, assume the plasma has a size of 1m and is singly ionized with effective charge of $Z = 1$. The relevant intrinsic time scales are listed in Table 1.1 and the length scales are listed in Table 1.2.

Tables 1.1 and 1.2 make it clear a large range of time and length scales exist in a hot, dense plasma. However, these are not the only scales involved in realistic situations where plasmas and magnetic fields are rarely uniform. The presence of inhomogeneities introduces free energy to drive plasma waves and nonlinear phenomena like turbulence, all of which have distinct time and spatial scales and can modify the transport time scales over which macroscopic quantities evolve. Often for fusion purposes, the time scales of interest are how quickly particles and energy are transported perpendicular to the magnetic field. The time scale for collisions to transport

Time scale	Magnitude	Physical importance
Inverse Plasma Frequency ω_p^{-1}	$\sim 10^{-11}$ s (e), $\sim 10^{-9}$ s (i)	Time scale over which Debye shielding occurs
Inverse Cyclotron Frequency Ω_c^{-1}	$\sim 10^{-10}$ s (e), $\sim 10^{-7}$ s (i)	Time scale for particle gyration around magnetic field
Inverse Collision Frequency ν_c^{-1}	$\sim 10^{-4}$ s (ee, ei), $\sim 10^{-2}$ s (ii), ~ 1 s (ie)	Time scale over which plasma relaxes to collisional equilibrium distribution
Transport Time τ_h	$\sim 10^3$ s (ii)	Time scale over which heat and particles are transported by collisional effects

Table 1.1: Intrinsic time scales for a uniform plasma with $T_{i,e} = 2keV$, $n_{i,e} = 10^{20}m^{-3}$ in a background magnetic field of 1 T. The ion species is hydrogen, with an ion-to-electron mass ratio $m_i/m_e = 1837$. Time scales are identified by species in parentheses, with interspecies interactions denoted by letter combinations.

quantities can be estimated from diffusive transport, for example for the density $\partial n/\partial t \approx D\partial^2 n/\partial x^2$, where x is perpendicular to the direction of the magnetic field. The diffusion coefficient is obtained from random walk arguments, $D \sim (\Delta x)^2/\Delta t$, where Δx is a characteristic step size and Δt is the characteristic time between steps. For cross-field transport in a uniform plasma, this is simply $\Delta x = \rho_L$ and $\Delta t = \nu_c^{-1}$, leading to long time scales for hot collisionless plasmas. However, the characteristic step sizes for collective plasma behavior, like waves and turbulence, can be significantly larger

Length scale	Value	Physical importance
Debye Length λ_D	$\sim 10^{-5}$ m	Distance over which Debye shielding occurs
Gyroradius ρ_L	$\sim 10^{-3}$ m (e), $\sim 10^{-2}$ m (i)	Radius of particle orbiting a field line
Macroscopic Size L	~ 1 m	Typically scales over which background profiles vary
Collision length λ_c	$\sim 10^3$ m (ii)	Distance an ion travels between collisions

Table 1.2: Intrinsic length scales for a uniform plasma of size 1m with $T_{i,e} = 2keV$, $n_{i,e} = 10^{20}m^{-3}$ in a background magnetic field of 1 T. The ion species is hydrogen, with an ion-to-electron mass ratio $m_i/m_e = 1837$. Length scales are identified by species in parentheses, with interspecies interactions denoted by letter combinations.

than the gyroradius. Turbulent correlation lengths for ion scale turbulence, relevant for this thesis, are often on the order of tens of gyroradii, with corresponding time scales that are often significantly faster than the inverse collision frequency. This intermediate-scale transport is responsible for a large fraction of heat and particle transport in fusion devices (Liewer, 1985), and understanding and reducing these transport processes is key to realizing magnetic confinement fusion.

When the collision frequency is significantly smaller than the cyclotron frequency, $\nu_{ei} \ll \Omega_{ce}, \Omega_{ci}$ and the Larmor radius is significantly smaller than perpendicular macroscopic lengths $\rho_L \ll L_{\perp}$, the plasma is considered

magnetized. This is generally the case for magnetic confinement fusion and implies that the magnetic field, rather than collisions, determine the behavior of the plasma on short time scales. Spatially, this manifests with a plasma that is *anisotropic* where typical perpendicular plasma scales are much smaller than parallel scales $l_{\perp} \ll l_{\parallel}$, where perpendicular and parallel are measured with respect to the magnetic guide field direction. For magnetized plasmas, typified by the above example, it is clear that a range of time scales exist between the cyclotron frequency and the collision frequency, with approximately five orders of magnitude between the two. If one wants to investigate phenomena occurring on intermediate time scales, resolving the details of phenomena with time scales faster than cyclotron frequencies or slower than collisions may be unnecessary. This has important implications for reducing expense in plasma turbulence simulations, as most kinetic plasma turbulence in magnetic fusion experiments occur in this intermediate range of time and length scales as discussed in Sec. 1.4, and is the motivation for the computational methods discussed in Ch. 3.

1.3 Drift Waves

Realistic plasmas tend not to be uniform nor quiescent. As was shown in Sec. 1.2.1, non-uniform magnetic fields lead to drift motion of ions and electrons. This drift motion, when coupled with non-uniformities, such as pressure gradients, 3D geometry, collisions, and Landau damping can lead to distinct drift motion between ions and electrons, which in turn generate *drift waves*. Drift waves occurring on gyroradius length scales are often referred to as *microinstabilities*, and are not captured with an MHD treatment. Toroidally-confined fusion plasmas are necessarily non-uniform, with density and temperature profiles that peak in the core of plasma and disappear at the plasma edge. Despite being characterized by small scales compared to equilibrium scales, drift waves are capable of driving significant

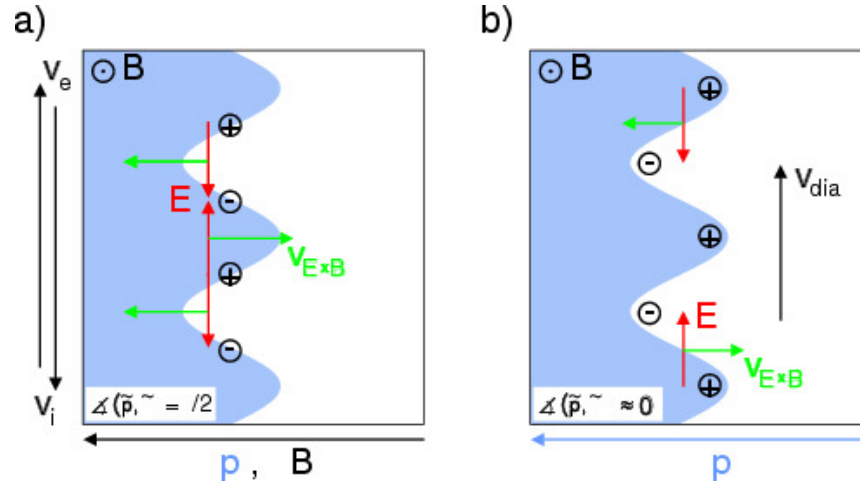


Figure 1.3: Schematic of a curvature-driven drift wave (left) and a slab drift wave (right). The pressure gradient is in the $-x$ direction, the magnetic field is out of the page in the z direction. Source: Grulke and Klinger (2002)

transport and are believed to be largely responsible for the observed losses in toroidally-confined fusion experiments (Liewer, 1985).

A useful way to gain an intuition for the physical mechanisms behind drift waves is to examine the collisional “universal” instability, where the plasma has a density gradient and is schematically shown in Fig. 1.3b. It is universal because all plasmas with finite extent must have a density gradient. Furthermore, the universal instability highlights the benefit of ignoring scales irrelevant to the problem at hand to reduce complexity. The plasma is assumed to be in a nearly equilibrium state such that any quantity g can be written as $g = g_0 + g_1 + \dots$, where $g_{i+1}/g_i \sim \delta \ll 1$, and g_0 satisfies the equilibrium equations. *Linearized* equations are obtained when terms of order δ^2 and higher are neglected. Assume an infinite Cartesian domain with a z -directed uniform magnetic field and a plasma density gradient in the x direction, $n_0 \sim \exp(x/L_n)$, where L_n is the scale length of the density variation. Consider a periodic potential perturbation,

$\Phi_1 = \tilde{\Phi}_1 \exp(ik_y y + ik_z z - i\omega t)$. For the universal instability, we assume $v_{i,th} \ll \omega/k \ll v_{e,th}$, so that the ions have a cold, adiabatic response and electrons have a hot, isothermal response. Additionally, we will adopt the plasma frame where Φ_0 vanishes.

Detailed mathematical analysis of this instability is presented elsewhere (Krall and Trivelpiece, 1973; Bellan, 2006), while here emphasis will be placed on the physical mechanisms behind the drift wave. The collisional universal drift-wave can be analyzed with the fluid plasma equations. Using the assumption $\omega/k \ll \sqrt{T_e/m_e}$, the parallel electron momentum equation reads

$$-q_e \frac{\partial \Phi_1}{\partial z} - \frac{T_e}{n_e} \frac{\partial n_e}{\partial z} - \nu_{ei} m_e u_{ez} = 0, \quad (1.24)$$

where u_{ez} is the fluid electron velocity in the z -direction and ν_{ei} is the electron-ion collision frequency. If collisions are absent, this yields a Boltzmann response for the electrons

$$n_e = n_{e0} \exp(-q_e \Phi_1 / T_e). \quad (1.25)$$

Linearizing Eq. (1.25) gives the perturbed density response $n_{e1}/n_{e0} = -q_e \Phi_1 / T_e$, so that the perturbed density and perturbed potential are in phase. Physically, the electron Boltzmann response means electrons stream infinitely fast along field lines (compared to the wave) to cancel out any charge imbalances. If there are collisions, electrons can no longer respond infinitely quickly to potential perturbations, meaning the density and potential are no longer in phase. At lowest order, the perpendicular ion drift is described by the perturbed $\mathbf{E} \times \mathbf{B}$ drift and associated polarization drift

$$\mathbf{u}_{i\perp} = \frac{-\nabla \Phi_1 \times \mathbf{B}}{B^2} + \frac{m_i}{q_i B^2} \frac{d}{dt} (-\nabla \Phi_1) \quad (1.26)$$

while the parallel ion velocity is given by

$$u_{i1z} = \frac{k_z q_i \Phi_1}{\omega m_i}. \quad (1.27)$$

In the absence of collisions, the physical picture of the drift wave emerges. The perturbed $\mathbf{E} \times \mathbf{B}$ drift advects ions and electrons in the x -direction. Because of the presence of the density gradient, more density is advected from the higher density region to the lower-density region, but because the density and potential are in phase, the induced $\mathbf{E} \times \mathbf{B}$ drift does not enhance the perturbation. Conservation of ion density implies another y -directed drift exists proportional to the density gradient, called the diamagnetic drift as indicated by the vertical drift in Fig. 1.3b. At lowest order, the plasma is quasineutral so that $n_{e1} = n_{i1}$. The Boltzmann response means electrons move instantaneously to ensure quasineutrality and the density and potential perturbations are in phase. This gives a wave dispersion relation

$$(1 + k_y^2 \rho_s^2) \omega^2 - \omega_* \omega + k_z^2 c_s^2 = 0, \quad (1.28)$$

where $\omega_* = (k_y T_e / q_e n_e B) dn_{e0} / dx$ is the diamagnetic frequency, $c_s = \sqrt{T_e / m_i}$ is the ion acoustic velocity and $\rho_s = c_s / \Omega_{ci}$ is the ion acoustic Larmor radius. Equation 1.28 has solutions

$$\omega = \frac{\omega_*}{1 + k_y^2 \rho_s^2} \pm \frac{\sqrt{\omega_*^2 / 4 + 4k_z^2 c_s^2}}{1 + k_y^2 \rho_s^2}, \quad (1.29)$$

which are always real. Thus the wave neither grows nor decays, it only propagates with the frequency given by Eq. (1.29). Adding collisions modifies Eq. (1.28)

$$(1 + k_y^2 \rho_s^2) \omega^2 - \omega_* \omega + k_z^2 c_s^2 + i(\omega - \omega_*) \frac{\nu_{ei} m_e}{k_z^2 T_e} = 0, \quad (1.30)$$

so that now solutions of Eq. (1.30) also have an imaginary part. For $k_z c_s \ll \omega$

one can show the imaginary part is given by

$$\omega_i = \gamma = \pm \frac{\omega_*^2 k_y^2 \rho_s^2}{(1 + k_y^2 \rho_s^2)^3} \frac{\nu_{ei} m_e}{k_z^2 T_e}, \quad (1.31)$$

so that there is a solution where the wave is always growing in time. When the electrons can no longer respond infinitely quickly to potential perturbations because of collisions, there is a phase shift between the density and potential such that when the perturbed $\mathbf{E} \times \mathbf{B}$ drift advects the plasma density along the gradient in the x direction, there is an excess of ion density that is not canceled by a Boltzmann response. The perturbed ion density then enhances the perturbed electrostatic potential, which in turn amplifies the perturbed drift, continuing the cycle. Thus the wave grows with time. One should note that the universal instability has a somewhat restrictive set of parametric conditions and need not be satisfied in many conditions. The key concept is that breaking the electron Boltzmann response with additional physics, such as through collisions, is responsible for linear instability. This allows for a slew of possible drift waves to exist in toroidal plasmas. Equation (1.31) also displays an important aspect of drift waves, as there is a stable solution where the growth rate is negative. When analyzing plasma dynamics using only linear instability analysis, these solutions are often regarded as unimportant. However, when stable modes nonlinearly interact with other stable and unstable modes, they can play an important role in the turbulent state. This idea is explored further in Sec. 1.4 and is integral to the results of Ch. 5.

1.3.1 Trapped particle modes

Trapped electron modes (Kadomtsev and Pogutse, 1967) are drift waves that arise from particle trapping in toroidal magnetic configurations in the presence of density or temperature gradients. For simplicity, we will assume a background density gradient in the negative x direction, a magnetic field

line in the z direction, and a potential perturbation that varies periodically in the y direction, as is shown in Fig. 1.3a. If particles are not trapped (passing) both the magnetic drifts and the perturbed $\mathbf{E} \times \mathbf{B}$ drift average out as the particle circulates around the torus. Deeply trapped particles with $v_{\parallel} = 0$, on the other hand, experience drifts in the $\pm y$ -direction that do not average out. From Eqs. (1.12) and (1.13), electrons and ion will drift in opposite directions with different velocities. The fluctuating $\mathbf{E} \times \mathbf{B}$ velocity advects plasma in the $\pm x$ direction and the ∇B and curvature drifts cause electrons and ions to drift in the y direction with different speeds. Because of the density gradient, a higher density of ions and electrons drifts from $x - \Delta x$ to x , while a lower density of ions and electrons drifted from $x + \Delta x$, to x . This establishes a y -directed electric field that induces an $\mathbf{E} \times \mathbf{B}$ drift that reinforces the original $\mathbf{E} \times \mathbf{B}$ drift, thus causing the mode to grow, as is shown in Fig. 1.3a. If the mode frequency is smaller than the electron bounce frequency, but larger than the ion bounce frequency, it is called a *trapped electron mode* (TEM). If the wave frequency is smaller than both the electron and ion bounce frequencies, it is called a *trapped ion mode* (TIM).

Trapped particle modes may also be destabilized by temperature gradients. Instead of density differences, the differences in the velocities along the temperature gradient create charge separation and reinforce the $\mathbf{E} \times \mathbf{B}$ drift. TEMs can present a significant problem for toroidal plasmas, as there is always a non-negligible thermal population of trapped particles available to drive the instability. Instability occurs if the plasma gradients are pushed above a critical value, generally dependent on plasma parameters and specifics of the magnetic geometry, and can significantly degrade plasma confinement.

1.3.2 Temperature gradient modes

Another class of drift waves are temperature gradient modes (see Tang (1978) and references therein). The *ion temperature gradient* (ITG) mode

can exist even if the electrons have a Boltzmann response. Using the same setup as Sec. 1.3.1, but replacing the density gradient with a temperature gradient in the negative x -direction, it is easy to see a charge separation again occurs. The ions coming from $x - \Delta x$ to x have faster drift velocities in the y -direction than ions coming from $x + \Delta x$ to x . Even if the densities are the same, this creates a charge separation because the ions are at different y positions. The y -directed electric field induces an $\mathbf{E} \times \mathbf{B}$ drift that reinforces the original drift and the mode grows. If kinetic electrons are considered, the differences in drift velocities lead to a further charge separation and an enhancement of growth rates. A density gradient can be used to stabilize the ITG, as it will change the phase of the wave.

An analogous instability exists for electrons called the *electron temperature gradient* (ETG) mode. However, the ETG occurs on a smaller scale than the ITG, by a factor $\sqrt{m_e/m_i}$, and generally is not as impactful as the ITG. Like TEMs, controlling ITGs poses a serious challenge for toroidal confinement fusion.

1.4 Plasma turbulence

Understanding plasma turbulence represents one of the grand challenges of plasma physics. A wide body of literature exists on the subject and no justice can be done to the breadth of the field here. The purpose of this section is to introduce turbulence concepts essential to the rest of this thesis and concepts presented here will not be rigorously derived. Turbulence in a fluid or plasma is characterized by unpredictable motions and interactions over a large range of spatial scales as the result of nonlinear coupling. The seemingly random evolution of a turbulent flow motivates studying the statistical properties of turbulence, for example, see the exhaustive treatment in Krommes (2002), and is the approach taken in this thesis. Typically, plasma turbulence in the core of toroidal fusion devices is characterized

by small amplitude fluctuations in quantities around an equilibrium value and a common goal of turbulence theory and computation is to describe the statistical behavior of these fluctuations. Despite possessing small amplitudes, fluctuations play an important role in fusion plasma physics as turbulent advection of heat and particles occurs on a much faster time scale than collisional diffusive processes and can drastically increase transport and degrade plasma confinement. For the purpose of understanding this thesis, the following concepts are emphasized.

Turbulence occurs over a range of spatial scales

When turbulence occurs on time scales slower than the inverse cyclotron frequency, plasma motion is effectively described by guiding center motion. Averaging Eq. (1.3) over the cyclotron motion gives the evolution for the guiding center distribution function where the guiding center velocity is specified by the drift velocities, Eqs. (1.12)–(1.15). The presence of Φ in the $\mathbf{E} \times \mathbf{B}$ drift means the term $\mathbf{v}_E \cdot \nabla f$ is a quadratic nonlinear term. Assuming a Fourier decomposition $f(\mathbf{x}) = \sum_{\mathbf{k}} \hat{f}_{\mathbf{k}} \exp(i\mathbf{k} \cdot \mathbf{x})$ for the fluctuating quantities and a guide field in the z direction, the Fourier transform of the $\mathbf{E} \times \mathbf{B}$ nonlinearity becomes

$$\mathcal{F}(\mathbf{v}_E \cdot \nabla f) = \frac{c}{B} \sum_{\mathbf{k}'} (\mathbf{k} \times \mathbf{k}' \cdot \hat{\mathbf{z}}) \hat{\Phi}_{\mathbf{k}-\mathbf{k}'} \hat{f}_{\mathbf{k}'}. \quad (1.32)$$

By virtue of involving the sum over \mathbf{k}' , the distribution function at a particular \mathbf{k} involves coupling between modes at all scales. The wavenumber dependence of quantities like $\hat{\Phi}_{\mathbf{k}}$ and $\hat{f}_{\mathbf{k}}$ is in general not uniform across \mathbf{k} and thus the contribution of each coupling term of the sum in Eq. (1.32) will also be non-uniform. If the majority of the coupling occurs between modes where $|\mathbf{k}|$ and $|\mathbf{k}'|$ are similar in magnitude, the turbulence is considered *local*, otherwise it is considered *non-local*.

Background gradients introduce perpendicular anisotropy

When combined with the $\mathbf{E} \times \mathbf{B}$ drift, radial plasma pressure gradients in fusion plasmas break the symmetry of the Vlasov equation. This generates anisotropic structures perpendicular to the magnetic field. To see this, consider a plasma with a z -directed magnetic field and a gradient in the x direction. Using the splitting $f = f_0 + f_1$, where the plasma pressure gradients appear in ∇f_0 , the $\mathbf{E} \times \mathbf{B}$ drift introduces a linear wave term into Eq. (1.3) for f_1 :

$$\frac{\partial f_1}{\partial t} + \underbrace{\frac{\partial \Phi_1}{\partial y} \frac{\partial f_1}{\partial x} - \frac{\partial \Phi_1}{\partial x} \frac{\partial f_1}{\partial y}}_{\text{nonlinear}} + \underbrace{\frac{\partial \Phi_1}{\partial y} \frac{\partial f_0}{\partial x}}_{\text{linear}} + \dots = 0. \quad (1.33)$$

The nonlinear term is symmetric in x and y , but since the zeroth order distribution function has no gradients in the y -direction, the equation for f_1 now has an anisotropic linear term that breaks the symmetry of the equations. This confers special status on the y direction. When the turbulence is in statistical equilibrium, the wave term and nonlinear term must balance, which in turn makes the nonlinear energy transfer anisotropic and energy condenses at $k_y = 0$ (Gatto et al., 2006), which is possible because the y direction is physically periodic in a toroidal plasma. The $k_y = 0$ structures that form are called *zonal flows* and play an important role in the dynamics of plasma turbulence, and in particular, the dynamics of ITG and ∇n -driven TEM turbulence. Zonal flows have electric potential structure in the x direction, which in turn generate y -directed, sheared $\mathbf{E} \times \mathbf{B}$ flows. Velocity shear has the ability to shear apart turbulent eddies and can lead to *shear suppression* of turbulence, and is an important feature of the enhanced confinement regimes of tokamaks (Burrell, 1997; Terry, 2000).

Energy transfer to stable modes

For a turbulent flow to be in a quasi-steady state the energy input into the flow must be balanced by some dissipative process so that the total energy is essentially constant, in a process known as *turbulence saturation*. In standard theories of forced or decaying turbulence, energy is transferred conservatively by the nonlinearity between scales in a *turbulent cascade* until it reaches a scale where dissipative processes like viscosity or friction dominate (Kolmogorov, 1991a,b; Frisch, 1995). In instability-driven turbulence, like drift-wave-driven plasma turbulence studied in this thesis, gradients of mean profiles, such as pressure, provide a source of free energy to drive turbulence. However, as was seen in Sec. 1.3, *stable* drift waves also exist at the same wavenumbers as linearly unstable drift waves and have largely been ignored by most standard theories of plasma turbulence, as they do not contribute to energy drive. Through the action of the nonlinearity in the Vlasov equation, these stable modes can be excited to finite amplitudes, and by virtue of having negative growth rates, provide effective sources of energy dissipation (Terry et al., 2006). Including the impact of stable modes in the turbulent energy budget paints a fundamentally different picture of fusion plasma turbulence compared to standard turbulence theories, as now there is both a source and sink of energy at the same spatial scales. Recent computational studies have shown that stable modes play a large role the saturation of drift-wave-driven plasma turbulence in fusion devices, for example see Hatch et al. (2009, 2011a); Makwana et al. (2012); Pueschel et al. (2016); Terry et al. (2018); Hegna et al. (2018); Whelan et al. (2018); Faber et al. (2018). This provides strong evidence that the role of stable modes should be accounted for in future investigations of plasma turbulence and will be further examined in this thesis.

1.5 Thesis Outline

The remainder of this thesis is organized as follows. Chapter 2 covers important concepts for toroidally confined plasmas. Derivations of magnetic coordinates and collisionless orbit confinement in toroidal plasmas is presented and different classes of stellarators are introduced based on magnetic geometry, including the Helically Symmetric eXperiment stellarator (HSX). Chapter 3 gives a brief derivation of the gyrokinetic Vlasov equation and gyrokinetic Maxwell's equations and introduces the GENE (Gyrokinetic Electromagnetic Numerical Experiment) code, a massively-parallel simulation code used to study plasma turbulence. Also introduced in Ch. 3 is the concept of a flux tube, the numerical simulation domain used in this thesis. The first comprehensive studies of ∇n -driven TEM turbulence in HSX using GENE are presented in Ch. 4, focusing on the unique features present in HSX simulations. The impact of low global magnetic shear on stellarator turbulence simulations is the focus of Ch. 5, demonstrating that subdominant and stable modes play an important role in the dynamics of turbulence saturation in HSX. In Ch. 6, these observations are used to motivate a fluid model of ITG turbulence saturation for stellarators, which has been implemented numerically and applied to different stellarator configurations. Chapter 7 provides a summary of the important results of this thesis and a look at future research directions.

2 TOROIDAL MAGNETIC FIELDS AND STELLARATORS

The main thrust of magnetic confinement fusion is in the area of toroidal confinement. The aim of this chapter is to introduce key concepts and mathematical tools for studying stellarators. Magnetic coordinates are introduced, which provide a useful coordinate system for analyzing toroidally-confined plasmas. The physics of collisionless particle orbits is discussed to provide the context to introduce quasi-symmetry and quasi-omnigeneity, crucial features of modern stellarator design. The chapter concludes with a brief overview of current stellarator experiments, focusing on the HSX stellarator.

2.1 Magnetic Coordinates

It is useful when discussing toroidal configurations to make use of toroidal-like coordinates (r, θ, ϕ) , as is shown in Fig. 2.1 for the simplest configuration. These toroidal-like coordinates have an inverse mapping to a cylindrical coordinate system (R, Θ, Z) centered in the middle of the torus defined by

$$\begin{aligned} R &= R_0 + r \cos(\theta) \\ \Theta &= -\phi \\ Z &= r \sin(\theta), \end{aligned} \tag{2.1}$$

where $r \in [0, a]$ with $\theta \in [0, 2\pi)$ and $\phi \in [0, 2\pi)$ as geometric angles. Note that this is not the true definition of toroidal coordinates, see D'haeseleer et al. (1991) for more discussion. For a complex three-dimensional toroidal plasma equilibrium, it is difficult to construct this mapping using the geometric angles θ and ϕ . Nevertheless, much of the nomenclature used to describe Fig. 2.1 is useful when discussing generalized toroidal configurations. In

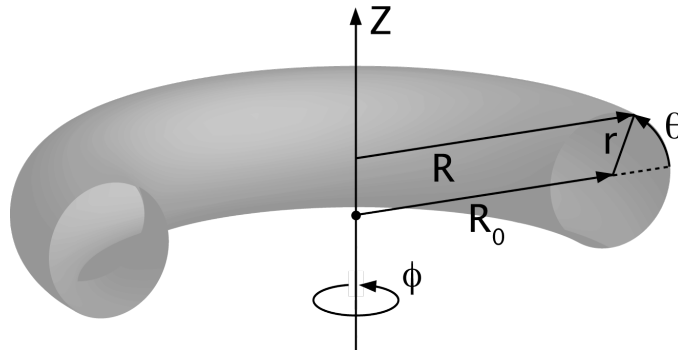


Figure 2.1: Simple toroidal coordinate system. Source: FusionWiki.

Fig. 2.1, the circle with radius R_0 defines the minor axis and is centered around the major axis, hence R_0 denotes the major radius and a denotes the minor radius. The device aspect ratio is defined as R_0/a . The coordinate θ revolves around the minor axis and is called the *poloidal* angle. The angle ϕ revolves around the major axis and is called the *toroidal* angle. As will be shown in Sec. 2.1, transforming to *magnetic coordinates* is highly useful for toroidal magnetic configurations, however the “poloidal” and “toroidal” angles are now generalized angles, but will still have the same effective meaning. The *radial* coordinate will refer to any coordinate serving as a flux surface label that is independent of poloidal and toroidal angle and is measured from the magnetic axis where it has zero value.

When describing toroidal MHD equilibria, it is beneficial for theory and computational purposes to introduce *magnetic coordinates*. The following derivations follow that of Helander (2014). The key feature of magnetic coordinates is that the equation for a magnetic field line in magnetic coordinates is a straight line. The coordinate system will be chosen such that the magnetic field is a straight line in a poloidal angle ϑ and a toroidal angle ϕ . The third coordinate can be chosen such that it is constant on constant-pressure surfaces, for simplicity the kinetic pressure p will be used. It should be noted that these coordinates are curvilinear, but in general not

orthogonal.

2.1.1 General magnetic coordinates

Equation (1.23) allows the magnetic field to be written as

$$\mathbf{B}(p, \vartheta, \phi) = B_\vartheta(p, \vartheta, \phi) \nabla p \times \nabla \vartheta + B_\phi(p, \vartheta, \phi) \nabla p \times \nabla \phi. \quad (2.2)$$

Since the magnetic field must be divergence free, we have

$$\left(\frac{\partial B_\vartheta}{\partial \phi} + \frac{\partial B_\phi}{\partial \vartheta} \right) \nabla p \cdot \nabla \vartheta \times \nabla \phi = 0. \quad (2.3)$$

The most general forms of B_ϑ and B_ϕ that satisfy Eq. (2.3) are

$$B_\vartheta = \frac{\partial f(p, \vartheta, \phi)}{\partial \vartheta} + g(p), \quad (2.4)$$

$$B_\phi = -\frac{\partial f(p, \vartheta, \phi)}{\partial \phi} + h(p), \quad (2.5)$$

where $f(p, \vartheta, \phi)$, $g(p)$, and $h(p)$ are continuously differentiable functions. Equation (2.2) now reads

$$\mathbf{B} = \left(\frac{\partial f}{\partial \vartheta} + g(p) \right) \nabla p \times \nabla \vartheta + \left(h(p) - \frac{\partial f}{\partial \phi} \right) \nabla p \times \nabla \phi. \quad (2.6)$$

We can note that by letting $g(p) = \psi'(p)$, $h(p) = \chi'(p)$, and $\nu(p, \vartheta, \phi) = f(p, \vartheta, \phi)/\psi'(p)$, where the primes denote derivatives with respect to p , Eq. (2.6) can be transformed into an equation involving only total derivatives:

$$\begin{aligned} \mathbf{B} &= \psi' \nabla p \times \nabla \vartheta + \psi' \frac{\partial \nu}{\partial \vartheta} \nabla p \times \nabla \vartheta - \chi' \nabla p \times \nabla \phi + \psi' \frac{\partial \nu}{\partial \phi} \nabla p \times \nabla \phi \\ &= \nabla \psi \times \nabla \vartheta + \nabla \psi \times \nabla \nu + \nabla \phi \times \nabla \chi. \end{aligned} \quad (2.7)$$

One can now define a new poloidal angle $\theta = \vartheta + \nu$, where $\nu = \nu(p, \vartheta, \phi)$ is a periodic function of ϑ and ϕ , so that the magnetic field has the representation

$$\mathbf{B} = \nabla\psi \times \nabla\theta + \nabla\phi \times \nabla\chi. \quad (2.8)$$

The functions ψ and χ have special designation. They are constant on constant-pressure surfaces since they are functions of p alone, and can be shown to be equivalent to the toroidal and poloidal magnetic flux. This can easily be seen by integrating Eq. (2.8) over $\phi = \text{constant}$ or $\theta = \text{constant}$ domains bounded by a constant pressure surface, denoted by ψ . The Jacobian is defined by

$$\sqrt{g}^{-1} = (\nabla\psi \times \nabla\theta) \cdot \nabla\phi = \mathbf{B} \cdot \nabla\phi. \quad (2.9)$$

The magnetic field can be written in the contravariant representation $\mathbf{B} = B^\psi \mathbf{e}_\psi + B^\theta \mathbf{e}_\theta + B^\phi \mathbf{e}_\phi$, where \mathbf{e}_j is the covariant basis vector of the j coordinate. The components B^j are defined by the dual relation with the contravariant basis vectors $B^j = \mathbf{B} \cdot \nabla j$, thus the toroidal component of the magnetic field is $B^\phi = \mathbf{B} \cdot \nabla\phi$. The toroidal magnetic flux is simply

$$\int_0^\psi d\bar{\psi} \int_0^{2\pi} \frac{\mathbf{B} \cdot \nabla\phi}{(\nabla\bar{\psi} \times \nabla\theta) \cdot \nabla\phi} = 2\pi\psi. \quad (2.10)$$

Thus ψ can be interpreted as the toroidal flux. A similar expression can be used to show χ is the poloidal flux. Since both ψ and χ are functions only of pressure, they cannot vary independently, and one can regard χ as a function of ψ so that $\nabla\chi = (d\chi/d\psi)\nabla\psi$. The quantity $d\chi/d\psi$ is known as the rotational transform ι , an extremely useful quantity when describing toroidal magnetic configurations. The equation for a magnetic field line can be written as (D'haeseleer et al., 1991)

$$\frac{\mathbf{B} \cdot \nabla\psi}{d\psi} = \frac{\mathbf{B} \cdot \nabla\theta}{d\theta} = \frac{\mathbf{B} \cdot \nabla\phi}{d\phi}. \quad (2.11)$$

Equating the last two terms and rearranging, we have

$$\frac{d\theta}{d\phi} = \frac{\mathbf{B} \cdot \nabla\vartheta}{\mathbf{B} \cdot \nabla\phi} = \frac{d\chi}{d\psi} = \iota. \quad (2.12)$$

Thus the rotational transform measures the field line pitch, or the number of poloidal turns the field makes for each toroidal turn and is related to the quantity known as the safety factor q used in tokamak literature by $q = 1/\iota$. More importantly, Eq. (2.12) is a straight line in θ and ϕ . Generally, ι is an irrational number, then according to Eq. (2.12) a field line will densely cover the flux surface. Noting that θ and ϕ are now not independent, we can define the *field line label* as $\alpha = \theta - \iota\phi$ and choose either θ or ϕ as the independent coordinate. Equation (2.8) can be re-written in a final form in (ψ, α, s) coordinates, where s is used to parameterize distance along the field line, and is referred to as the Clebsch representation:

$$\mathbf{B} = \nabla\psi \times \nabla\alpha. \quad (2.13)$$

Equation (2.13) has the property $\mathbf{B} \cdot \nabla\alpha = 0$, meaning α is constant on a field line, hence designation field line label. One should note that the field line angles θ and ϕ cannot both represent the geometric poloidal and toroidal angles due to the presence of the periodic function ν . One can choose either θ or ϕ to be a geometric angle, but should be mindful that the non-chosen coordinate will then no longer be the standard geometric angle.

2.1.2 Boozer coordinates

The above-presented coordinates are not unique, due to the freedom to define the generalized toroidal and poloidal angles. When discussing quasi-symmetry and stellarators, it is useful to use *Boozer coordinates* (Boozer, 1981). Boozer coordinates are defined by modifying both the poloidal and

toroidal angles

$$\begin{aligned}\theta &= \theta' + \epsilon\nu, \\ \phi &= \phi' + \nu,\end{aligned}\tag{2.14}$$

respectively. First, note that the plasma current in a static equilibrium has the same properties as the magnetic field, $\mathbf{J} \cdot \nabla p = 0$ and $\nabla \cdot \mathbf{J} = 0$. Thus we can write an equation for the plasma current in a similar form to Eq. (2.6):

$$\mathbf{J} = \left(I'(\psi) - \frac{\partial K}{\partial \theta} \right) \nabla \psi \times \nabla \theta + \left(-G'(\psi) + \frac{\partial K}{\partial \phi} \right) \nabla \phi \times \nabla \psi.\tag{2.15}$$

Using the identities $\nabla \times \nabla f = 0$ and $\nabla \times (f\mathbf{A}) = f\nabla \times \mathbf{A} + \nabla f \times \mathbf{A}$, Eq. (2.15) can be written as

$$\mathbf{J} = \nabla \times (I\nabla\theta + G\nabla\phi + K\nabla\psi),\tag{2.16}$$

which has the form of Ampere's law, $\mu_0\mathbf{J} = \nabla \times \mathbf{B}$, implying the magnetic field can be written in the covariant form

$$\mathbf{B} = I\nabla\theta + G\nabla\phi + K\nabla\psi + \nabla H,\tag{2.17}$$

where ∇H is an integration constant. Like ψ and χ , I and G have physical meaning. $I(\psi)$ denotes the toroidal current inside the flux surface ψ , while $G(\psi)$ is the poloidal current between ψ and a surface at infinity. If we use the transformation given in Eq. (2.14), the magnetic field given by Eq. (2.17) can be modified to read

$$\mathbf{B} = I\nabla\theta' + G\nabla\phi' + K'\nabla\psi + \nabla H',\tag{2.18}$$

with

$$\begin{aligned} H' &= H + (\iota I + G)\nu, \\ K' &= K - \nu \frac{d}{d\psi}(\iota I + G). \end{aligned}$$

Boozer coordinates are defined by choosing ν such that H' vanishes,

$$\nu = -\frac{H}{\iota I + G}, \quad (2.19)$$

yielding a magnetic field of the form (dropping the primes):

$$\mathbf{B} = I(\psi)\nabla\theta + G(\psi)\nabla\phi + K(\psi, \theta, \phi)\nabla\psi. \quad (2.20)$$

2.2 Collisionless Orbit Confinement

The essential property for plasma confinement is that collisionless particle orbits do not exit the plasma. Toroidal confinement requires one to account for effects of the grad-B and curvature drifts, which move particles across flux surfaces as they travel along field lines. Even when collisionless orbits are confined, it is still desirable to limit the excursion across flux surfaces. If the particle drifts are large compared to the gyroradius, collisions occurring at the point of maximum excursion will significantly enhance diffusive transport due to increased characteristic radial step sizes. As mentioned in Sec. 1.2.2, historically, stellarators have been plagued by high levels of neoclassical transport. To understand this, it is helpful to examine the particle orbits and orbit confinement in a magnetized toroidal plasma, where $\rho_L/L \ll 1$. In this limit, particle orbits are described at lowest order by the motion of the guiding center, where the gyrocenter Lagrangian is given by (Taylor, 1964)

$$L = \frac{m \left(\hat{\mathbf{b}} \cdot \dot{\mathbf{R}} \right)^2}{2} + \frac{Ze}{c} \mathbf{A} \cdot \dot{\mathbf{R}} - \mu B - Ze\Phi. \quad (2.21)$$

Here, \mathbf{R} is the guiding center position, $\dot{\mathbf{R}} = v_{\parallel} \hat{\mathbf{b}} + \mathbf{v}_d$ is the guiding center velocity, \mathbf{A} is the vector potential such that $\mathbf{B} = \nabla \times \mathbf{A}$, the effective charge number is Z , and μ is an invariant quantity that is the magnetic moment at zeroth-order in ρ_L/L . The electrostatic potential Φ is in general a flux function at zeroth-order, $\Phi \approx \Phi_0(\psi)$. The drift velocity is given by the drifts in Sec. 1.2.1, $\mathbf{v}_d = \mathbf{v}_E + \mathbf{v}_{\nabla B} + \mathbf{v}_c$.

In a static equilibrium, both the particle energy H and magnetic moment μ are conserved and constants of the motion. In tokamaks, ϕ is an ignorable coordinate, thus the canonical momentum p_ϕ is also a constant of the motion. In (ψ, θ, ϕ) coordinates, the Euler-Lagrange equation for ϕ gives (with R the major radius)

$$p_\phi = mRv_\phi - \frac{Ze}{c}\chi, \quad (2.22)$$

where χ is the poloidal magnetic flux. Since p_ϕ is constant, $\Delta p_\phi = 0$, leading to an estimate for the excursion of particle orbits. The velocity v_ϕ can be estimated as the thermal velocity v_{th} , giving a maximum excursion of $\Delta\chi = mcRv_{th}/Ze = RB_p\rho_p$, where B_p is the poloidal magnetic field and $\rho_p = mcv_{th}/qB_p$ is the poloidal gyroradius. The poloidal flux goes as $\chi \sim B_p Rr$, giving $\Delta\chi = B_p R\Delta r$. Thus equating the two expressions for $\Delta\chi$, we find the radial excursion $\Delta r \sim \rho_p$ and that collisionless orbits in a tokamak do not deviate by more than a poloidal gyroradius and are therefore confined, a result known as Tamm's theorem (Tamm, 1961). As such, neoclassical transport in tokamaks is only dominant deep in the plasma core where $B_p \rightarrow 0$.

In stellarator geometry, the largest neoclassical transport contributions come from trapped particles. In a tokamak, the magnetic field is often close to up-down symmetric and the grad-B and curvature drift is in the vertical direction everywhere. Particles on the top side will then drift out of the plasma, while particles on the bottom side will drift into the plasma. Up-down symmetry and energy conservation implies that trapped particles bouncing between mirror points spend equal time on the top and bottom

of the plasma and thus drifts exactly cancel over a bounce time. In a stellarator, particles are often trapped in spatially localized regions that are not up-down symmetric, allowing trapped particles to have non-zero bounce averaged drifts and to drift off flux surfaces. This can enhance transport via direct orbit loss or by increasing the effective radial step size in diffusive transport. For collisionless plasmas, one finds the diffusion coefficient goes like $D \propto T^{7/2}$, leading to prohibitively large losses for classical stellarators (Hinton, 1976; Helander, 2014).

The time rate of change of the radial position of a particle is given by

$$\frac{d\psi}{dt} = \left(v_{\parallel} \hat{\mathbf{b}} + \mathbf{v}_d \right) \cdot \nabla \psi = \left(\frac{v_{\perp}^2}{2\Omega_c B^2} \mathbf{B} \times \nabla B + \frac{v_{\parallel}^2}{\Omega_c B} \mathbf{B} \times \boldsymbol{\kappa} \right) \cdot \nabla \psi, \quad (2.23)$$

Using the identity $\mathbf{B} \times \nabla B \cdot \nabla \psi = \mathbf{B} \times \boldsymbol{\kappa} \cdot \nabla \psi$, we can expand the quantity $\mathbf{B} \times \nabla B \cdot \nabla \psi$ into components, finding

$$\mathbf{B} \times \nabla B \cdot \nabla \psi \propto \mathbf{B} \times \left(\frac{\partial B}{\partial \psi} \nabla \psi + \frac{\partial B}{\partial \alpha} \nabla \alpha + \frac{\partial B}{\partial s} \nabla s \right) \cdot \nabla \psi. \quad (2.24)$$

The first term on the right hand side of Eq. (2.24) cancels by vector identity, showing that the radial drift is determined by the variation of the *magnitude* of B in the flux surface in a direction perpendicular to the magnetic field, $\partial B/\partial \alpha$ and $\partial B/\partial s$. The $\partial B/\partial \alpha$ term is unique to stellarators and conveys the fact that in a general stellarator, the magnetic field strength will be different on different field lines. Particles can then be trapped if the B_{\max} values are different from field line to field line, further enhancing transport.

2.2.1 Quasi-symmetry

If one can construct magnetic field configurations where the magnetic field strength is independent of field line label α , it will eliminate one source of drift motion off flux surfaces in Eq. (2.23). This implies that a particle

drifting from one field line to another on the same flux surface with the same magnetic field and magnetic field gradient will not be able to tell what field line it is on. This condition can be stated succinctly as (Landreman, 2011; Helander, 2014)

$$\frac{\mathbf{B} \times \nabla \psi \cdot \nabla B}{\mathbf{B} \cdot \nabla B} = F(\psi), \quad (2.25)$$

which expresses that the ratio of the magnetic drift term to the mirror force is a flux function. Expressing Eq. (2.25) in Boozer coordinates (ψ, θ, ϕ) gives

$$G \frac{\partial B}{\partial \theta} - I \frac{\partial B}{\partial \phi} = F(\psi) \left(\iota \frac{\partial B}{\partial \theta} + \frac{\partial B}{\partial \phi} \right). \quad (2.26)$$

Using a Fourier decomposition for the field strength

$$B(\psi, \theta, \phi) = \sum_{m,n} B_{m,n}(\psi) \exp [i(m\theta - n\phi)] \quad (2.27)$$

implies the condition

$$(mG + nI - F(\iota m - n)) B_{m,n} = 0. \quad (2.28)$$

For Eq. (2.28) to be satisfied for all (m, n) , either $B_{m,n} = 0$ or

$$F(\psi) = \frac{(m/n)G + I}{(m/n)\iota - 1}. \quad (2.29)$$

The left side of Eq. (2.29) is independent of the ratio m/n , thus it can only be satisfied for one particular value of m/n . This implies that the magnetic field can only have a certain helicity, $m = kM$ and $n = kN$, where M and N are unique integers such that

$$B(\psi, \theta, \phi) = \sum_k B_{kM, kN} \exp (ik(M\theta - N\phi)). \quad (2.30)$$

The magnetic field strength depends only on the linear combination $M\theta - N\phi$ and is effectively independent of one of the Boozer angles. As such, magnetic field configurations with this property are called *quasi-symmetric* (Boozer, 1981). If $N = 0$, the magnetic field is called *quasi-axisymmetric*, if $M = 0$ it is *quasi-poloidally symmetric*, and if $M, N \neq 0$ it is *quasi-helically symmetric*. It should be made clear that quasi-symmetry is a property of the magnetic field strength B and *not* the vector magnetic field \mathbf{B} . In general, the direction of \mathbf{B} is not the same between field lines even if B has quasi-symmetry.

Importantly, we can demonstrate a substantial benefit of quasi-symmetric stellarators: guiding-center orbits are also confined to within a gyroradius of the flux surface. It is useful to write the guiding-center Lagrangian of Eq. (2.21) in Boozer coordinates (Helander and Sigmar, 2002; Helander, 2014)

$$L = \frac{m}{2B^2} \left(I\dot{\theta} + G\dot{\phi} \right)^2 + Ze \left(\psi\dot{\theta} + \chi\dot{\phi} \right) - \mu B(\psi, \theta, \phi) - Ze\Phi. \quad (2.31)$$

Particle energies and magnetic moments are still conserved in stellarator magnetic fields, however if the magnetic field strength is not quasi-symmetric, B has dependence on both θ and ϕ . This implies the canonical momenta conjugate to θ and ϕ are not conserved, since $\partial L/\partial\theta = \mu\partial B/\partial\theta \neq 0$ and $\partial L/\partial\phi = \mu\partial B/\partial\phi \neq 0$. If the magnetic field is quasi-symmetric, we may introduce a new coordinate $\eta = \theta - N\phi/M$ so that $B = B(\psi, \eta)$ and Eq. (2.31) becomes

$$L = \frac{m}{2B^2} \left(I\dot{\eta} + \left(G + \frac{NI}{M} \right) \dot{\phi} \right)^2 + \frac{Ze}{c} \left(\psi\dot{\eta} - \left(\chi - \frac{N\psi}{M} \right) \dot{\phi} \right) - \mu B - Ze\Phi. \quad (2.32)$$

Since ϕ does not appear in B and Φ is a flux function at lowest order, the canonical momentum associated with ϕ is conserved:

$$p_\phi = \frac{mv_{\parallel}(G + NI/M)}{B} - \frac{Ze}{c} \left(\chi - \frac{N\psi}{M} \right). \quad (2.33)$$

This supplies the third constant of motion necessary for Tamm's theorem to apply. Equation (2.33) has a similar form as (2.22), where the first term on the right hand side has dimensions of gyroradii and $\chi - N\psi/M$ serves as a radial coordinate. Using $\Delta\chi = \iota\Delta\psi$, the change in ψ is expressed as

$$\Delta\psi = \frac{mcv_{th}}{ZeB} \frac{G - NI/M}{\iota - N/M}. \quad (2.34)$$

The toroidal flux goes as $\psi \sim Br^2$ implying $\Delta\psi \sim 2B_t r \Delta r$. The toroidal current goes as $I \sim B_p r \sim \iota B_t r$ and the poloidal current as $G \sim B_t R$. This yields a radial excursion that goes as

$$\Delta r \sim \rho_p \frac{\iota}{N/M - \iota}. \quad (2.35)$$

Thus we find that in quasi-symmetric stellarators, guiding center orbits are confined within a poloidal gyroradius of flux surfaces. If $N/M - \iota > 1$, which occurs by design in quasi-symmetric stellarators, we see that the orbit confinement is *enhanced* compared to tokamaks. This effectively reduces neoclassical transport to levels commensurate with, or even better than, and equivalent tokamak. It should be noted that it is not possible to achieve exact quasi-symmetry everywhere, except in the case of perfect axisymmetry (Garren and Boozer, 1991a,b). The necessary deviations from quasi-symmetry can be small, as they are order $(r/R)^3$ and an effectively quasi-symmetric configuration can be obtained.

2.2.2 Quasi-omnigenity

Quasi-symmetry is not the only method for confining trapped particle orbits. Any magnetic field where the bounce-averaged radial drift of a particle vanishes is called *omnigenous*. If the magnetic fields change on scales large compared to particle orbits, there is another invariant quantity, called the

action invariant, which is defined as

$$\mathcal{J}(H, \mu, \psi, \alpha) = \int_{s_1}^{s_2} ds m v_{\parallel}, \quad (2.36)$$

where s_1 and s_2 are two points along the field line. For trapped particles, this implies \mathcal{J} is conserved when s_1 and s_2 are the bounce points, where $v_{\parallel} = 0$. In the Clebsch representation the particle Lagrangian has the form

$$L = \frac{m\dot{s}^2}{2} - \frac{Ze}{c}\alpha\dot{\psi} - \mu B - Ze\Phi. \quad (2.37)$$

As the $\dot{\alpha}$ does not explicitly appear in Eq. (2.37), the Euler-Lagrange equation for α yields an expression for $\dot{\psi}$:

$$\dot{\psi} = -\frac{\mu}{Ze} \frac{\partial B}{\partial \alpha} - \frac{\partial \Phi}{\partial \alpha}. \quad (2.38)$$

The energy of the particle is conserved, thus one may use Eq. (1.17) to express the time rate of change of the radial position of the particle's guiding center as a function of parallel velocity

$$\dot{\psi} = \frac{mv_{\parallel}}{Ze} \frac{\partial v_{\parallel}}{\partial \alpha} \Big|_{H, \mu, \psi, s}. \quad (2.39)$$

This expresses that the radial drift of the particle's guiding center is dependent on the field line label α . Similarly, the drift in α can be found through the Euler-Lagrange equation for ψ :

$$\dot{\alpha} = -\frac{mv_{\parallel}}{Ze} \frac{\partial v_{\parallel}}{\partial \psi} \Big|_{H, \mu, \psi, s}. \quad (2.40)$$

The accumulated drift as the particle moves along the field line is given by

$$\Delta\psi = \int_{t_1}^{t_2} dt \dot{\psi} = \frac{1}{Ze} \frac{\partial}{\partial \alpha} \int_{s_1}^{s_2} ds m v_{\parallel} = \frac{1}{Ze} \frac{\partial \mathcal{J}}{\partial \alpha}, \quad (2.41)$$

and

$$\Delta\alpha = \int_{t_1}^{t_2} dt\dot{\alpha} = -\frac{1}{Ze} \frac{\partial}{\partial\psi} \int_{s_1}^{s_2} ds m v_{\parallel} = -\frac{1}{Ze} \frac{\partial\mathcal{J}}{\partial\psi}, \quad (2.42)$$

As a particle moves from s_1 to s_2 the change in \mathcal{J} is given by

$$\Delta\mathcal{J} = \frac{\partial\mathcal{J}}{\partial H} \Delta H + \frac{\partial\mathcal{J}}{\partial\mu} \Delta\mu + \frac{\partial\mathcal{J}}{\partial\psi} \Delta\psi + \frac{\partial\mathcal{J}}{\partial\alpha} \Delta\alpha = 0, \quad (2.43)$$

as \mathcal{J} is a conserved quantity. The magnetic-moment-like coordinate μ is conserved, thus $\Delta\mu = 0$. For particles in orbits where there is no source of energy, e.g. no heating or instability drive, the total energy is conserved, thus $\Delta H = 0$. For this situation, Eq. (2.43) gives

$$\Delta\psi = -\frac{\partial\mathcal{J}/\partial\alpha}{\partial\mathcal{J}/\partial\psi} \Delta\alpha. \quad (2.44)$$

Taking s_1 and s_2 to be the bounce points for trapped particles, Eq. (2.44) implies that trapped particle orbits are confined if $\partial\mathcal{J}/\partial\alpha = 0$. Ideally, a configuration would be omnigenous where $\mathcal{J} = \mathcal{J}(\psi)$ everywhere for trapped particles. However, in practice this is not achievable for all trapped particle populations (Mynick et al., 1982; Cary and Shasharina, 1997; Mynick, 2006). Configurations that have $\mathcal{J} = \mathcal{J}(\psi)$ for deeply trapped particles are called *quasi-omnigenous*. Deeply trapped particles have very small parallel velocity, thus Eq. (2.36) implies $\mathcal{J} \approx 0$. As the particle drifts to different field lines, conservation of \mathcal{J} means the particle remains deeply trapped at the magnetic field minimum on each field line. Conservation of energy and magnetic moment on a particle trajectory implies $H/\mu = B = B_{\min}$, which in turn implies that all the magnetic field minima on a flux surface are identical, since H/μ must be conserved as the particle drifts. Since the drift is continuous, quasi-omnigenous configurations have the property that contours of B_{\min} are closed, and can close in the poloidal, toroidal, or helical direction.

2.3 Stellarator Experiments

The discovery of realizable magnetic configurations with quasi-symmetry (Nührenberg and Zille, 1988; Garabedian, 1996) and quasi-omnigenity (Nührenberg and Zille, 1986; Wobig, 1993) reinvigorated stellarator research and paved the way for the stellarator as a viable candidate for fusion. Stellarators designed to confine collisionless trapped particle orbits are called “neoclassical-transport-optimized” stellarators, or simply optimized stellarators, as the neoclassical transport is greatly reduced and no longer the dominant transport channel. Several quasi-symmetric stellarators have been designed, but only one has been built. The Helically Symmetric eXperiment (HSX) at the University of Wisconsin-Madison (Anderson et al., 1995) is a quasi-helically symmetric (QHS) stellarator with $(M = 1, N = 4)$ helical symmetry. As the only quasi-symmetric stellarator ever built, HSX has played an important role confirming experimentally many of the predictions of quasi-symmetry. Importantly, energy confinement roughly twice as large in the QHS configuration as compared to a configuration where QHS is intentionally spoiled has been observed (Canik et al., 2007). Other beneficial properties of QHS, such as reduced damping of plasma flows, have also been demonstrated (Gerhardt et al., 2005). Having shown the crucial reduction in neoclassical transport, the natural next step is to study microturbulence in the HSX configuration, which is the subject of this thesis.

Quasi-omnigenity has been realized in the Wendelstein 7-X (W7-X) experiment at the Max Planck Institute for Plasma Physics in Greifswald, Germany (Nührenberg et al., 1995). W7-X is a *quasi-isodynamic* stellarator, the name given to the class of quasi-omnigenous stellarators where the contours of B_{\min} close poloidally. W7-X is the largest stellarator experiment ever constructed, has recently demonstrated record energy confinement times for stellarators (Dinklage et al., 2018), and is projected to improve further as it reaches full operation capacity. Non-optimized stellarators, like the Large Helical Device (LHD), a heliotron (Wakatani, 1988) at the National Institute

for Fusion Studies in Toki, Japan, have also demonstrated milestones for stellarator research. Despite higher levels of neoclassical transport, LHD has performed record-long discharges (Yoshimura et al., 2005) and achieved central ion temperatures in excess of 8 keV (Nagaoka et al., 2015), important milestones for stellarator research.

One point that should be stressed is that optimized stellarators like HSX and W7-X are not exactly quasi-symmetric or quasi-isodynamic, thus the theoretical requirements for collisionless trapped particle confinement are not completely satisfied. The experimental results of HSX and W7-X do show that even though perfect optimization is not achieved, there is a substantial benefit to pursuing such optimization strategies. This suggests that there may be some flexibility on the requirements of quasi-symmetry or quasi-omnigeneity in stellarator design. This flexibility could be exploited to achieve other physics goals, such as decreased coil complexity or decreased turbulent transport, and provide an attractive basis for continued stellarator optimization research.

2.4 Chapter Summary

Magnetic coordinates, useful for performing calculations in toroidal geometry were derived, and will be used in the next chapter to construct the simulation domain for turbulence simulations in toroidal configurations. The concepts of quasi-symmetry and quasi-omnigeneity were shown to lead to confined collisionless particle orbits, reducing neoclassical transport and motivating the study of turbulence in optimized stellarators, which will be presented in Chs. 4 and 5 for the HSX stellarator.

3 GYROKINETIC SIMULATION OF PLASMA TURBULENCE

A derivation of the gyrokinetic Vlasov-Maxwell system of equations used to simulate plasma turbulence in magnetically-confined fusion plasmas is presented. The presentation here follows the modern derivation, making use of the Hamiltonian structure of particle motion in electromagnetic fields. An explanation of the flux-tube computational domain follows Faber et al. (2018). The normalized gyrokinetic equations solved by the gyrokinetic code GENE, the code used in this thesis, are presented. A brief literature review of gyrokinetic simulation of turbulence in stellarators is also presented.

3.1 Gyrokinetic Theory

The fundamental motivation behind *gyrokinetic* theory is to describe the kinetic behavior of fluctuations in strongly magnetized plasmas on time scales long compared to particle cyclotron frequencies. Drift waves and drift-wave-driven turbulence described in Secs. 1.3 and 1.4 typically have frequencies smaller than cyclotron frequencies, however the perpendicular fluctuation wavelengths λ_{\perp} can be on the order of, or smaller than, the ion gyroradius, $k_{\perp}\rho_i \geq 1$ where $k_{\perp} = 2\pi/\lambda_{\perp}$. Thus it is beneficial to average over the unimportant fast timescales associated with particle gyromotion, reducing the phase space dimension by one degree, while still retaining gyroradius effects. Conceptually, the gyroaverage can be viewed as replacing the exact helical orbits of particles by charged rings with a radius given by the particle's gyroradius, which are then subject to the same drift dynamics and nonlinear interactions as particles. This is highly advantageous for computational schemes as it significantly reduces the expense associated with resolving particle orbits.

Deriving the gyrokinetic system of equations is a complex endeavor and

an extensive body of literature already exists on the subject; as such it is not the purpose of this thesis to comprehensively re-derive gyrokinetic theory, see Brizard and Hahm (2007) and Abel et al. (2013) and references therein for rigorous derivations. Rather, the following presentation of the gyrokinetic Vlasov-Maxwell system will focus on the physical underpinnings of modern gyrokinetic theory, which can be somewhat opaque. In order to provide a tractable theory, gyrokinetics relies on what is called the gyrokinetic ordering, which is defined in terms of the background magnetized plasma and the fluctuating fields. Following Brizard and Hahm (2007), fluctuations are described by a characteristic frequency ω , parallel and perpendicular wavenumber k_{\parallel} and k_{\perp} respectively, Ω_{ci} and ρ_i are the ion cyclotron frequency and thermal radius, L_B is the characteristic background magnetic field nonuniformity scale length, and L_F is the characteristic background plasma density and temperature nonuniformity scale length. The plasma distribution function F and the electric and magnetic fields are decomposed into a mean and fluctuating part:

$$\begin{aligned} F &= F_0 + \delta f, \\ \mathbf{E} &= \mathbf{E}_0 + \delta \mathbf{E}, \\ \mathbf{B} &= \mathbf{B}_0 + \delta \mathbf{B}. \end{aligned} \tag{3.1}$$

The gyrokinetic ordering is given by the following orderings:

- $|\rho_i \nabla \ln B| \sim \epsilon_B$, $|(1/\Omega_{ci}) \partial B / \partial t| \sim \epsilon_B^3$ and $\rho_i / L_F \sim \epsilon_F$, where $\epsilon_B = \rho_i / L_B \ll 1$ and $\epsilon_F = \rho_i / L_F \ll 1$. This expresses that the plasma is magnetized and that the background magnetic field is essentially static in time.
- $k_{\perp} \rho_i \sim \epsilon_{\perp} \sim 1$, $\omega / \Omega_{ci} \sim \epsilon_{\omega} \ll 1$. The assumption $\epsilon_{\perp} \sim 1$ means that finite-Larmor-radius (FLR) effects must be retained, while ϵ_{ω} expresses the time scale separation between fluctuation frequencies and the cyclotron frequency.

- $k_{\parallel}/k_{\perp} \sim \epsilon_{\omega}/\epsilon_{\perp} \ll 1$ is an expression of the anisotropic nature of fluctuations. Fluctuations have long parallel wavelengths along magnetic field lines, but have short perpendicular wavelengths.
- $|\delta f/F| \sim |\delta \mathbf{E}_{\perp}|/Bv_{th} \sim |\delta \mathbf{B}|/B \sim \epsilon_{\delta} \ll 1$ expresses that the fluctuations are small in amplitude compared to mean values. Note $|\delta \mathbf{E}_{\perp}|/Bv_{th} \sim \epsilon_{\perp} q \delta \Phi / T_1 \sim \epsilon_{\delta}$, thus the electrostatic potential fluctuations are small. A similar expression can be derived for the vector potential. Furthermore, the ordering implies $|\delta E_{\parallel}|/|\delta \mathbf{E}_{\perp}| \sim k_{\parallel}/k_{\perp} \sim \epsilon_{\omega}/\epsilon_{\perp}$ and $|\delta B_{\parallel}|/B \sim \beta \epsilon_{\delta}$, where $\beta = 2\mu_0 P/B^2$ is the ratio of kinetic pressure to magnetic pressure.

Multiple approaches can be taken to derive the gyrokinetic equations. One route is the “traditional” derivation that uses rigorous multiple scale analysis and can be found in Abel et al. (2013). The “modern” method involves using techniques from geometrical mechanics and Lie transforms to derive equations that manifestly conserve energy at every order in the gyrokinetic ordering and is thoroughly reviewed in Brizard and Hahm (2007). This thesis will summarize the modern approach and follows the presentation of Brizard and Hahm (2007), Merz (2008), Görler (2009), and Pueschel (2009).

3.1.1 Phase space transformations

The central idea behind the modern derivation of the gyrokinetic equations is to construct a time-dependent phase-space transformation that takes the old, gyrophase-dependent phase-space coordinates $\mathbf{z} = (\mathbf{x}, \mathbf{p})$ to new gyrocenter phase-space coordinates \mathbf{Z} such that the gyrocenter equations of motion are independent of the gyrophase *at every order* in a perturbation expansion defined by ϵ_B and ϵ_{δ} . This transformation makes full use of the power of Hamiltonian canonical perturbation theory to transform the original particle Hamiltonian and Poisson bracket (Goldstein et al., 2002) in a manner such that the conservation properties of the original Hamiltonian system, such as

energy and entropy, are manifestly conserved. Furthermore, by eliminating explicit dependence on the gyrophase in the gyrocenter Lagrangian, there is an associated conjugate variable also conserved to all orders in ϵ_B and ϵ_δ and is a generalization of the magnetic moment. As was seen in Ch. 2, the existence of conserved quantities is necessary for proper collisionless orbit confinement. These phase-space transformations are accomplished by a series of near-identity transformations called *Lie transformations*, see Brizard and Hahm (2007) for more detail.

Schematically, the derivation of the nonlinear gyrokinetic equation can be viewed as two separate phase-space transformations acting on a phase-space Lagrangian and associated Poisson bracket (Goldstein et al., 2002). The first transformation is the guiding center transformation, which decouples the fast gyromotion associated with the *unperturbed*, but non-uniform, background magnetic field. This is accomplished by performing a Lie transformation in the parameter ϵ_B so that the resulting unperturbed phase-space Lagrangian in guiding-center coordinates has no explicit dependence on the gyrophase. Adding the perturbed fluctuating fields, ordered by ϵ_δ , re-introduces gyrophase dependence into the phase-space Lagrangian and Hamiltonian, as the fluctuating fields need to be evaluated at the exact particle position to account for gyroradius effects. A second phase-space transformation is accomplished by performing a Lie transformation on the perturbed phase-space Lagrangian in the parameter ϵ_δ so that the gyrophase dependence again disappears at each order in ϵ_δ , yielding the gyrocenter perturbed phase-space Lagrangian and Hamiltonian. The guiding center and gyrocenter transformations induce pull-back and push-forward operators that act on quantities like the plasma distribution function and ultimately generate the gyrokinetic Vlasov-Maxwell system of equations.

The major steps of the derivation of the gyrokinetic equation are as follows, while the detailed mathematical steps can be found in Brizard and Hahm (2007) and references therein. It is beneficial to use the *extended*

phase-space Lagrangian for a charged particle in a magnetic field and express it as differential one-form Γ defined as

$$\Gamma(\mathcal{Z}) = \left(\frac{q}{c} \mathbf{A} + m\mathbf{v} \right) \cdot d\mathbf{x} - w dt - \mathcal{H} d\tau \equiv \Gamma_a(\mathcal{Z}) d\mathcal{Z}^a - \mathcal{H}(\mathcal{Z}) d\tau, \quad (3.2)$$

with the extended Hamiltonian

$$\mathcal{H} = \frac{m|\mathbf{v}|^2}{2} + q\Phi(\mathbf{x}, t) - w \equiv H(\mathbf{z}, t) - w, \quad (3.3)$$

where w is the conserved particle energy in the time-independent case such that $H(\mathbf{z}, t) - w = 0$, τ is the Hamiltonian orbit parameter, and d is the exterior derivative with the property $d^2 f = 0$ for any scalar f . The extended phase-space coordinates $\mathcal{Z} = (t, \mathbf{x}, w, \mathbf{v})$ are used so that the extended Poisson brackets are symplectic (Goldstein et al., 2002). Symplectic structure allows one to use the standard tools of canonical transformations and perturbation theory to construct quantities that are conserved at all orders of the perturbation expansion, not only for the unperturbed equations. For gyrokinetics, this generates equations where the energy and a magnetic-moment-like quantity canonically conjugate to the gyrophase are conserved at all orders. Equation (3.2) is used to obtain the extended Hamilton's equations of motion through the single particle action integral

$$S = \int \Gamma \quad (3.4)$$

subject to Hamilton's principle $\delta S = \int \delta \Gamma = 0$, which yield the extended Euler-Lagrange equations. The Lagrange tensor $d\omega$ has components defined by

$$\omega_{ab} = \frac{\partial \Gamma_b}{\partial \mathcal{Z}^a} - \frac{\partial \Gamma_a}{\partial \mathcal{Z}^b}. \quad (3.5)$$

and is related to the Poisson brackets by

$$(\omega_{ab})^{-1} = \{\mathcal{Z}_a, \mathcal{Z}_b\} = J^{ab}, \quad (3.6)$$

which satisfies

$$J^{ac}\omega_{ab} = \delta_b^c, \quad (3.7)$$

where δ_b^c is the Kronecker delta function. The Poisson brackets provide succinct expressions for the extended Hamilton's equations of motion

$$\frac{d\mathcal{Z}^a}{d\tau} = \{\mathcal{Z}^a, \mathcal{H}\}_{\mathcal{Z}}, \quad (3.8)$$

and for the extended Vlasov equation for the extended plasma distribution function \mathcal{F} :

$$\frac{d\mathcal{F}}{d\tau} = \{\mathcal{F}, \mathcal{H}\}_{\mathcal{Z}}. \quad (3.9)$$

Here, $d/d\tau$ is the total derivative along a particle orbit in extended phase space and $\{, \}_{\mathcal{Z}}$ denotes the Poisson bracket in the extended phase space. One may now proceed with a near-identity transformation on the extended particle phase-space \mathcal{Z} to transform to new phase-space coordinates $\bar{\mathcal{Z}}$ where the fast gyromotion is removed at every order in the dimensionless ordering parameter ϵ (such as ϵ_B or ϵ_δ). The near identity transformation is given by

$$\mathcal{T}_\epsilon : \mathcal{Z} \rightarrow \bar{\mathcal{Z}}(\mathcal{Z}, \epsilon) \equiv \mathcal{T}_\epsilon \mathcal{Z} \quad (3.10)$$

with $\bar{\mathcal{Z}}(\mathcal{Z}, 0) = \mathcal{Z}$ and the inverse transformation

$$\mathcal{T}_\epsilon^{-1} : \bar{\mathcal{Z}} \rightarrow \mathcal{Z}(\bar{\mathcal{Z}}, \epsilon) \equiv \mathcal{T}_\epsilon^{-1} \bar{\mathcal{Z}}. \quad (3.11)$$

These transformations can be expressed in terms of the generating vector fields \mathbf{G}_n by

$$\mathcal{T}_\epsilon^{\pm 1} \equiv \exp \left(\pm \sum_{n=1}^{\infty} \epsilon^n \mathbf{G}_n \cdot \mathbf{d} \right), \quad (3.12)$$

where \mathbf{G}_n is the n th-order generating vector field that is chosen to remove the fast gyrophase motion at order ϵ^n . These transformations induce what are called pull-back and push-forward operators that act on differential forms

to map between the manifolds defined by the two different phase-space coordinates. The pull-back operator on a scalar field $\bar{\mathcal{F}}$ is given by

$$T_\epsilon : \bar{\mathcal{F}} \rightarrow \mathcal{F} \equiv T_\epsilon \bar{\mathcal{F}} \quad (3.13)$$

and transforms $\bar{\mathcal{F}}$ on the phase space $\bar{\mathcal{Z}}$ to \mathcal{F} on the phase space \mathcal{Z} . The push-forward operator is defined as

$$T_\epsilon^{-1} : \mathcal{F} \rightarrow \bar{\mathcal{F}} \equiv T_\epsilon^{-1} \mathcal{F}. \quad (3.14)$$

The push-forward and pull-back operators transform Eq. 3.9 between phase-space coordinates \mathcal{Z} and phase-space coordinates $\bar{\mathcal{Z}}$ to obtain the Vlasov equation where the fast gyrophase motion is eliminated:

$$\frac{df}{d\tau} = T_\epsilon^{-1} \left(\frac{d}{d\tau} T_\epsilon \bar{\mathcal{F}} \right) = \{\bar{\mathcal{F}}, \bar{\mathcal{H}}\}_{\bar{\mathcal{Z}}} \quad (3.15)$$

where the transformed Poisson bracket is defined in terms of the transformed phase-space coordinates $\bar{\mathcal{Z}}$ and the transformed extended phase-space Lagrangian $\bar{\Gamma}$, while equations of motion rely on the transformed Hamiltonian $\bar{\mathcal{H}} = T_\epsilon^{-1} \mathcal{H}$. The transformation of the one-form extended phase-space Lagrangian is given by

$$\bar{\Gamma} = T_\epsilon^{-1} \Gamma + \mathbf{d}S \quad (3.16)$$

where S is a scalar gauge field that does not alter the transformed Poisson bracket structure since $\mathbf{d}^2 S = 0$. The proper choice of gauge field is crucial to the gyrokinetic derivation and will be chosen to remove the fast gyrophase dependence. The pull-back and push-forward operators are defined in terms of Lie derivatives by

$$T_\epsilon^{\pm 1} = \exp \left(\pm \sum_{n=1}^{\infty} \epsilon^n \mathbf{L}_n \right), \quad (3.17)$$

where \mathbb{L}_n is the Lie derivative generated by \mathbf{G}_n . The Lie derivative is a derivative along the vector field \mathbf{G}_n that preserves the tensorial nature of the object on which it is acting. This property is necessary to ensure that the symplectic structure of the Poisson brackets are unaltered by the pull-back and push-forward operators on the extended phase-space Lagrangian. The action of \mathbb{L}_n on a scalar field H is given by

$$\mathbb{L}_n H = G_n^a \partial_a H \quad (3.18)$$

and on the one-form $\Gamma \equiv \Gamma_a d\mathcal{Z}^a$ by

$$\mathbb{L}_n \Gamma = \mathbf{G}_n \cdot d\Gamma + d(\mathbf{G}_n \cdot \Gamma) = [G_n^a \Omega_{ab} + \partial_b (G_n^a \Gamma_a)] d\mathcal{Z}^b, \quad (3.19)$$

where there is an implicit sum over repeated indicies and $\partial_a = \partial/\partial\mathcal{Z}^a$. Consider now perturbations to the Lagrangian and Hamiltonian given by $\Gamma = \Gamma_0 + \epsilon\Gamma_1 + \epsilon^2\Gamma_2$ and $\mathcal{H} = \mathcal{H}_0 + \epsilon\mathcal{H}_1 + \epsilon^2\mathcal{H}_2$. Applying the Lie transforms, with $\bar{\Gamma}_0 = \Gamma_0$ and $\bar{\mathcal{H}}_0 = \mathcal{H}_0$, one obtains

$$\bar{\Gamma}_1 = \Gamma_1 - \mathbf{G}_1 \cdot \Omega_0 + dS_1, \quad (3.20)$$

$$\bar{\Gamma}_2 = -\mathbf{G}_2 \cdot \omega_0 - \frac{1}{2}\mathbf{G}_1 \cdot (\Omega_1 + \bar{\omega}_1) + dS_2 \quad (3.21)$$

where $\omega_{0,1}$ is the Lagrange tensor associated with $\Gamma_{0,1}$ and

$$\bar{H}_1 = H_1 - \mathbf{G}_1 \cdot d\mathcal{H}_0, \quad (3.22)$$

$$\begin{aligned} \bar{H}_2 = & -\{S_2, \mathcal{H}_0\}_0 - \frac{1}{2}G_1^a \partial_a (K_1 + \bar{K}_1) \\ & - \frac{1}{2}G_1^b \{\Gamma_{1b} + \bar{\Gamma}_{1b}, \mathcal{H}_0\}_0 - \frac{1}{2}(\Gamma_{1b} + \bar{\Gamma}_{1b})(G_1^a \partial_a \dot{\mathcal{Z}}_0^b). \end{aligned} \quad (3.23)$$

Equation (3.20) can be solved for \mathbf{G}_1 using Eq. (3.7) given a choice of $\bar{\Gamma}_1$,

yielding

$$G_1^a = \{S_1, \mathcal{Z}^a\}_0 + (\Gamma_{1b} - \bar{\Gamma}_{1b}) J_0^{ba}, \quad (3.24)$$

where $\{, \}_0$ is the unperturbed Poisson bracket. $\bar{\Gamma}_1$ is usually chosen to satisfy specific properties, i.e. so that the Poisson brackets maintain symplectic structure, and determines the final form of the transformed coordinates as Eq. (3.24) is used in Eqs. (3.10) and (3.12). Equation (3.24) can then be inserted in Eq. (3.22) giving

$$\bar{H}_1 = K_1 + \bar{\Gamma}_{1a} \dot{\mathcal{Z}}_0^a - \{S_1, \mathcal{H}_0\}_0, \quad (3.25)$$

where $K_1 = H_1 - \Gamma_{1a} \dot{\mathcal{Z}}_0^a$ and $\dot{\mathcal{Z}}_0^a = \{\mathcal{Z}^a, \mathcal{H}_0\}_0$ are the unperturbed equations of motion. In Eq. (3.25), \bar{H}_1 is the desired perturbed Hamiltonian where the fast gyrophase time scale has been removed, however K_1 still retains the fast time scales and is used to define the gauge function S_1 . Defining a fast gyrophase averaging operator $\langle A \rangle$ as

$$\langle A \rangle = \frac{1}{2\pi} \int_0^{2\pi} d\zeta A(\zeta) \quad (3.26)$$

and applying to Eq. (3.25), the fast gyrophase dependence is eliminated if S_1 satisfies

$$\{S_1, \mathcal{H}_0\}_0 = \frac{dS_1}{d\tau} = K_1 - \langle K_1 \rangle, \quad (3.27)$$

which has the formal solution $S_1 = \Omega_c^{-1} \int d\bar{\zeta} (K_1 - \langle K_1 \rangle)$. Equation (3.25) is transformed into the desired

$$\bar{H}_1 = \langle K_1 \rangle + \bar{\Gamma}_{1a} \dot{\mathcal{Z}}^a \quad (3.28)$$

where the fast gyrophase dependence has been eliminated. Similar, but more complex, results are found for the second order gyrocenter extended phase-space Lagrangian and Hamiltonian and are necessary for ensuring conservation of energy in the gyrokinetic equations. These resulting perturbed

\bar{I} and $\bar{\mathcal{H}}$ are used to define the perturbed Poisson bracket to construct the perturbed Vlasov equation, Eq. (3.9).

3.1.2 Gyrokinetic Vlasov-Maxwell equations

Using the above phase-space transformations, the gyrokinetic Vlasov equation is derived from the dynamics of charged particles in a stationary background magnetic field $\mathbf{B}_0 = \nabla \times \mathbf{A}_0$ subject to low-frequency electromagnetic fluctuations $\delta\Phi$ and $\delta\mathbf{A}$, where the fluctuation amplitude is ordered by ϵ_δ following the gyrokinetic ordering. The extended phase-space Lagrangian is given by $\Gamma = \Gamma_0 + \epsilon_\delta \Gamma_1$ with $\Gamma_0 = [(q/c)\mathbf{A}_0 + m\mathbf{v}] \cdot d\mathbf{x} - wdt$ and $\Gamma_1 = (q/c)\delta\mathbf{A} \cdot d\mathbf{x}$. The extended phase-space Hamiltonian is similarly defined as $\mathcal{H} = \mathcal{H}_0 + \epsilon_\delta H_1$ where $\mathcal{H}_0 = m|\mathbf{v}|^2/2 - w$ and $H_1 = q\delta\Phi$. The background electrostatic potential is assumed to vanish, $\Phi_0 = 0$, as it does not appear in the physical situations described in this thesis.

Guiding center transformation

The first Lie transformation is the guiding center transformation from the extended particle phase space $\mathbf{z} = (\mathbf{x}, \mathbf{v}, w, t)$ to the *unperturbed* guiding center phase space defined by $\mathbf{Z}_{gc} = (\mathbf{X}, v_\parallel, \mu, \zeta, w, t)$, where \mathbf{X} is the guiding center position, $v_\parallel = |\mathbf{v} \cdot \hat{\mathbf{b}}_0|$ with $\hat{\mathbf{b}}_0 = \mathbf{B}_0/B_0$ is the guiding center parallel velocity, $\mu = mv_\perp/2B$ is the guiding center magnetic moment with $v_\perp = |\mathbf{v} - v_\parallel \hat{\mathbf{b}}_0|$, ζ is the gyroangle, and (w, t) are canonically-conjugate energy-time coordinates. This is accomplished by performing the perturbation expansion in the magnetic field non-uniformity parameter ϵ_B , so that particle drifts are taken into account, where again, the generating vector field \mathbf{G}_n are chosen to eliminate the fast gyromotion at every order in ϵ_B^n . The guiding center coordinates are related to the particle coordinates (at first order in ϵ_B) by $\mathbf{x} = \mathbf{X} + \mathbf{r}(\mathbf{X}, \mu, \zeta)$, where $\mathbf{r}(\mathbf{X}, \mu, \zeta) = \rho(\mathbf{X}, \mu)\mathbf{a}(\zeta)$ is the gyroradius vector with magnitude $\rho(\mathbf{X}, \mu) = v_\perp(\mathbf{X})/\Omega_c(\mathbf{X})$. The particle velocity is given

by $\mathbf{v} = v_{\parallel} \hat{\mathbf{b}}_0(\mathbf{X}) + v_{\perp}(\mathbf{X}, \mu) \mathbf{c}(\zeta)$. The directional vectors $\mathbf{a}(\zeta)$ and $\mathbf{c}(\zeta)$ are defined by

$$\mathbf{a}(\zeta) = \cos(\zeta) \hat{\mathbf{e}}_1 + \sin(\zeta) \hat{\mathbf{e}}_2, \quad \mathbf{c}(\zeta) = -\sin(\zeta) \hat{\mathbf{e}}_1 + \cos(\zeta) \hat{\mathbf{e}}_2, \quad (3.29)$$

where $(\hat{\mathbf{e}}_1, \hat{\mathbf{e}}_2, \hat{\mathbf{b}}_0)$ is a local Cartesian coordinate system centered at \mathbf{X} . For the following results, it is helpful to define the following quantities: $\mathbf{A}_0^* = \mathbf{A}_0 + (mc/q)v_{\parallel} \hat{\mathbf{b}}_0$, $\mathbf{B}_0^* = \nabla \times \mathbf{A}_0^*$, and $B_{0\parallel}^* = \hat{\mathbf{b}}_0 \cdot \mathbf{B}_0^*$. The unperturbed guiding center phase-space Lagrangian is given by

$$\Gamma_{gc} = \frac{q}{c} \mathbf{A}_0^* \cdot d\mathbf{X} + \frac{mc}{q} \mu d\zeta - w dt, \quad (3.30)$$

and the unperturbed guiding center phase-space Hamiltonian by

$$\mathcal{H}_{gc} = \frac{mv_{\parallel}^2}{2} + \mu B_0 - w \equiv H_{gc} - w. \quad (3.31)$$

The form of Eq. (3.30) induces the unperturbed guiding center Poisson bracket, defined for arbitrary function F and G as

$$\begin{aligned} \{F, G\}_{gc} = & \underbrace{\frac{q}{mc} \left(\frac{\partial F}{\partial \zeta} \frac{\partial G}{\partial \mu} - \frac{\partial F}{\partial \mu} \frac{\partial G}{\partial \zeta} \right)}_{\text{gyromotion}} + \underbrace{\frac{m\mathbf{B}_0^*}{B_{0\parallel}^*} \cdot \left(\nabla F \frac{\partial G}{\partial v_{\parallel}} - \frac{\partial F}{\partial v_{\parallel}} \nabla G \right)}_{\text{transit motion}} \\ & - \underbrace{\frac{c\hat{\mathbf{b}}_0}{qB_{0\parallel}^*} \cdot \nabla F \times \nabla G}_{\text{cross field drift}} + \left(\frac{\partial F}{\partial w} \frac{\partial G}{\partial t} - \frac{\partial F}{\partial t} \frac{\partial G}{\partial w} \right). \quad (3.32) \end{aligned}$$

The motion described by the labels in Eq. (3.32) is obtained by evaluating charged particle guiding center equations of motion $\dot{Z}_{gc}^a = \{Z_{gc}^a, \mathcal{H}_{gc}\}_{gc}$. Note that since Eq. (3.31) is independent of ζ , the fast gyromotion is eliminated from the equations of motion for the unperturbed guiding center particle motion.

Gyrocenter transformation

The guiding center phase-space Lagrangian and Hamiltonian given by Eqs. (3.30) and (3.31) are perturbed by the introduction of fluctuating electromagnetic fields $(\delta\Phi, \delta\mathbf{A})$, $\Gamma_{gc} = \Gamma_{0gc} + \epsilon_\delta \Gamma_{gc}$ and $\mathcal{H}_{gc} = \mathcal{H}_{0gc} + \epsilon_\delta H_{1gc}$ respectively, where Γ_{0gc} and \mathcal{H}_{0gc} are the unperturbed guiding center quantities. The gyrokinetic ordering $\epsilon_\perp \sim 1$ implies that the perturbed fields cannot be evaluated at the guiding center coordinate, as perpendicular gradients are large that $\delta\Phi(\mathbf{X}) \not\approx \delta\Phi(\mathbf{x})$, thus the fluctuating fields must be evaluated at the particle coordinates, re-introducing gyrophase dependence as $\mathbf{x} = \mathbf{X} + \mathbf{r}(\mathbf{X}, \mu, \zeta)$. The perturbed guiding-center phase space Lagrangian is given by

$$\Gamma_{1gc} = \frac{q}{c} \delta\mathbf{A}(\mathbf{X} + \mathbf{r}, t) \cdot d(\mathbf{X} + \mathbf{r}) = \frac{q}{c} \delta\mathbf{A}_{gc}(\mathbf{X}, \mu, \zeta, t) \cdot d(\mathbf{X} + \mathbf{r}) \quad (3.33)$$

and the perturbed guiding center phase-space Hamiltonian by

$$H_{1gc} = q\delta\Phi(\mathbf{X} + \mathbf{r}, t) = q\delta\Phi_{gc}(\mathbf{X}, \mu, \zeta, t). \quad (3.34)$$

The gyrophase dependence is eliminated by performing a second Lie transformation in ϵ_δ , by transforming from guiding center coordinates to gyrocenter coordinates:

$$\mathbf{Z}_{gc} = (\mathbf{X}, v_\parallel, \mu, \zeta, w, t) \rightarrow \bar{\mathbf{Z}}_{gy} = (\bar{\mathbf{X}}, \bar{v}_\parallel, \bar{\mu}, \bar{\zeta}, \bar{w}, t), \quad (3.35)$$

so that that the transformed gyrocenter phase-space Lagrangian $\bar{\Gamma}_{gy}$ and Hamiltonian $\bar{\mathcal{H}}_{gy}$ are independent of $\bar{\zeta}$ at every order in ϵ_δ . Using Eq. (3.24) and choosing $\hat{I}_1 = 0$ (which preserves the Hamiltonian form), the generators of the Lie transformation are found to be (Brizard and Hahm, 2007)

$$G_1^{\mathbf{X}} = -m\hat{\mathbf{b}}_0 \frac{\partial S_1}{\partial v_\parallel} - \frac{c}{qB_0} \hat{\mathbf{b}}_0 \times \nabla S_1 + \delta\mathbf{A}_{gc} \times \frac{\hat{\mathbf{b}}_0}{B_0}, \quad (3.36)$$

$$G_1^{v\parallel} = \hat{\mathbf{b}}_0 \cdot \nabla S_1 + \frac{q}{c} (\delta A_{\parallel gc}), \quad (3.37)$$

$$G_1^\mu = \frac{q}{mc} \left(\frac{q}{c} \delta \mathbf{A}_{\perp gc} \cdot \frac{\partial \mathbf{r}}{\partial \bar{\zeta}} + \frac{\partial S_1}{\partial \bar{\zeta}} \right), \quad (3.38)$$

$$G_1^\zeta = -\frac{q}{mc} \left(\frac{q}{c} \delta \mathbf{A}_{\perp gc} \cdot \frac{\partial \mathbf{r}}{\partial \mu} + \frac{q}{mc} \frac{\partial S_1}{\partial \mu} \right), \quad (3.39)$$

$$G_1^{av} = -\frac{\partial S_1}{\partial t}. \quad (3.40)$$

Equation (3.25) is used to find \bar{H}_1 , with $K_1 = q\delta\Phi_{gc} - \delta\mathbf{A}_{gc} \cdot \mathbf{v}/c$. Defining the generalized potential as $\delta\xi_{gc} = \delta\Phi_{gc} - \delta\mathbf{A}_{gc} \cdot \mathbf{v}/c$ and letting $\tilde{\delta\xi}_{gc} = \delta\xi_{gc} - \langle \delta\xi_{gc} \rangle$ denote the gyroangle-dependent part of $\delta\xi_{gc}$, Eq. (3.27) gives the form of the gauge function S_1 necessary to eliminate dependence on $\bar{\zeta}$ in \bar{H}_1 :

$$S_1 = \frac{q}{\Omega_{c0}} \int^{\bar{\zeta}} d\bar{\zeta}' \tilde{\delta\xi}_{gc}(\bar{\zeta}'). \quad (3.41)$$

Finally, Eq. (3.28) gives the first-order gyroaveraged gyrocenter Hamiltonian

$$\bar{H}_1 = q \langle \delta\Phi_{gc} \rangle - \frac{q}{c} \langle \mathbf{v} \cdot \delta\mathbf{A}_{gc} \rangle. \quad (3.42)$$

The gyroaverages of the potentials evaluated at the particle positions are computed as follows (Pueschel, 2009)

$$\langle \delta\Phi \rangle = \frac{1}{2\pi} \int_0^{2\pi} d\bar{\zeta} \delta\Phi(\mathbf{X} + \mathbf{r}) = J_0(\lambda) \delta\Phi(\mathbf{X}), \quad (3.43)$$

$$\langle v_{\parallel} \delta\mathbf{A}_{gc} \cdot \hat{\mathbf{b}}_0 \rangle = \frac{v_{\parallel}}{2\pi} \int_0^{2\pi} d\bar{\zeta} \delta A_{\parallel gc}(\mathbf{X} + \mathbf{r}) = v_{\parallel} J_0(\lambda) \delta A_{\parallel gc}(\mathbf{X}), \quad (3.44)$$

$$\langle \mathbf{v}_{\perp} \cdot \delta\mathbf{A}_{gc} \rangle = \frac{qv_{\perp}}{2\pi c} \int_0^{2\pi} d\bar{\zeta} \delta A_{gc}(\mathbf{X} + \mathbf{r}) \cdot \mathbf{c}(\bar{\zeta}) = \frac{2i\mu}{\lambda} I_1(i\lambda) \delta B_{\parallel gc}(\mathbf{X}), \quad (3.45)$$

where $J_0(\lambda)$ is the Bessel function of the first kind, $I_1(i\lambda)$ is the modified Bessel function of the first kind, and $\lambda = i\rho\nabla$. The second-order Hamiltonian \bar{H}_2 that is needed to obtain the exact gyrokinetic energy conservation law

and the proper form of polarization and magnetization in the gyrokinetic field equations is given by:

$$\bar{H}_2 = -\frac{1}{2} \left\langle \{S_1, \delta\tilde{\xi}_{gc}\}_0 \right\rangle + \frac{q^2}{2mc^2} \langle |\delta\mathbf{A}_{gc}|^2 \rangle, \quad (3.46)$$

with $\{, \}_0$ the unperturbed guiding center Poisson bracket given by Eq. (3.32).

Gyrokinetic Vlasov equation

With the extended gyrocenter phase-space Lagrangian and Hamiltonian defined, it is now straight forward to compute the gyrokinetic Vlasov equation. The choice $\bar{I}_1 = 0$ leaves the Poisson bracket defined by Eq. (3.32) unaltered, thus Eq. (3.15) for the gyrocenter distribution function \bar{F} becomes

$$\frac{d\bar{F}}{d\tau} + \{\bar{F}, \mathcal{H}_0 + \epsilon_\delta \bar{H}_1 + \epsilon_\delta^2 \bar{H}_2\}_{gc} = 0. \quad (3.47)$$

This can be re-written in a more common form, using the identity $\{\bar{F}, \bar{\mathcal{H}}\} = \sum_i \partial_i \bar{F} \{\bar{Z}^i, \bar{\mathcal{H}}\}$, as

$$\frac{\partial \bar{F}}{\partial t} + \dot{\bar{\mathbf{X}}} \cdot \frac{\partial \bar{F}}{\partial \bar{\mathbf{X}}} + \dot{v}_\parallel \frac{\partial \bar{F}}{\partial v_\parallel} = 0, \quad (3.48)$$

where $\dot{\bar{Z}}^i = \{\bar{Z}^i, \bar{\mathcal{H}}\}$ yields the equations of motion and $\dot{\mu} = 0$, as μ is an invariant quantity canonically conjugate to the gyroangle. For a clearer presentation, following notation will be used: $\bar{\Phi}_1 = J_0(\lambda) \delta\Phi_{gc}(\bar{\mathbf{X}})$, $\bar{A}_{1\parallel} = J_0(\lambda) \delta A_{\parallel gc}(\bar{\mathbf{X}})$, and $\bar{B}_{1\parallel} = (i/\lambda) I_1(i\lambda) B_{\parallel gc}(\bar{\mathbf{X}})$ and the overbar will be dropped from the gyrocenter coordinates. Using the Poisson bracket of Eq. (3.32) and Eqs. (3.42) and (3.46) for the gyrocenter Hamiltonian,

Eq. (3.48) for particle species σ evaluates to

$$\frac{\partial \bar{F}_\sigma}{\partial t} + \left[v_\parallel \hat{\mathbf{b}}_0 + \frac{B_0}{B_{0\parallel}^*} (\mathbf{v}_{\bar{\chi}} + \mathbf{v}_{\nabla B} + \mathbf{v}_c) \right] \cdot \left(\nabla \bar{F}_\sigma - \left(q_\sigma \nabla \bar{\Phi}_1 + \frac{q_\sigma}{c} \hat{\mathbf{b}}_0 \dot{\bar{A}}_{1\parallel} - \mu \nabla (B_0 + \bar{B}_{1\parallel}) \right) \frac{\partial \bar{F}}{\partial v_\parallel} \right) = 0, \quad (3.49)$$

where ∇ is evaluated with respect to the gyrocenter coordinates \mathbf{X} . In Eq. (3.49), the modified potential

$$\bar{\chi}_1 = \bar{\Phi}_1 - \frac{v_\parallel}{c} \bar{A}_{1\parallel} + \frac{\mu}{q} \bar{B}_{1\parallel} \quad (3.50)$$

has been used as well as the drift velocities

$$\mathbf{v}_{\bar{\chi}} = -\frac{c}{B_0^2} \nabla \bar{\chi}_1 \times \mathbf{B}_0, \quad (3.51)$$

$$\mathbf{v}_{\nabla B} = \frac{\mu}{m_\sigma \Omega_{c\sigma}} \hat{\mathbf{b}}_0 \times \nabla B_0, \quad (3.52)$$

$$\mathbf{v}_c = \frac{v_\parallel^2}{\Omega_{c\sigma}} \left(\hat{\mathbf{b}}_0 \times \left[\frac{\nabla B_0}{B_0} + \frac{\beta_p}{2} \frac{\nabla P_0}{P_0} \right] \right), \quad (3.53)$$

with $\beta_p = 8\pi P_0/B_0^2$. Equation (3.49) is the evolution equation for the full gyrocenter distribution function, however in assessing the impact of fluctuations in the electromagnetic fields on the distribution function, it is useful to also split the distribution function into a mean and fluctuating part $\bar{F} = \bar{F}_0 + \bar{f}_1$ where $\bar{f}_1/\bar{F}_0 \sim \epsilon_\delta$ and \bar{F}_0 solves the Vlasov equation in the static, unperturbed background magnetic field. Defining the non-adiabatic part of the perturbed distribution function (which has origins in the pull-back of \bar{F} , see Brizard and Hahm (2007) for further details) as

$$g_{\sigma 1} = \bar{f}_{\sigma 1} - \frac{q_\sigma}{m_\sigma c} \bar{A}_{1\parallel} \frac{\partial \bar{F}_{\sigma 0}}{\partial v_\parallel} \quad (3.54)$$

and the derived quantity

$$G_{\sigma 1} = g_{\sigma 1} - \frac{q_{\sigma}}{m_{\sigma} v_{\parallel}} \bar{\chi}_1 \frac{\partial \bar{F}_{\sigma 0}}{\partial v_{\parallel}}, \quad (3.55)$$

the Vlasov equation for the perturbed gyrocenter distribution function is

$$\begin{aligned} \frac{\partial g_{\sigma 1}}{\partial t} + \frac{B_0}{B_{0\parallel}^*} \mathbf{v}_{\bar{\chi}} \cdot \left(\nabla \bar{F}_{\sigma 0} - \frac{\mu}{m_{\sigma} v_{\parallel}} \nabla B_0 \frac{\partial \bar{F}_{\sigma 0}}{\partial v_{\parallel}} \right) \\ + \frac{B_0}{B_{0\parallel}^*} (\mathbf{v}_{\bar{\chi}} + \mathbf{v}_{\nabla B} + \mathbf{v}_c) \cdot \nabla G_{\sigma 1} + v_{\parallel} \hat{\mathbf{b}}_0 \cdot \nabla G_{\sigma 1} \\ - \left(\frac{1}{m_{\sigma}} \mathbf{b}_1 + \frac{B_0}{m_{\sigma} v_{\parallel} B_{0\parallel}^*} \mathbf{v}_c \right) \\ \cdot \left(q_{\sigma} \nabla \bar{\Phi}_1 + \frac{q_{\sigma}}{c} \hat{\mathbf{b}}_0 \dot{A}_{1\parallel} - \mu \nabla (B_0 + \bar{B}_{1\parallel}) \right) \frac{\partial \bar{f}_{\sigma 1}}{\partial v_{\parallel}} = 0. \end{aligned} \quad (3.56)$$

Gyrokinetic field equations

The field equations Eqs. (1.5) and (1.7) are defined in terms of velocity moments of the particle distribution function, Eqs. (1.9) and (1.10). The moment equations have the following form in particle phase space $\mathbf{z} = (\mathbf{x}, \mathbf{v})$:

$$\mathcal{M}_g(\mathbf{x}') = \int d^6 \mathbf{z} g(\mathbf{z}) f(\mathbf{z}) \delta^3(\mathbf{x} - \mathbf{x}'), \quad (3.57)$$

where g is the moment function and $\delta^3(\mathbf{x} - \mathbf{x}')$ is the Dirac delta function. For example, $g(\mathbf{z}) = \mathbf{v}$ is used to evaluate the plasma current and $g(\mathbf{z}) = 1$ gives the density integral. The gyrokinetic field equations for the gyrocenter distribution function are derived through application of the coordinate transforms in Eqs. (3.11) and (3.12) to the guiding center variables, $\mathbf{z} = \mathcal{T}_{gc}^{-1} \mathbf{Z}$, transforming Eq. (3.57) into

$$\mathcal{M}_g(\mathbf{x}') = \int \frac{B_{0\parallel}^*}{m} d^3 \mathbf{X} dv_{\parallel} d\mu d\zeta [T_{gc}^{-1} g](\mathbf{Z}) [T_{gy} \bar{F}](\mathbf{Z}) \delta^3(\mathbf{X} + \mathbf{r} - \mathbf{x}'). \quad (3.58)$$

The guiding center push-forward operator acts on the moment function, while the gyrocenter pull-back operator acts on the gyrocenter distribution function. By Eqs. (3.13) and (3.14), $F = T_{gy}\bar{F} = \bar{F}_0 + \bar{f}_1 + \mathbf{G}_1 \cdot \mathbf{d}\bar{F}_0$, which uses the generators of Eqs. (3.36)–(3.40) and the solution for the gauge function S_1 from (3.41). The pull-back of the distribution function yields

$$T_{gy}\bar{F} = \bar{F}_0 + \bar{f}_1 + \frac{1}{B_0} \left[\frac{\mathbf{B}_0^*}{B_{0\parallel}} \left(\Omega_{c\sigma} \frac{\partial \bar{F}_0}{\partial v_{\parallel}} - \frac{q_{\sigma} v_{\parallel}}{c} \frac{\partial \bar{F}_0}{\partial \mu} \right) \cdot \tilde{\mathbf{A}}_1 + \left(q_{\sigma} \tilde{\Phi}_1 - \mu \bar{B}_{1\parallel} \right) \frac{\partial \bar{F}_0}{\partial \mu} \right], \quad (3.59)$$

and is then used in Eq. (3.58). To save space, only the results will be quoted here, see Görler (2009) and Merz (2008) for the detailed derivation. Several simplifications are useful for deriving the gyrokinetic field equations. The background gyrocenter distribution function is assumed to be a Maxwellian distribution

$$\bar{F}_{\sigma 0}(v_{\parallel}, \mu) = \left(\frac{m_{\sigma}}{2\pi T_{\sigma}} \right)^{3/2} n_0 \exp \left(-\frac{m_{\sigma} v_{\parallel}^2 / 2 + \mu B_0}{T_{\sigma}} \right) \quad (3.60)$$

so that the velocity derivatives of \bar{F}_0 can be easily evaluated, however this choice of \bar{F}_0 does not solve the unperturbed guiding center Vlasov equation. The equations for the evolution of electromagnetic fields in particle phase space Φ , A_{\parallel} and B_{\parallel} are as follows (Pueschel, 2009):

$$\sum_{\sigma} q_{\sigma} (1 - \Gamma_0(b_{\sigma})) \frac{q_{\sigma} \Phi_1}{T_{\sigma 0}} = \sum_{\sigma} q_{\sigma} \left((\Gamma_0(b_{\sigma}) - \Gamma_1(b_{\sigma})) \frac{B_{1\parallel}}{B_0} + \frac{2\pi B_0}{m_{\sigma} n_{\sigma 0}} \int dv_{\parallel} d\mu (J_0(\lambda_{\sigma}) \bar{f}_{\sigma 1}) \right), \quad (3.61)$$

$$\begin{aligned} & \left(1 + \sum_{\sigma} 4b_{\sigma}\beta_{\sigma}(\Gamma_0(b_{\sigma}) - \Gamma_1(b_{\sigma})) \right) \frac{B_{1\parallel}}{B_0} = \\ & - \sum_{\sigma} 2\beta_{\sigma} \left[\frac{B_0}{n_{\sigma 0} T_{\sigma 0}} \int dv_{\parallel} d\mu \left(\frac{2i\mu}{\lambda_{\sigma}} I_1(\lambda_{\sigma}) \bar{f}_{\sigma 1} \right) + \frac{q_{\sigma} \Phi_1}{T_{\sigma 0}} (\Gamma_0(b_{\sigma}) - \Gamma_1(b_{\sigma})) \right], \end{aligned} \quad (3.62)$$

$$\nabla_{\perp}^2 A_{1\parallel} = -\frac{8\pi^2 B_0}{c} \sum_{\sigma} \frac{q_{\sigma}}{m_{\sigma}} \int dv_{\parallel} d\mu J_0(\lambda_{\sigma}) \bar{f}_{\sigma 1}, \quad (3.63)$$

where $\beta_{\sigma} = 8\pi P_{\sigma}/B^2$ is the ratio of kinetic pressure to magnetic pressure, $\Gamma_{0,1}(b_{\sigma}) = I_{0,1}(b_{\sigma}) \exp(-b_{\sigma})$ for the modified Bessel functions $I_{0,1}$, and $b_{\sigma} = -(T_{\sigma}/(m_{\sigma}\Omega_{\sigma}^2))\nabla_{\perp}^2$. These field equations coupled with Eq. (3.56) represent a system of closed equations for \bar{f}_1 , Φ_1 , $A_{1\parallel}$, and $B_{1\parallel}$ that can be used to study plasma turbulence in fusion plasmas.

3.2 Flux Tube Geometry

Gyrokinetic simulations of local plasma turbulence utilize the flux-tube approach (Beer et al., 1995), where the gyrokinetic equations are solved in a small domain around a magnetic field line. This approach takes advantage of the anisotropic nature of plasma turbulence, where perpendicular wavelengths of fluctuations are generally much smaller than parallel wavelengths, $k_{\parallel} \ll k_{\perp}$. As such, only a small domain perpendicular to the field line, on the order of a few perpendicular correlation lengths, need be simulated with periodic boundary conditions. The scale L_{eq} of perpendicular variations of background quantities such as the equilibrium magnetic field is assumed to be much larger than turbulent correlation lengths λ_{turb} . Equilibrium quantities are then expanded to first order in the perpendicular direction around the center of the simulation domain while still incorporating nontrivial dependence along the parallel field line coordinate.

The flux-tube approach is related to the ballooning transformation

formulated for axisymmetric geometries (Connor et al., 1978, 1979) and subsequently extended to general three-dimensional systems (Dewar and Glasser, 1983), which transforms a multi-dimensional eigenvalue calculation into a sequence of one-dimensional eigenvalue equations along field lines. This transformation is facilitated by the assumption $k_{\parallel} \ll k_{\perp}$ for ballooning modes, allowing one to assume a WKB-like solution where the slow scale only appears in the mode amplitude: $\boldsymbol{\xi}(\mathbf{x}, t) = \hat{\boldsymbol{\xi}}(\mathbf{x}, \epsilon) \exp(iS(\mathbf{x})/\epsilon - i\omega t)$, where $\boldsymbol{\xi}$ is the mode displacement. $\epsilon \ll 1$ is an expansion parameter and denotes the rapid variation of the wave phase perpendicular to the magnetic field line. At lowest order in ϵ , the instabilities are approximately incompressible, $\nabla \cdot \boldsymbol{\xi} \approx (i\nabla S(\mathbf{x})/\epsilon) \cdot \boldsymbol{\xi} = 0$. We can identify $\nabla S(\mathbf{x})$ as the wavevector \mathbf{k} . Requiring the displacement at lowest order to be perpendicular to the magnetic field gives $\mathbf{k}_{\perp} \cdot \mathbf{B} = 0$. We may write the magnetic field in Clebsch form,

$$\mathbf{B} = \nabla\psi \times \nabla\alpha, \quad (3.64)$$

where ψ is the poloidal magnetic flux function and $\alpha = q(\psi)\theta - \zeta$ is the field line label defined in terms of the straight-field-line poloidal and toroidal angles θ and ζ , respectively, and $q(\psi)$ is the safety factor. The condition $\mathbf{k}_{\perp} \cdot \mathbf{B} = 0$ implies $S(\mathbf{x})$ is a function of (ψ, α) alone, yielding an instructive form for \mathbf{k}_{\perp} :

$$\mathbf{k}_{\perp} = k_{\alpha} [q\nabla\theta - \nabla\zeta + q'(\theta + \theta_k)\nabla\psi]. \quad (3.65)$$

Here, $q' = dq/d\psi$ is the global magnetic shear and $\theta_k = k_{\psi}/q'k_{\alpha}$ is the ballooning angle. This implies that radial variations (finite- k_{ψ} effects) are transformed into a dependence along the field line. Furthermore, it is easy to see that Eq. (3.65) is invariant under the substitution $\theta \rightarrow 2\pi M$, $\theta_k \rightarrow -2\pi M$ for some integer M . Thus, in principle, one may compute effects for increasing θ by considering the geometry from a limited range of θ , say $\theta \in (-\pi, \pi)$ and incrementing $k_{\psi} \rightarrow -2\pi M q' k_{\alpha}$ for integer M .

The flux-tube simulation domain is defined in straight-field-line (SFL)

coordinates (ψ, α, z) . Depending on whether one chooses $\alpha = q\theta - \zeta$ or $\alpha = \theta - \iota\zeta$, ψ is the poloidal or toroidal flux label, respectively, and the rotational transform ι is related to q by $\iota = 1/q$. For subsequent discussion and to be consistent with the formalism employed by the gyrokinetic code GENE (see Sec. 3.3), we will choose ψ to be the *poloidal* flux and $\alpha = q(\psi)\theta - \zeta$. The parallel coordinate z is chosen to be identical to the straight-field-line poloidal angle θ . In these coordinates, the flux-tube simulation domain is defined to be a small rectangular domain centered around ψ_0 and α_0 in SFL coordinates, given by

$$\begin{aligned} \psi_0 - \Delta\psi &\leq \psi < \psi_0 + \Delta\psi, \\ \alpha_0 - \Delta\alpha &\leq \alpha < \alpha_0 + \Delta\alpha, \\ -z_0/2 &\leq z < z_0/2. \end{aligned} \tag{3.66}$$

The flux-tube approach assumes periodic boundary conditions in the perpendicular directions, however this is an assumption of *statistical*, not physical, periodicity; that is, the statistical properties of the fluctuations at ψ and $\psi + 2\Delta\psi$ while holding α fixed, or at α and $\alpha + 2\Delta\alpha$ while holding ψ fixed, are the same. Provided the domain dimensions are larger than physical correlation lengths of the fluctuations, which are typically on the order of tens of gyroradii in the radial direction, periodic boundary conditions are an efficient means to represent turbulent eddies entering and leaving the domain. A benefit of prescribing periodic perpendicular boundary conditions is that quantities can be decomposed in a Fourier basis in ψ and α :

$$f(\psi, \alpha, z, t) = \sum_{m=-\infty}^{\infty} \sum_{n=-\infty}^{\infty} \hat{f}_{m,n}(z, t) \exp \left[i\pi \frac{m(\psi - \psi_0)}{\Delta\psi} + i\pi \frac{n(\alpha - \alpha_0)}{\Delta\alpha} \right], \tag{3.67}$$

for each physical quantity f .

A more subtle treatment is required for the parallel boundary condition, as enforcing strictly periodic boundary conditions in the parallel

direction, $f(\psi, \alpha, -z_0, t) = f(\psi, \alpha, z_0, t)$, leads to rational field lines, which is inaccurate for toroidal magnetic confinement configurations. Like the perpendicular boundary conditions, the parallel boundary condition should be an expression of statistical properties of the fluctuations. In order for this statistical invariance to successfully be satisfied, the parallel simulation domain must be longer than the parallel correlation length of the fluctuation. This is accomplished by applying periodic boundary conditions at different θ values, while holding ψ and ζ fixed, rather than holding ψ and α fixed and is expressed as

$$f[\psi, \alpha(\theta, \zeta), z(\theta)] = f[\psi, \alpha(\theta + 2\pi N, \zeta), z(\theta + 2\pi N)], \quad (3.68)$$

where N is the number of poloidal turns necessary to resolve parallel correlation lengths. Using Eq. (3.67) to represent f and taking $\alpha_0 = 0$, we have

$$f[\psi, \alpha(\theta, \zeta), z(\theta), t] = \sum_{m=-\infty}^{\infty} \sum_{n=-\infty}^{\infty} \hat{f}_{m,n}(z(\theta), t) \exp \left[i\pi \frac{m(\psi - \psi_0)}{\Delta\psi} - i\pi \frac{n\zeta}{\Delta\alpha} + i\pi \frac{nq(\psi)\theta}{\Delta\alpha} \right]. \quad (3.69)$$

Under the assumption that the perpendicular dimensions of the flux tube are small compared to background variations, we can expand $q(\psi)$ around the center of the domain ψ_0 : $q(\psi) \approx q(\psi_0) + (\psi - \psi_0)q'(\psi)$, where $q'(\psi) = dq/d\psi$. Furthermore, let $q_0 = q(\psi_0)$. We can then write Eq. (3.69) as

$$f[\psi, \alpha(\theta, \zeta), z(\theta), t] = \sum_{m=-\infty}^{\infty} \sum_{n=-\infty}^{\infty} \hat{f}_{m,n}(\theta, t) \exp \left[i\pi(\psi - \psi_0) \left(\frac{m}{\Delta\psi} + \frac{nq'\theta}{\Delta\alpha} \right) - i\pi \frac{n\zeta}{\Delta\alpha} + i\pi \frac{nq_0\theta}{\Delta\alpha} \right]. \quad (3.70)$$

Applying the parallel periodicity condition gives

$$\begin{aligned}
& \sum_{m=-\infty}^{\infty} \sum_{n=-\infty}^{\infty} \hat{f}_{m,n}(\theta + 2\pi N, t) C_n \cdot \\
& \quad \exp \left[i\pi(\psi - \psi_0) \left(\frac{m}{\Delta\psi} + \frac{nq'(\theta + 2\pi N)}{\Delta\alpha} \right) - i\pi \frac{n\zeta}{\Delta\alpha} + i\pi \frac{nq_0\theta}{\Delta\alpha} \right] \\
& = \sum_{m=-\infty}^{\infty} \sum_{n=-\infty}^{\infty} \hat{f}_{m,n}(\theta, t) \exp \left[i\pi(\psi - \psi_0) \left(\frac{m}{\Delta\psi} + \frac{nq'\theta}{\Delta\alpha} \right) - i\pi \frac{n\zeta}{\Delta\alpha} + i\pi \frac{nq_0\theta}{\Delta\alpha} \right].
\end{aligned} \tag{3.71}$$

where $C_n = \exp(i2\pi N n q_0 / \Delta\alpha)$ is a phase factor associated with the boundary condition. For Eq. (3.71) to be valid at any ζ , the coefficient of each $\exp(-in\pi\zeta/\Delta\alpha)$ term must be equal. We can re-write this in a more transparent way as

$$\begin{aligned}
& \sum_{m=-\infty}^{\infty} \hat{f}_{m,n}(\theta + 2\pi N, t) C_n \cdot \\
& \quad \exp \left[i\pi(\psi - \psi_0) \left(\frac{1}{\Delta\psi} \left(m + \frac{2\pi N n q' \Delta\psi}{\Delta\alpha} \right) + \frac{nq'\theta}{\Delta\alpha} \right) + i\pi \frac{nq_0\theta}{\Delta\alpha} \right] \\
& = \sum_{m=-\infty}^{\infty} \hat{f}_{m,n}(\theta, t) \exp \left[i\pi(\psi - \psi_0) \left(\frac{m}{\Delta\psi} + \frac{nq'\theta}{\Delta\alpha} \right) + i\pi \frac{nq_0\theta}{\Delta\alpha} \right], \tag{3.72}
\end{aligned}$$

To make the exponential factors identical, we can re-index with $m' = m + \delta m$, where

$$\delta m = 2\pi N n q' \frac{\Delta\psi}{\Delta\alpha}. \tag{3.73}$$

In order for δm to be integer-valued, this introduces a quantization on $\Delta\psi$ set by when $\Delta\psi$ is largest, which occurs at $n = 1$:

$$\Delta\psi = \frac{\mathcal{N} \Delta\alpha}{2\pi N q'}, \tag{3.74}$$

for some integer \mathcal{N} . We may then rewrite Eq. (3.72) as

$$\begin{aligned} & \sum_{m'=-\infty}^{\infty} \hat{f}_{m'-\delta m,n}(\theta + 2\pi N, t) C_n \exp \left[i\pi(\psi - \psi_0) \left(\frac{m'}{\Delta\psi} + \frac{nq'\theta}{\Delta\alpha} \right) + i\pi \frac{nq_0\theta}{\Delta\alpha} \right] \\ &= \sum_{m=-\infty}^{\infty} \hat{f}_{m,n}(\theta, t) \exp \left[i\pi(\psi - \psi_0) \left(\frac{m}{\Delta\psi} + \frac{nq'\theta}{\Delta\alpha} \right) + i\pi \frac{nq_0\theta}{\Delta\alpha} \right]. \end{aligned} \quad (3.75)$$

As the coefficients of each term in the sum must be equal, we may drop the primes from m . This gives the final form of the parallel boundary condition

$$\hat{f}_{m-\delta m,k}(\theta + 2\pi N, t) C_n = \hat{f}_{m,n}(\theta, t), \quad (3.76)$$

$$\delta m = nM, \quad M = 2\pi Nq' \frac{\Delta\psi}{\Delta\alpha}. \quad (3.77)$$

Equation (3.76) expresses that the amplitude of a mode with index m at one end of the parallel simulation domain is coupled to a mode with index $m - \delta m$ at the other end of the parallel simulation domain, with the coupling dependent on the global magnetic shear, q' . Equation (3.76) contains the phase factor $C_n = \exp(i2\pi Nnq_0/\Delta\alpha)$. For further use in GENE, the following field-aligned coordinate system is used:

$$x = \frac{q_0}{B_0 r_0} (\psi - \psi_0), \quad y = \frac{r_0}{q_0} (\alpha - \alpha_0), \quad z = \theta, \quad (3.78)$$

where r_0 is the geometrical radius of the the magnetic surface at the center of the simulation domain, $\psi_0 = \psi(r_0)$, with q_0 the safety factor, B_0 the magnetic field, and α_0 the field line label at the center of the simulation domain. Similarly, the radial wavenumber k_ψ and binormal wavenumber k_α can be redefined as

$$k_x = \frac{m\pi B_0 r_0}{q_0 \Delta\psi}, \quad k_y = \frac{n\pi q_0}{r_0 \Delta\alpha}. \quad (3.79)$$

The local magnetic shear is defined by the vector relation

$$s_{\text{loc}}(z) = \hat{\mathbf{b}}(z) \times \nabla \hat{\mathbf{n}}(z) \cdot \nabla \times \left(\hat{\mathbf{b}}(z) \times \nabla \hat{\mathbf{n}}(z) \right), \quad (3.80)$$

where $\hat{\mathbf{b}}$ is the unit vector in the direction of the magnetic field and $\hat{\mathbf{n}} = \nabla \psi(z)/|\nabla \psi(z)|$. Due to the complicated magnetic field structures stellarators, Eq. (3.80) has non-trivial dependence along field lines. The global magnetic shear is defined as the flux surface average of Eq. (3.80) and can be shown to be equal to

$$\hat{s} = (r_0/q_0) dq/dr. \quad (3.81)$$

Mapping from Cartesian coordinates to the field-aligned coordinate system induces a new *metric tensor* \mathbf{g} , which is a symmetric tensor that generalizes inner products between tangent vectors on differentiable manifolds (D'haeseleer et al., 1991). The metric tensor in the coordinates x^i has components defined by the contravariant basis vectors ∇x^i :

$$g^{ij} = \nabla x^i \cdot \nabla x^j. \quad (3.82)$$

For the field-aligned coordinate system (x, y, z) , where x and y are given by Eq. (3.78) so that the magnetic field has the representation $\mathbf{B}(z) = \nabla x(z) \times \nabla y(z)$, the metric tensor is given by

$$\mathbf{g} = \begin{pmatrix} g^{xx} & g^{xy} & g^{xz} \\ g^{xy} & g^{yy} & g^{yz} \\ g^{xz} & g^{yz} & g^{zz} \end{pmatrix}. \quad (3.83)$$

One can attribute physical significance to the metric elements. As $g^{xx} \propto \nabla \psi \cdot \nabla \psi$, this is a measure of the flux surface compression along the field line. The quantities g^{xy} and g^{yy} are measures of local magnetic shear. Using

Eq. (3.64) for the magnetic field representation, $\hat{\mathbf{b}} \times \hat{\mathbf{n}}$ in Eq. (3.80) becomes

$$\hat{\mathbf{b}} \times \hat{\mathbf{n}} = \frac{1}{B|\nabla\psi|} |\nabla\psi|^2 \nabla\alpha - (\nabla\psi \cdot \nabla\alpha) \nabla\psi, \quad (3.84)$$

and $\nabla \times (\hat{\mathbf{b}} \times \hat{\mathbf{n}})$ becomes

$$\begin{aligned} \nabla \times (\hat{\mathbf{b}} \times \hat{\mathbf{n}}) &= \frac{1}{B|\nabla\psi|} [\nabla (|\nabla\psi|^2) \times \nabla\alpha - \nabla (\nabla\psi \cdot \nabla\alpha) \times \nabla\psi] \\ &\quad + \nabla \left(\frac{1}{B|\nabla\psi|} \right) \times (\mathbf{B} \times \nabla\psi), \end{aligned} \quad (3.85)$$

where the identity $\nabla \times \nabla\phi = 0$ for any twice-differentiable scalar field ϕ was used. The last term in Eq. (3.85) vanishes when dotted with $\mathbf{B} \times \nabla\psi$, since $\mathbf{G} \cdot \mathbf{H} \times \mathbf{G} = 0$ for any \mathbf{G} and \mathbf{H} . Equation (3.80) then becomes

$$\begin{aligned} s_{\text{loc}} &= \frac{1}{B^2 g^{\psi\psi}} [g^{\psi\psi} (\nabla\psi \times \nabla\alpha) \cdot \nabla (g^{\psi\alpha}) - (\nabla\psi \cdot \nabla\alpha) g^{\psi\alpha} \cdot \nabla (g^{\psi\psi})] \\ &= \frac{1}{B^2 g^{\psi\psi}} [g^{\psi\psi} \mathbf{B} \cdot \nabla g^{\psi\alpha} - g^{\psi\alpha} \mathbf{B} \cdot \nabla g^{\psi\psi}] \\ &= \frac{g^{\psi\psi}}{B^2} \mathbf{B} \cdot \nabla \frac{g^{\psi\alpha}}{g^{\psi\psi}}. \end{aligned} \quad (3.86)$$

Thus the expression for the local shear involves $\mathbf{B} \cdot \nabla g^{\psi\alpha}$, which is the derivative along the field line of $g^{\psi\alpha}$ and when inverted implies $g^{\psi\alpha}$ (which is g^{xy} up to a normalization) is a measure of the *integrated* local shear, which has contributions from the global magnetic shear \hat{s} and the local magnetic shear ripple. The metric element g^{yy} is also a measure of the local shear, as $g^{yy} = (B^2 + (g^{xy})^2) / g^{xx}$. The scalar Jacobian measure of the flux-tube coordinate transformation is given by the square root of the determinant of \mathbf{g} and has the following relation to the contravariant basis vectors:

$$\sqrt{g} = \frac{1}{\nabla x \cdot \nabla y \times \nabla z}, \quad (3.87)$$

where $g = \det(\mathbf{g})$. These geometric elements provide the machinery to compute all of the inner products and integrals involved in solving the gyrokinetic Vlasov-Maxwell equations in a flux tube.

3.3 The GENE Code

The Gyrokinetic Electromagnetic Numerical Experiment (GENE) code (Jenko et al., 2000) is a massively-parallel gyrokinetic turbulence code that solves the Vlasov-Maxwell system of equations, Eqs. (3.56) and (3.61)–(3.63). While GENE was originally written to compute turbulence in flux tubes in axisymmetric toroidal geometry, it has since been extended to compute turbulence in the full toroidal plasma volume with fixed radial boundary conditions as well as in fully three-dimensional geometry necessary for stellarator simulations. Comprehensive stellarator gyrokinetic turbulence simulations are a relatively recent achievement (see Sec. 3.4 for a review of the existing literature), thus there is still much to be learned by focusing on stellarator flux-tube simulations and is the approach taken in this thesis. Equations (3.56) and (3.61)–(3.63) cannot be solved numerically as is, they must first be *non-dimensionalized*. The normalizations used in GENE and the normalized equations used in GENE are given below.

3.3.1 GENE Normalizations

The normalizations for each physical quantity in the Vlasov-Maxwell equations are chosen such that the non-dimensional values of physically important quantities take on characteristic values of order unity. This ensures that numerical errors resulting from the finite representation of numbers on a computer, which occur at the extremes of the representation, are minimized. The reference quantities, referred to by the subscript “ref” should be chosen to best suit the physics being simulated. For example, if one is simulating ion-scale turbulence due to ITG drift waves, the proper choice of the

reference temperature, density, and mass are those of the ion species so that $\rho_{\text{ref}} = \rho_i$. Conversely for electron-scale turbulence, one would select the corresponding electron quantities so that $\rho_{\text{ref}} = \rho_e$. In stellarator applications, it is conventional to set the reference length scale to the average minor radius a . The GENE normalizations for the variables are as follows:

$$\begin{aligned}
(x, y) &\rightarrow \rho_{\text{ref}}(x, y) & z &\rightarrow z \\
v_{\parallel} &\rightarrow c_{\text{ref}} v_{T\sigma} v_{\parallel} & \mu &\rightarrow \frac{T_{\text{ref}}}{B_{\text{ref}}} T_{\sigma 0} \mu \\
t &\rightarrow \frac{L_{\text{ref}}}{c_{\text{ref}}} t & B_0 &\rightarrow B_{\text{ref}} B_0, \\
q_{\sigma} &\rightarrow e q_{\sigma} & m_{\sigma} &\rightarrow m_{\text{ref}} m_{\sigma} \\
n_{\sigma 0} &\rightarrow n_{\text{ref}} n_{\sigma 0} & T_{\sigma 0} &\rightarrow T_{\text{ref}} T_{\sigma 0}
\end{aligned} \tag{3.88}$$

where e is the elementary charge. The derived normalizations are

$$c_{\text{ref}} = \sqrt{\frac{T_{\text{ref}}}{m_{\text{ref}}}}, \quad \rho_{\text{ref}} = \frac{m_{\text{ref}} c_{\text{ref}}}{e B_{\text{ref}}}, \quad v_{T\sigma} = \sqrt{\frac{2T_{\sigma 0}}{m_{\sigma}}}. \tag{3.89}$$

The gyrocenter distribution function and fields have the following normalizations:

$$\begin{aligned}
(\bar{f}_{\sigma}, g_{\sigma}) &\rightarrow \frac{\rho_{\text{ref}}}{L_{\text{ref}}} \frac{n_{\text{ref}} n_{\sigma 0}}{c_{\text{ref}}^3 v_{T\sigma}^3} (\bar{f}_{\sigma}, g_{\sigma}) & \bar{F}_{\sigma 0} &\rightarrow \frac{n_{\text{ref}} n_{\sigma 0}}{c_{\text{ref}}^3 v_{T\sigma}^3} \bar{F}_{\sigma 0} \\
(\Phi, \chi) &\rightarrow \frac{\rho_{\text{ref}}}{L_{\text{ref}}} \frac{T_{\text{ref}}}{e} (\Phi, \chi) & (A_{\parallel}, B_{\parallel}) &\rightarrow \frac{\rho_{\text{ref}}}{L_{\text{ref}}} B_{\text{ref}} (\rho_{\text{ref}} A_{\parallel}, B_{\parallel})
\end{aligned} \tag{3.90}$$

The derived quantity G_{σ} is now $G_{\sigma} = g_{\sigma} + (q_{\sigma}/T_{\sigma 0}) \bar{F}_{\sigma 0} \chi$ and the normalized plasma pressure is $\beta = 8\pi n_{\text{ref}} T_{\text{ref}} / B_{\text{ref}}^2$. The curvature terms involved in Eqs. (3.52) and (3.53) are expressed in terms of the metric by evaluating the individual components of $(\hat{\mathbf{b}}_0 \times \nabla B_0) / B_0$:

$$\begin{aligned}
\frac{1}{B_0} \hat{\mathbf{b}}_0 \times \nabla B_0 \cdot \nabla x &= -\frac{(g^{xx} g^{yy} - g^{xy} g^{xy})}{B_0^2} \frac{\partial B_0}{\partial y} - \frac{(g^{xx} g^{yz} - g^{xy} g^{xz})}{B_0^2} \frac{\partial B_0}{\partial z} \\
&= -\frac{\partial B_0}{\partial y} - \frac{g^{xx} g^{yz} - g^{xy} g^{xz}}{B_0^2} \frac{\partial B_0}{\partial z},
\end{aligned} \tag{3.91}$$

$$\begin{aligned} \frac{1}{B_0} \hat{\mathbf{b}}_0 \times \nabla B_0 \cdot \nabla y &= \frac{(g^{xx} g^{yy} - g^{xy} g^{xy})}{B_0^2} \frac{\partial B_0}{\partial x} + \frac{(g^{xz} g^{yy} - g^{xy} g^{yz})}{B_0^2} \frac{\partial B_0}{\partial z} \\ &= \frac{\partial B_0}{\partial x} + \frac{g^{xz} g^{yy} - g^{xy} g^{yz}}{B_0^2} \frac{\partial B_0}{\partial z}. \end{aligned} \quad (3.92)$$

Thus the normalized curvature terms become

$$\mathcal{K}_x = \frac{L_{\text{ref}}}{B_{\text{ref}}} \left(-\frac{\partial B_0}{\partial y} - \frac{g^{xx} g^{yz} - g^{xy} g^{xz}}{B_0^2} \frac{\partial B_0}{\partial z} \right), \quad (3.93)$$

$$\mathcal{K}_y = \frac{L_{\text{ref}}}{B_{\text{ref}}} \left(\frac{\partial B_0}{\partial x} + \frac{g^{xz} g^{yy} - g^{xy} g^{yz}}{B_0^2} \frac{\partial B_0}{\partial z} \right). \quad (3.94)$$

The derivatives of the background gyrocenter distribution function can be computed analytically using Eq. (3.60), yielding

$$\nabla \bar{F}_{\sigma 0} = \bar{F}_{\sigma 0} \left(\frac{\nabla n_{0\sigma}}{n_{0\sigma}} + \left(\frac{m_\sigma v_{\parallel}^2}{2T_{0\sigma}} + \frac{\mu B_0}{T_{0\sigma}} - \frac{3}{2} \right) \frac{\nabla T_{0\sigma}}{T_{0\sigma}} - \frac{m u}{T_{0\sigma}} \nabla_{\mathbf{x}} B_0 \right), \quad (3.95)$$

$$\frac{\partial \bar{F}_{\sigma 0}}{\partial v_{\parallel}} = -\frac{m_\sigma v_{\parallel}}{T_{0\sigma}} \bar{F}_{\sigma 0}, \quad (3.96)$$

$$\frac{\partial \bar{F}_{\sigma 0}}{\partial \mu} = -\frac{B_0}{T_{0\sigma}} \bar{F}_{\sigma 0}. \quad (3.97)$$

3.3.2 Vlasov-Maxwell equations in GENE

This gives the final normalized version of the Vlasov equation for the non-adiabatic part of the perturbed gyrocenter distribution function that is

solved by GENE:

$$\begin{aligned}
& \frac{\partial g_\sigma}{\partial t} + \frac{B_0}{B_{0\parallel}^*} \left[\omega_n + \omega_{T\sigma} \left(v_{\parallel}^2 + \mu B_0 - \frac{3}{2} \right) \right] \bar{F}_{\sigma 0} \frac{\partial \chi}{\partial y} \\
& + \frac{B_0}{B_{0\parallel}^*} \left(\frac{\partial \chi}{\partial y} \frac{\partial g_\sigma}{\partial x} + \frac{\partial \chi}{\partial x} \frac{\partial g_\sigma}{\partial y} \right) + \frac{B_0}{B_{0\parallel}^*} \frac{T_{\sigma 0} (2v_{\parallel}^2 + \mu B_0)}{q_\sigma B_0} \\
& \cdot \left[\mathcal{K}_x \frac{\partial G_\sigma}{\partial x} + \mathcal{K}_y \frac{\partial G_\sigma}{\partial y} - \mathcal{K}_x \bar{F}_{\sigma 0} \left(\omega_n + \omega_{T\sigma} \left(v_{\parallel}^2 + \mu B_0 - \frac{3}{2} \right) \right) \right] \\
& - \frac{B_0}{B_{0\parallel}^*} \frac{T_{\sigma 0} v_{\parallel}^2}{q_\sigma B_0^2} \beta \left(\sum_{\sigma} n_{\sigma 0} T_{\sigma 0} (\omega_n + \omega_{T\sigma}) \right) \frac{\partial G_\sigma}{\partial y} \\
& - \frac{v_{T\sigma} v_{\parallel}}{J B_0} \frac{\partial G_\sigma}{\partial z} + \frac{v_{T\sigma} v_{\parallel}}{2 J B_0} \frac{\partial B_0}{\partial z} \frac{\partial \bar{f}_{\sigma 1}}{\partial v_{\parallel}} = 0, \quad (3.98)
\end{aligned}$$

where $J = B^\phi / B_{\text{ref}}$ is the Jacobian. The background density and temperature gradients are denoted by

$$\omega_{n,T} = \frac{L_{\text{ref}}}{(n, T)_{\sigma 0}} \frac{d(n, T)_{\sigma 0}}{dx}. \quad (3.99)$$

The normalized field equations are given by

$$\begin{aligned}
& \left(\frac{B_{\text{ref}}^2}{4\pi c^2 m_{\text{ref}} n_{\text{ref}}} k_{\perp}^2 + \sum_{\sigma} \frac{q_{\sigma}^2 n_{\sigma 0}}{T_{\sigma 0}} (1 - \Gamma_0(b_{\sigma})) \right) \Phi \\
& - \left(\sum_{\sigma} \frac{q_{\sigma} n_{\sigma 0}}{B_0} (\Gamma_0(b_{\sigma}) - \Gamma_1(b_{\sigma})) \right) B_{\parallel} \\
& = \sum_{\sigma} \pi q_{\sigma} n_{\sigma 0} B_0 \int dv_{\parallel} d\mu J_0(\lambda_{\sigma}) g_{\sigma}, \quad (3.100)
\end{aligned}$$

$$\begin{aligned}
& \left(\sum_{\sigma} \frac{q_{\sigma} n_{\sigma 0}}{B_0} (\Gamma_0(b_{\sigma}) - \Gamma_1(b_{\sigma})) \right) \Phi \\
& + \left(-\frac{2}{\beta} + \sum_{\sigma} \frac{2n_{\sigma 0} T_{\sigma 0}}{B_0^2} (\Gamma_0(b_{\sigma}) - \Gamma_1(b_{\sigma})) \right) B_{\parallel} \\
& = - \sum_{\sigma} \frac{\pi q_{\sigma} v_{T\sigma} B_0^{3/2} n_{\sigma 0}}{k_{\perp}} \int dv_{\parallel} d\mu \mu^{1/2} J_1(\lambda_{\sigma}) g_{\sigma}, \quad (3.101)
\end{aligned}$$

$$\begin{aligned}
A_{\parallel} = & \left(\sum_{\sigma} \frac{\pi}{2} q_{\sigma} v_{T\sigma} n_{\sigma 0} B_0 \beta \int dv_{\parallel} d\mu v_{\parallel} J_0(\lambda_{\sigma}) g_{\sigma} \right) \\
& \cdot \left(k_{\perp}^2 + \sum_{\sigma} \frac{q_{\sigma}^2}{m_{\sigma}} \pi n_{\sigma 0} B_0 \beta \int dv_{\parallel} d\mu v_{\parallel}^2 J_0(\lambda_{\sigma}) 2\bar{F}_{\sigma 0} \right)^{-1}, \quad (3.102)
\end{aligned}$$

with $k_{\perp}^2 = k_x^2 g^{xx} + 2k_x k_y g^{xy} + k_y^2 g^{yy}$. The GENE equations are solved in a pseudospectral approach, where the equations are evolved in the Fourier representation of Eq. (3.67). However, instead of computing the $\mathbf{E} \times \mathbf{B}$ nonlinearity in the spectral representation, the potential χ and distribution function g_{σ} are transformed back into real space, where a pointwise multiplication is performed, before transforming back into wavenumber space. Due to the advantages of Fast Fourier Transforms, this significantly reduces the cost of evaluating the nonlinearity compared to that of a 2D convolution if the nonlinearity was to be computed only in wavenumber space.

3.4 Stellarator Turbulence Simulations

A significant body of literature exists studying turbulence in toroidal geometries by means of gyrokinetic simulation in flux tube simulation domains, see e.g., Dimits et al. (1996); Jenko et al. (2000); Dorland et al. (2000); Candy and Waltz (2003); Sugama and Watanabe (2006); Peeters et al. (2009); Chen et al. (2013). Most of the early gyrokinetic simulation work

focused turbulence in axisymmetric geometries, as the cost incurred by the 3D geometry of stellarators makes simulations significantly more expensive. Nonetheless, over the past decade, there has been significant understanding gained through gyrokinetic simulations of ITG and ETG modes in stellarator plasmas (Jenko and Dorland, 2002; Jenko and Kendl, 2002; Rewoldt et al., 2005; Xanthopoulos and Jenko, 2007; Xanthopoulos et al., 2007; Baumgaertel et al., 2011, 2012; Plunk et al., 2014; Xanthopoulos et al., 2016; Plunk et al., 2017) and subsequent turbulent transport optimization (Mynick, 2006; Mynick et al., 2009, 2010, 2011, 2014; Xanthopoulos et al., 2014). However, only recently have computational capabilities reached the point where TEMs in stellarators can be simulated effectively. As such, relatively little comprehensive analysis of TEM-driven turbulence in stellarators has been performed, however the body of work on the subject is growing, with publications on TEMs in the W7-X stellarator (Baumgaertel et al., 2012; Proll et al., 2012a,b; Helander et al., 2013; Proll et al., 2013), HSX (Faber et al., 2015), and LHD (Nakata et al., 2017), as well as early investigations of TEM optimization (Proll et al., 2016).

In this thesis, calculations of linear eigenmodes and nonlinear turbulence for the HSX stellarator are performed using GENE. The GIST package (Xanthopoulos et al., 2009) is used to generate the necessary components for flux-tube simulations of the magnetic geometry along a field line from reconstructed equilibria. Linear eigenmode calculations may be performed as initial value calculations, converging onto the most unstable mode. However, simulations of ITG turbulence in the HSX configuration (see Pueschel et al. (2016) and Ch. 5) indicate that resolving the subdominant eigenmode spectrum is crucial for accurate turbulence simulations. Eigenmode calculations presented in Chs. 4 and 5 are accomplished using fast iterative eigenvalue routines implemented from the Scalable Library for Eigenvalue Problem Computations (SLEPc) package (Hernandez et al., 2005). In Ch. 5, calculations make use of the recently implemented “matrix function” computation

technique, which has shown significant improvement in efficiency for the calculation of the subdominant spectrum for stellarator geometry. More traditional iterative techniques, such as Jacobi-Davidson methods, proved ineffective in accessing the subdominant spectrum, often failing to return a single subdominant eigenmode in 10^3 CPU hours. The accuracy of the iterative method has been confirmed by finding perfect agreement with the unstable spectrum obtained in Pueschel et al. (2016) through full-matrix inversion performed with the ScaLAPACK code (Blackford et al., 1997). More detailed information about the matrix function technique can be found in Faber et al. (2018, Appendix B).

3.5 Chapter Summary

This chapter presented the derivation of the gyrokinetic Vlasov-Maxwell system of equations used by the GENE code to simulate the evolution of plasma fluctuations in toroidal fusion geometries. The derivation made full use of the symplectic structure of the single particle Lagrangian and Hamiltonian on extended phase space. The fast gyrophase dependence of particle motion was removed by successive Lie transformations, moving from particle phase space to guiding center phase space to gyrocenter phase space. The flux-tube computation domain used in GENE, as well as the normalizations used to non-dimensionalize the gyrokinetic equations in GENE were presented, along with a brief literature review of gyrokinetic turbulence simulations in stellarators.

4 TRAPPED ELECTRON MODE TURBULENCE IN HSX

In this chapter, comprehensive linear calculations and the first nonlinear gyrokinetic simulations of ∇n -driven TEM turbulence in HSX are shown. Simulation results are presented for parameters representative of an HSX plasma and for a ∇n scan. Heat fluxes consistent with experimental values are obtained, providing evidence that ∇n -driven turbulence is responsible for the observed heat fluxes in HSX. In this chapter, the computational domains use geometry from one poloidal turn, but will be relaxed in Ch. 5. The chapter closely follows Faber et al. (2015).

4.1 TEM Instability in HSX

The TEM destabilization condition (see Sec. 1.3) is easily met in HSX, as is shown below in Figs. 4.1 and 4.2, due to the overlap of regions of bad curvature and magnetic wells, a property that generally occurs for quasi-symmetric stellarator configurations (Rewoldt et al., 2005; Rafiq and Hegna, 2006). One would then expect TEMs to be linearly unstable in HSX for some density gradient, which has been shown in the linear gyrokinetic growth rate calculations performed in Guttenfelder et al. (2008). The present work represents the first examination of the nonlinear state of TEM-driven turbulence in HSX, and together with the work published in Proll et al. (2013) the first examination of TEM turbulence in neoclassical-transport-optimized stellarators.

In a tokamak, one flux tube is identical to all other flux tubes on the same magnetic surface, and thus a single flux tube can be used to represent a magnetic surface. This is not the case in stellarators (Dewar and Glasser, 1983), where different flux tubes can experience different curvatures and trapping regions along the field line, with resulting changes to drift-wave

behavior. The two representative flux tubes used in this work at the half-radius in the toroidal flux coordinate $\Psi/\Psi_0 \simeq 0.5$ ($r/a \simeq 0.71$) are identified by the shape of the plasma cross-section at zero poloidal angle. The normalized normal curvature and normalized magnetic field strength of the flux tubes are given in Fig. 4.1, corresponding to a bean shaped cross-section, and Fig. 4.2, corresponding to a triangular cross-section. The flux tubes will hereafter be identified as HSX-b and HSX-t, respectively, and are the up-down symmetry planes one-half field period away from each other. As seen in Figs. 4.1 and 4.2, a feature of both flux tubes is the correlation of the regions of bad (negative) curvature and magnetic field minima (trapped particle regions), which is similar to tokamak geometry. However, unlike a tokamak, the majority of particles trapped in these wells are not toroidally, but rather helically trapped.

In order to minimize deleterious effects from large near-resonant Pfirsch-Schlüter currents and low-order rational surfaces, stellarators are often designed to operate in regions where the rotational transform is considerably constrained (Boozer, 1998; Helander, 2014), such that the global magnetic shear $|\hat{s}| \lesssim 0.1$. The rotational transform for HSX is constrained such that $t_{\text{axis}} \approx 1.05$ and $t_{\text{edge}} \approx 1.1$, and at the half-toroidal flux surface, $\hat{s} \approx -0.046$. If \hat{s} becomes small, the box size in the radial direction can become quite large, as shown by Eq. (3.74), and is in contrast to many tokamak applications with $\hat{s} \sim \mathcal{O}(1)$. At the half-toroidal flux surface this leads to typical box sizes $L_x \gtrsim 200\rho_s$, where ρ_s is the ion sound gyroradius. As the numerical resolution in the radial direction is set such that $\mathcal{O}(\rho_s)$ features are captured, the large radial box size provides a significant computational constraint for flux-tube simulations and is investigated further in Ch. 5.

Here, two different TEM parameter sets will be investigated. As HSX operates with primarily ECRH heating, the ions have a flat temperature profile for a majority of the minor radius. As such there will be no ion temperature gradient in the following simulations. The first parameter

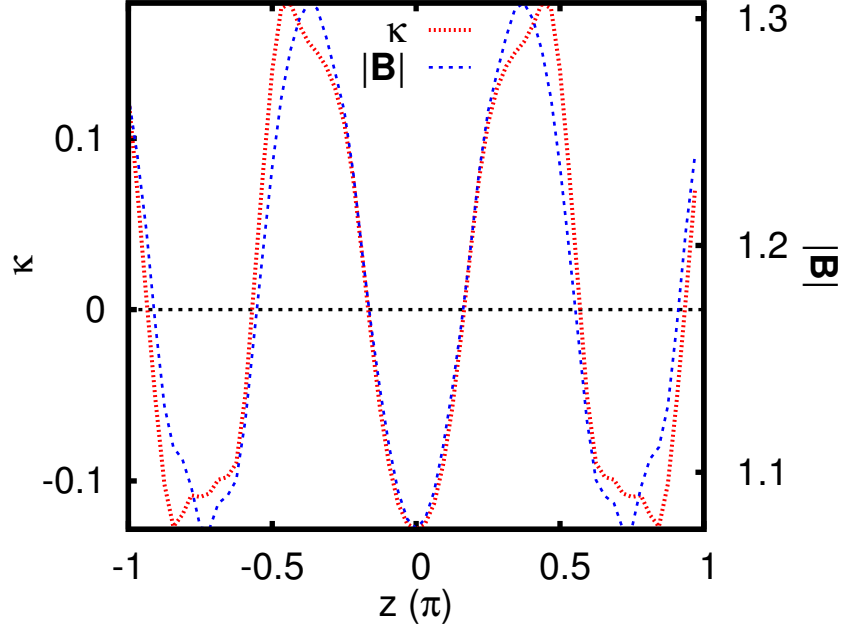


Figure 4.1: Normalized normal curvature (red dotted line) and normalized magnetic field strength (blue dashed line) in the parallel direction in HSX-b. Negative curvature indicates bad curvature. Source: Faber et al. (2015).

set will be called the “standard” TEM and was selected to capture the essential physics of the density-gradient-driven TEM when both a density and electron temperature gradient are present but the density gradient is larger ($\eta_e = d\ln T_e/d\ln n_e < 1$). It uses the normalized density gradient $a/L_n = 2$ and normalized electron temperature gradient $a/L_{T_e} = 1$, where a is the averaged minor radius, $L_\xi = \frac{1}{\xi} \frac{d\xi}{dx}$ is the inverse length scale for any scalar ξ and $T_{e0}/T_{i0} = 1$ with $m_i/m_e = 1836$, where T_{s0} , m_s is the background temperature and mass of species s . The standard TEM parameter set will be applied to simulations in both flux tubes.

The second parameter set was selected to examine the sensitivity of the TEM to only the driving density gradient. This parameter set uses four different density gradient values, $a/L_n = 1, 2, 3, 4$ and no electron

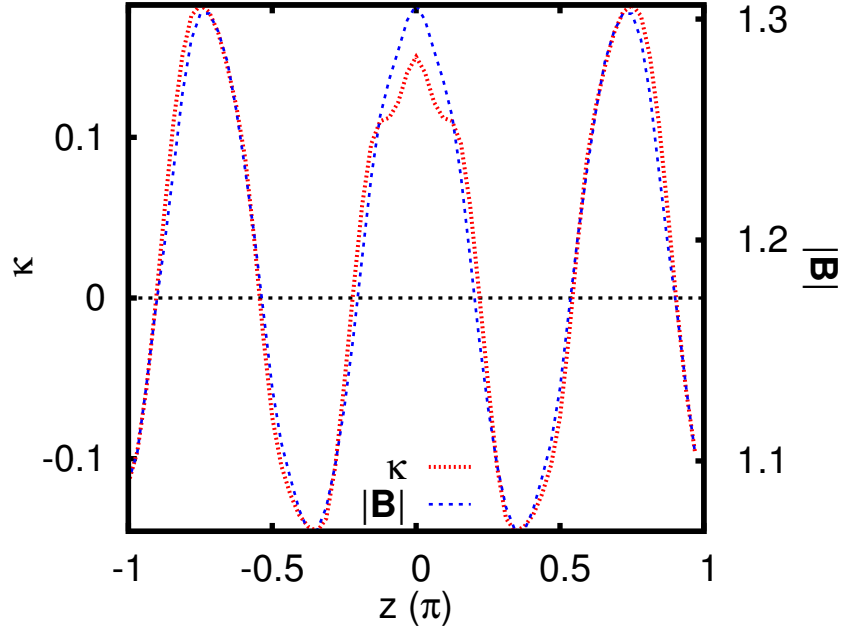


Figure 4.2: Normalized normal curvature (red dotted line) and normalized magnetic field strength (blue dashed line) in the parallel direction in HSX-t. Negative curvature indicates bad curvature. Source: Faber et al. (2015).

temperature gradient. This parameter set will only be used in simulations done for HSX-b. The normalized electron pressure is $\beta = 8\pi n_{e0}T_{e0}/B_0^2 = 0.05\%$, where n_{e0} is the background electron density.

4.2 Linear Instability Analysis

The linear growth rates, frequencies and mode structures presented in this section have been calculated by two different methods. Initial value simulations are used to obtain only the fastest growing mode at each k_y . Eigenvalue simulations calculate both the dominant and subdominant modes at each k_y . The three-dimensional nature of the magnetic geometry makes for a rich eigenmode landscape characterized by many subdominant, but

growing modes for each k_y .

The growth rates have been checked for convergence with resolution, by performing a series of simulations with increasingly fine resolution until the growth rates show no change. Two factors make these simulations substantially more expensive than tokamak simulations: (1) the magnetic field along the field line has more structure, and as such, stellarator simulations may require between 3 and 10 times as much resolution in the parallel direction (Xanthopoulos and Jenko, 2007; Proll et al., 2013); and (2) the low \hat{s} allows linear modes at low k_y to become very extended along the field line and require large numbers of radial connections to resolve, corresponding to increasingly fine radial grids in real space. For linear simulations, we used a numerical grid size of $N_z \times N_{v_{\parallel}} \times N_{\mu} = 64 \times 36 \times 8$ with $17 \leq N_x \leq 97$, where μ is the magnetic moment. The parallel hyper-diffusion coefficient, see Pueschel et al. (2010), was set to $\epsilon_z = 4$.

4.2.1 Linear dispersion relation

First we examine the linear behavior for both HSX-b and HSX-t. The growth rates and real frequencies for the standard TEM case in both flux tubes are presented in Fig. 4.3. The magnitude of the maximum growth rates are different ($\gamma = 0.643$ in HSX-b vs. $\gamma = 0.443$ in HSX-t), and the peak occurs at slightly different k_y ($k_y = 2.1$ in HSX-b vs. $k_y = 1.6$ in HSX-t). The difference in growth rate magnitudes can be explained by examining Figs. 4.1 and 4.2. With z in Figs. 4.1, 4.2 as the parallel coordinate, one can see in Fig. 4.1 (HSX-b) a region centered around $z = 0$ corresponding to a magnetic field minimum and unfavorable curvature. The situation is reversed in HSX-t, where modes localized near $z = 0$ see favorable curvature. The observed faster growth at high- k_y in HSX-b is more strongly ballooning, i.e. its structure is mainly confined to $k_x = 0$, whereas its HSX-t counterpart peaks at a finite $|k_x| = \pm 4, 6\pi$.

The peak growth rates in HSX are at larger k_y compared with density-

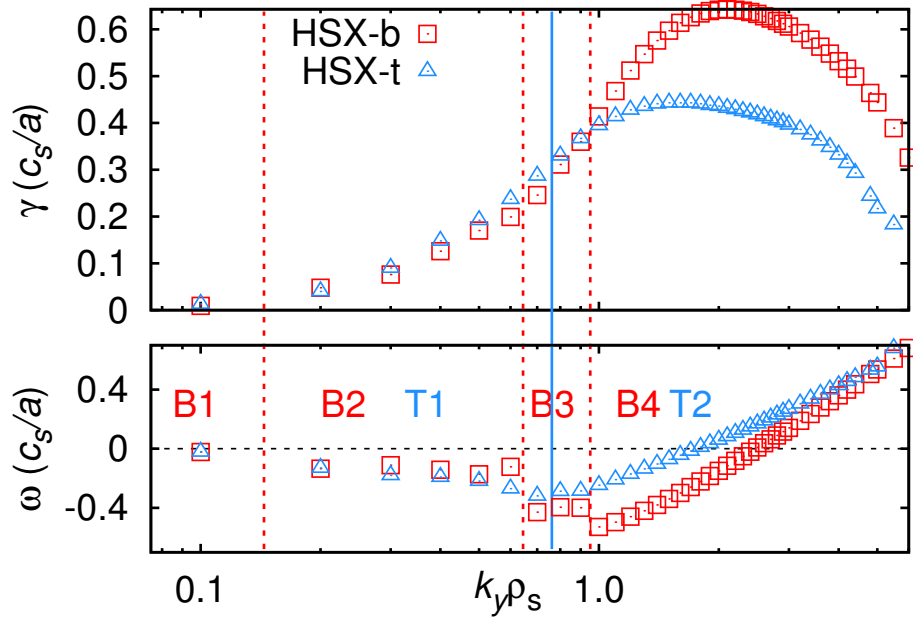


Figure 4.3: Linear growth rates (top) and real frequencies (bottom) in HSX flux tubes for canonical TEM parameter set: $a/L_n = 2$, $a/L_{Te} = 1$. The different dominant mode regions are identified as the B modes for HSX-b and the T modes for HSX-t. The red dashed lines indicate the approximate boundaries between different dominant B modes and the blue solid line is the approximate boundary between T modes. Negative real frequencies indicate modes with electron-direction drift frequencies. Source: Faber et al. (2015).

gradient-driven TEM in tokamaks (Ernst et al., 2004, 2009), where $k_y(\gamma_{\max}) \lesssim 0.7$. They are comparable to the k_y of peak growth rates in W7-X (Proll et al., 2013), where $k_y(\gamma_{\max}) \approx 1.6$. Applying a simple quasilinear estimate for the heat flux, $Q_{k_y}^{QL} \propto \gamma_k / (k_y)^2$ (assuming $k_x = 0$) suggests that scales at $k_y < 1$, where both HSX-b and HSX-t have similar linear growth rates, will likely dominate transport. Thus despite there being a significant difference in the maximum linear growth rates between the two flux tubes, the nonlinear behavior of the flux tubes may be similar.

The real frequencies show electron-propagation-direction modes for $k_y \leq 2$. This feature of the linear modes is robust against variations in β , where the low- k_y linear modes maintain electron propagation direction. No kinetic ballooning modes are expected, as $\beta = 0.05\%$ is well below marginal ideal MHD ballooning stability point for HSX (Hudson et al., 2004). The real frequencies in Fig. 4.3 show discontinuities in k_y for $k_y < 1$, which is indicative of the coexistence of different modes. These modes will be classified in Sec. 4.2.3. At the high- k_y end of the spectrum, the real frequencies for both flux tubes cross the $\omega_r = 0$ boundary shortly after the peak growth rate, switching from electron to ion propagation direction. This type of mode has been observed in linear TEM simulations for a variety of configurations from stellarators (Proll et al., 2013) to tokamaks (Rewoldt and Tang, 1990; Ernst et al., 2004, 2009) and the reversed-field pinch (Carmody et al., 2015), and is referred to as the “ubiquitous” mode (Coppi et al., 1990). Despite the high growth rates in these modes, the high k_y modes contribute a relatively small amount to the overall transport, as is shown in Sec. 4.3, due to the quasilinear k_{\perp}^{-2} scaling.

To isolate the role of the density gradient, we set the electron temperature gradient to zero and only vary the density gradient. The growth rates and real frequencies for the density gradient scan in HSX-b are presented in Fig. 4.4. Without an electron temperature gradient, the linear growth rates and frequencies for the density gradient scan are similar to that of the standard

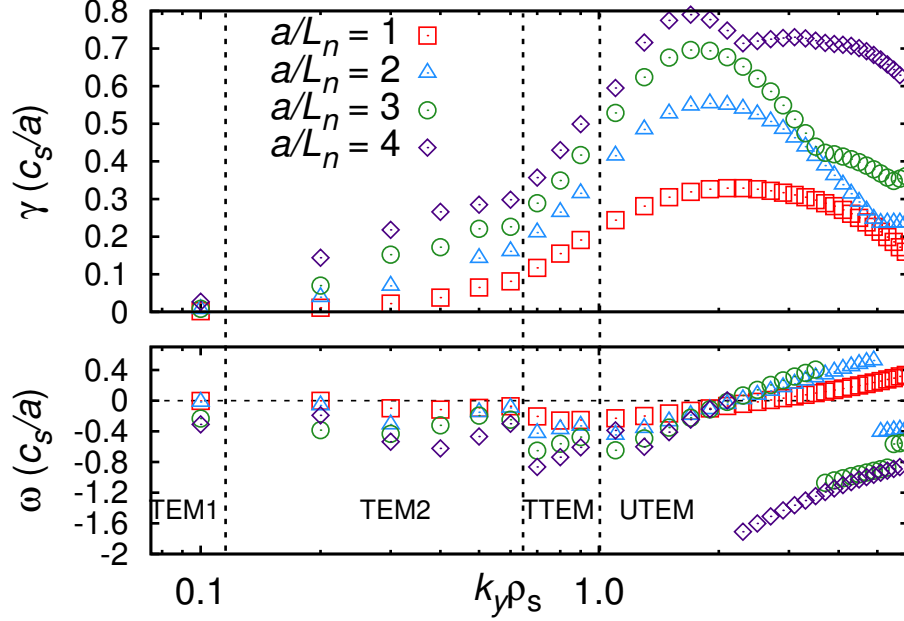


Figure 4.4: Linear growth rates (top) and real frequencies (bottom) in HSX-b for the density gradient scan: $a/L_n = 1 - 4$, $a/L_{Te} = 0$. Approximate mode boundaries are indicated by the dashed vertical lines. The mode types are determined by the analysis in Secs. 4.2.2 and 4.2.3. Source: Faber et al. (2015).

TEM, providing evidence that the standard TEM is a density-gradient driven TEM with little sensitivity to a/L_{Te} , and is a general property of HSX plasmas, consistent with previous work (Rewoldt et al., 2005; Rafiq and Hegna, 2006; Guttenfelder et al., 2008). The high k_y ubiquitous mode transitions to a different mode at even higher k_y as a/L_n is increased. The behavior of the different modes at low k_y becomes clearer, as the different mode boundaries are delineated by discontinuities in the real frequencies. Examination of the potential mode structures, shown for the standard TEM parameters in Sec. 4.2.3, reveal that the dominant mode at each k_y for each a/L_n are the same as the modes at each k_y for the standard TEM. At

$k_y = 0.1$, the growth rate for each a/L_n is small, which was also observed in the standard TEM simulations, indicating it may not be necessary to resolve lower k_y in nonlinear simulations.

4.2.2 Linear eigenmode structure

The eigenmodes in Figs. 4.3 and 4.4 are distinguished under the assumption that the real frequencies of a particular mode branch should be a continuous function in k_y . One can distinguish four different dominant linear modes in HSX-b but only two different dominant linear modes in HSX-t. The potential structure in the ballooning representation for the different mode branches of HSX-b and HSX-t are shown in Figs. 4.5 and 4.6, respectively, as a function of the ballooning angle $\theta = z + 2\pi p$, where p is an integer (Candy et al., 2004). For HSX-b, there is significant variation in the structure between modes. At $k_y = 0.1$, mode B1 in Fig. 4.5 has a strongly extended envelope in θ with maxima symmetrically located at roughly $\theta \sim \pm 10\pi$ in the ballooning angle. On top of the extended envelope, there are spikes in the mode amplitude within each radial connection (every 2π in θ), which correspond to the localized bad curvature at $z = 0$ in Fig. 4.1. These spikes are well-resolved. The broad envelope and narrow spikes indicate two disparate scales in the modes at low k_y . The combination of low k_y and small \hat{s} leads to a slab-like mode that extends along the field line, where the larger scale is related to the magnetic shear \hat{s} and the small scale is related to the localization via bad curvature. This result is consistent with what occurs in a tokamak, where lower k_y modes have broader ballooning structure (Tang, 1978), particularly in the $\hat{s} \ll 1$ limit (Candy et al., 2004; Citrin et al., 2012).

For $0.2 \leq k_y \leq 0.6$, corresponding to mode B2 of Fig. 4.5, the mode still has an extended structure, but the envelope peaks more narrowly at $\theta \approx \pm 20\pi$, which corresponds to a finite- k_x mode. Mode B3, dominant for $0.7 \leq k_y \leq 0.9$, is considerably more localized but possesses tearing parity,

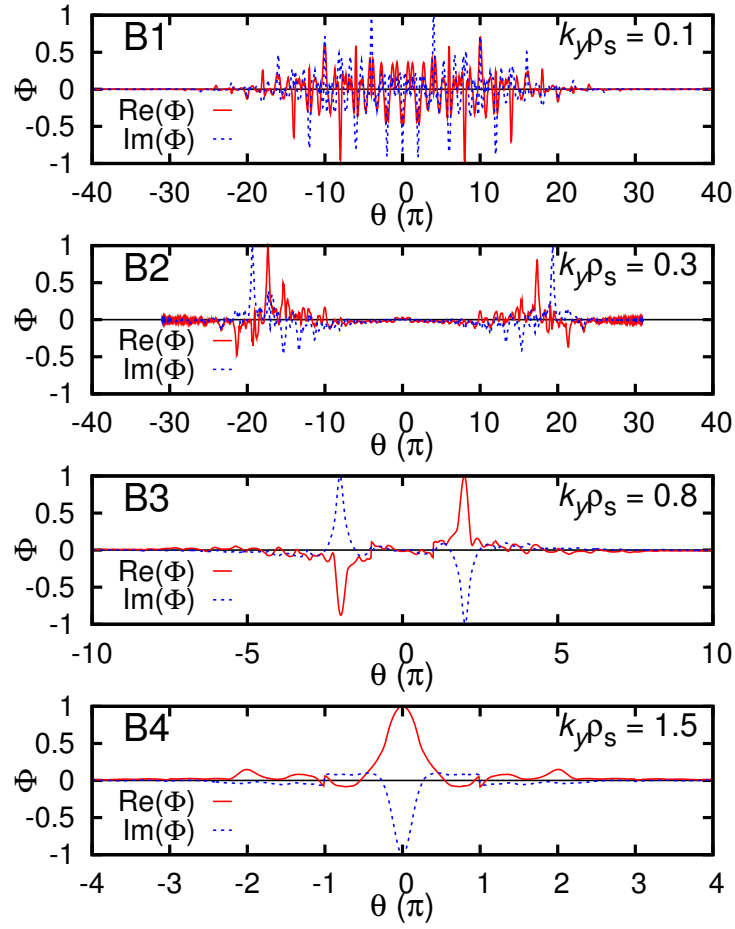


Figure 4.5: The normalized real and imaginary parts of the extended mode structure in the electrostatic potential Φ for the four different dominant modes in Fig. 4.3 for HSX-b for standard TEM parameters: $a/L_n = 2$, $a/L_{Te} = 1$. Source: Faber et al. (2015).

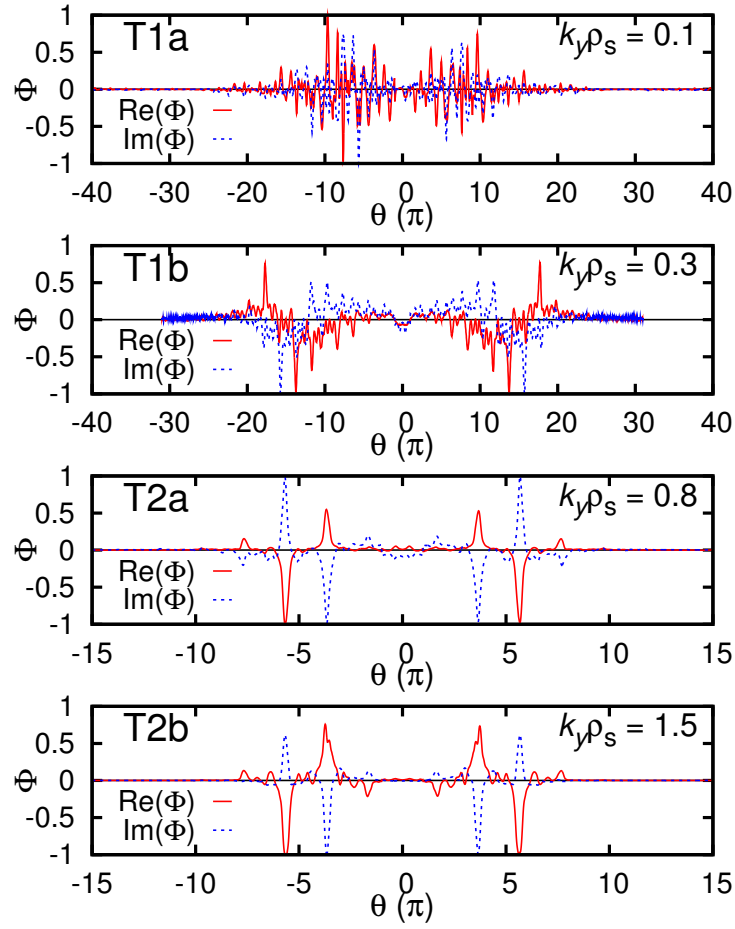


Figure 4.6: The normalized real and imaginary parts of the extended mode structure in the electrostatic potential Φ for the two different dominant modes in Fig. 4.3 in HSX-t for standard TEM parameters: $a/L_n = 2$, $a/L_{Te} = 1$. Source: Faber et al. (2015).

Φ has odd parity, unlike the other modes. The mode peaks in the first radial connection, $\pm 2\pi$, indicating it is a finite- k_x mode. For $k_y > 0.9$, the ubiquitous mode is now highly localized to $\theta = 0$. This mode is responsible for the maximum growth rate and the structure of the mode does not change as the real frequency changes from electron to ion propagation direction.

Some of the modes in HSX-t show a markedly different character than the modes at equivalent k_y for HSX-b. The mode T1a at $k_y = 0.1$ has two distinct, extended lobes that peak at $\theta = \pm 9\pi$. Unlike the mode B1 of Fig. 4.5, the amplitude in the central $-\pi < \theta < \pi$ range, corresponding to $k_x = 0$, is small. The T2 modes of Fig. 4.6, dominant for $k_y \geq 0.8$ have the same character and parity, with peak amplitudes on either side at $\theta = \pm 5\pi$. The T2 modes are identified with the ubiquitous mode for HSX-t and are distinct from the B3 mode due to lack of tearing parity. There does not appear to be an equivalent mode with tearing parity in HSX-t.

4.2.3 Linear eigenmode classification

The sensitivity of these modes to the driving gradients was examined by independently applying a 10% variation to the density and temperature gradients of the standard TEM parameter set. For each of the different modes in Figs. 4.3 and 4.4, the growth rates have a positive correlation with increasing density and electron temperature gradient, but consistently show a stronger dependence on the density gradient. Increases in β generally result in moderately decreasing growth rates, hence partial stabilization, for all modes except B1.

With all of these considerations in mind, we have classified the B modes in HSX-b and the T modes in HSX-t according to Table 4.1. We will call the B1 mode TEM1 and mode B2 TEM2. The B3 modes are called “tearing-parity” TEM (TTEM) and behave much like the ubiquitous mode B4. Finally, the

Table 4.1: Classification of the different linear modes in HSX-b and HSX-t based on $\Delta\gamma/\gamma_0$ change in growth rate for 10% increases in driving density and temperature gradient, stabilization due to β , negative (positive) sign denotes propagation in electron (ion) drift direction, and mode parity (ballooning or tearing). The acronyms are explained in the text.

Mode	B1	B2	B3	B4	T1	T2
$a/L_n + 10\%$	0.5	0.076	0.044	0.058	0.068	0.076
$a/L_{Te} + 10\%$	0.0	0.020	0.001	0.012	0.05	0.012
β stab.	No	Yes	Yes	Yes	Yes	Yes
Drift Dir.	–	–	–	–/+	–	–/+
Parity	Ball.	Ball.	Tear.	Ball.	Ball.	Ball.
Name	TEM1	TEM2	TTEM	UTEM	TEM	UTEM

B4 modes are ubiquitous modes (UTEM). HSX-t shows only two distinct modes, with the T1 mode being a more traditional TEM and the T2 mode the ubiquitous mode (UTEM) for that flux tube.

To examine the behavior of the dominant eigenmodes in Figs. 4.3 and 4.4, we computed the first five most unstable linear eigenmodes for the standard TEM at every k_y . The results are shown in Fig. 4.7 with the five eigenvalues denoted as EV#1 to EV#5. An aspect of the eigenvalue decomposition that is pervasive in HSX simulations and markedly different from tokamak results is the clustering of linear eigenmodes. The first four most subdominant modes in the range $k_y \leq 0.6$ all have growth rates that are only slightly smaller than that of the dominant mode and very similar real frequencies. As such, the precise ordering of the four subdominant modes was not investigated for $k_y \leq 0.6$.

Fig. 4.7 shows that the TTEM is the dominant mode for $0.7 \leq k_y \leq 0.9$ (the red \square) but becomes subdominant to the ubiquitous mode for $k_y \geq 1$. At no point in the range $0.7 \leq k_y \leq 2.1$ does the TTEM cease to exist and all the subdominant modes at high k_y exhibit the same real frequency behavior as the ubiquitous mode. One feature of Fig. 4.7 is the pairing of two subdominant, unstable modes which are almost identical in both growth

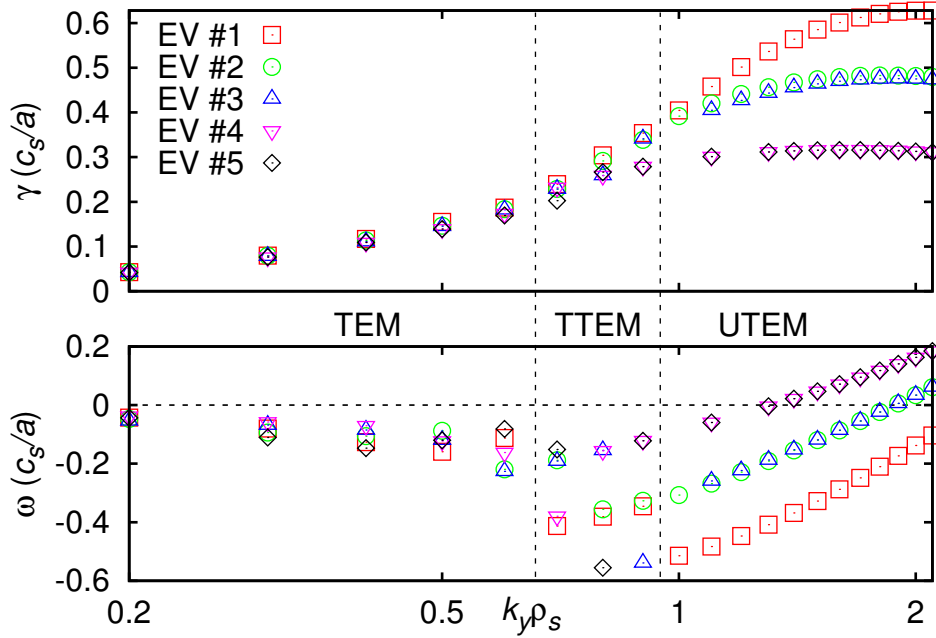


Figure 4.7: First 5 largest eigenmodes for the standard TEM parameter set in HSX-b. The eigenvalues at each k_y are ordered from largest to smallest linear growth rate. Continuity in real frequencies (bottom) shows the existence of at least 5 distinct mode branches for $k_y \geq 0.7$. The different dominant modes (red \square) identified by the designations in Table 4.1. Source: Faber et al. (2015).

rate and frequency, but not mode structure. For example, in Fig. 4.7, for $1 \leq k_y$, EV#2 has tearing parity (it is the TTEM) and EV#3 has ballooning parity.

This analysis shows that HSX is unstable to TEM turbulence and there is a variety of linear modes that exist in the transport-relevant regime in HSX. HSX-b exhibits multiple TEMs in the range $k_y \leq 1$ while HSX-t exhibits only two different modes. The linear growth rates calculated in each flux tube are similar in this range despite differences in mode structure. A quasilinear estimate predicts that despite the large growth rates of the ubiquitous mode,

it will not contribute significantly to transport. The existence of a significant number of multiple, subdominant, unstable eigenmodes at each k_y adds complexity to subsequent nonlinear analysis as multiple modes at the same k_y can contribute to the turbulence. As a consequence, energy input to the nonlinear state may be significantly greater than what is inferred from the dominant mode alone.

4.3 Nonlinear Simulations of Turbulence in HSX

Using the insight gained from linear simulations, nonlinear simulations were performed on the standard TEM and density gradient scan parameter sets. The default nonlinear resolution settings use $N_{ky} = 48$ modes and $k_y^{\min} = 0.1$, which sets the radial box size according to Eq. (3.74), where $\mathcal{N} = 1$ was chosen to yield the smallest radial box size possible. The value of k_y^{\min} was checked for convergence by halving k_y^{\min} and ensuring that the saturated flux does not change. With $k_y^{\min} = 0.1$, the radial box size is $L_x = 222\rho_s$ and the radial resolution is set at $N_x = 192$, but as we will show *a posteriori*, the nonlinear structures are considerably smaller than the radial box size. Doubling the N_x resolution does not change saturated flux values. The linear resolutions $N_z \times N_{v_{\parallel}} \times N_{\mu} = 64 \times 36 \times 8$ also result in nonlinearly converged fluxes.

Quantities of interest, such as the heat flux, are determined, unless otherwise noted, by time averaging over the quasi-stationary state. All heat fluxes reported here have gyro-Bohm normalization, $Q_{gB} = c_s n_{e0} T_{e0} (\rho_s^*)^2$, where $\rho_s^* = \rho_s/a$ with a the average minor radius, n_{e0} is the background electron density and T_{e0} is the background electron temperature. The fluctuating electrostatic potential Φ and electron density n_e are reported as normalized values: Φ in terms of $(T_{e0}/e) \rho_s^*$ and n in terms of $n_{e0} \rho_s^*$.

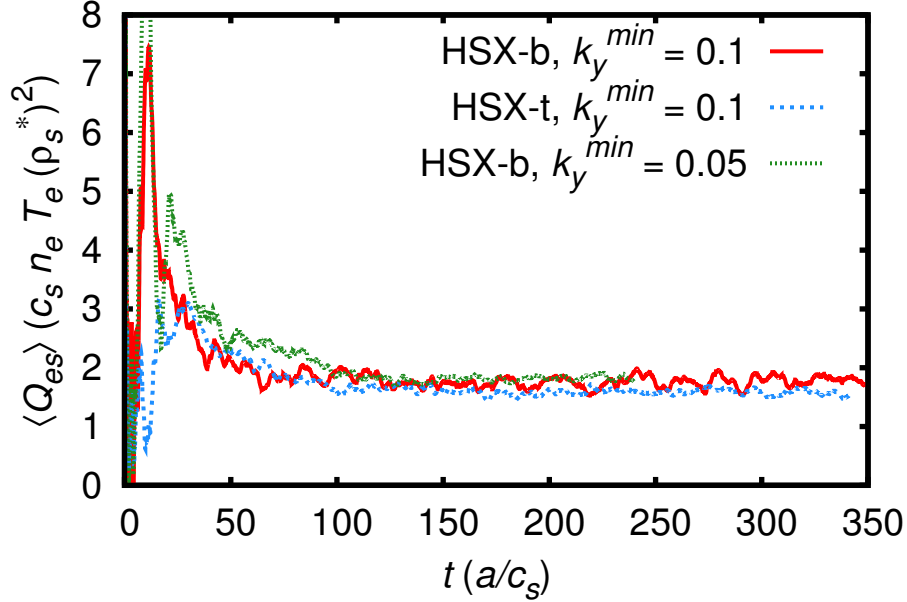


Figure 4.8: Time trace of the electron heat flux in HSX-bean (solid red) and HSX-triangle (dashed blue) flux tubes for standard TEM parameters: $a/L_n = 2$, $a/L_{Te} = 1$. Also shown is the time trace of the heat flux in a simulation for HSX-b where k_y^{\min} was halved (dotted green), showing that the simulations are converged. Source: Faber et al. (2015).

4.3.1 Standard TEM

The time traces of the electron heat flux for both HSX-b and HSX-t are shown in Fig. 4.8. From the time traces, it is apparent that the quasi-stationary electrostatic electron heat fluxes in the two flux tubes are very similar, with $\langle Q_{es} \rangle = 1.75$ for HSX-b and $\langle Q_{es} \rangle = 1.59$ for HSX-t. This result is consistent with the arguments made in Sec. 4.2.1, where the quasilinear estimate predicts that the $k_y < 1$ modes, where both flux tubes have similar growth rates, dominate the transport.

The electron heat fluxes in Fig. 4.8 have been decomposed into spectral components in k_y in Fig. 4.9, highlighting some moderate differences between

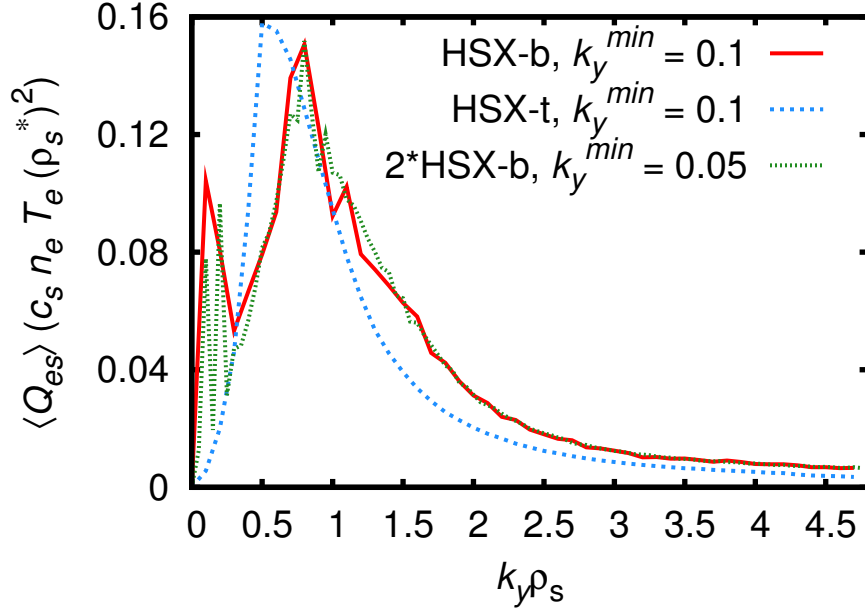


Figure 4.9: Heat flux spectrum in HSX-b with $k_y^{\min} = 0.1$ (red solid), $k_y^{\min} = 0.05$ (green dotted) and HSX-t with $k_y^{\min} = 0.1$ (blue dashed) for standard TEM parameters: $a/L_n = 2$, $a/L_{Te} = 1$. The simulation with $k_y^{\min} = 0.05$ has been scaled by a factor of 2 to illustrate more clearly its near-identical integrated flux level. Source: Faber et al. (2015).

the flux tubes while confirming the relevance of the $k_y \leq 1$ region. The heat flux spectrum for HSX-t has only one peak at $k_y = 0.5$ – 0.6 and exhibits a quick decay toward high k_y . The spectrum in HSX-b is similar, but the peak heat flux occurs at slightly higher $k_y = 0.7$ – 0.8 . The important difference between the flux tubes, however, is the presence of significant flux at $k_y = 0.1$ for HSX-b, which is not predicted by the linear growth rate results of Sec. 4.2.1.

In a numerically resolved simulation, it is desired to have only a small amount of flux in the k_y^{\min} wavenumber of the simulation. Fig. 4.8 shows that HSX-b exhibits no change in the integrated flux when k_y^{\min} is lowered

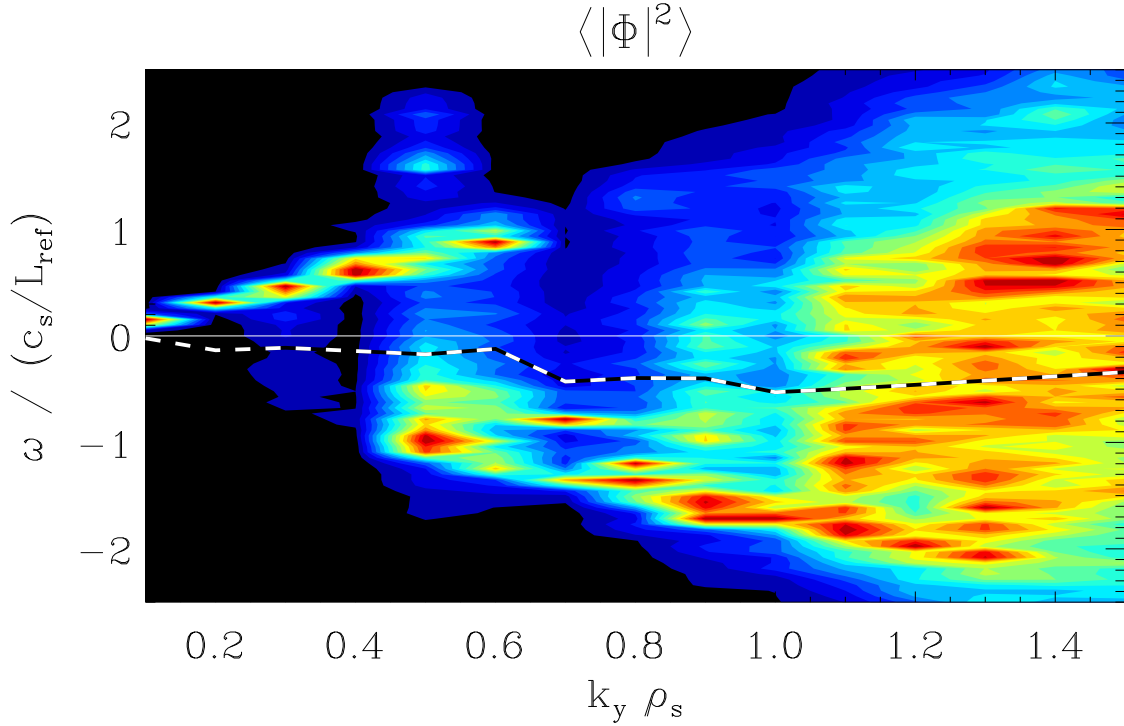


Figure 4.10: Nonlinear frequencies ω in HSX-b for standard TEM parameters. The frequencies are obtained by performing a Fourier transform in time over the quasi-stationary state. The color scale is linear and independent for each k_y . Linear frequencies from Fig. 4.3 are overlaid with the white and black dash line. Source: Faber et al. (2015).

to $k_y = 0.05$. Fig. 4.9 demonstrates there is little flux in the $k_y = 0.05$ wavenumber but a peak in the heat flux spectrum remains at $k_y = 0.1$ (and a second peak at $k_y = 0.2$). This indicates that the overall flux in this low- k_y feature is captured in either case. As such, every result hereafter that we will show uses $k_y^{\min} = 0.1$.

The nonlinear real frequencies vs. k_y are shown in Fig. 4.10 for HSX-b with the linear frequencies overlaid. The modes corresponding to the dominant transport peak ($k_y \geq 0.5$) have negative frequency, which indicates

they are TEM. The difference in magnitude between the linear and nonlinear frequencies could be the result of either subdominant modes with higher frequencies or of three wave coupling between different unstable modes. Without any ion temperature gradient, no ITG modes are present in these simulations, however, the modes at low k_y , near to the low- k_y transport peak, all propagate in the ion direction. It is important to reiterate that no linear subdominant mode with positive frequency was found at these k_y .

The contours of the electrostatic potential and electron density for HSX-b and HSX-t are shown in Figs. 4.11a and 4.11b, respectively. These contours are a representative snapshot taken at the final time step of the simulation and are not averaged over the saturated phase. There is zonal flow activity in both flux tubes, as evidenced by the well-defined, alternating vertical bands of positive and negative potential. Zonal density structures are relatively weak in the present case, indicating that they do not play an important role in nonlinear saturation, consistent with corresponding density-gradient-driven tokamak results (Lang et al., 2008; Ernst et al., 2009). The density fluctuations do show that the turbulence has a somewhat different character between the two flux tubes. The density fluctuations in HSX-b (Fig. 4.11a) away from $x = 0$ are anisotropic in the x - y plane with radial elongation not exceeding the zonal flow width, which is consistent with one requirement for eddy shearing by the zonal flows (Terry, 2000; Diamond et al., 2005). The HSX-triangle density fluctuations (Fig. 4.11b) are more isotropic but are still appear sheared along the zonal flow boundaries.

The appearance of the zonal flow corresponds with the turnover of the heat flux at $t \approx 15a/c_s$ in Fig. 4.8 and the development of the quasi-stationary state. This indicates that the zonal flows may play a role as the nonlinear saturation mechanism in these simulations, however the time-averaged, fluctuation-driven $\mathbf{E} \times \mathbf{B}$ shearing rate $\omega_E = \langle d^2\Phi_{k_y=0}/dx^2 \rangle \approx 0.35$ in both flux tubes and is on the order of the respective linear growth rates. This shearing rate has not been corrected for the finite-frequency effects

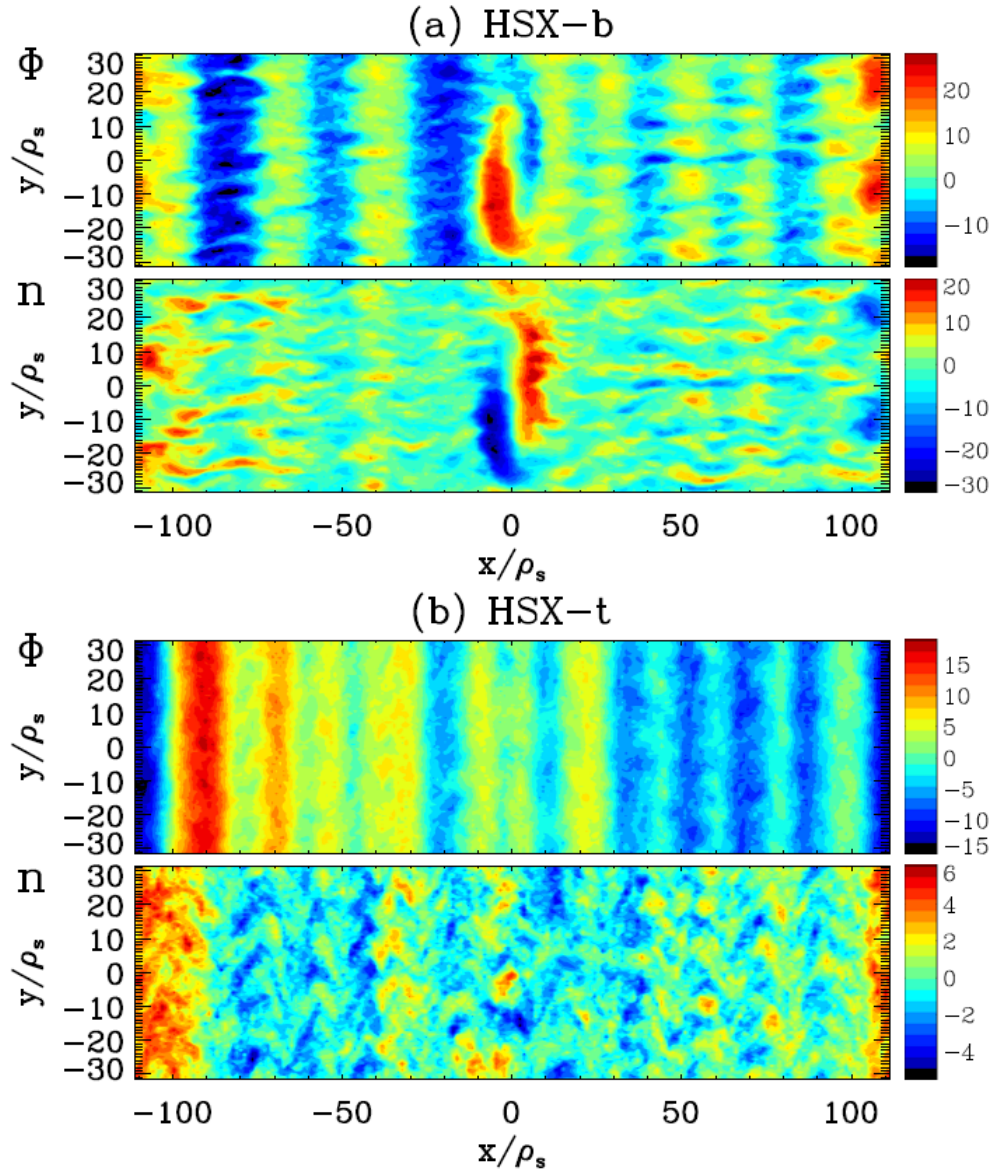


Figure 4.11: Contours of Φ (normalized by $T_{e0}\rho_s^*/e$) and n_e (normalized by $n_{e0}\rho_s^*$) fluctuations at zero poloidal angle in (a) HSX-b and (b) HSX-t. The x direction is radial and the y direction is poloidal. Zonal flows are present in both flux tubes, however a coherent structure centered at $x = 0$ is only observed in HSX-b. Source: Faber et al. (2015).

of Hahm et al. (1999). Typically, uncorrected values of ω_E as defined are consistent with the rule of thumb established in Xanthopoulos et al. (2007); Pueschel and Jenko (2010), where $\omega_E \simeq 10\gamma_{\max}$ should be satisfied if the zonal flows are to be an important nonlinear saturation mechanism. A different definition of the shearing rate was used in Nevins et al. (2006); Ernst et al. (2009), where time scales shorter than an eddy lifetime and spatial scales smaller than the radial correlation length were filtered from fluctuating zonal potential, as a result of which their subsequent shearing rate has to be compared directly to the linear growth rate, without the application of finite-frequency corrections or a factor of $\simeq 10$. To confirm equivalence of both approaches, our present formalism was applied to the data of Nevins et al. (2006), and our definition was found to yield a shearing rate value about eight times as large as the other definition, consistent with the aforementioned rule of thumb.

For the present case, the values of ω_E reported here indicate that the zonal flows may not play as big a role as a saturation mechanism. A simulation performed with the zonal flows artificially removed showed that the TEM turbulence still saturates in the absence of the zonal flows but with a quasi-stationary flux level 2.7 times larger. This result confirms that zonal flows are important to the saturation of the TEM in HSX; this is consistent with previous results of density-gradient driven TEMs in tokamaks (Lang et al., 2008; Pueschel and Jenko, 2010), where the absence of zonal flows leads to larger transport. As a consequence, it is concluded that the use of the shearing rate to determine saturation via zonal flows does not apply in the present case, perhaps due to low magnetic shear or the specifics of the saturation.

In the contours of HSX-b in Fig. 4.11, there is a large scale coherent structure at $x = 0$ in the fluctuating potential and density that is not present in HSX-t. This coherent structure is not static and drifts in the $-y$ (ion) direction. Filtering out the $0.1 \leq k_y \leq 0.3$ components in Fig. 4.11 removes

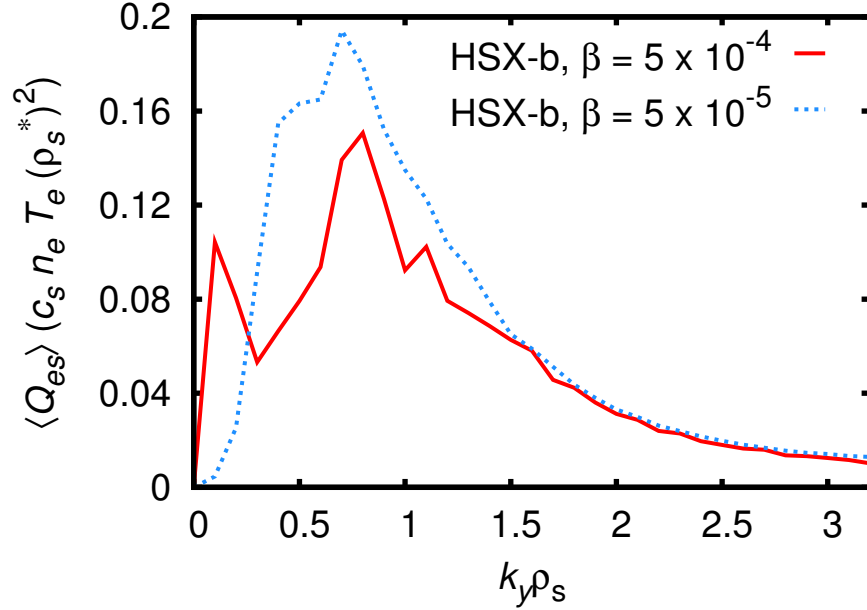


Figure 4.12: k_y resolved electron heat flux spectrum for standard TEM parameters in HSX-b for $\beta = 5 \times 10^{-4}$ (solid red) and $\beta = 5 \times 10^{-5}$ (dashed blue). While these values appear to be rather low, when normalizing to the ballooning threshold, they become more sizable. Source: Faber et al. (2015).

this structure and reveals an underlying zonal flow smaller in amplitude than the coherent structure and similar in amplitude to the zonal flows at other radial positions in the box. The large flux seen in the flux spectrum of Fig. 4.9 at $k_y \approx 0.1$ is a product of this coherent structure.

The coherent structure observed in Fig. 4.11a shows a significant dependence on several parameters: the presence of zonal flows, β , and the background magnetic shear. In the zonal-flow-free simulation, the coherent structure was also absent, suggesting that the evolution of the coherent structure may be moderated by the zonal flow. Fig. 4.12 shows that the low- k_y peak in transport is eliminated when β is changed from $\beta = 5 \times 10^{-4}$ to $\beta = 5 \times 10^{-5}$. The time trace (not shown) of heat flux has slightly

higher quasi-stationary flux levels for the lower- β case, consistent with the linear result where growth rates throughout most of the k_y range are slightly stabilized with increasing β . Simulations performed with an artificially increased background magnetic shear (not shown) have reduced the low- k_y flux and lack a nonlinear coherent structure at $x = 0$, while the integrated flux levels are not affected as much.

The cross phases of Φ with n_e , $T_{e\parallel}$, and $T_{e\perp}$, shown in Fig. 4.13, show a clear difference between linear and nonlinear simulations at low k_y in HSX-b. In all three phase relations, the potential is out of phase with the other quantities at $k_y \leq 0.2$, corresponding to the coherent structure. As k_y increases, the linear and nonlinear phases agree reasonably well for $k_y > 0.3$. The Φ vs. n_e and Φ vs. $T_{e\perp}$ cross phases, Figs. 4.13a,c, follow the same trend as the trapped-particle population in Dannert and Jenko (2005) for temperature-gradient-driven turbulence, where the phase angle increases with increasing k_y . This indicates that despite the linear-nonlinear frequency mismatch, the turbulence is of TEM type. Next, this interpretation shall be confirmed by comparing dependencies in the driving density gradient.

4.3.2 Impact of the density gradient

The nonlinear electrostatic electron heat fluxes for the density gradient scan parameters, where $a/L_{Te} = 0$, are presented in Fig. 4.14. These values are on the order of the observed experimental fluxes obtained from calculations of the power deposition profile (Weir et al., 2015), where $3 \lesssim a/L_n \lesssim 4$ and $2 \lesssim \langle Q_{es}^{\text{exp}} \rangle / Q_{gB} \lesssim 7$ in the region $0.4 \leq r/a \leq 0.6$. This suggests that TEM turbulence is responsible for the observed heat fluxes in HSX.

The scaling of the nonlinear saturated heat flux with driving gradient is shown in Fig. 4.15 and compared with the linear growth rates at $k_y = 0.7$, approximately where the nonlinear heat flux spectrum peaks in Fig. 4.16. A linear fit has been applied to the nonlinear flux data for $a/L_n \leq 3$. An upshift in critical density gradient is observed for the nonlinear saturated

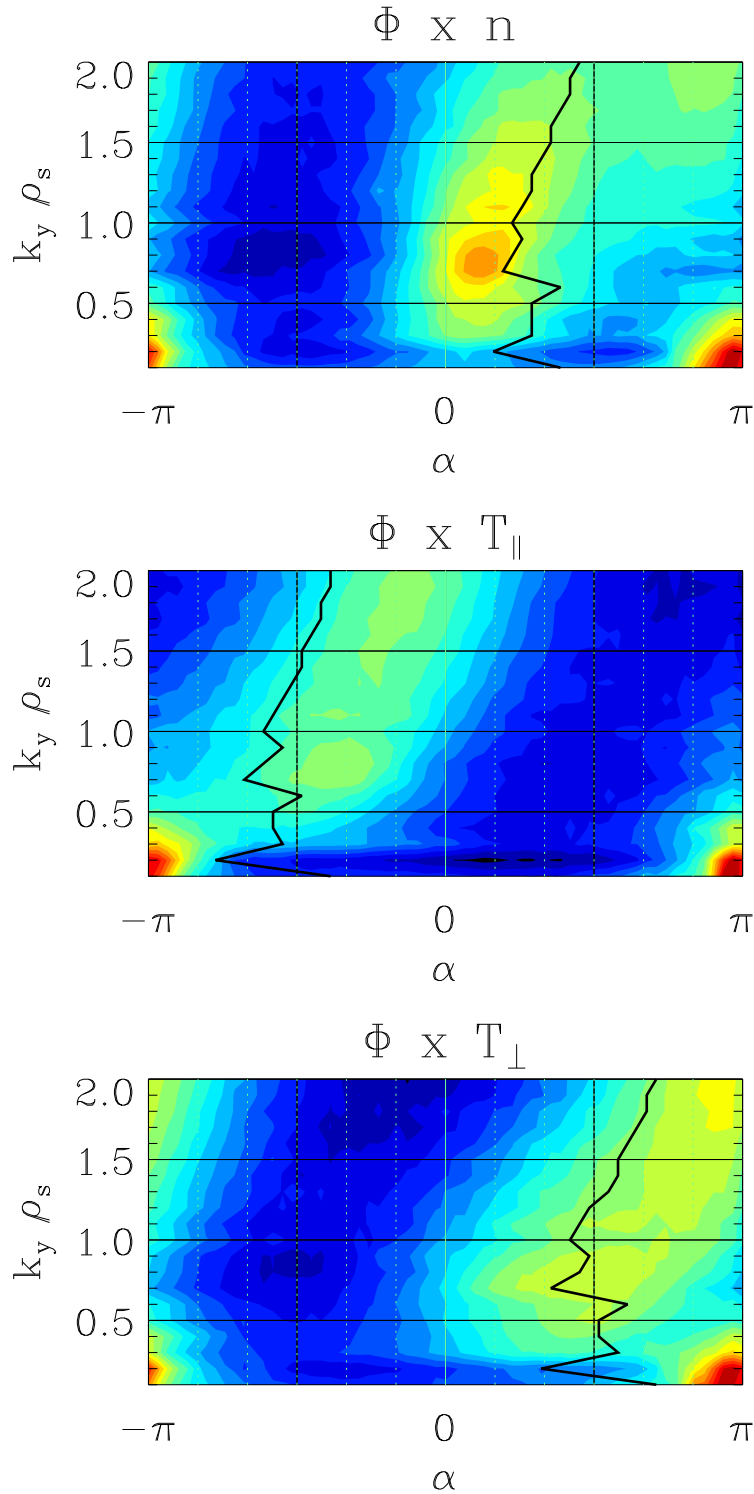


Figure 4.13: Nonlinear cross phases between Φ and n_e , Φ and $T_{e\parallel}$, and Φ and $T_{e\perp}$ for the standard parameters in HSX-b. Overlaid are the linear cross phases (black line) for each quantity. The color scale for the nonlinear cross phases is logarithmic. The linear and nonlinear phases differ for $k_y \leq 0.2$ where the coherent structure lies, but generally agree for $k_y > 0.3$, where linearly the TEM is dominant. Source: Faber et al. (2015).

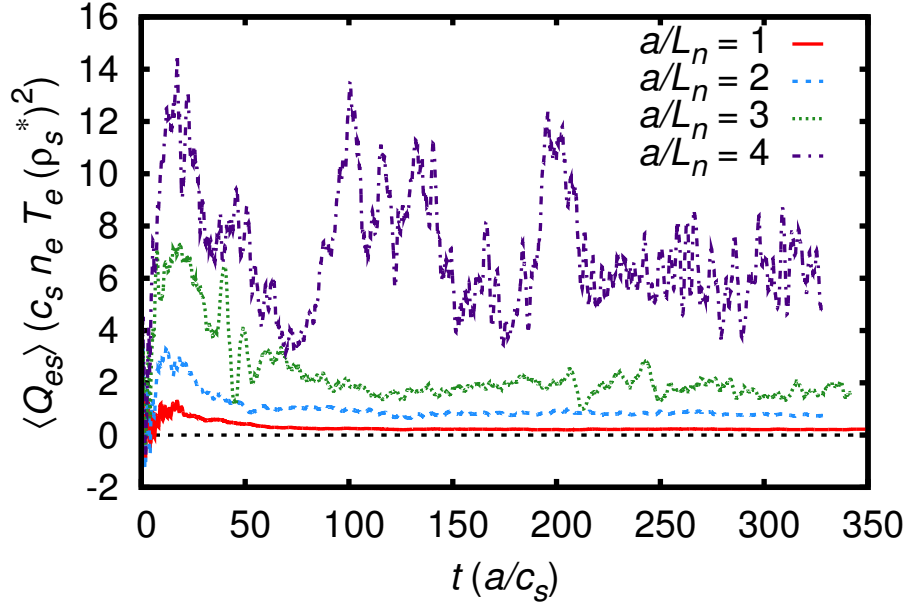


Figure 4.14: Time trace of the electron electrostatic heat fluxes in HSX-beam for density gradient scan: $a/L_n = 1 - 4$, $a/L_{Te} = 0$. Larger variability in the flux corresponds with the growth of the central coherent structure, much like in Fig. 4.11a. Source: Faber et al. (2015).

fluxes, consistent with the TEM nonlinear upshift discovered in tokamak simulations (Ernst et al., 2004), with a critical density gradient at $a/L_n \approx 0.8$ as compared with a critical density gradient at $a/L_n \approx 0.2$ predicted by the linear growth rate scaling. The fact that there is an upshift again provides evidence that zonal flows play a role in moderating the turbulence (Ernst et al., 2009).

The electron heat flux spectrum presented in Fig. 4.16 shows that the fraction of the flux contributed by the low- k_y wavenumbers increases with driving density gradient. At $a/L_n = 4$, the fraction of flux for $k_y \leq 0.3$ is approximately 22% of total integrated flux. Again, the nonlinear frequencies for the low- k_y modes are ion frequencies, consistent with Fig. 4.10.

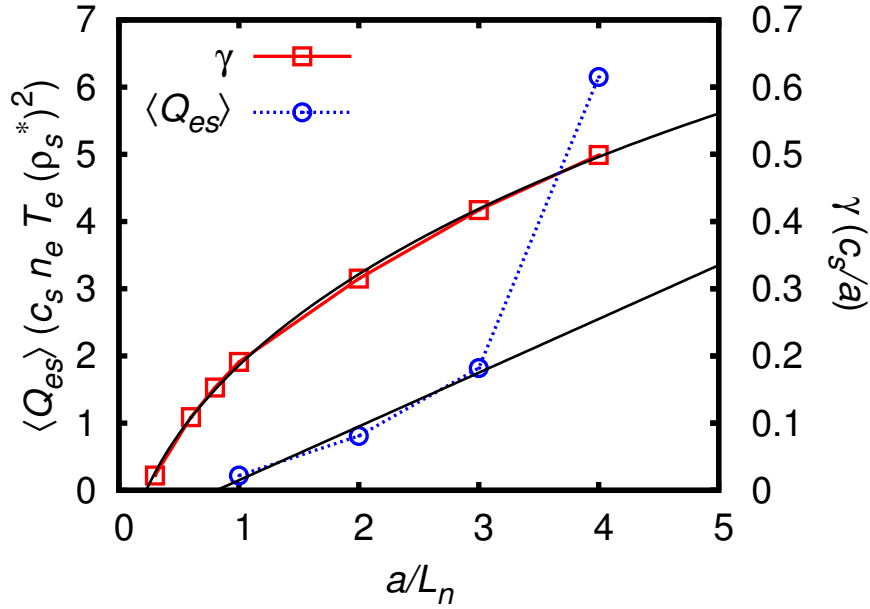


Figure 4.15: Density gradient scaling of the linear growth rates at $k_y = 0.7$ (red \square) and nonlinear electron heat flux (blue \odot) in HSX-b. A square root fit predicts a linear critical gradient at $a/L_n \approx 0.2$. A linear fit of the $a/L_n \leq 3$ range of the nonlinear fluxes produces an upshift with a nonlinear critical gradient predicted at $a/L_n \approx 0.8$. Source: Faber et al. (2015).

The increase in a/L_n leads to an increase both in the variability of the heat flux and in the transport in the lowest- k_y wavenumbers, the cause of which can be determined by examining the contours of electrostatic potential, shown for all four a/L_n in Fig. 4.17. The potential structures in Figs. 4.17a and 4.17b are similar to both Fig. 4.11a and Fig. 4.11b for standard TEM parameters, showing clear zonal flows. However, there is no coherent structure observed for $a/L_n = 1$ and subsequently no low- k_y transport peak in Fig. 4.16. For $a/L_n = 2$ (Fig. 4.17b), the coherent structure is located near the radial boundary of the box and is responsible for the low- k_y transport peak in Fig. 4.16. For $a/L_n = 3$ and $a/L_n = 4$,

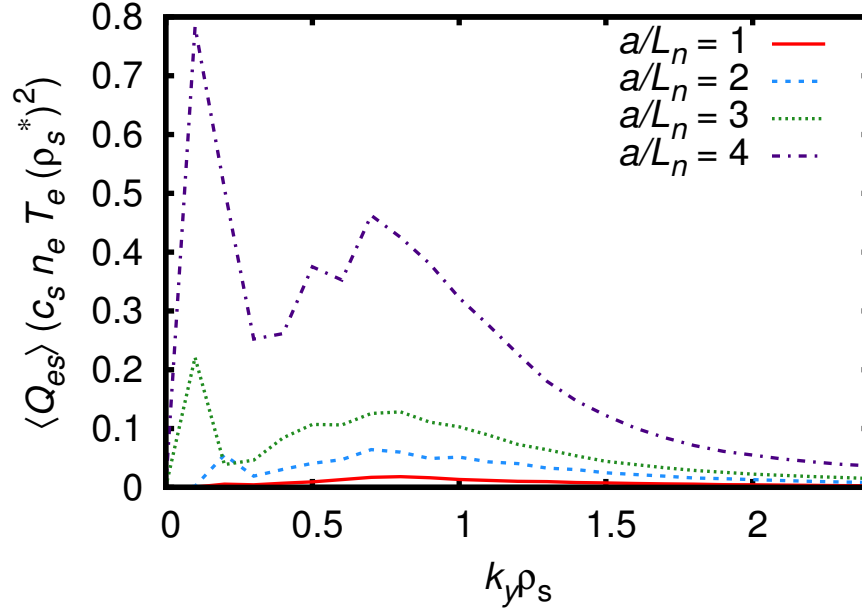


Figure 4.16: Electron electrostatic heat flux spectrum for HSX-b for the density gradient scan: $a/L_n = 1 - 4$, $a/L_{Te} = 0$. The flux at low- k_y increases steadily with increasing a/L_n , however the TEM peak at $k_y = 0.7-0.8$ still determines the overall flux level. Source: Faber et al. (2015).

Figs. 4.17c and 4.17d show a large amplitude potential structure centered at $x = 0$ that drifts in the ion direction and locally dominates the zonal flows.

Decreasing k_y^{\min} to 0.05 (equivalent to doubling the box size in the y direction) for the $a/L_n = 4$ simulation shows the coherent structure at $x = 0$ retains a similar scale as in Fig. 4.17d and that the quasi-stationary flux level is similar to the $k_y^{\min} = 0.1$ simulation, indicating that the $a/L_n = 4$ simulations presented here are sufficiently resolved to capture the turbulent dynamics at low k_y . The bursts and fluctuations seen in Fig. 4.14 for $a/L_n = 4$ are also present in the higher resolution simulation due to the large size and amplitude of the coherent structure at $x = 0$.

The same observations about the zonal flow as the saturation mechanism

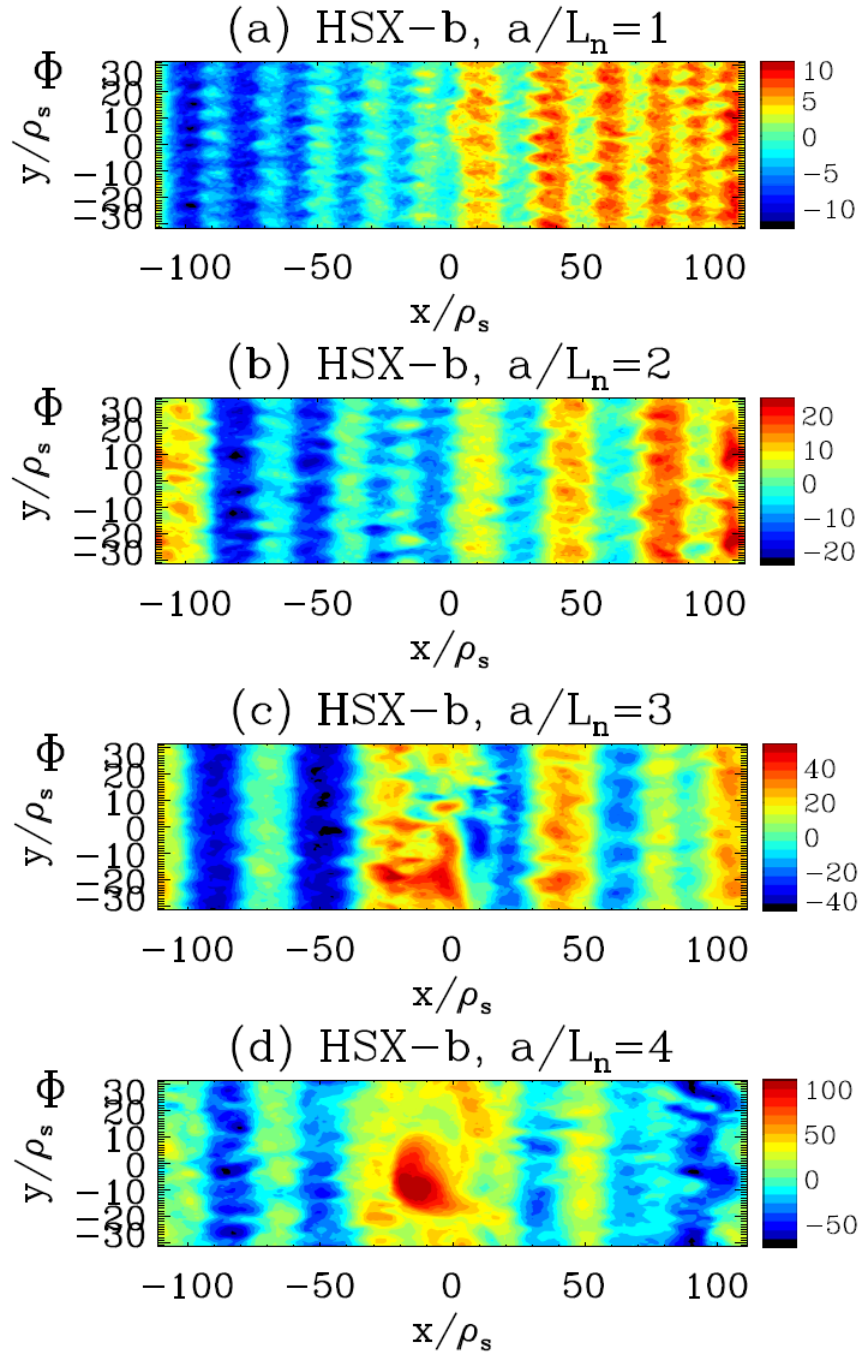


Figure 4.17: Contours of Φ fluctuations at zero poloidal angle in HSX-bean tube with $a/L_{Te} = 0$ in all simulations. Zonal flows are present in all simulations and the coherent structure develops as a/L_n is increased. Source: Faber et al. (2015).

as for the standard TEM parameters apply here. For $a/L_n \leq 3$, the shearing rate ω_E is always smaller than the maximum linear growth rate and only slightly larger than the maximum linear growth rate for $a/L_n = 4$. Therefore, zonal-flow-based turbulent saturation may rely on energy transfer to damped modes rather than shearing. The associated density fluctuations to Fig. 4.17 are comparable to the potential fluctuations but zonal density as a saturation mechanism is again precluded by the absence of zonal structures in the density.

4.4 Chapter Summary

In this chapter, the first comprehensive linear and nonlinear turbulence simulations were presented for ∇n -driven TEMs in HSX. Linear simulations show distinct branches of TEMs exist for HSX and transition between dominant and subdominant growth rates depending on wavenumber k_y . These modes exhibit a wide variety of structure along field lines as the result of 3D geometry. Nonlinear simulations of ∇n -driven TEM turbulence show prominent zonal flow activity, however based on shear suppression analysis, the shearing rate is too small to be solely responsible for turbulence saturation. This suggests some other mechanism, possibly energy transfer to stable modes, may be responsible for saturation, which will be investigated in Ch. 5. Also present in the nonlinear simulations is a low- k_y coherent fluctuation that drives significant transport, particularly at high ∇n . This feature is not predicted by linear stability analysis and will also be further investigated in Ch. 5. The overall flux values obtained are consistent with experimental findings and suggest that ∇n -driven TEM turbulence is responsible for observed transport.

5 MICROINSTABILITIES AND TURBULENCE AT LOW MAGNETIC SHEAR

Small values of global magnetic shear can have a large impact on plasma instabilities and turbulence. The influence of low global magnetic shear in HSX on both TEM/ITG instabilities and TEM-driven turbulence is examined in this chapter. In particular, attention is paid to subdominant/stable modes and their impact on turbulent dynamics. This chapter closely follows Faber et al. (2018).

5.1 Gyrokinetic Simulations at Low Magnetic Shear

A challenge to performing flux tube simulations for stellarators is that by design, global magnetic shear for many modern stellarator configurations is small. Magnetic shear tends to localize fluctuations, in tokamak core plasmas typically to the outboard midplane. In the absence of large global magnetic shear, mode localization is determined by the interplay of local shear and curvature, which is nontrivial for stellarators. This can manifest with modes that extend far along field lines or balloon in locations other than the outboard midplane (Merz, 2008; Faber et al., 2015) and was seen in Ch. 4, adding significant complexity to the simulation and analysis of stellarator turbulence. Furthermore, the computational domain dimensions for flux tube simulations are inversely proportional to global magnetic shear (Eq. (3.74)), which can make flux tube simulations for low-magnetic-shear stellarators expensive. One method to reduce the computational cost is to approximate a low-magnetic-shear flux tube with a zero-magnetic-shear domain, where the domain dimensions are independent of global magnetic shear and can be specified to reasonable values.

In this chapter, a gyrokinetic study of HSX demonstrates that properly resolving parallel correlation lengths with extended simulation domains is crucial for accurate theoretical predictions. Modes that extend far along field lines tend to have subdominant growth rates and usually do not merit detailed investigation. For HSX geometry these modes prove essential to determining the turbulent state at high gradient drive. In particular, when the zero-shear computational technique was used with an insufficiently large parallel simulation domain, the resulting simulations showed no flux, in direct contradiction with finite-shear simulations. Using parallel simulation domains comprised of multiple poloidal turns resolves parallel correlation lengths and leads to agreement between finite-shear and zero-shear simulations. It is observed that despite the extended modes being linearly stable for the larger parallel simulation domains, they play a prominent role in the nonlinear dynamics of the turbulence, acting as both an energy drive and an important nonlinear energy transfer channel at long wavelengths. Fundamentally, the results shown in this chapter can be seen as part of a larger picture, where subdominant eigenmodes with growth rates $0 < \gamma < \gamma_{\max}$ and stable eigenmodes with $\gamma \leq 0$ have a significant impact on the nonlinear state (Terry et al., 2006; Hatch et al., 2011a,b; Pueschel et al., 2016). This should motivate the consideration of such modes in the design of reduced models.

5.1.1 Parallel correlations

Drift-wave instabilities in flux tube simulations typically have a ballooning nature, thus \mathbf{k}_{\perp} takes on the same form as Eq. (3.65). Instead of solving the gyrokinetic equations over a long parallel domain, one may make use of this form of \mathbf{k}_{\perp} and the parallel boundary condition to construct fluctuations that extend along field lines by adding more radial modes, which takes advantage of fast Fourier transform techniques (Jenko et al., 2000; Dorland et al., 2000; Peeters et al., 2009). The approach is well-suited for axisymmetric

configurations. After one poloidal turn ($\theta \rightarrow \theta + 2\pi$), all geometric quantities are periodic, even though the flux tube ends generally lie at different ζ values. This is guaranteed by axisymmetry, as ζ is an ignorable coordinate and the flux tube is parameterized only by θ . Thus, one may use the geometric data from one poloidal turn and “build” an extended flux tube by adding more radial modes. A geometrically accurate computational domain can then be constructed for fluctuations that have arbitrarily large parallel correlation lengths, as one may always add a sufficient number of radial modes to resolve parallel scales.

While often yielding reasonably accurate results, this procedure is formally incorrect for most stellarator simulations. In general, geometric quantities for stellarators are *not* periodic after one poloidal turn, which can have serious consequences for stellarator flux tube simulations. As a fluctuation extends along a field line in a stellarator, it samples different geometry depending on the field-line label. The exact geometry may be important in setting the physical parallel correlation length. Due to the complicated interplay of magnetic trapping regions, curvature drive, and local magnetic shear, it has been observed that drift-wave instabilities in stellarators may be most unstable in regions away from $\theta_k = 0$ at the outboard midplane (Merz, 2008; Faber et al., 2015), where one might naively expect the fastest-growing instabilities are centered. This is readily apparent in low-global-magnetic-shear stellarators, such as HSX, where fluctuations have been observed to extend to $|\theta| \geq 30\pi$ or peak well away from $\theta = 0$, depending on wavenumber k_y (Faber et al., 2015). Increasing global magnetic shear has a localizing and stabilizing effect on drift-wave fluctuations due to the energy cost associated with field line bending (Pearlstein and Berk, 1969; Nadeem et al., 2001; Plunk et al., 2014). When the global magnetic shear is small, such as $|\hat{s}| \lesssim 0.05$ for the HSX core region, fluctuations can extend long distances along the field line and consequently have long parallel correlation lengths. While these effects are accentuated in low-shear stellarators,

tors, they are not unique to them. Recent studies of strongly-driven regions of axisymmetric configurations, such as the important pedestal region in tokamaks, show slab-like ITG and micro-tearing modes can exist with strong finite- θ_k dependence (Fulton et al., 2014; Hatch et al., 2016b; Chen and Chen, 2018).

It is crucial then that the geometry spanned by a fluctuation in the flux tube domain have the proper instability drive and damping physics. Due to the lack of periodicity in a stellarator after one poloidal turn, the procedure to extend the parallel flux tube domain using geometry elements for only one poloidal turn will result in physically incorrect geometric elements after one poloidal turn. This can lead to unfaithful drive and damping physics, which can in turn induce artificial self-correlations, leading to a breakdown of the statistical invariance posited by the parallel boundary condition. A superior way to deal with this issue is to construct the flux tube domain using geometry from *multiple* poloidal turns $n_{\text{pol}} > 1$. In principle, one must choose n_{pol} to be large enough that the magnetic field geometry over a parallel correlation length is accurate. In practice, for modes with very long correlation lengths, one cannot in certain cases accurately capture all of the geometry due to computational cost constraints. However, using multiple poloidal turns does decrease the error induced by the flux tube construction for higher radial wavenumbers. As such, the n_{pol} parameter is part of the convergence checking procedure.

An example of this is readily seen in Fig. 5.1, where the finite Larmor radius (FLR) term and the normal curvature term are shown for flux tubes constructed from different numbers of poloidal turns. The FLR term is expressed as

$$k_{\perp}^2(z) = k_x^2 g^{xx}(z) + 2k_x k_y g^{xy}(z) + k_y^2 g^{yy}(z), \quad (5.1)$$

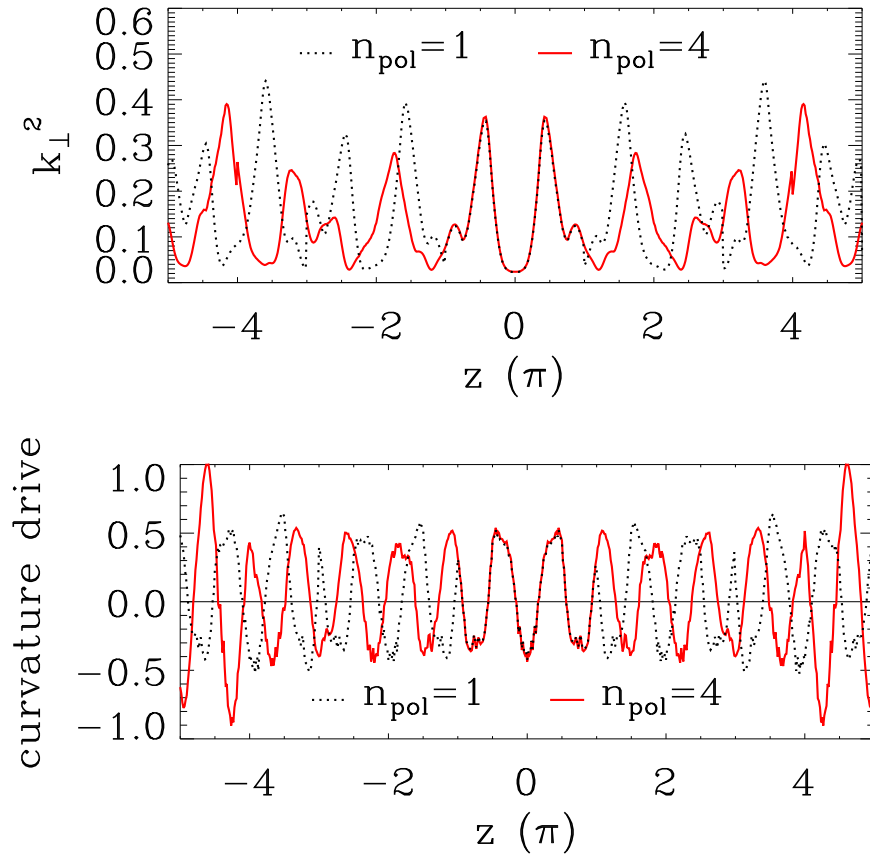


Figure 5.1: Comparison of HSX geometry terms for a flux tube constructed from one poloidal turn (black) and four poloidal turns (red solid lines). The FLR term, defined by Eq. (5.1), is shown on top, while the curvature drive, defined by Eq. (5.2), is on bottom. Both quantities are plotted as functions of the parallel coordinate. Source: Faber et al. (2018).

and the curvature drive at $\beta = 0$ is

$$\mathcal{K}_y = \frac{1}{B(z)} \hat{\mathbf{b}}(z) \times \nabla B(z) \cdot \nabla y(z). \quad (5.2)$$

It is clear that the geometry terms diverge after $z = \pi$, which is a manifestation of the lack of periodicity in the poloidal angle for stellarators. Comparing the curvature drive and the FLR terms at $z = 2\pi$, one can see that for one poloidal turn, there is bad curvature and a small value of the FLR term, favorable conditions for driving a mode unstable. If a mode has parallel correlation lengths longer than one poloidal turn, the drive and damping terms at $z = 2\pi$ will be unphysical with artificially high drive. This can lead to self-correlation and artificial pumping of the instability. Increasing the number of poloidal turns more realistically captures the geometry and enables the mode to sample geometry corresponding to more physical parallel correlation lengths. It should be stressed however, that this phenomenon is highly geometry-dependent. Low-global-magnetic-shear geometries can exist where the local magnetic shear has large enough variation to provide mode localization within one poloidal turn or where the geometry is essentially periodic after one poloidal turn. In such circumstances, accurate flux tube simulations can be performed using the geometry for only one poloidal turn, as was done in Xanthopoulos and Jenko (2007); Xanthopoulos et al. (2007).

Recently, a more accurate parallel boundary condition for stellarator symmetric flux tubes has been derived in Martin et al. (2018). This approach removes the discontinuities present at the ends of the simulation domain in the current conventional treatment, which can be seen at $\theta = \pm 4\pi$ of the k_{\perp}^2 curve in Fig. 5.1. Without a doubt, this is a step forward towards more accurate simulation of turbulence in stellarators. However, if the parallel correlation lengths of modes remain large, the above considerations will still apply and multiple poloidal turns will be needed.

5.1.2 Impact of small global magnetic shear

Magnetic shear tends to have a localizing effect on drift-wave instabilities, primarily by making the stabilizing FLR effects large. In Fig. 5.1, it is observed that modes localize along the field line to regions between local shear maxima. Curvature can also provide mode localization by modulating the drift frequency along a field line (Plunk et al., 2014). The structure of local magnetic shear along a field line is known to lead to different eigenmode types in the limit of small global magnetic shear. The work of Waltz and Boozer (1993) indicated that local magnetic shear can provide mode confinement along field lines and Plunk et al. (2014) demonstrated increased mode localization by artificially enhancing local shear spikes, essentially by “boxing” the mode in, similar to a quantum state in a potential well. In the limit of zero magnetic shear, as has been studied for reverse shear regions of internal transport barriers in tokamaks (Connor and Hastie, 2004; Candy et al., 2004) and recently for the low-shear stellarator Wendelstein 7-X (Zocco et al., 2018), the gyrokinetic equation is known to take the form of a Mathieu equation. In the analysis of ITG modes in the Wendelstein 7-AS configuration, Bhattacharjee et al. (1983) demonstrated the existence of weakly localized eigenmodes that extend far along field lines. These modes are bound due to resonances between the wave period and effective bounding potential and occur in regions where the Mathieu function is decaying. These regions are determined by the particular form and magnitude of the local shear along the field line and will vary between stellarator configurations. This subject was explored in-depth for MHD ballooning modes in 3-D geometry in Cuthbert and Dewar (2000) and Hegna and Hudson (2001) and numerically for drift waves by Nadeem et al. (2001) for the H-1NF configuration, which demonstrated a transition between localized and extended modes dependent on decreasing global magnetic shear.

A significant consequence of both 3D geometry and small global shear is the existence of a plethora of unstable, but subdominant eigenmodes at

every k_y wavenumber (Merz, 2008; Faber et al., 2015). Modes localized to the outboard midplane, modes with strong k_x dependence ($\theta_k \neq 0$), and modes that extend along field lines can all be unstable concurrently at the same k_y wavenumber. These subdominant modes have been shown to play an important role in the saturation dynamics of ITG turbulence in the HSX configuration (Pueschel et al., 2016; Hegna et al., 2018). In particular, Hegna et al. (2018) present a theory describing ITG turbulence saturation in stellarator geometry, where saturation occurs through nonlinear energy transfer to stable modes (Terry et al., 2006) and is the subject of Ch. 6. It is found that for the HSX configuration, energy is primarily transferred to stable modes through subdominant, marginally stable modes. Furthermore, this observation was shown to be a function of geometry and was not observed in a quasi-axisymmetric configuration with higher magnetic shear, which showed behavior similar to conventional stellarators and high- \hat{s} tokamaks. There, typically only at most a few modes tend to be destabilized at each wavenumber, and the turbulence is strongly influenced by unstable mode/zonal flow interactions (Hatch et al., 2011b; Terry et al., 2018; Whelan et al., 2018; Hegna et al., 2018). Thus care must be taken to properly simulate not only the most unstable eigenmode, but also a significant part of the subdominant spectrum.

5.2 Linear Mode Calculations

To more thoroughly examine the impact of low global magnetic shear, ITG and TEM eigenmode calculations have been performed for the quasi-helically symmetric (QHS) configuration of the HSX device. The calculations are done in flux-tube domains centered on the half-toroidal flux surface, where the global magnetic shear is $\hat{s} \approx -0.046$ in the QHS configuration. This radial location has previously been used to study TEM turbulence in HSX (Faber et al., 2015). To demonstrate that low-magnetic-shear effects are not limited

to the choice of instability, results for both ITG and density-gradient-driven TEM will be shown.

5.2.1 Trapped electron modes

Calculations of TEM, relevant for HSX operation (Faber et al., 2015) focuses on high-density-gradient drive, where the impact of extended modes is the most prominent. The parameters used are $a/L_n = 4$, $a/L_{T_i} = 0$, $a/L_{T_e} = 0$, $T_i/T_e = 1$, $\beta = 5 \times 10^{-4}$, and $m_i/m_e = 1837$. The gradient scales for the density and temperature normalized to the average plasma minor radius are $a/L_{n,T}$, where $L_\xi = |\nabla\xi|/\xi$. The ion and electron temperatures are $T_{i,e}$ and $\beta = 8\pi n_e T_e / B_0^2$ is the normalized ratio of electron pressure to magnetic pressure. The eigenspectrum is examined for $k_y = (0.2, 0.4, 0.6, 0.8)$, and is shown in Fig. 5.2. As expected for pure ∇n -driven TEM, almost all of the unstable modes are propagating in the electron-diamagnetic direction, corresponding to negative value for real frequency using GENE conventions. Examples of different mode types are given by the letter labels and the corresponding mode structures are shown in Fig. 5.3. There is a clustering of modes around zero real frequency, labeled by “C”, which have extended structure along field lines, consistent with the previous findings of Nadeem et al. (2001). The modes with definite non-zero frequencies, “A” and “B” tend to be much more strongly localized in helical drift wells. These modes do not need to balloon around $\theta = 0$, and they display significant finite- k_x amplitudes as well as tearing parity in electrostatic potential Φ , consistent with previous observations of TEMs in HSX (Faber et al., 2015). For most modes in the spectrum, increasing the number of poloidal turns leads to a decrease in the growth rates, and is shown in Fig. 5.4 for $k_y = 0.2$ for one and four poloidal turns. This behavior is connected to the fact that by using more poloidal turns to construct the flux tube, more correct drive and damping physics is included, leading to a more accurate growth rate and frequency calculation for extended modes.

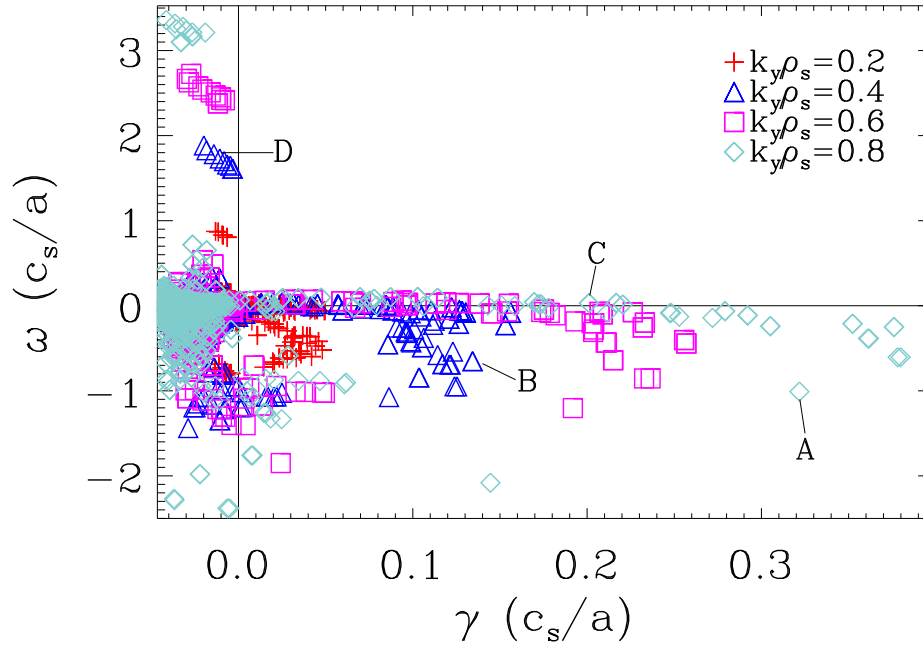


Figure 5.2: Eigenspectrum for the strongly driven ∇n TEM in HSX. The horizontal axis is the growth rate γ and the vertical axis is the real frequency ω . Different k_y are indicated different symbols and colors. Examples of different types of modes are given by the labels “A”, “B”, “C”, and “D”, and the mode structure is shown in Fig. 5.3. Source: Faber et al. (2018).

A peculiar branch of eigenmodes, labeled “D” in Fig. 5.2, is characterized by marginal-stability modes, with a real frequency proportional to k_y in the ion diamagnetic direction. The structure of the electrostatic potential along the field line for the eigenmodes in HSX, shown in Fig. 5.3D, displays an extended, two-scale structure, with the outer scale varying on scales much longer than local helical drift wells. While these modes appear connected to small global magnetic shear values, the exact mechanism responsible for setting the outer scale envelope has not yet been determined. In the reverse-shear tokamak scenario studied in Candy et al. (2004), the small, but non-zero global magnetic shear set the envelope scale. In 3-D configura-

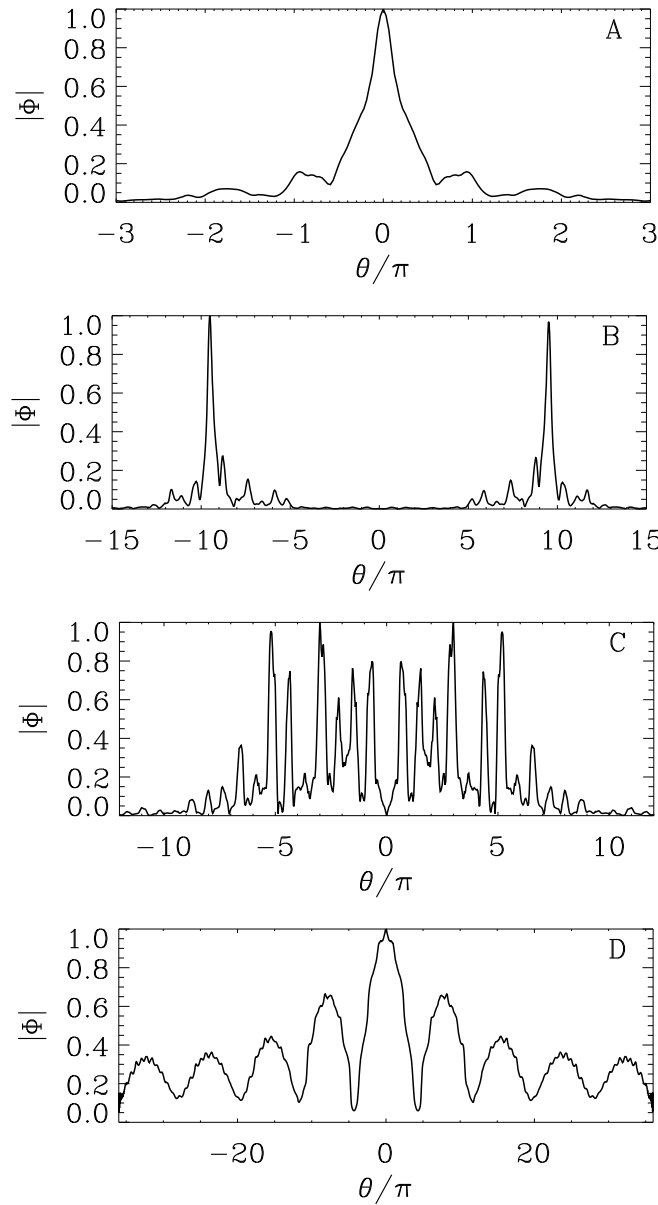


Figure 5.3: Electrostatic potential eigenmode structures for the TEM branches labeled “A”, “B”, “C”, and “D” from Fig. 5.2. The modes show conventional ballooning behavior (A), finite k_x dependence (B), extended structure along the field line (C), and two-scale structure with an extended envelope along the field line (D). Source: Faber et al. (2018).

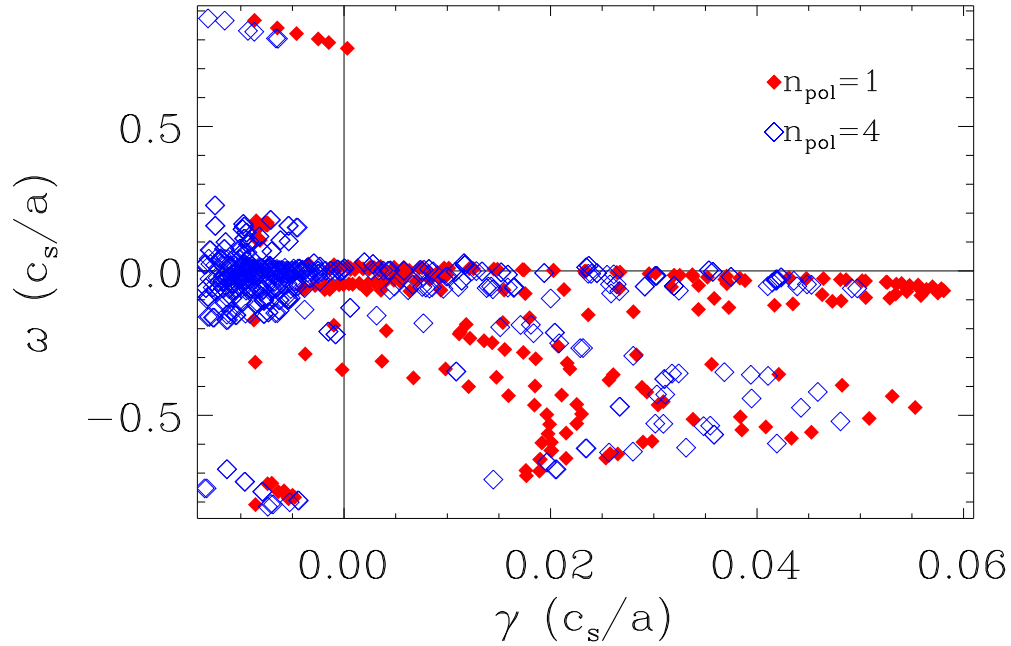


Figure 5.4: TEM eigenspectrum at $k_y = 0.2$ for different poloidal turn values. Modes from one poloidal turn are the solid red diamonds and from four poloidal turns are the hollow blue diamonds. Generally, the modes at four poloidal turns are more stable, and there are fewer unstable modes than for one poloidal turn. Importantly, the extended ion mode branch (mode “D” in Fig. 5.3), transitions from unstable to stable at four poloidal turns. Source: Faber et al. (2018).

tions, variations in the local shear can determine mode localization through Mathieu resonances (Bhattacharjee et al., 1983) or through a method similar to Anderson localization, where incommensurate helical periods in the magnetic equilibrium cause localization (Cuthbert and Dewar, 2000; Hegna and Hudson, 2001). The mode branch displays eigenmode structures with higher-harmonic envelopes that are increasingly damped.

Like the other eigenmodes, the growth rate of the extended ion mode branch is sensitive to the number of poloidal turns used to resolve the

geometry. Figure 5.4 shows the extended ion mode branch at $\omega \approx 0.8$ is sensitive to the number of poloidal turns and that the linear damping increases with number of poloidal turns. At one poloidal turn, this mode branch even shows slight instability at $k_y \rho_s = 0.2$. This sensitivity is observed despite the parallel correlation lengths of these modes being significantly larger than a few poloidal turns. In the analysis presented in Cuthbert and Dewar (2000) and Candy et al. (2004), the eigenvalue is dependent on the solution to the inner-scale equation. More accurately resolving the inner-scale solution associated with the helical drift wells serves to stabilize the overall growth rate. Improperly resolving this extended scale mode has consequences for nonlinear simulation, as will be detailed in Sec. 5.3.

5.2.2 Ion temperature gradient modes

Calculations of ITG eigenmodes in the HSX configuration have been performed, focusing on a pure collisionless ITG drive with kinetic electrons and the following parameters: $a/L_{Ti} = 3$, $a/L_{Te} = 0$, $a/L_n = 0$, $T_i/T_e = 1$, $\beta = 5 \times 10^{-4}$, $m_i/m_e = 1837$. Because the impact of eigenmodes with large parallel correlation lengths is more prevalent at low k_y , the eigenspectrum is shown for $k_y < 1$ in Fig. 5.5. As was observed with the TEM calculations, there are many unstable eigenmodes for every k_y . A similar mix of mode structures is observed, including strongly ballooning modes, $k_x \neq 0$ modes, and extended modes along the field line. Also observed are two-scale, ion-direction-propagating modes with extended envelope structure, labeled by “A”, “B”, and “C” in Fig. 5.5. The corresponding mode structures are shown in Fig. 5.6. While these modes have similar envelope behavior as in the TEM case, a distinguishing characteristic of the ITG case is that these modes are much more unstable and do not become stable with increasing poloidal turns. Additionally, instability of the extended ion modes is observed at high k_y for the ITG case, as shown for $k_y = 0.9$ in Fig. 5.5, while only marginal instability is observed at low k_y in Fig. 5.2 for the TEM case.

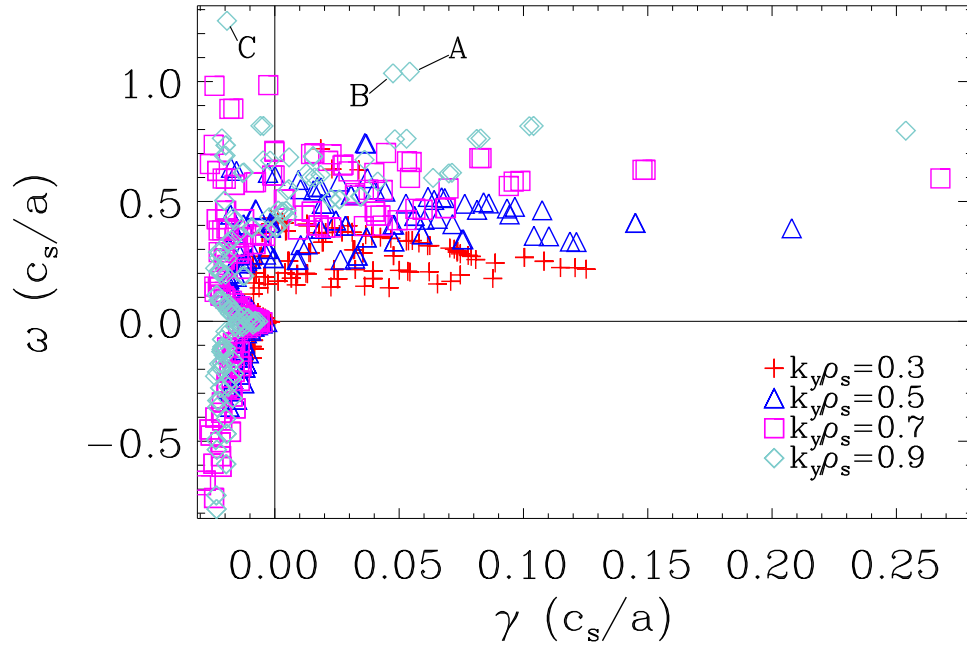


Figure 5.5: ITG eigenmode spectrum for different k_y values, denoted by different symbols and colors. The modes labeled “A”, “B”, and “C” are modes with two-scale behavior, and the mode structures are shown in Fig. 5.6. Source: Faber et al. (2018).

Despite these differences, given that these two-scale, extended-envelope ion modes are observed in both TEM and ITG calculations, the existence of these modes is connected to the low-magnetic-shear nature of devices such as HSX rather than a particular instability drive. An important observation is that these modes are not observed in the unstable eigenspectrum when an adiabatic electron approximation is used. This is shown in Fig. 5.7, where the eigenvalue spectrum is computed for both the adiabatic and kinetic electron treatment for a particular k_y . Thus to fully resolve the drift-wave dynamics in a low-shear stellarator like HSX, it is important that kinetic electrons are used, so that crucial physics is not overlooked.

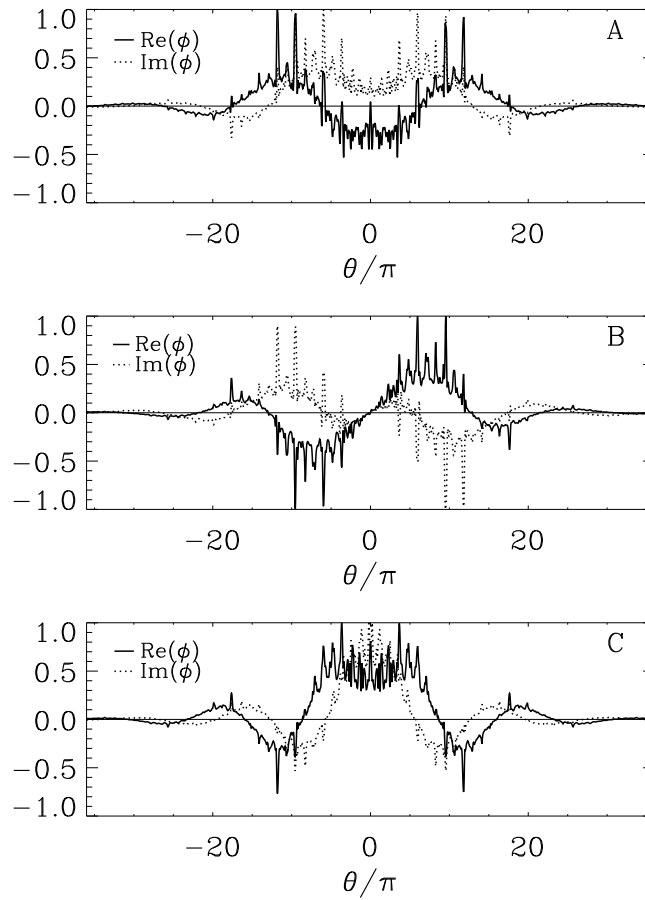


Figure 5.6: Electrostatic potential for eigenmodes “A”, “B”, and “C” from Fig. 5.5. The real part is the solid line and the imaginary part is the dotted black line. Similar to the mode “D” in Fig. 5.3, the ITG eigenmodes display two-scale structure, with an outer scale envelope and inner-scale structure set by the helical magnetic structure. Source: Faber et al. (2018).

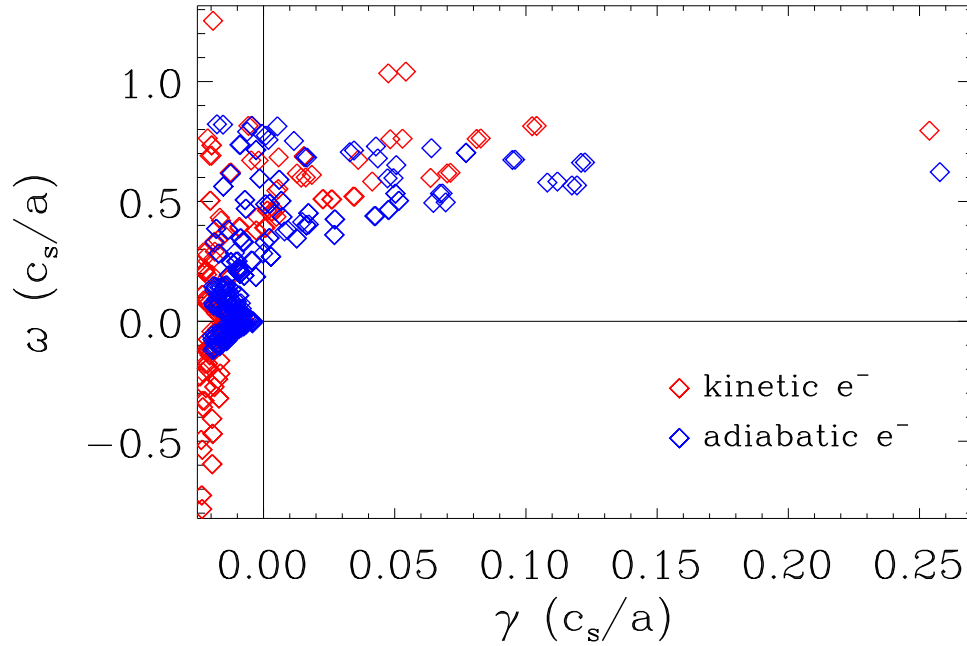


Figure 5.7: Comparison of the ITG eigenmode spectrum at $k_y = 0.9$ for kinetic electrons (red) and adiabatic electrons (blue). Adding kinetic electron effects primarily the real frequency and reduces the number of unstable modes. However the extended ion modes that are unstable for kinetic electrons are absent from adiabatic electron calculations. Source: Faber et al. (2018).

5.2.3 Zero-magnetic-shear approximation

The HSX shear value $\hat{s} = -0.046$ represents only a small deviation from $\hat{s} = 0$. Equation (3.65) shows that order unity variations in $\nabla\theta$ and $\nabla\zeta$ terms will dominate over the secular $\nabla\psi$ term, provided $\theta - \theta_k$ is small. A reasonable approximation is then to neglect the global magnetic shear, which will be referred to as the zero-shear technique. In the zero-shear approach, linear modes no longer couple through magnetic shear, as the boundary condition is strictly periodic. A substantial benefit of this approach to low magnetic shear configurations is that the radial box size of the simulation is no longer

determined by Eq. (3.74), which states $L_x \geq (\hat{s}k_y^{\min})^{-1}$. As seen in Ch. 4, using $k_y^{\min} = 0.1$ yields $L_x \approx 220\rho_s$, a value comparable with macroscopic equilibrium scale lengths. Despite such large simulation domains, this is not physically problematic provided the turbulent correlation lengths are both smaller than experimental correlation lengths and the background length scales, such as $L_{n,T}$. A large radial box can be thought of as equivalent to multiple “independent” simulation domains and turbulent statistics can be accumulated quickly. The numerical resolution, however, must also be scaled appropriately, making such simulations expensive to carry out. With zero magnetic shear, one may choose a more reasonable radial domain size and resolution, potentially reducing computational costs.

With $\hat{s} = 0$, an extended parallel computational domain cannot be constructed by adding radial modes, as demonstrated in Sec. 5.1. Zero-shear calculations then require that the parallel computation domain extend sufficiently far along the field line to better accommodate physical parallel correlation lengths. The strictly periodic boundary condition makes it easier to enhance growth rates through self-correlation if an eigenmode is not sufficiently decayed at the ends of the simulations domain. This is not only an issue for linear eigenmode calculations. A nonlinear simulation can be dominated by artificial linear self-correlation if growth rates are large enough compared to nonlinear decorrelation rates, which is demonstrated in Sec. 5.3.

A zero-shear calculation can be accomplished in two different ways. In the first method, $\hat{s} = 0$ can be specified in the GIST routine used to generate the flux tube geometry from a VMEC equilibrium. The resulting geometry components, such as g^{xy} , g^{yy} , and curvature \mathcal{K}_y will not have secular terms in \hat{s} , but still contain the effects of local magnetic shear. The second method is to use a finite-shear flux tube but set $\hat{s} = 0$ in the GENE simulation. The geometry elements will still retain the effect of the \hat{s} secularity, so it is not a “true” zero-shear domain, but the modes in GENE will not be

linearly coupled. For HSX, no significant difference was seen between the two methods. However, it should be noted that if a large number of poloidal turns are required, the first method will break down, as the secular terms that are ignored by setting $\hat{s} = 0$ in the GIST calculation will become important at large field line angles.

Figure 5.8 shows the application of the zero-shear computational technique to HSX for dominant TEM eigenmode calculations where only one poloidal turn was used for the geometry. As linear modes are not coupled, one must scan over k_x values to capture finite k_x modes. At higher k_y , the dominant finite-shear and the zero-shear calculations agree quite well for $k_x = 0$. At higher k_y , modes that strongly balloon at the outboard midplane are the dominant instability and are sufficiently localized within one poloidal turn. For intermediate values $0.3 \leq k_y \leq 0.7$, strong growth at finite k_x is observed and scanning k_x for the zero-shear modes reproduces the finite-shear values. However, for $k_y < 0.2$, clear divergences are observed between the zero-shear and finite-shear calculations. The zero-shear growth rates exhibit significantly larger growth rates than the finite-shear counterparts and can be identified as the zero-shear equivalent to the extended envelope ion modes in the finite-shear case. As is shown in Fig. 5.9, for geometry using one poloidal turn, this zero-shear mode branch (red diamonds) tracks the finite-shear (black diamonds) growth rates and frequencies relatively well for higher k_y values. Around $k_y = 0.3$, the zero-shear growth rates diverge and become significantly more unstable. This is problematic for nonlinear simulations that require $k_y^{\min} \leq 0.1$, and will be discussed in Sec. 5.3.

Linear mode differences between the finite and zero-shear techniques become small when multiple poloidal turns are utilized, and in particular, growth rate differences at wavenumbers $k_y \leq 0.1$ are significantly reduced. The periodic parallel boundary conditions coupled with geometry from one poloidal turn does not allow modes to sufficiently decay and the growth rate is artificially enhanced. This indicates that for the low- k_y modes, the

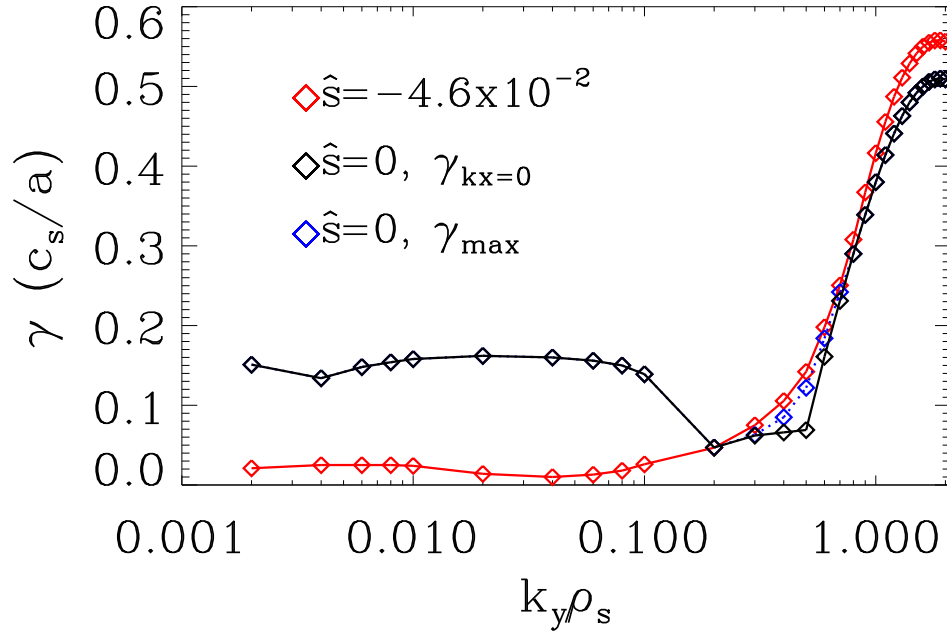


Figure 5.8: Linear growth rate spectrum of TEMs for one poloidal turn for the finite-shear approach (red) and the zero-shear approach (black and blue). The blue points are from calculations where the k_x value was varied to find the maximum growth rate, while the black points are the $k_x = 0$ streamer instability. The non-zero k_x effects are required to reproduce the finite-shear spectrum for $0.3 \leq k_y \leq 0.7$. Source: Faber et al. (2018).

parallel correlation lengths for HSX are longer than one poloidal turn and that the enhanced growth rates for the zero-shear calculations were due to self-correlating fluctuations. For the half-toroidal flux surface in HSX, linear TEMs show convergence at 4 poloidal turns.

As noted previously, for stellarator purposes, it is not sufficient to just examine convergence of the most unstable mode, as subdominant modes can play an important role in the turbulent dynamics. Figure 5.10 shows a comparison of the eigenmode spectrum between the finite and zero-shear techniques for a TEM case in HSX, using four poloidal turns at $k_y = 0.7$.

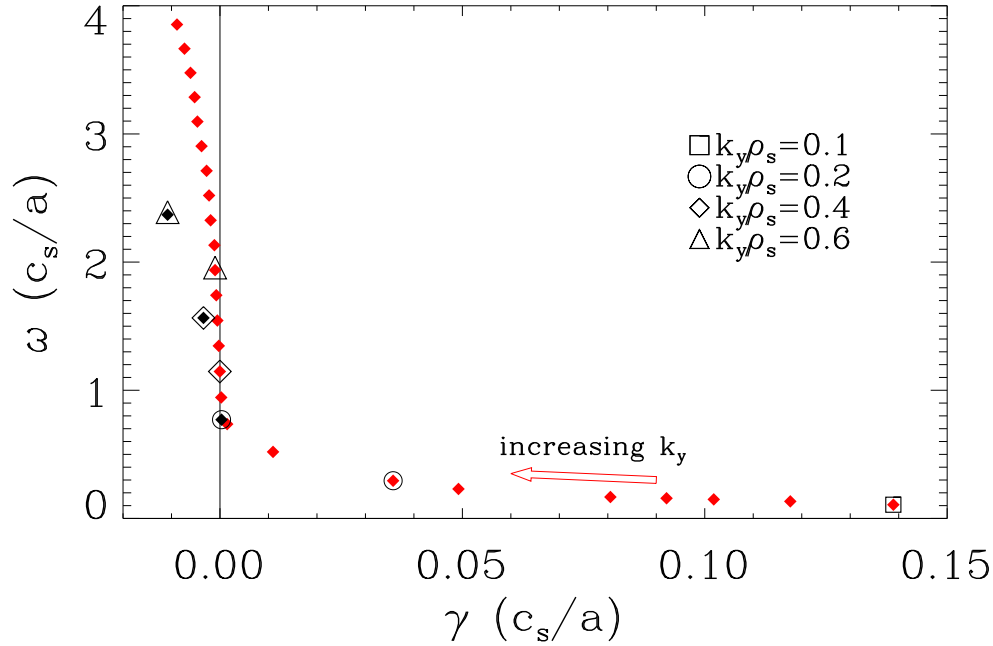


Figure 5.9: Eigenspectrum of the artificially enhanced mode (red diamonds) of Fig. 5.8 for a range of wavenumbers k_y . Select k_y modes are identified by the outlined symbols and compared with the finite-shear counterpart for one poloidal turn (black diamonds). All finite-shear eigenvalues are clustered near marginal stability, whereas zero-shear modes are artificially enhanced at one poloidal turn. Source: Faber et al. (2018).

The zero-shear eigenmodes are computed by scanning k_x values that would be coupled via the parallel boundary condition in the finite-shear calculation. Figure 5.10 shows that both the zero-shear and finite-shear growth rates across the spectrum are replicated. It is not necessary to match exactly every single subdominant mode between the two approaches. Pueschel et al. (2016) demonstrated the impact of the subdominant modes in HSX is to generate broadband turbulence, lessening the impact of any particular eigenmode. More importantly, the clustering of eigenmodes in the spectrum is very well reproduced between the calculation techniques in Fig. 5.10, which leads to

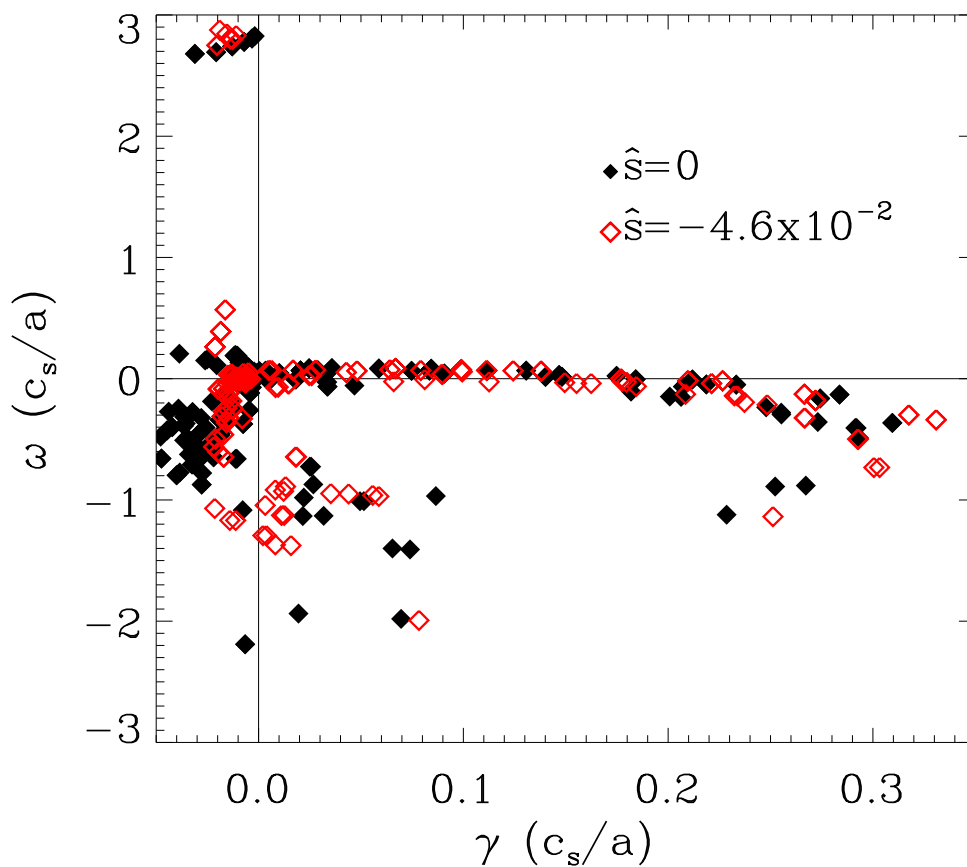


Figure 5.10: Comparison of the finite-shear (hollow red diamonds) and zero-shear (solid black diamonds) eigenspectrum at $k_y = 0.7$ for the ∇n -driven TEM. Sufficient agreement is observed between the two computational approaches when multiple poloidal turns are used. In particular, the zero-shear technique recovers the appropriate clustering of eigenmodes, including the marginally stable ion mode branch (branch “D” of Fig. 5.2). Source: Faber et al. (2018).

consistent turbulence energy drive and dissipation. This gives confidence that the zero-shear technique is accurately calculating the eigenmode spectrum when the parallel correlation length is sufficiently resolved.

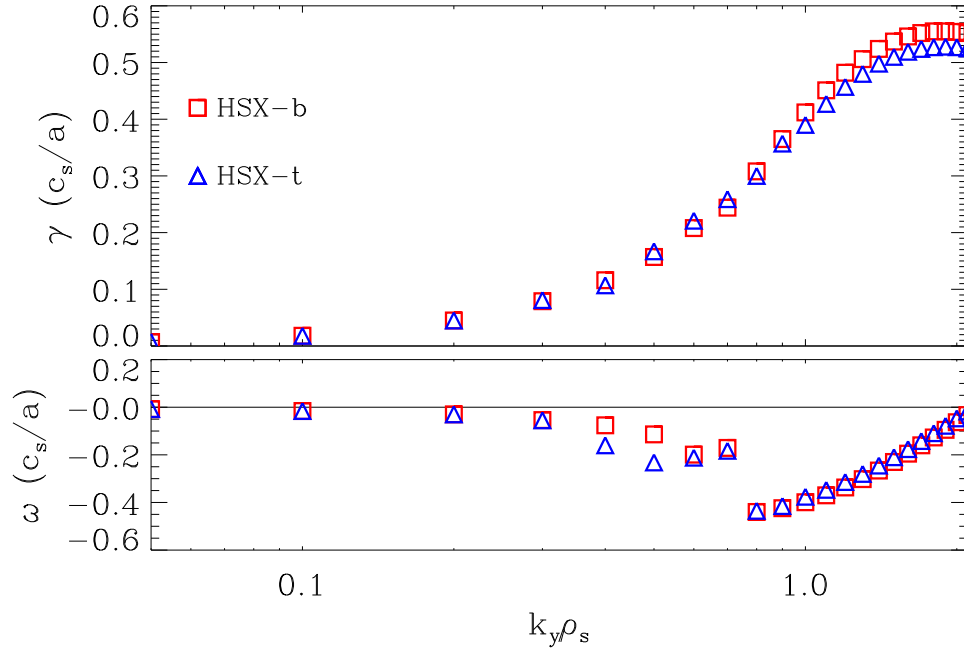


Figure 5.11: Dominant linear growth rates for the HSX-bean flux and HSX-triangle flux tube with $n_{\text{pol}} = 4$. This figure should be compared with Fig. 4.3.

5.2.4 Flux-tube equivalence

In Ch. 4, it was shown that linear growth rates were a function of the flux tube label, where HSX-t had lower growth rates than HSX-b for the same wavenumbers (see Fig. 4.3). Repeating the calculations of Sec. 4.2.1, but with $n_{\text{pol}} = 4$, reveals that the flux tube differences disappear, as is shown in Fig. 5.11, where near identical linear growth rates and frequencies are computed for both flux tubes. Examining where the eigenmode is localized along the field line in HSX-b and HSX-t shows they balloon in nearly same location in SFL coordinates. In HSX-b, this occurs at the outboard midplane, which can be chosen as $(\theta = 0, \zeta = 0)$ for convenience. For HSX-t, the field line label is $\alpha = \pi/4$. The point $(\theta \approx 2\pi n, \zeta \approx 2\pi n)$ point is

reached (corresponding to $(\theta \approx 0, \zeta \approx 0)$ as θ and ζ are 2π periodic) when $n(2\pi \iota + \pi/4) \bmod 2\pi \approx 0$. Using the HSX value $\iota \approx 1$ gives $n = 8$, implying that if the mode physically prefers to localize to this point, eight poloidal turns are necessary to properly resolve the drive and damping physics. Figure 5.11 was computed for $n_{\text{pol}} = 4$, but it was shown using even four poloidal turns significantly improves the accuracy of the representation of the HSX geometry along a field line. Why an eigenmode may prefer to localize in the same location regardless of field line label is again a consequence of the low shear nature of HSX. The secular term proportional to \hat{s} is simply not large enough to significantly alter the FLR and curvature terms between flux tubes and thus a mode “sees” the same geometry regardless of flux tube label and can “jump” to the most preferable helical well. In practice, this implies flux tubes are now “equivalent” and only one flux tube with sufficient n_{pol} need be used for HSX analysis.

5.3 Nonlinear Effects

The impact of multiple poloidal turns and the necessity to accurately resolve the subdominant spectrum can be seen in nonlinear simulations. Figure 5.12 shows values of electron electrostatic heat flux from ∇n -driven TEM turbulence simulations of HSX as a function of number of poloidal turns used to construct the flux tube geometry. The heat flux shows convergence only at four poloidal turns. Furthermore, convergence is seen between the finite-shear and zero-shear flux-tube approaches, but again only when multiple poloidal turns are used. For the high-density-gradient case here, with $a/L_n = 4$, it is seen that with only one poloidal turn, even the finite-shear flux tubes with different k_y^{min} values have different transport levels, and only after four poloidal turns do the flux values agree. This suggests it is necessary to check for convergence in the number of poloidal turns used to construct the geometry when performing nonlinear simulations.

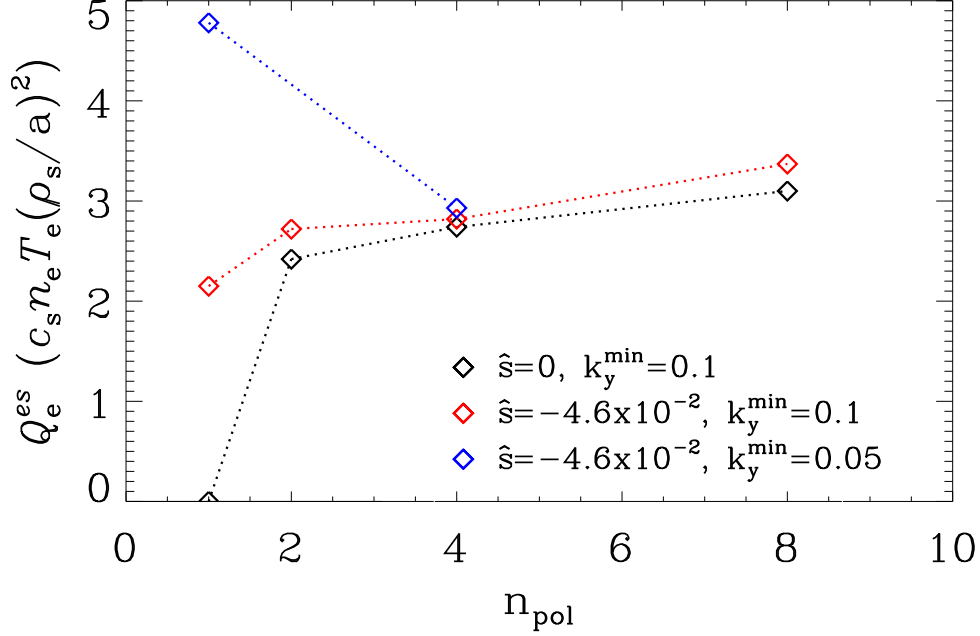


Figure 5.12: Nonlinear TEM heat fluxes for HSX as function of poloidal turns. In red and blue are finite shear simulations with $k_y^{\text{min}} = 0.1$ and 0.05 respectively, while zero-shear simulations are shown in black. Simulations agree for $n_{\text{pol}} \geq 4$. Source: Faber et al. (2018).

A striking observation from ∇n -driven TEM simulations in HSX (Faber et al., 2015) is a peak in the electrostatic heat flux spectrum at $k_y^{\text{min}} \approx 0.1$. This feature becomes more prominent as a/L_n increases. The flux spectrum for the nonlinear TEM simulations of Fig. 5.12 is shown in Fig. 5.13. At only one poloidal turn, the magenta and teal curves, the flux peaks at the lowest non-zero k_y and increases significantly as k_y^{min} is decreased. However, when 4 poloidal turns are used, the flux continues to peak at $k_y = 0.1$, and is substantially smaller at $k_y = 0.05$ for the $k_y^{\text{min}} = 0.05$ simulation. This again indicates that only with four poloidal turns are the low- k_y modes sufficiently resolved in the parallel direction such that accurate turbulence simulations are achieved.

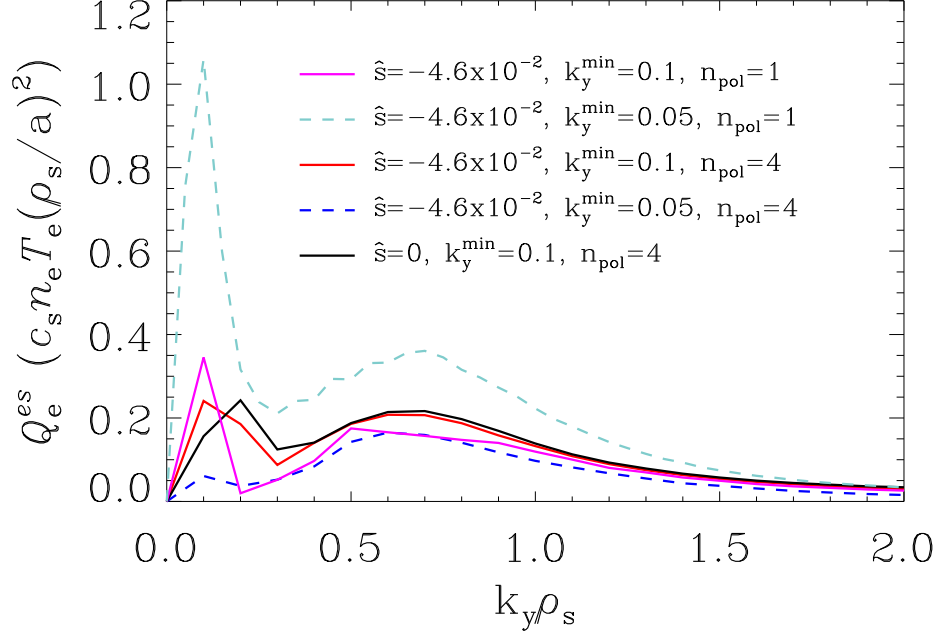


Figure 5.13: Flux spectrum from nonlinear TEM simulations for HSX. The different curves represent different combinations of poloidal turns used for the geometry and k_y^{\min} values. All curves, except for the black curve, were simulations with non-zero shear. The blue and teal dashed curves have been scaled by a factor of two due to having twice the k_y resolution as the solid curves. Source: Faber et al. (2018).

Insight into the physics driving transport at $k_y \approx 0.1$ and why simulations with only one poloidal turn are not converged can be obtained from nonlinear energy transfer considerations. For example, the equation for entropy transfer between modes at wavenumbers k and k' can be written as (Bañón Navarro et al., 2011):

$$\mathcal{T}_f^{k,k'} = \int dz dv_{\parallel} d\mu \left[\frac{T_{0i}}{F_{0i}} f_k^* \left((k - k') \bar{\phi}_{1(k-k')} k'_y f_{k'} - (k - k') \bar{\phi}_{1(k-k')} k'_x f'_k \right) \right], \quad (5.3)$$

where the perturbed distribution function f_k is a function of the parallel

coordinate z and velocity space coordinates v_{\parallel} and μ . The gyroaveraged fluctuating potential $\bar{\phi}_{1k}$ is a function of z alone. While other nonlinear transfer terms can be identified in the energy budget equations, Bañón Navarro et al. (2011) shows this term is the dominant transfer mechanism. The amount of entropy transferred by Eq. (5.3) can be increased by two methods. Large values of $\mathcal{T}_f^{k,k'}$ can be achieved when eigenmodes are correlated in both the parallel direction and in velocity space. Eigenmodes that are not well correlated, but still have some overlap, can have large $\mathcal{T}_f^{k,k'}$ if the amplitudes are large enough to compensate for the lack of mode correlation.

These considerations make it clear why zonal flows, which are uniform in z , can efficiently transfer energy. Zonal flows, however, are linearly stable and only driven to large amplitudes by nonlinear energy transfer and cannot input energy into the system. Similar to zonal flows, the marginally stable ion mode branch has extended structure along field lines and Maxwellian velocity space structure, enabling efficient transfer of energy between modes. As seen in Secs. 5.2.1 and 5.2.2, however, the ion modes can be linearly unstable when an insufficient number of poloidal turns are used for the computational domain. These modes, which are more unstable at low k_y , can then also provide an energy drive for turbulence. This can be problematic for nonlinear simulations, as simulations of ion scale turbulence generally require $k_y^{\min} \lesssim 0.1$, and an important factor for converged nonlinear simulations is the avoidance of significant energy drive at the domain scales. The contribution to the linear energy drive from the modes at $k_y = 0.2$ can be seen in Fig. 5.14, where the non-conservative energy evolution terms, including terms proportional to the driving density gradient, are plotted as a function of (k_x, k_y) . In situations where a single instability dominates, such as in most high-shear situations, Fig. 5.14 would show only the conical yellow structure seen for $|k_y| \gtrsim 0.3$. The presence of strong energy drive at $|k_y| = 0.2$ suggests a connection to the extended ion modes, possibly through nonlinear, finite-amplitude instability as described in Friedman et al.

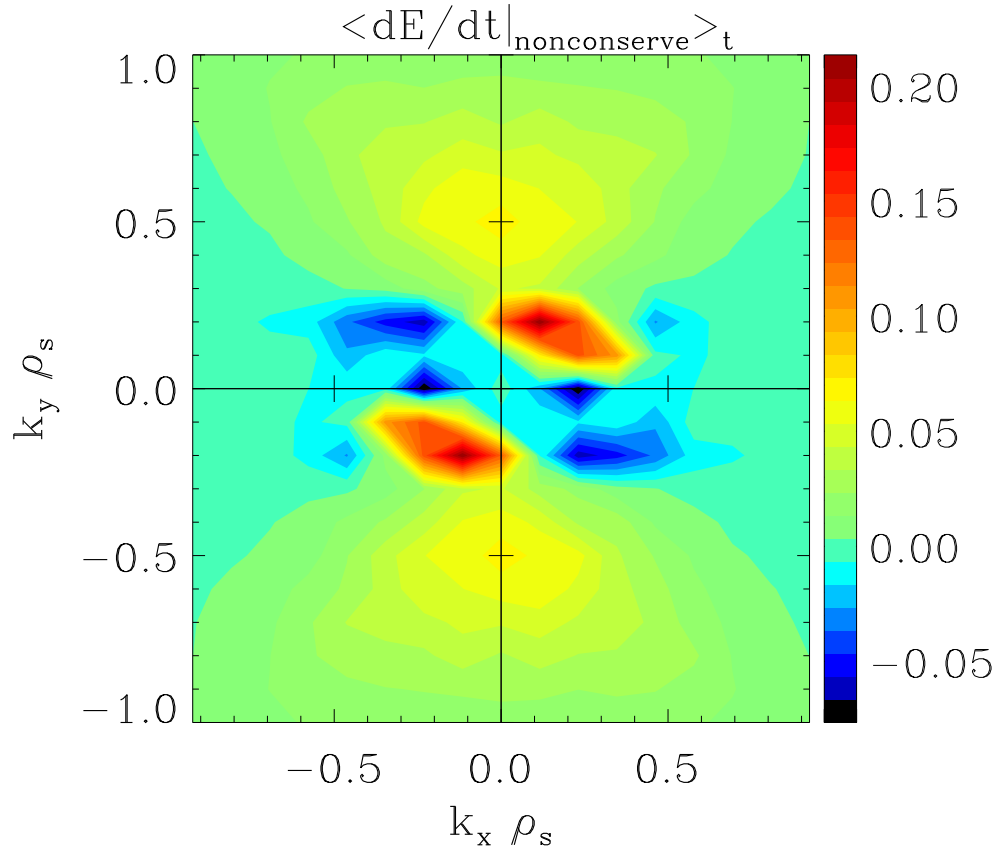


Figure 5.14: Spectrum of non-conservative energy terms in the high- ∇n TEM simulation for HSX. A positive (red) dE/dt value at a (k_x, k_y) indicates energy is being input into the system. The modes at $k_y = 0.2$ have the largest dE/dt values, coinciding with the heat flux peak at $k_y = 0.2$ in Fig. 5.13. Source: Faber et al. (2018).

(2013); Friedman and Carter (2014), or a pseudospectral response (Hatch et al., 2016a). Techniques for directly analyzing the energy dynamics of specific eigenmodes (Whelan et al., 2018) will be employed on this data in future work.

The impact of the stability of the extended ion modes on nonlinear convergence are not just limited to the direct linear energy drive. If these

modes are linearly unstable, they can grow to significant amplitudes and enhance nonlinear entropy and energy transfer. Due to their extended structure along the field line and Maxwellian velocity space structure, they can provide efficient coupling between eigenmodes, similar in manner to a zonal flow, and by extension also efficiently couple directly to zonal flows. This can have significant consequences for nonlinear simulations. Erroneously large zonal flow amplitudes will enhance the ability of zonal flows to transfer energy nonlinearly to damped modes. This is the mechanism responsible for the near zero heat flux observed in the zero-shear simulations at one poloidal turn in Fig. 5.12. The linear growth rates at low k_y for the zero-shear simulations are significantly enhanced compared to the finite-shear simulations, as was seen in Fig. 5.8. Visually, this impact can be seen by examining the contours of fluctuating potential and density from a zero-shear nonlinear simulation, as shown in Fig. 5.15. The contours indicate the simulation is dominated by a coherent interaction between the zonal flows and a linear mode that spans the box, which for $k_y^{\min} = 0.1$ is the artificially enhanced branch in Fig. 5.8.

Signatures of the extended ion mode persist in the finite-shear simulations when multiple poloidal turns are used so that the extended ion modes transition from unstable to stable at low k_y . To obtain the amplitude of an eigenmode in the nonlinear turbulent state, one can project the nonlinear distribution function onto the eigenmodes with the following relation:

$$p_j = \frac{|\int d\mathbf{x}d\mathbf{v}f_j^*f_{\text{NL}}|}{(\int d\mathbf{x}d\mathbf{v}|f_j|^2 \int d\mathbf{x}d\mathbf{v}|f_{\text{NL}}|^2)^{1/2}}. \quad (5.4)$$

Here, p_j is the projection of the eigenmode f_j and f_{NL} is the nonlinear distribution function. The eigenmodes are not orthogonal, thus the projection p_j is not uniquely associated with the amplitude for eigenmode f_j , but it can illuminate general trends in the underlying aspects of the turbulence. The projection onto the eigenmodes at $k_y = 0.2$ of the turbulent distribution

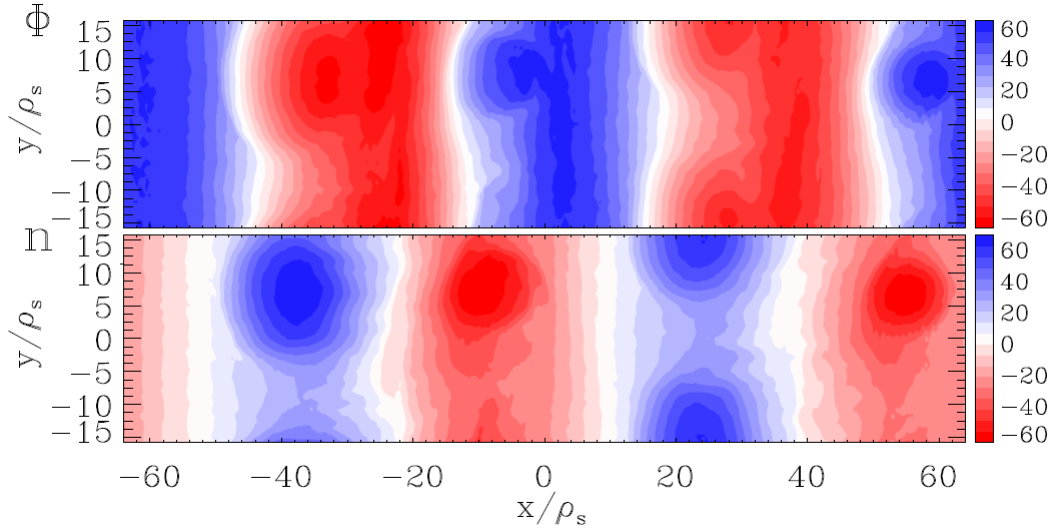


Figure 5.15: Instantaneous contours of fluctuating electrostatic potential Φ (top) and density n (bottom) from a zero-shear simulation with one poloidal turn (black curve of Fig. 5.12). Both Φ and n display dominant zonal components, and the density shows a clear coherent mode. Source: Faber et al. (2018).

function for the high ∇n -driven TEM case is shown in Fig. 5.16. This wavenumber corresponds to a region of low heat flux in Fig. 5.13. The figure demonstrates, consistent with previous observations, that subdominant modes have strong projection values while the most unstable modes have considerably smaller projections. The inset figures in Fig. 5.16 show that the modes with large projections have extended structure along the field line and that, somewhat counter-intuitively, the stable, extended-envelope ion modes have increasingly large projection values with increasing damping rate. At higher k_y , where the majority of the flux is driven in Fig. 5.13, the projection selects the most unstable mode as having the largest imprint on the turbulence, as one would expect, even when subdominant modes are important (Pueschel et al., 2016). This provides more evidence supporting the preceding discussion pertaining to Eq. (5.3) and Fig. 5.14 that the

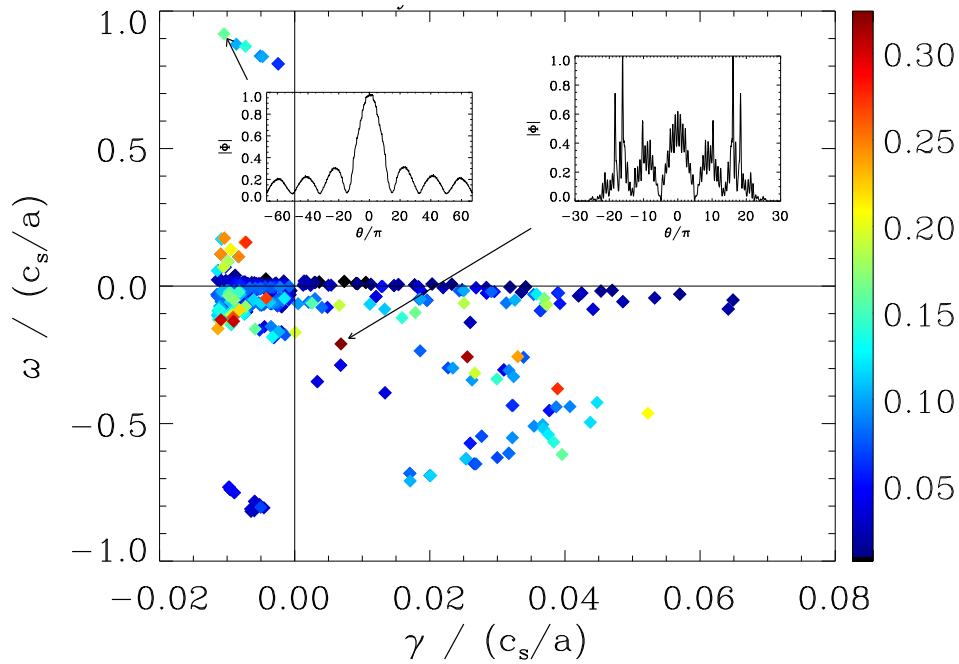


Figure 5.16: Projection of TEM turbulence onto eigenmodes at $k_y = 0.2$ using geometry with four poloidal turns. The colorbar gives the projection value. The projection shows subdominant and stable modes have higher projection values than the most unstable modes. The inset figures show the potential mode structure of the high-projection modes, emphasizing that at $k_y = 0.2$, modes with extended structure along the field line play a large role in the nonlinear state. Source: Faber et al. (2018).

extended ion modes are acting as both a linear energy drive and have a dominant role nonlinear energy transfer.

A plausible picture then emerges concerning both the lack of nonlinear convergence with one poloidal turn and the appearance of substantial heat flux seen in Fig. 5.13 at low k_y . When the geometry is insufficiently resolved, the low- k_y extended ion modes are linearly unstable due to self-correlation effects and can grow to high amplitudes in nonlinear simulations. Efficient nonlinear coupling can then pump both zonal flows and finite- k_y modes

that further enhance transport at low k_y . When multiple poloidal turns are used to more accurately describe the geometry along the field line, the now linearly stable extended ion modes are still efficient channels for nonlinear energy transfer, but with much smaller amplitudes. Low- k_y modes can still be pumped to large enough amplitudes to drive the observed transport peak, but the relative lack of linear energy drive at low k_y limits the amount of flux produced. It should be emphasized that this is an effect of subdominant and stable modes. If the turbulence was set by interactions between the most unstable mode and the nonlinearity, the turbulence would be insensitive to the parallel domain, as the most unstable modes are accurately resolved by geometries constructed using one poloidal turn. This supports the concept that for low-magnetic-shear stellarators, one must ensure the subdominant eigenspectrum is accurately simulated.

5.4 Chapter Summary

In this chapter, a detailed study of the influence of low global magnetic shear on flux-tube gyrokinetic simulations of the HSX configuration has been presented. In order to achieve converged nonlinear simulations, the flux tube needs to be constructed with geometry data from multiple poloidal turns. Using multiple poloidal turns more accurately resolves parallel mode structure and correlation crucial to accurately describing instability drive and damping physics. Many different unstable eigenmodes are observed at each k_y for both TEM and ITG calculations. Of particular interest is a branch of modes propagating in the ion diamagnetic direction that has two-scale structure, with an outer-scale envelope extending far along the field line and the inner scale is set by the local helical structure along the field line. These modes are marginally stable for TEM calculations, but are unstable, though still subdominant, for ITG calculations.

In nonlinear TEM turbulence simulations for HSX, these extended ion

modes play a prominent role in the nonlinear dynamics. Owing to their extended structure along field lines and Maxwellian velocity space structure, they provide efficient channels for nonlinear energy transfer, similar in manner to zonal flows. Furthermore, and unlike zonal flows since they have non-zero k_y , these marginally stable modes can also provide energy drive to the simulations if driven to finite amplitude. This appears responsible for the observation of significant heat flux at long wavelength in HSX. These observations are connected to the small value of global magnetic shear in HSX and highlight the complexity low magnetic shear can add to the drift wave spectrum and corresponding turbulence. As low magnetic shear is a likely property of future advanced stellarator concepts, care should be taken to ensure proper resolution of parallel scales when performing corresponding gyrokinetic turbulence simulations.

6 ROLE OF GEOMETRY IN TURBULENCE SATURATION

Building on the results of Ch. 5, the role of stable modes and geometry on turbulence saturation in stellarators is investigated in the present chapter. The turbulence optimization efforts performed by Mynick and co-authors (see Sec. 3.4 for a review of the turbulence optimization literature) used turbulence proxies that relied only on information from the dominant linear instability. This did lead to new configurations, particularly quasi-axisymmetric configurations, that showed reduced turbulent transport as calculated by GENE. However, as was shown in the previous chapters, this analysis can be misleading. For example, the quasi-helically symmetric (QHS) configuration of HSX can be intentionally spoiled by the addition of toroidal mirror terms in the magnetic spectrum. For large density gradients, the linear growth rates for the Mirror configuration are smaller than QHS, as shown in Fig. 6.1. However, the nonlinear heat fluxes at high density gradients are *larger* in Mirror than QHS, as shown in Fig. 6.2. Optimization analysis based on dominant linear growth rates would not capture this feature, thus one is motivated to develop turbulence proxies based on *nonlinear* physics, which is the subject of this chapter.

To this end, saturation of ITG turbulence in stellarators is modeled by a three-field fluid model with an analytic closure that has been adapted to accommodate general three-dimensional geometry. The model has been implemented numerically to examine how nonlinear three-wave energy transfer to stable modes changes with geometry. A proxy for nonlinear energy transfer is given by a product of a complex linear triplet correlation lifetime τ_{qst} and a complex coupling coefficient C_{qst} , where q , s , and t label the three interacting waves. The model predicts turbulence saturation in HSX is dominated by energy transfer to stable modes mediated by a third, finite- k_y mode, while in the quasi-axisymmetric stellarator NCSX, the dominant

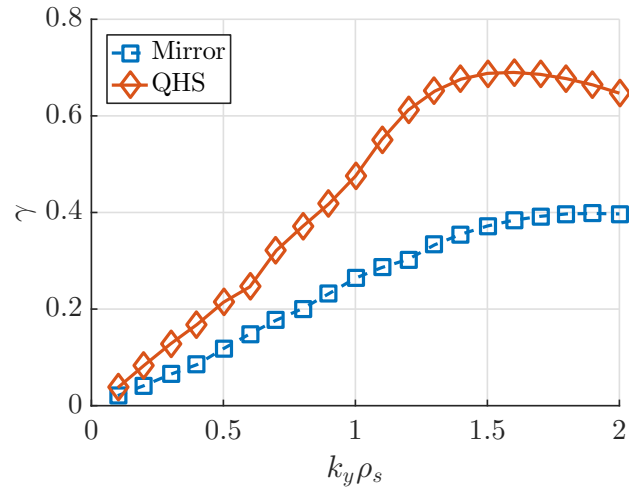


Figure 6.1: Growth rate spectrum for the HSX QHS configuration (red diamonds) and the HSX Mirror configuration (blue squares) for ∇n TEMs with $a/L_n = 4$. Courtesy J. Smoniewski.

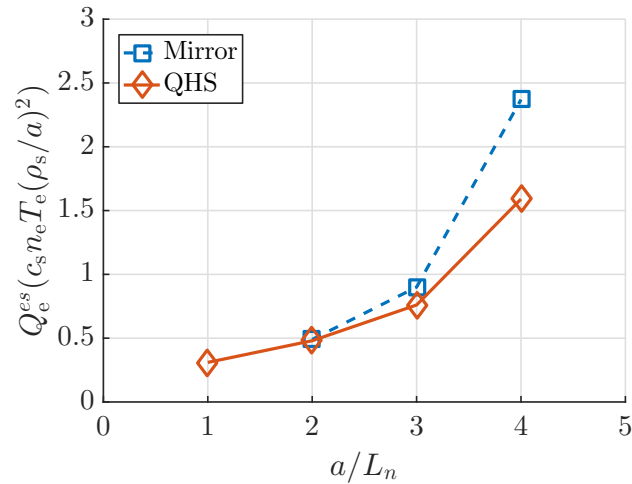


Figure 6.2: Nonlinear heat fluxes HSX QHS configuration (red diamonds) and the HSX Mirror configuration (blue squares) for ∇n -driven TEM turbulence as a function of a/L_n . Courtesy J. Smoniewski.

saturation mechanism is energy transfer to stable modes through zonal flows. The model is applied to different HSX geometries where the magnetic hill and well depth is altered and compared against GENE simulations. The triplet correlation lifetimes reproduce the trends observed in the gyrokinetic simulations, with smaller triplet correlation lifetimes corresponding to higher gyrokinetic fluxes and vice versa. Remarkably, the non-monotonic behavior observed in the gyrokinetic fluxes for increasing magnetic hill percentage is also reproduced by the reduced fluid model. This provides compelling evidence that using triplet correlation times as a nonlinearly-derived turbulence saturation proxy is a suitable tool for use in stellarator turbulence optimization efforts.

6.1 Fluid Modeling of Turbulence Saturation

The nonlinear gyrokinetic analysis of TEM turbulence for HSX in Sec. 5.3 indicates that nonlinear energy transfer between subdominant and stable modes plays an important role in determining saturated turbulent amplitudes and transport. The details of energy transfer dynamics will depend on the specific plasma parameters and type of turbulence under consideration, but the observation of similar linear and nonlinear features for both ITG and TEM suggests geometry plays an influential role in determining the dominant turbulence saturation mechanism. To better investigate this, a simplified, three-field fluid model of ITG turbulence for general three-dimensional geometry has been derived in Hegna et al. (2018). To summarize, the fluid model describes the evolution of the ion density (n_i), ion parallel momentum (v_{\parallel}), and ion temperature (T_i) in the electrostatic limit with the assumption of an adiabatic electron response. These equations yield energy evolution equations (second-order mode correlations) for ITG modes (which have $k_y \neq 0$) and for zonal modes (with $k_y = 0$), and are dependent

on third-order mode correlations. The nonlinear evolution equations for the third-order correlations are closed by an eddy-damped quasi-normal Markovian (EDQNM) closure argument, so that the fourth-order correlations are expressed in terms of the second-order correlations (see Terry et al. (2018) for further details). The detailed calculations can be found in Hegna et al. (2018), in the following discussion only important results will be reproduced to provide context for the numerical results that follow.

6.1.1 Three-Field Fluid Model

Fluid ITG drift waves are described by the following equations:

$$\frac{\partial n_i}{\partial t} + \nabla \cdot (n_i \mathbf{v}_E + n_i \mathbf{v}_{i*}) + \nabla \cdot (n_i \mathbf{v}_{pi} + n_i \mathbf{v}_{\pi i}) + \mathbf{B} \cdot \left(n_i \frac{v_{\parallel}}{B} \right) + \cdot (n_i \mathbf{v}_{dis}) = 0, \quad (6.1)$$

$$m_i n_i \frac{dv_{\parallel} B}{dt} + (\mathbf{B} \cdot \nabla) (n_i \phi + p_i) + \mathbf{B} \cdot (\nabla \cdot \boldsymbol{\pi})_{gyro} + \mathbf{B} \cdot (\nabla \cdot \boldsymbol{\pi})_{dis} = 0, \quad (6.2)$$

$$\frac{3}{2} n_i \frac{dT_i}{dt} + n_i T_i \nabla \cdot \mathbf{v}_i + \nabla \cdot \mathbf{q}_{Di} + \nabla \cdot \mathbf{q}_{dis} = 0, \quad (6.3)$$

where ϕ is the electrostatic potential, p_i is the ion pressure, $d/dt = \partial/\partial t + (\mathbf{v}_E + \mathbf{v}_{i*}) \cdot \nabla$, and $\mathbf{v}_i = v_{\parallel} \mathbf{B}/B + \mathbf{v}_E + \mathbf{v}_{i*} + \mathbf{v}_{pi} + \mathbf{v}_{\pi i}$. The viscosity tensor is given by $\boldsymbol{\pi}$ and has can be decomposed into the gyroviscous and dissipative parts. For subsequent discussion, only collisionless drift waves are considered by neglecting the dissipative components. The $\mathbf{E} \times \mathbf{B}$ and diamagnetic velocities are given by

$$\mathbf{v}_E + \mathbf{v}_{i*} = \frac{\mathbf{B} \times \nabla \phi}{B^2} + \frac{\mathbf{B} \times \nabla p_i}{n_i e B^2}, \quad (6.4)$$

while the polarization drift and gyroviscosity combine to form

$$\nabla \cdot (n_i \mathbf{v}_{pi} + n_i \mathbf{v}_{\pi i}) = -\nabla \cdot \left[\frac{n_i m_i}{e B^2} \left(\frac{\partial}{\partial t} + \mathbf{v}_E \cdot \nabla \right) \left(\nabla \phi + \frac{1}{n_i e} \nabla p_i \right) \right]. \quad (6.5)$$

The diamagnetic heat flux \mathbf{q}_{Di} is given by

$$\mathbf{q}_{Di} = \frac{5}{2} \frac{p_i}{eB^2} \mathbf{B} \times \nabla T_i. \quad (6.6)$$

The quantity $\nabla \cdot (\mathbf{v}_E + \mathbf{v}_{i*})$ can be expressed in terms of the field line curvature vector $\boldsymbol{\kappa} = \hat{\mathbf{b}} \cdot \nabla \hat{\mathbf{b}}$ as

$$\nabla \cdot (\mathbf{v}_E + \mathbf{v}_{i*}) = \frac{e}{T_i} \mathbf{v}_{Di} \cdot \nabla \phi + \frac{1}{T_i} \mathbf{v}_{Di} \cdot \nabla p_i, \quad (6.7)$$

where $\mathbf{v}_{Di} = (2T_i/eB^2) \mathbf{B} \times \boldsymbol{\kappa}$.

To account for general three-dimension geometry, the usual Clebsch representation of the magnetic field is used:

$$\mathbf{B} = \psi' \nabla \rho \times \nabla \alpha, \quad (6.8)$$

where $\psi(\rho)$ is the toroidal flux, ρ is a radial-like variable, $\psi' = d\psi/d\rho$, and $\alpha = \theta - \epsilon\zeta$ with θ and ζ as poloidal and toroidal straight field line angles. The curvature can be decomposed into

$$\boldsymbol{\kappa} = \kappa_n \hat{\mathbf{n}} + \kappa_g \hat{\mathbf{b}} \times \hat{\mathbf{n}} \quad (6.9)$$

where $\hat{\mathbf{n}} = \nabla \rho / |\nabla \rho|$ and κ_n and κ_g are the normal and geodesic curvatures. The integrated local magnetic shear, see Eq. (3.80) and subsequent discussion, is represented by the parameter $\Lambda = -g^{\rho\alpha}/B$. This allows the drift frequency, which enters into Eq. (6.7), to be written as

$$\frac{\mathbf{k} \cdot \mathbf{B} \times \boldsymbol{\kappa}}{B^2} = \frac{1}{\psi' |\nabla \rho|} \left[k_\alpha (\kappa_n + \Lambda \kappa_g) - k_\rho \frac{g^{\rho\rho} \psi'}{B} \kappa_g \right], \quad (6.10)$$

where $\mathbf{k}_\perp = k_\rho \nabla \rho + k_\alpha \nabla \alpha$ is the perpendicular wave vector. Fluctuating quantities are written in the Fourier representation $\tilde{\phi} = \sum_{\mathbf{k}} \phi_{\mathbf{k}} \exp(i\mathbf{k} \cdot \mathbf{x} - i\omega t)$ so that $\nabla \rightarrow i\mathbf{k}$. Furthermore, the usual flute-like ordering $k_\parallel \ll k_\perp$ is

assumed for fluctuations. The square of the perpendicular wave vector then takes the form

$$k_{\perp}^2 = \frac{B^2}{\psi'^2 g^{\rho\rho}} \left[k_{\alpha}^2 + \left(k_{\alpha} \Lambda - k_{\rho} \frac{g^{\rho\rho} \psi'}{B} \right)^2 \right]. \quad (6.11)$$

Equations (6.1)–(6.3) can be non-dimensionalized with the following normalizations:

$$\frac{e\tilde{\phi}_k}{T_{e0}} = \rho_* \Phi_k, \quad \frac{\tilde{T}_{ik}}{T_{e0}} = \rho_* T_k, \quad \frac{\tilde{v}_{\parallel k}}{c_s} = \rho_* U_k, \quad (6.12)$$

with $\rho_* = c_s m_i / e\psi$ and $c_s = \sqrt{T_e / m_i}$. Time is normalized by $\tau = L_{eq} / c_s$ for a chosen equilibrium scale length, the magnetic field by B_0 , and the non-dimensional wavenumbers are $k_x = k_{\rho} \rho_* \psi' / B_0$ and $k_y = k_{\alpha} \rho_*$. The full non-dimensional evolution equations are written as

$$\begin{aligned} \frac{\partial}{\partial t} [\Phi_k + B_k (\Phi_k + T_k)] - i D_k (\Phi_k + T_k) + \nabla_{\parallel} \frac{U_k B_0}{B} \\ = \sum_{\mathbf{k}'} (k_x k'_y - k_y k'_x) B_{k'k} \Phi_{k-k'} (\Phi_{k'} + T_{k'}), \end{aligned} \quad (6.13)$$

$$\frac{\partial U_k}{\partial t} + \frac{B_0}{B} \nabla_{\parallel} (\Phi_k + T_k) = \sum_{\mathbf{k}'} (k_x k'_y - k_y k'_x) \Phi_{k-k'} U_{k'}, \quad (6.14)$$

$$\frac{\partial T_k}{\partial t} + i k_y \epsilon_T \Phi_k = \sum_{\mathbf{k}'} (k_x k'_y - k_y k'_x) \Phi_{k-k'} T_{k'}, \quad (6.15)$$

where $\nabla_{\parallel} = (L_{eq} / B_0) \mathbf{B} \cdot \nabla$ and $\epsilon_T = -(L_{eq} / T_{e0}) dT_i / d\rho$. The geometry is encoded in the quantities D_k , B_k and $B_{k'k}$:

$$D_k = -k_y \frac{2L_{eq}(\kappa_n + \Lambda \kappa_g)}{|\nabla \rho|} + k_x \frac{2L_{eq} \Lambda_0 \kappa_g}{|\nabla \rho|}, \quad (6.16)$$

$$B_k = k_y^2 b_{yy} - 2k_x k_y b_{xy} + k_x^2 b_{xx}, \quad (6.17)$$

$$B_{k'k} = k'_y k_y b_{yy} - (k'_x k_y + k_x k'_y) b_{xy} + k'_x k_x b_{xx}, \quad (6.18)$$

$$\Lambda_0 = \frac{g^{\rho\rho} B_0}{B}, \quad b_{yy} = \frac{1 + \Lambda^2}{g^{\rho\rho}}, \quad g^{xy} = \frac{\Lambda \Lambda_0}{g^{\rho\rho}}, \quad b_{xx} = \frac{\Lambda_0^2}{g^{\rho\rho}}. \quad (6.19)$$

The major advantage to analyzing turbulence saturation with the three-field fluid model is simplicity without sacrificing important physics. By virtue of involving three fields, at every \mathbf{k} where instability exists there are three eigenmodes: an unstable mode, a nearly complex conjugate stable mode, and a nearly marginally stable mode, which were shown to be important for TEM turbulence in Sec. 5.3. When dissipation is neglected, the stable mode is exactly a complex conjugate to the unstable mode and the third mode is exactly marginally stable. Furthermore, when the nonlinear terms are neglected in Eqs. (6.13)–(6.15) and an appropriate ansatz for the eigenmode structure is made, an analytic dispersion relation can be derived, making the model an attractive candidate for use in stellarator optimization studies.

Ignoring the nonlinear terms, the system of equations given in Eqs. (6.13)–(6.15) can be transformed into a differential equation along the field line for Φ_k :

$$\begin{aligned} \nabla_{\parallel} \left(\frac{B_0^2}{B^2} \nabla_{\parallel} \Phi \right) \left[1 + \frac{k_y \epsilon_T}{\omega} \right] \\ + \omega^2 \left[1 + B_k \left(1 + \frac{k_y \epsilon_T}{\omega} \right) \Phi \right] + D_k \omega \left[1 + \frac{k_y \epsilon_T}{\omega} \right] = 0. \end{aligned} \quad (6.20)$$

Further progress may be made by assuming a form of the eigenmode Φ_k , which can be informed by comprehensive gyrokinetic simulations. Multiplying Eq. (6.20) by Φ_k^* , where A^* is the complex conjugate of some quantity A , and defining a field-line average by

$$\langle A \rangle = \frac{\int_{-\infty}^{\infty} \sqrt{g} d\eta A(\eta) |\Phi(\eta)|^2}{\int_{-\infty}^{\infty} \sqrt{g} d\eta |\Phi(\eta)|^2}, \quad (6.21)$$

Eq. (6.20) is transformed into a third-order polynomial in the eigenvalue ω :

$$\omega^3 (1 + \langle B_k \rangle) + \omega^2 (\langle B_k \rangle k_y \epsilon_T + \langle D_k \rangle) + \omega (\langle D_k \rangle k_y \epsilon_T - \langle k_{\parallel}^2 \rangle) - \langle k_{\parallel}^2 \rangle k_y \epsilon_T = 0, \quad (6.22)$$

where

$$\langle k_{\parallel}^2 \rangle = \frac{\int_{-\infty}^{\infty} \sqrt{g} d\eta \left| \frac{B_0}{B} \nabla_{\parallel} \Phi(\eta) \right|^2}{\int_{-\infty}^{\infty} \sqrt{g} d\eta |\Phi(\eta)|^2} \quad (6.23)$$

is an effective parallel wavenumber of the eigenmode. Equation (6.22) can be solved analytically, yielding three solutions. Where the instability criterion is satisfied, the unstable mode eigenvalue will be denoted by ω_1 , the conjugate stable mode by $\omega_2 = \omega_1^*$, and the marginally stable mode by ω_3 , where $\Im(\omega_3) = 0$. Equations (6.13)–(6.15) can be recast in matrix form

$$\mathcal{L} \cdot \boldsymbol{\beta} + \mathcal{N}[\boldsymbol{\beta}] = 0, \quad (6.24)$$

where \mathcal{L} is a linear operator and \mathcal{N} a nonlinear operator, and $\boldsymbol{\beta} = (\Phi_k(\eta), T_k(\eta), U_k(\eta))^T$. For each eigenvalue ω_p , there is a corresponding eigenvector β_p that satisfies $\mathcal{L}(\omega_p) \cdot \beta_p = 0$. The fluid variables $\boldsymbol{\Phi} = (\Phi_k, T_k, U_k)^T$ have a linear relationship with the eigenmodes $\boldsymbol{\beta} = (\beta_1, \beta_2, \beta_3)$ defined by $\boldsymbol{\Phi} = M_k \boldsymbol{\beta}$. The entries of M_k and its inverse are given in terms of the linear eigenvalues and can be found in Hegna et al. (2018). The evolution equation for eigenmode β_p can then be expressed in terms of the other eigenmodes and coupling coefficients C_{qst} , where (q, s, t) are the mode labels where 1 is the unstable mode, 2 is the stable mode, and 3 is the marginally stable mode. As zonal modes play an important role in turbulent dynamics, the evolution equation will be segregated into coupling between zonal modes (denoted by the indices F for Φ^Z coupling, T for T^Z coupling and U for U^Z

coupling) and non-zonal modes and is given by (Hegna et al., 2018, Eq. (68))

$$\begin{aligned}
\frac{\partial \beta_p}{\partial t} + i\omega_p \beta_p = & \sum_{k'_x (k'_y=k'_y)} C_{pqF} \Phi_{k-k'}^Z \beta'_q + \sum_{k'_x (k'_y=0)} C_{pFq} \Phi_{k'}^Z \beta' \\
& + \sum_{k'_x (k'_y=0)} C_{pTq} T_{k'}^Z \beta''_q + \sum_{k'_x (k'_y=0)} \int_{-\infty}^{\eta} \sqrt{g} d\eta C_{pUq} U_{k'}^Z \\
& + \sum'_{k'} C_{pqr} \beta'_q \beta''_r + \sum'_{k'} \int_{-\infty}^{\eta} \bar{C}_{pqr} (\beta''_r \nabla_{\parallel} \beta'_q - \beta'_q \nabla_{\parallel} \beta''_r). \quad (6.25)
\end{aligned}$$

The sums denoted by $\sum'_{k'}$ exclude $k'_y = 0$ and $k'_y = k_y$ and the k dependence of the eigenmodes was suppressed: $\beta'_q = \beta_q(\mathbf{k}')$ and $\beta''_r = \beta_r(\mathbf{k} - \mathbf{k}')$. The specific form of the coupling coefficients C_{qst} is complicated (Hegna et al., 2018) and not important for this thesis, but one should note that they are computed from the elements of M_k and thus linear eigenvalues ω_p . Also, Eq. (6.25) shows the classic nonlinear hierarchy problem: the evolution of the eigenmodes is defined by correlations of the *product* of eigenmodes at different wavenumbers.

To explore turbulence saturation, it is necessary to examine how the energy of an eigenmode, defined by $|\beta_p(\mathbf{k})|^2$, evolves. The energy evolution equation is complicated and will not be repeated here (see Hegna et al. (2018, Eq. 80)), but like Eq. (6.25), the energy evolution equation is given in terms of *triplet* correlations between eigenmodes and zonal fields at different wavenumbers satisfying the triplet matching condition $\mathbf{k} - \mathbf{k}' - \mathbf{k}'' = 0$. Similarly, the triplet correlations are defined in terms of quartic correlations with the form

$$\left[\frac{d}{dt} + i(\omega''_r + \omega'_q - \omega_p^*) \right] \langle \beta_p^* \beta'_q \beta''_r \rangle = \mathcal{G}, \quad (6.26)$$

where \mathcal{G} contains the quartic correlations. However, the equations can be closed by employing the EDQNM closure, which expresses the quartic corre-

lations as products of lower-order correlations. The quadratic correlations themselves are defined in terms of triplet correlations, which effectively renormalizes the complex frequencies to

$$\hat{\omega}_r'' + \hat{\omega}_q' - \hat{\omega}_p^* = \omega_r'' + \omega_q' - \omega_p^* + \Delta\omega_r'' + \Delta\omega_q' - \Delta\omega_p^*, \quad (6.27)$$

where $\Delta\omega_p$ contains the nonlinear correction from the EDQNM closure. This three-wave frequency interaction defines what is referred to as the triplet correlation lifetime:

$$\tau_{pqr} = \frac{1}{i [\hat{\omega}_r'' + \hat{\omega}_q' - \hat{\omega}_p^*]}. \quad (6.28)$$

Physically, large values of τ_{pqr} imply the three interacting modes (which includes zonal modes) spend a long time interacting with each other. This has consequences for turbulence saturation, as one can show (Hegna et al., 2018, Eq. 105) the energy evolution equation for eigenmode β_p has the form

$$\frac{d}{dt} \langle |\beta_p|^2 \rangle = i (\omega_p^* - \omega_p) \langle |\beta_p|^2 \rangle + \sum_{k',s,t} C_{pst}(k, k') \tau_{pst}(k, k') F(\beta_i, k, k') + C.C. \quad (6.29)$$

Thus, the energy evolution of β_p is dependent on the product $\tau_{pst}C_{pst}$. If one of the interacting modes is an unstable mode and one a stable mode, then large values of $\tau_{pst}C_{pst}$ imply there is a large amount of time for the unstable mode to transfer energy to the stable mode through a third mode, and since the stable mode acts as a source of energy dissipation, the amplitude can be reduced. This has ramifications for reducing transport, as turbulent fluxes are proportional to mode amplitudes, and motivates using $\tau_{pst}C_{pst}$ as proxy for transport in turbulence optimization studies. Furthermore, due to the nature of plasma turbulence, the largest fluctuation amplitudes occur at small values of \mathbf{k} . Since the nonlinear corrections in Eq. (6.27) go as k^2 , they represent small corrections and thus both τ_{pst} and C_{pst} can be evaluated using only the *linear* eigenvalues of Eq. (6.22), which are

calculated analytically.

6.1.2 Numerical Implementation

The saturation theory of the previous subsection has been implemented numerically as the Plasma Turbulence Saturation Model-3D (PTSM3D, (Faber, 2018)). PTSM3D is a Fortran 90 program that solves the linear dispersion relation of Eq. (6.22) at every (k_x, k_y) point within a specified spectrum for realistic stellarator geometry. Like GENE, PTSM3D uses the GIST package to compute the necessary geometry elements from an actual three-dimensional MHD equilibrium. Calculations in PTSM3D are performed using the ballooning formalism discussed in Sec. 3.2, where a (k_x, k_y) point is translated to an angle along the field line η . The power of PTSM3D, making it suitable for use in turbulence optimization schemes, lies in the extremely fast calculation of the τC spectrum, as the roots of a third-order polynomial are computed algebraically. However, as previously referenced, this relies on an ansatz for the structure of the eigenmode. For present purposes, the eigenmode is assumed to be a singly-peaked Gaussian along the field line:

$$\Phi_k(\theta) = \exp\left(-\frac{(\theta - \theta_0)^2}{2\Delta^2}\right). \quad (6.30)$$

The location parameter θ_0 is related to the ballooning angle $\theta_k = (1/\hat{s})k_x/k_y$, but does not necessarily take the exact value. Detailed inspection of linear ITG eigenmode structures computed by GENE for HSX and NCSX indicate that B_k (Eq. (6.17)) plays a crucial role in determining where eigenmodes localize. B_k is related to the local magnetic shear that in general has complicated structure along field lines, providing multiple locations where modes might be confined (see the discussion in Ch. 5). ITG modes are generally observed to have an approximately Gaussian structure and be centered in a neighborhood of η_k where B_k is minimized. For PTSM3D, an

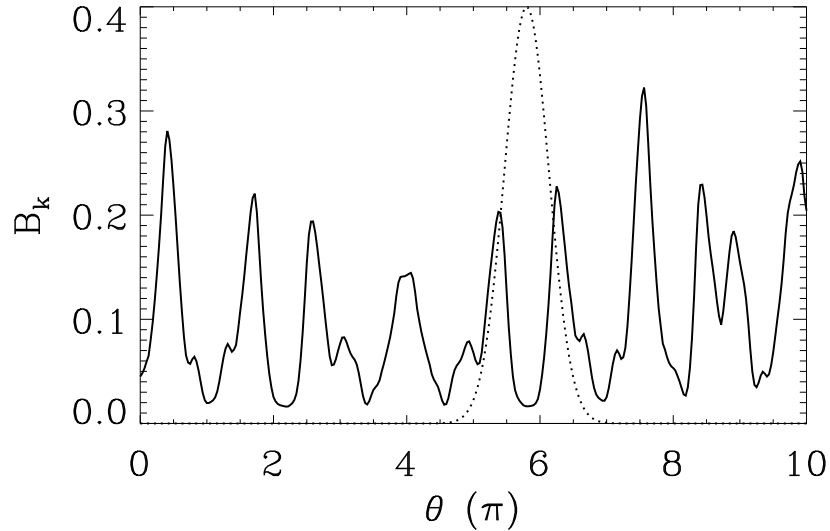


Figure 6.3: Example of an eigenmode (dashed line) compared with B_k (Eq. (6.17)) along a field line for a particular point in the \mathbf{k} -spectrum. The eigenmode is centered in a location where B_k is minimized and the adjacent B_k maxima are large enough to provide localization.

algorithm is used to identify candidate regions in B_k where the eigenmode may be located. The mode growth rate is then computed for each candidate region according to Eq. (6.22) and the region with the maximum growth rate is selected. An example of the eigenmode ansatz is shown in Fig. 6.3. The parameter Δ in Eq. (6.30) measures the full-width half-maximum of the Gaussian and is proportional to the distance between the immediate B_k maxima bounding the B_k minimum region under consideration.

After the complex frequency spectrum has been calculated, the triplet correlation times and coupling coefficients are computed using the complex mode frequencies. The saturation contributions are again segregated into zonal and non-zonal contributions. For the triplets involving zonal flows, the zonal flow is assumed to have zero frequency. The validity of this approximation has been verified for the cases presented in Sec. 6.2 by

comparing the zero-zonal-frequency τC spectrum to a τC spectrum where the zonal frequency was taken from a gyrokinetic simulation, and little difference was observed. For the non-zonal modes, all the possible combinations of triplets involving at least one stable mode were considered.

To generate a figure of merit to compare the zonal and non-zonal energy transfer channels as well as compare different configurations, an averaging denoted by $\langle \dots \rangle_k$ is performed over the absolute value of the τC spectrum, giving

$$\langle |\tau_{pst} C_{pst}| \rangle_k = \sum_{k_x, k_y} \mathcal{S}_G(k_x, k_y) |\tau_{pst}(k_x, k_y) C_{pst}(k_x, k_y)|. \quad (6.31)$$

The average is weighted by a fluctuation spectrum \mathcal{S}_G , which is obtained from a nonlinear gyrokinetic simulation and is not computed self-consistently within the model. It was observed that \mathcal{S}_G is relatively insensitive to changes in geometry and is more an expression of the characteristic scales of ITG turbulence itself.

While PTSM3D produces results that agree qualitatively with gyrokinetic results, as will be shown in Sec. 6.2, it is clear there are still several model deficiencies. Most glaringly, the eigenmode ansatz can break down dramatically, particularly at low k_y , where eigenmodes tend to extend long distances along field lines. Properly capturing the eigenmode structure at low k_y will modify both the drive and damping physics as well as the effective $\langle k_{\parallel}^2 \rangle$ of the mode, and as the low- k_y modes are generally the most important for turbulent dynamics, this may affect the final result. Furthermore, when modes become more extended, convolutions between modes that have been neglected in this simple model may become important. Secondly, the spectrum used to weight the τC average is a free parameter, and changes in the spectrum may also alter the final conclusions. Nevertheless, the model has been successfully applied to different stellarator configurations and yields physically relevant insights, as well be detailed in the next sections.

6.2 Turbulence Saturation in Quasi-Symmetric Stellarators

The PTSM3D code was used to qualify ITG turbulence saturation in two different quasi-symmetric stellarator configurations, HSX and NCSX (Reiman et al., 1999). HSX represents the quasi-helically symmetric (QHS) class of stellarators, while NCSX represents the quasi-axisymmetric (QAS) class. Importantly, by virtue of being a QAS configuration, NCSX is much more tokamak-like and as such, possesses significantly higher global magnetic shear than HSX. Intuitively, one would then expect the turbulence saturation characteristics for NCSX to resemble those of a $\hat{s} \sim 1$ tokamak, where zonal flows play an important role in ITG turbulence saturation. For the following discussion, the zonal and non-zonal saturation metric has been computed for HSX and NCSX on the half-toroidal-flux surface with $a/L_{T1} = 3$, which has previously been used for turbulence optimization studies (Mynick et al., 2011). The spectrum in PTSM3D is computed for $k_{\perp} \leq 1$, as the fluid approximation neglecting FLR effects breaks down for $k_{\perp} > 1$. To test the accuracy of the fluid eigenvalue calculation, the ITG growth rate spectrum for both configurations has also been computed with GENE. The results of this section have been published in Hegna et al. (2018).

6.2.1 Turbulence Saturation in HSX

Figure 6.4 shows the growth rate spectrum for QHS as computed by GENE, and two features should be noted. First, the growth rate spectrum at low k_y is largely independent of k_x . This is a hallmark of the “slab”-ITG modes that are dominant in QHS due to shorter connection lengths (Hegna et al., 2018). The second feature is that at higher k_y , the growth rate spectrum shows strong k_x dependence and structure, with the growth rate peaking at large $|k_x|$, with several growth rate peaks and valleys between $k_x = 0$ and $|k_x| = 1$. This structure is approximately reproduced by the fluid model, as

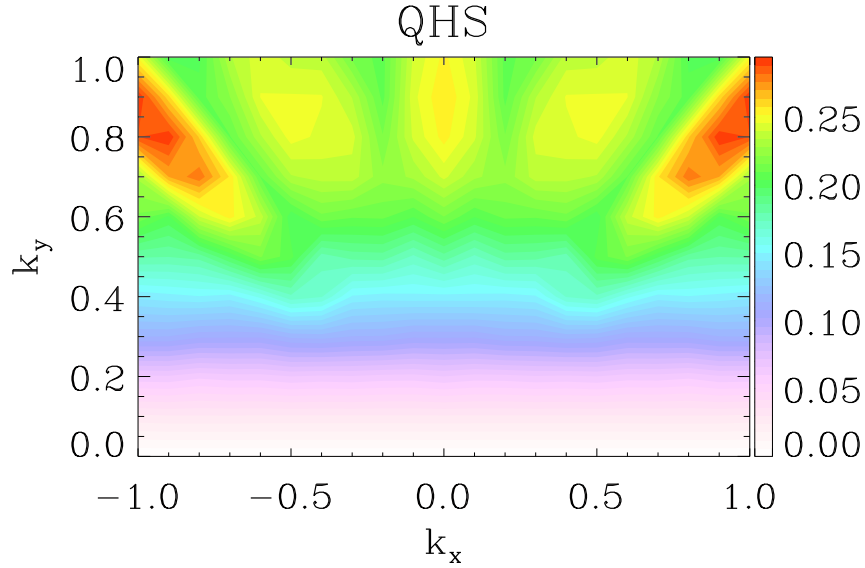


Figure 6.4: Growth rate spectrum for HSX (QHS) as computed by GENE. Source: Hegna et al. (2018).

is shown in Fig. 6.5. The growth rates are of comparable magnitude and similarly peak at large k_x for large k_y . However, somewhat more structure is observed in the PTSM3D spectrum, with more pronounced growth rate peaks and valleys. This is a product of the Gaussian eigenmode ansatz. At low k_y , the gyrokinetic modes are not Gaussian and extend along field lines, leading to the k_x independent slab-ITG growth rates. The low k_y , low k_x growth rates are fairly well replicated by the PTSM3D results, but at higher k_x , some growth rate “holes” appear where the eigenmode ansatz does not yield instability, a clear shortcoming of the model. Additionally, the growth rate peaks and valleys have finer structure than the gyrokinetic spectrum. This is because the eigenmode is not always localized to the same B_k region as the gyrokinetic eigenmode, and is the result of the approximate way in which the eigenmode was selected.

The QHS τC spectrum for the triplets involving an unstable mode, a

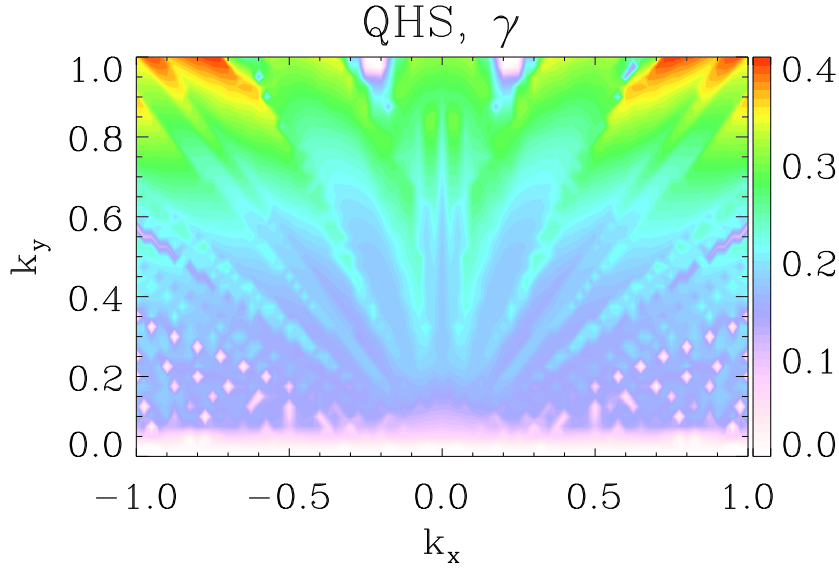


Figure 6.5: Linear growth rate spectrum for HSX (QHS) as computed by PTSM3D. Source: Hegna et al. (2018).

stable mode, and a zonal mode denoted by $|\tau_{12F}C_{12F}|$ is shown in Fig. 6.6. For the zonal triplets, the wavenumber matching condition implies that an unstable mode at (k_x, k_y) and a zonal mode at $(k_x^z, 0)$ couples to a stable mode at $(k_x - k_x^z, k_y)$. The k_x coordinate in Fig. 6.6 corresponds to k_x^z , while the k_y coordinate corresponds to the unstable mode. Figure 6.6 shows that for QHS the triplet interactions are maximized at the boundaries of the growth rate valleys, where the complex frequencies closely match. The vertical black lines at $|k_x| = 0.2$ denote the extent of the spectrum \mathcal{S}_G such that $\mathcal{S}_G(|k_x| \leq 0.2, k_y) = 1$ and $\mathcal{S}_G = 0$ otherwise.

The QHS τC spectrum for the non-zonal triplets is shown in Fig. 6.7 and denoted by $|\tau_{qst}C_{qst}|^{\max}$. The number of possible non-zonal triplet combinations involving an unstable mode at (k_x, k_y) , a stable mode at (k'_x, k'_y) and a third mode at $(k_x - k'_x, k_y - k'_y)$ is large due to freedom in both (k'_x, k'_y) and in the identity of the third mode. Thus what is plotted in

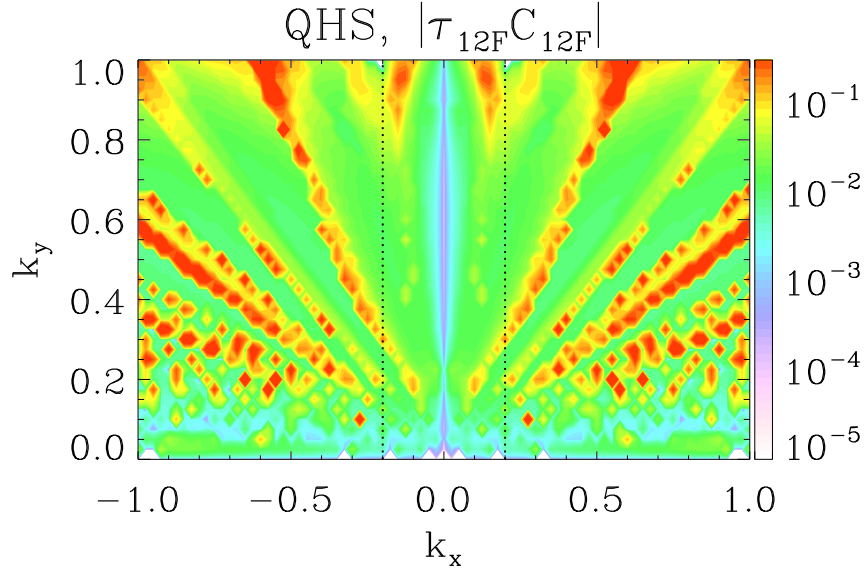


Figure 6.6: Contours of $|\tau_{12F}C_{12F}|$ for the HSX configuration as a function of k_x^z and k_y as computed by PTSM3D. Source: Hegna et al. (2018).

Fig. 6.7 is the triplet that *maximizes* the value of $|\tau_{qst}C_{qst}|$, corresponding to the most efficient transfer channel. The triplet correlation time τ_{qst} enters into mode correlations as the time constant for exponential decay, thus the triplet that maximizes this time should be the most physically relevant triplet. Figure 6.7 displays more complicated structure than Fig. 6.6 and is not necessarily maximized at the boundaries of the growth rate valleys. Importantly, the amplitudes of $|\tau_{qst}C_{qst}|^{\max}$ are roughly two orders-of-magnitude larger than those of $|\tau_{12F}C_{12F}|$. Applying the spectral average yields $\langle |\tau_{12F}C_{12F}| \rangle_k = 0.027$, while $\langle |\tau_{qst}C_{qst}| \rangle_k = 23.89$. This provides evidence that for ITG turbulence in HSX, it is most likely that energy transfer to stable modes through *non-zonal* modes is more important for turbulence saturation than through zonal flows, and agrees with the conclusions of Plunk et al. (2017) for HSX, which were achieved by secondary and tertiary instability analysis. This result is consistent with the TEM results in Chs. 4

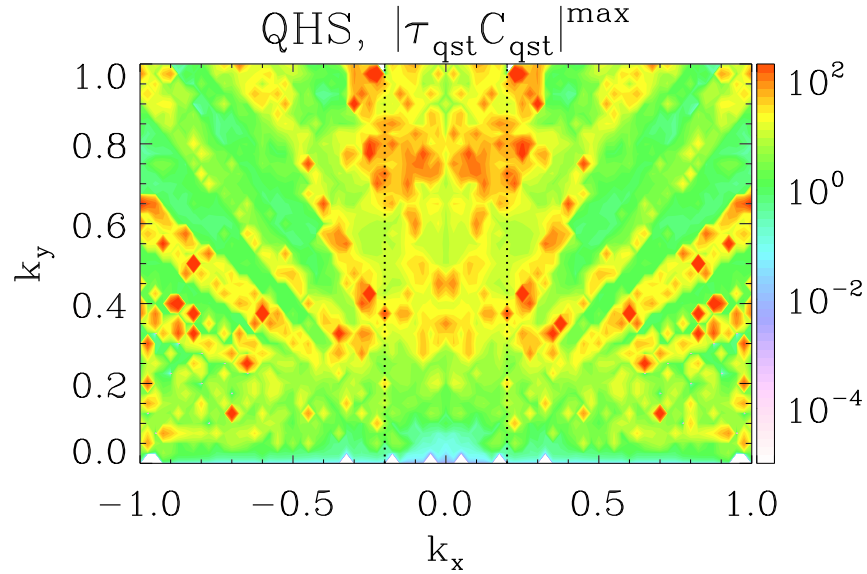


Figure 6.7: Contours of $|\tau_{qst} C_{qst}|^{\max}$ for the HSX configuration as a function of k_x and k_y as computed by PTSM3D. Source: Hegna et al. (2018).

and 5, which showed zonal flows are present in TEM turbulence but appear unimportant for turbulence saturation.

For optimization purposes, it is beneficial to examine which triplet combination is most important for non-zonal energy transfer to determine if the number of triplet correlations that need to be computed can be reduced. This is shown for HSX In Fig. 6.8. For the most part, particularly at the small (k_x, k_y) triplets that are dynamically important for turbulence, the triplet that maximizes $|\tau_{qst} C_{qst}|$ is a triplet involving an unstable mode, stable mode, and a marginally stable mode. This suggests that for optimization purposes one need not spend extra time computing other triplet combinations, further speeding up the method.

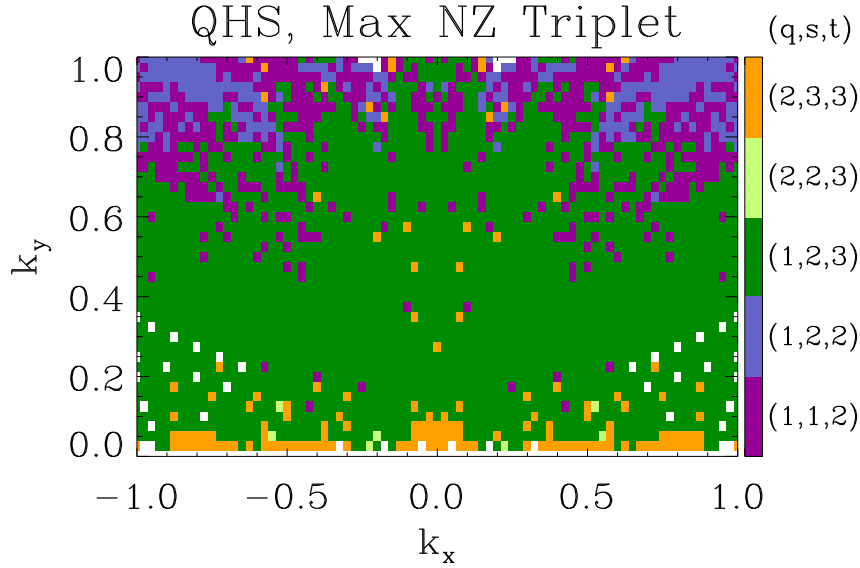


Figure 6.8: Identity of the triplets involved in maximizing $|\tau_{qst}C_{qst}|$. The color green indicates the triplet was comprised of an unstable mode, stable mode, and marginally stable mode. Source: Hegna et al. (2018).

6.2.2 Turbulence Saturation in NCSX

As expected, substantially different results are found for NCSX. Growth rates computed by GENE, in Fig. 6.9, show growth rates that peak at $k_x = 0$ and fall off rapidly with k_x . This is due to the “toroidal”-ITG branch being destabilized in NCSX, which is often the ITG branch found in axisymmetric configurations. This growth rate behavior is well reproduced by PTSM3D, shown in Fig. 6.10. Slightly more k_x structure is observed in the PTSM3D spectrum, however, most of this occurs at large k_x , where their contribution to nonlinear energy transfer should be small. The PTSM3D calculation does show modes ($|k_x| \gtrsim 0.2, k_y \geq 0.6$) that have zero growth rate, as opposed to the small but non-zero growth rates computed by GENE. It is believed that this region should also be unimportant for turbulence saturation.

The NCSX τC spectrum for zonal triplets is shown in Fig. 6.11 and

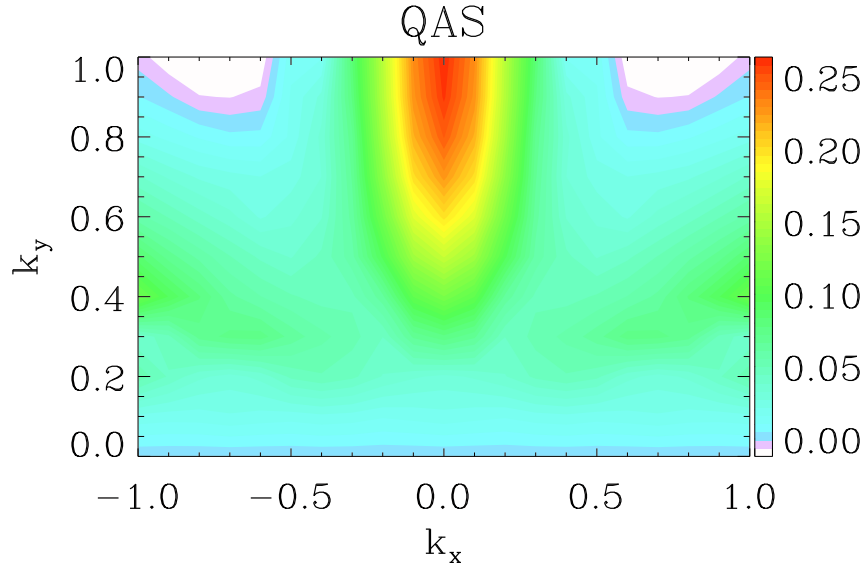


Figure 6.9: Growth rate spectrum for NCSX (QAS) as computed by GENE. Source: Hegna et al. (2018).

for the non-zonal triplets in Fig. 6.12. The zonal triplets for NCSX are dominated by triplets close to $k_x = 0$. This is a result of the toroidal nature of the ITG in NCSX, as the strong k_x dependence of eigenvalues makes minimizing the difference between ω_2 and ω_1^* difficult for $k_x \neq 0$. The non-zonal triplets in NCSX show that the largest resonances occur far from $k_x = 0$, where the turbulent amplitudes are significantly smaller and will not contribute significantly to saturation. Note that the amplitudes for the non-zonal and zonal triplets have commensurate magnitudes, this leads to similar magnitudes of the spectral average. The zonal triplets give $\langle |\tau_{12F} C_{12F}| \rangle_k = 0.159$ and the non-zonal triplets give $\langle |\tau_{qst} C_{qst}| \rangle_k = 0.261$. The actual energy transfer rate for zonal flows is proportional to the zonal amplitude, which is undetermined in this model, but is often 10–100 times larger than the fluctuating amplitudes in HSX and NCSX Gene simulations. This suggests that unlike HSX, where the non-zonal saturation was roughly

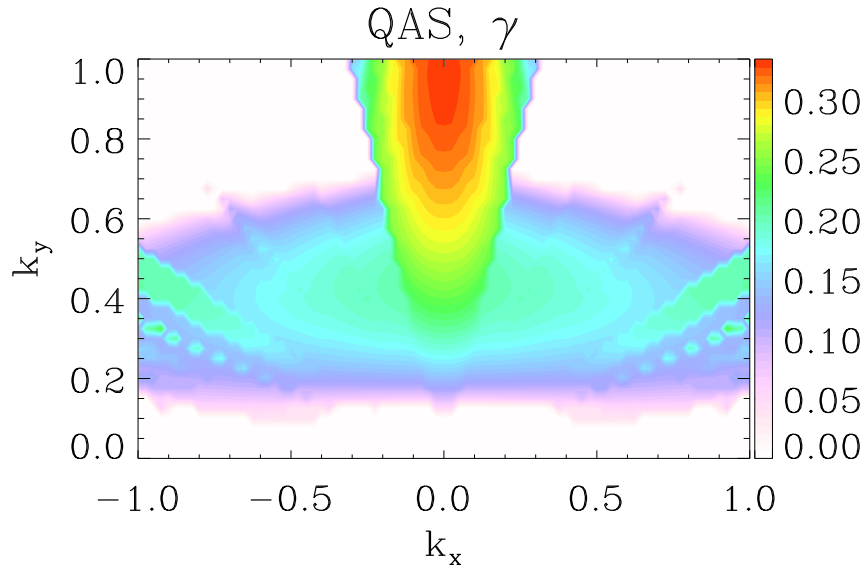


Figure 6.10: Linear growth rate spectrum for NCSX (QAS) as computed by PTSM3D. Source: Hegna et al. (2018).

a thousand times larger than the zonal saturation, NCSX is dominated by energy transfer to stable modes through zonal flows. This observation is consistent with the supposition that a quasi-axisymmetric stellarator is “tokamak-like”, where zonal-flow-catalyzed energy transfer is the dominant mechanism.

Examining the triplets that maximize $|\tau_{qst}C_{qst}|$ for NCSX, in Fig. 6.13, again confirms the marginally stable is the most important for non-zonal energy transfer. This provides further evidence that turbulence optimization with PTSM3D could be accomplished within this framework by considering only non-zonal triplets that involve a marginally stable mode.

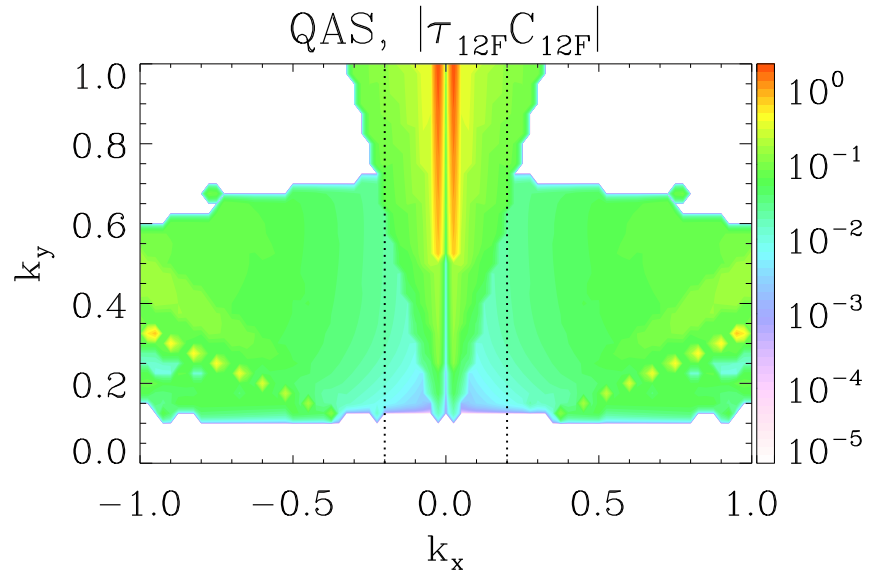


Figure 6.11: Contours of $|\tau_{12F}C_{12F}|$ for the NCSX configuration as a function of k_x^z and k_y as computed by PTSM3D. Source: Hegna et al. (2018).

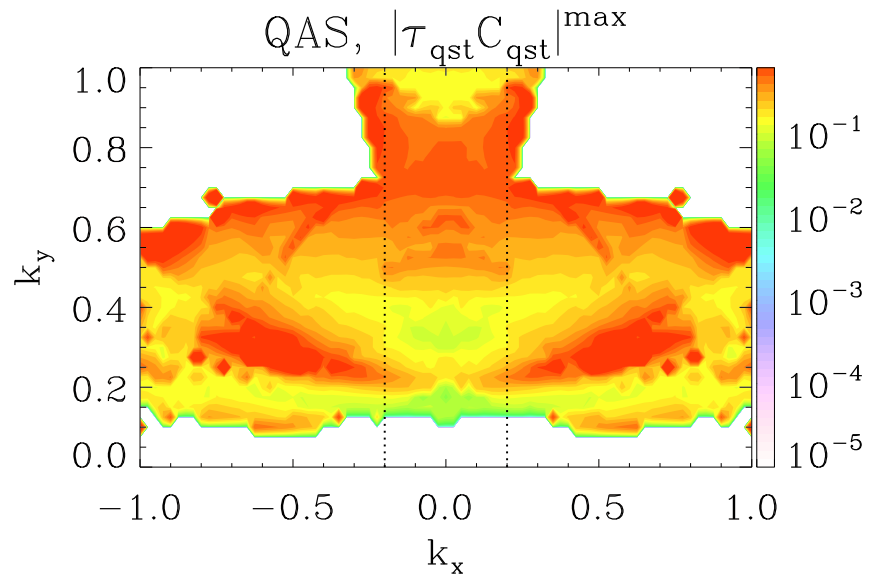


Figure 6.12: Contours of $|\tau_{qst}C_{qst}|^{\max}$ for the NCSX configuration as a function of k_x and k_y as computed by PTSM3D. Source: Hegna et al. (2018).

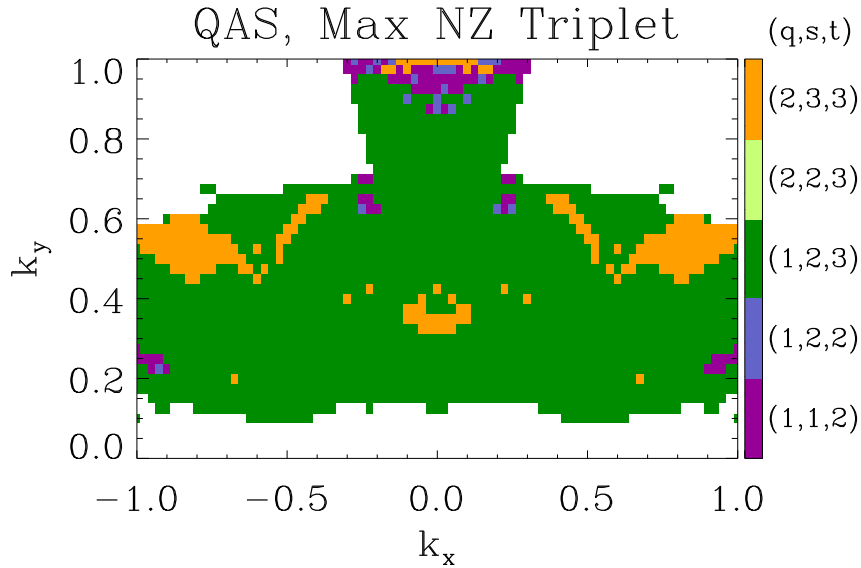


Figure 6.13: Identity of the triplets involved in maximizing $|\tau_{qst}C_{qst}|$. The color green indicates the triplet was comprised of an unstable mode, stable mode, and marginally stable mode. Source: Hegna et al. (2018).

6.3 HSX Hill/Well Calculations

Application of PTSM3D to HSX and NCSX provided a good qualitative test of the fluid model. However, for optimization purposes, it is necessary to also test the quantitative capabilities. This means that if the value of $\langle \tau C \rangle_k$ increases as the three-dimensional geometry is altered, the transport in a nonlinear gyrokinetic simulation should decrease and vice versa. This can be readily tested by exploiting the geometry flexibility of HSX to generate real stellarator equilibria. Energizing certain magnetic coils can increase the amount of magnetic “hill” or “well”, which serves to add a $M = 0$, $N = 1$ component to the Boozer spectrum, Eq. (2.30). The configurations are designated by hill percentage or well percentage, with 11% hill/well being the maximum value considered. The amplitudes of the 10 largest modes in the Boozer spectrum as a function of plasma radius are shown in

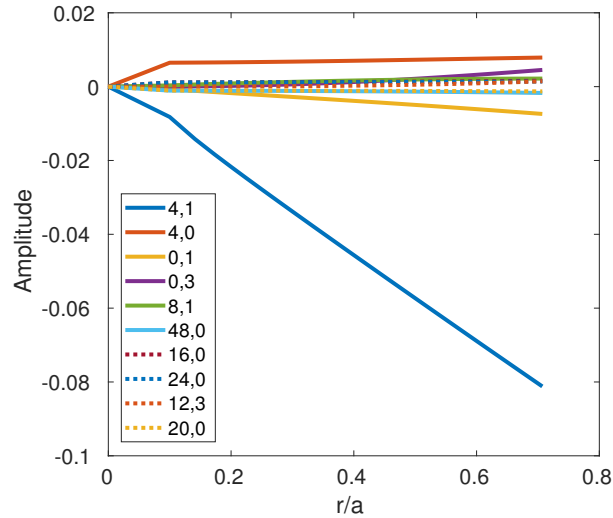


Figure 6.14: Amplitude of the 10 largest Boozer components at the half-toroidal flux surface of the 11% hill configuration, plotted as a function of plasma radius.

Fig. 6.14 for the 11% magnetic hill configuration and in Fig. 6.15 for the 11% well configuration. In both cases, the $M = 0$, $N = 1$ component has the second largest amplitude in the outer region of the plasma where the model is evaluated, but note that the sign of the amplitude is opposite between hill and well. PTSM3D has then been applied to HSX configurations with varying levels of hill/well percentage and compared against the transport values obtained through GENE simulations.

The parameters used to model HSX QHS and NCSX are chosen for this analysis, $\epsilon_T = 3$ with the geometry from the half-toroidal flux surface. One should note that the half-toroidal flux surface is not an exact quantity, as for equilibrium reconstruction purposes, often one must specify the location of the the last closed flux surface, which can be altered by the presence of magnetic islands. The scaling of the zonal and non-zonal $\langle \tau C \rangle_k$ and the nonlinear gyrokinetic fluxes as a function of hill/well percentage are presented in Fig. 6.16. The $\langle \tau C \rangle_k$ is normalized its to value at zero hill/well

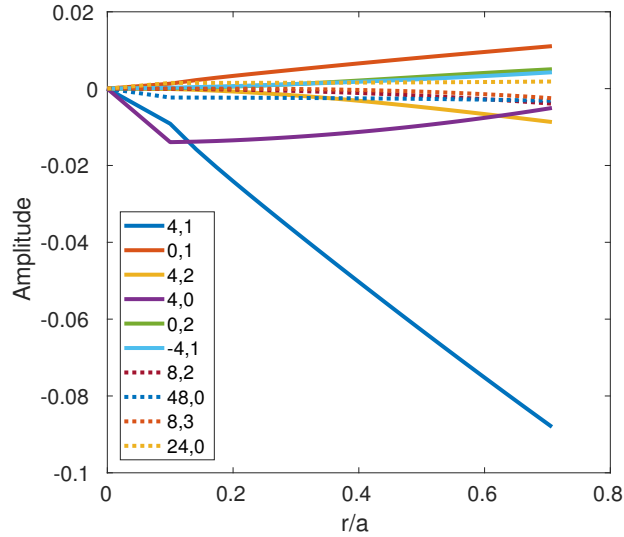


Figure 6.15: Amplitude of the 10 largest Boozer components at the half-toroidal flux surface of the 11% well configuration, plotted as a function of plasma radius.

percentage, which is the standard QHS geometry.

Focusing first on the changes with increasing well percentage, the non-linear flux (magenta diamonds in Fig. 6.16) as calculated in GENE increases monotonically to 11% well, where the flux is approximately three times as large as the base QHS case. The saturation metric shows behavior consistent with increased flux, as both the zonal and non-zonal triplets decrease. The zonal $\langle \tau C \rangle_k$ (red dotted diamonds), however, does not decrease by a significant enough amount to be solely responsible for the rise in transport. The non-zonal $\langle \tau C \rangle_k$ (blue dashed diamonds), on the other hand, decreases by almost a factor of two. Combined with the observation that non-zonal energy transfer is the dominant saturation mechanism for ITG turbulence in HSX, this suggests that the increase in flux for increasing well percentage is the result of smaller energy transfer to stable modes, because the nonlinear non-zonal interactions become less correlated.

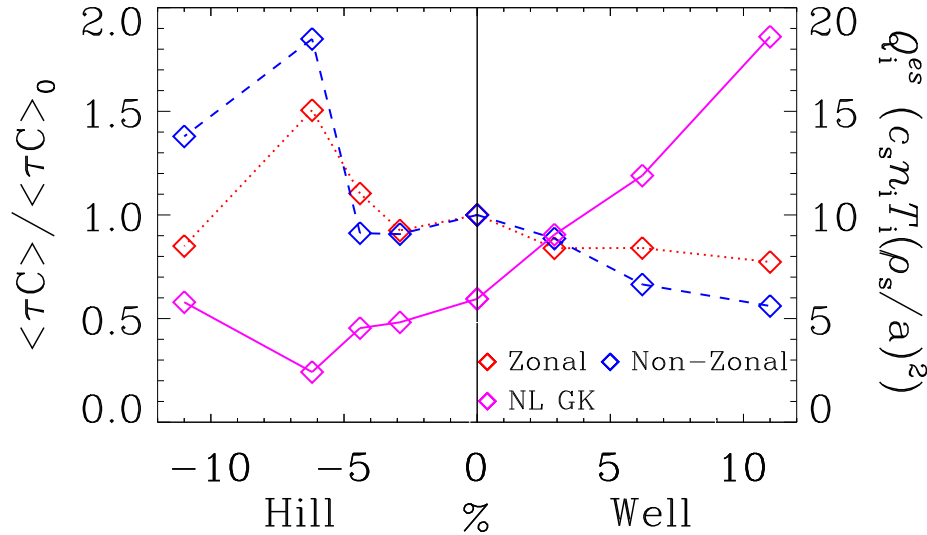


Figure 6.16: Scaling of nonlinear fluxes (solid magenta diamonds), normalized $\langle \tau_{12F} C_{12F} \rangle_k$ (dotted red diamonds) and $\langle \tau_{qst} C_{qst} \rangle_k$ (dashed blue diamonds) as a function of HSX hill and well percentage. The triplets are normalized to the value at zero hill/well percentage (the QHS geometry).

The addition of toroidal curvature for the 11% well configuration has the largest effect on the quantity B_k (or k_{\perp}^2), and in turn affects mode localization. The structure of k_{\perp}^2 along a field line is shown in Fig. 6.17 for 0% well and 11% well. The biggest change in k_{\perp}^2 is in the magnitude of the local maxima, which are in general larger at the same θ . Increasing k_{\perp}^2 generally serves to increase the mode localization along a field line (Plunk et al., 2014). Equation (5.3) shows nonlinear energy transfer is proportional to the amount of mode overlap along a field line. The top plot of Fig. 6.18 shows the gyrokinetic eigenmode shape at $(k_x \approx 0.3, k_y = 0.3)$ for 2.9% well, while the bottom plot shows the eigenmode shape at $(k_x \approx 0.3, k_y = 3)$ for 11% well. As the well percentage increases and the k_{\perp}^2 maxima become larger, the modes become more localized. Unless the three interacting modes are localized in close proximity to each other along the field line, the energy

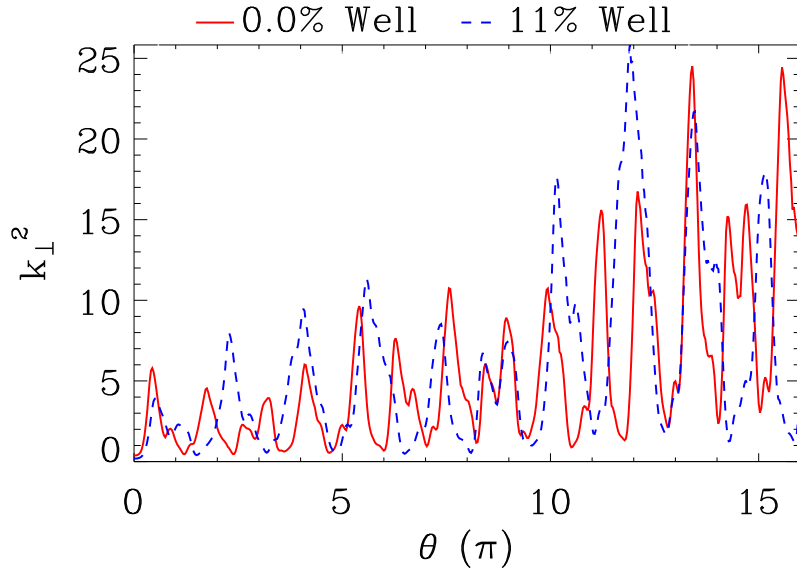


Figure 6.17: Value of k_{\perp}^2 along a field line for 0% well (solid red) and 11% well (dashed blue) configurations.

transfer given by Eq. (5.3) will decrease and less energy will be transferred to stable modes as the well percentage is increased. As the modes become more localized, the complex frequencies become more k_x dependent and achieving large τ_{qst} values becomes more difficult. This is reflected in the decreasing τC values, showing a correspondence to the increased nonlinear heat flux.

The hill results in Fig. 6.16 display more complex behavior, where a nonlinear flux minimum is observed at 6.2% hill. Remarkably, this non-monotonic behavior is reproduced by both the zonal and non-zonal $\langle \tau C \rangle_k$ values, as a maximum in $\langle \tau C \rangle_k$ is seen at 6.2% hill. The non-zonal triplets again seem to play the dominant role, as the flux at 6.2% hill is roughly one-third the QHS value and the non-zonal $\langle \tau C \rangle_k$ is roughly twice the QHS value. Recalling Figs. 6.14 and 6.15, increasing the hill percentage adds a

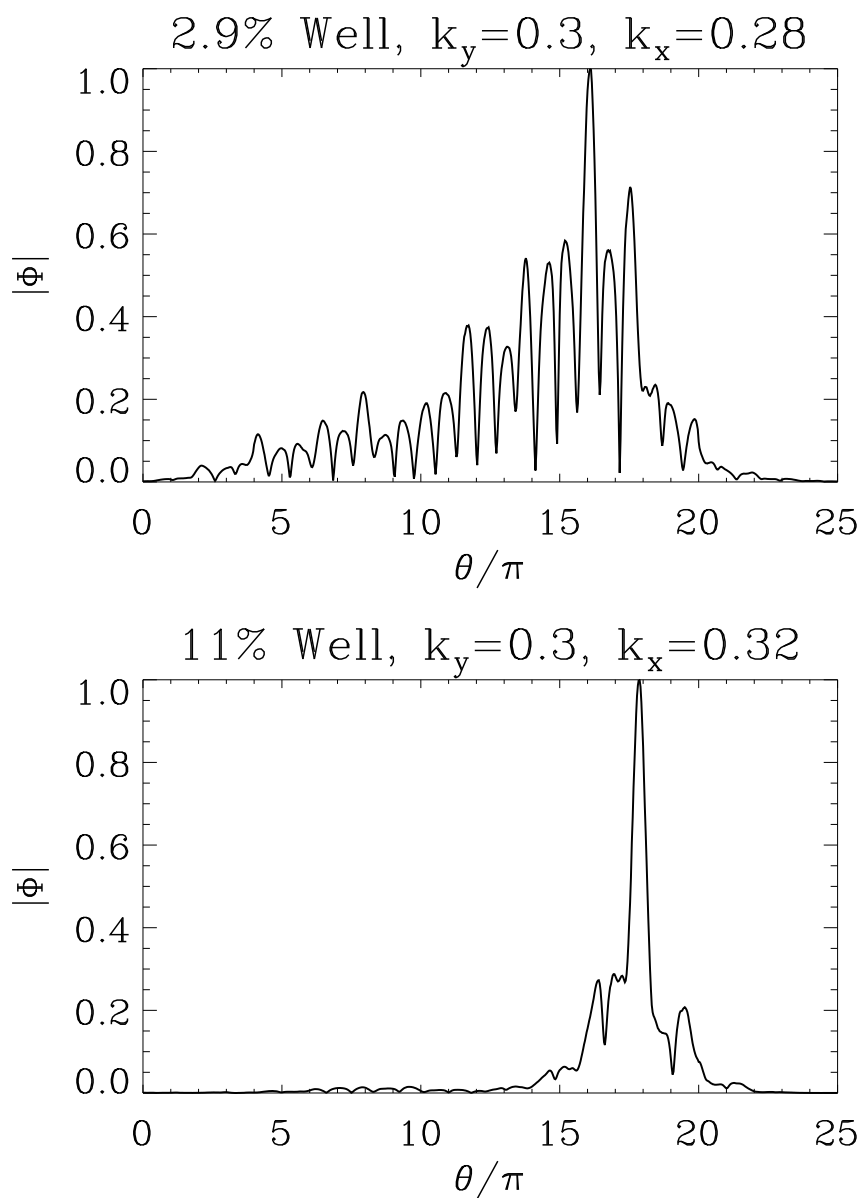


Figure 6.18: Electrostatic potential eigenmode structures for 2.9% well at $(k_x = 0.28, k_y = 0.3)$ (top) and 11% well at $(k_x = 0.32, k_y = 0.3)$ (bottom).

toroidal curvature component with opposite sign compared to increased well percentage. This is observed in Fig. 6.19, which compares k_{\perp}^2 along a field line for 0% hill and 6.2% hill. Instead of the local k_{\perp}^2 maxima becoming larger for 6.2% hill, they in general become smaller than the corresponding 0% hill maxima. In fact, for $0 \leq \theta \lesssim 8$, the k_{\perp}^2 maxima for 6.2% hill are approximately equal in magnitude. Echoing the arguments of Sec. 5.2.4, this relative homogeneity in B_k maxima can allow modes at different \mathbf{k} values to localize to the same regions along a field line. This is shown in Fig. 6.20 at 6.2% hill for gyrokinetic eigenmodes with $k_x = (0.5, 0.6, 0.7)$ and $k_y = 0.3$, where the eigenmodes are localized to the same region along the field line. Thus these modes can maximize nonlinear energy transfer in Eq. (5.3), leading to a heat flux minimum. By localizing in similar regions along the field line, the complex frequencies become similar, and larger values of τ_{qst} are obtained, demonstrating further the link between $\langle \tau C \rangle_k$ and nonlinear flux.

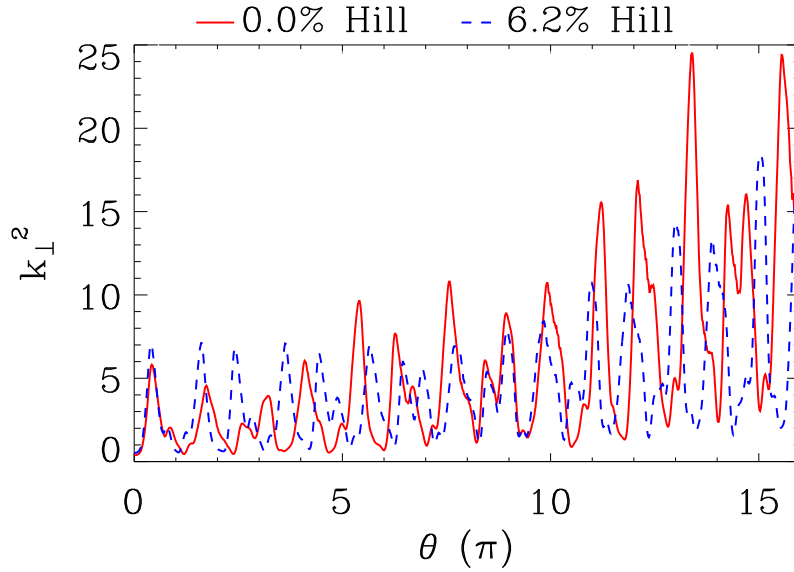


Figure 6.19: Value of k_{\perp}^2 along a field line for 0% hill (solid red) and 6.2% hill (dashed blue) configurations.

6.4 Chapter Summary

The fluid model of ITG turbulence saturation from Hegna et al. (2018) was reproduced to provide context for its numerical implementation in the PTSM3D code. PTSM3D computes complex linear ITG frequencies for an unstable, stable, and marginally stable eigenmode, which are in turn used to calculate nonlinear triplet correlation times and coupling coefficients. When the triplet involves a stable mode, the product τC is a proxy for turbulence saturation by energy transfer to stable modes. Triplets are differentiated between those involving a zonal mode with an assumed zero frequency, and a non-zonal, marginally stable mode. PTSM3D was used to evaluate saturation characteristics in the HSX QHS configuration and NCSX QAS configuration, and found that saturation in HSX was dominated by non-zonal triplets while saturation in NCSX was dominated by zonal triplets. PTSM3D

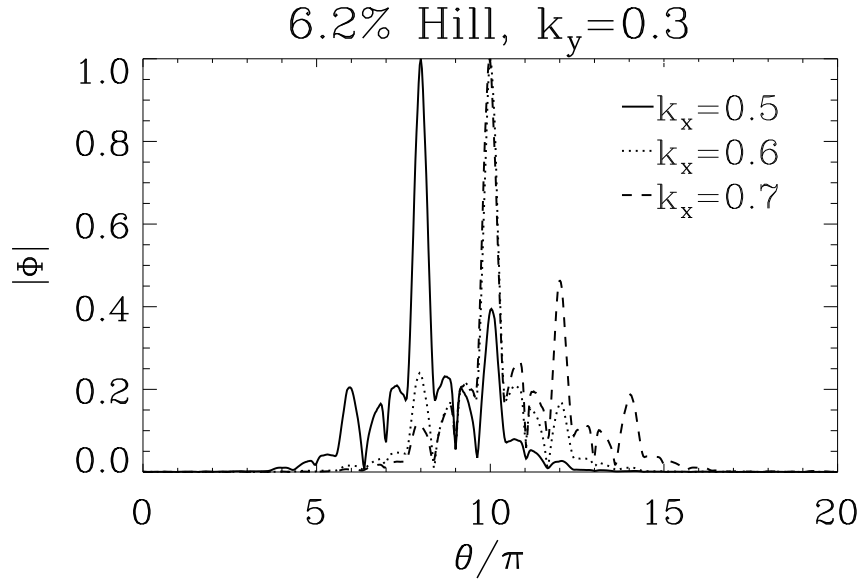


Figure 6.20: Electrostatic eigenmode structures for 6.2% hill for $k_y = 0.3$ and $k_x = 0.5$ (solid line), $k_x = 0.6$ (dotted line) and $k_x = 0.7$ (dashed line).

successfully reproduced the characteristics of GENE flux calculations for HSX configurations where the magnetic hill and well percentage was altered. Increasing the well term provided more mode localization, decreasing triplet correlation times, and increasing nonlinear transport. Increasing the hill percentage had the opposite impact; triplet correlation times were increased and nonlinear fluxes decreased. At 6.2% hill, where the flux is at a minimum, modes at different k_x are able to localize to the same region along the field line and significantly increase triplet correlations. These results give confidence PTSM3D can be implemented in stellarator optimization schemes to reduce turbulent transport.

7 CONCLUSIONS

The work contained in this thesis represents a significant contribution to the field of stellarator turbulence. Some of the first-ever nonlinear gyrokinetic simulations of TEM turbulence in stellarator geometry were performed, including the first ever for the HSX geometry. These simulations revealed both the specific structure of the magnetic geometry and the small value of global magnetic shear for HSX play an important role in determining the dynamics of TEM turbulence, leading to transport at long wavelengths and more complex turbulence saturation dynamics involving energy transfer to subdominant and stable modes. These findings motivated the construction of a reduced fluid model to study turbulence saturation in stellarators, which has been numerically implemented in the PTSM3D code. The major results from each section are summarized below and an outlook on future research is given.

7.1 Summary

7.1.1 First TEM turbulence simulations in HSX

The first TEM turbulence simulations of HSX show several distinguishing features as compared to TEM turbulence in tokamaks. The impact of low-magnetic-shear stellarator geometry is immediately observed in the linear growth rate spectrum. Different TEM branches are characterized by distinct eigenmode structures, which are strongly influenced by both the magnetic geometry and the wavenumber k_y of the mode. At high k_y , tokamak-like, strongly ballooning modes are the dominant instability. At intermediate k_y , however, localized modes with tearing parity are dominant, only to be subsumed at low k_y by modes that extend far along field lines. Calculations of the subdominant eigenmode spectrum reveal that these modes smoothly

transition between dominant and subdominant as a function of k_y and that many unstable modes exist at each wavenumber. In nonlinear simulations, strong divergence from linear physics is found at low k_y . A large transport peak is observed at $k_y \approx 0.1$, despite the corresponding linear growth rates approaching zero. Furthermore, strong deviations between linear and nonlinear cross-phases occur at low k_y , and the nonlinear frequencies are dominated by an ion mode, even though dominant low k_y instabilities are electron modes. Zonal flows are prominent in nonlinear simulations. However, the zonal shearing rates are never larger than the maximum linear growth rate and, as such, cannot account for turbulence saturation solely through shear suppression. Nevertheless, the nonlinear fluxes obtained are consistent with experimental flux measurements and provide evidence TEM turbulence drives transport in HSX.

7.1.2 Effect of low magnetic shear on turbulence

Efforts to investigate the low- k_y transport and linear/nonlinear physics differences identified the low global magnetic shear of HSX as having a large influence on turbulent dynamics and led to a new computational approach for low-shear stellarators. There should be little difference between simulations with exactly zero global magnetic shear and those with the experimental shear value at the HSX half-toroidal flux surface, $\hat{s} = -0.046$. Zero-shear simulations with strictly periodic parallel boundary conditions performed in a flux tube with geometry from only one poloidal turn were dominated by an artificially-enhanced low- k_y instability, inconsistent with the finite-shear calculations. At low k_y , modes extend far along field lines before decaying, with the decay length determined by the magnetic geometry along the field line. Geometry from one poloidal turn is insufficient to resolve parallel correlation lengths, thus the zero-shear simulations were dominated by artificially self-connecting linear modes. Using geometry from multiple poloidal turns removes the self-correlation effects and lead to agreement

between the zero-shear and finite-shear simulations.

Multiple poloidal turns prove to be necessary for finite-shear simulations as well. With one poloidal turn, the dynamics at low k_y eventually dominates TEM simulations at high density gradient drive, and simulations no longer converge numerically. Analysis of the subdominant eigenspectrum showed that a branch of extended, marginally stable eigenmodes are marginally unstable at low k_y for one poloidal turn, but become stable when multiple poloidal turns are utilized. Owing to favorable characteristics for nonlinear energy transfer, such as extended mode structures and Maxwellian velocity space structure, these modes play an important role in the low- k_y turbulent dynamics, as they couple efficiently to both zonal and non-zonal modes. When excited to finite amplitudes, they can enhance the energy drive and transport at low k_y through nonlinear energy transfer, while also acting as a source of dissipation due to negative growth rates. This result makes clear turbulence in HSX is significantly more complex than the oft-referenced paradigm of a dominant instability saturating via velocity shear by a mean flow, such as a zonal flow. Furthermore, accurately simulating the subdominant spectrum was key to properly simulating turbulence in HSX and must be accounted for in future investigations of low- magnetic-shear stellarators.

7.1.3 Turbulence saturation in stellarators

A reduced three-field fluid model designed to study ITG turbulence saturation in stellarators has been implemented numerically in the PTSM3D code. Turbulence saturation is quantified by $\tau_{qst}C_{qst}$, where τ_{qst} is a complex triplet correlation time and C_{qst} a complex coupling coefficient for three-wave interactions involving an unstable mode q , a stable mode s , and a third mode t . The identity of the third mode that maximizes this quantity is dependent on stellarator geometry. For HSX, t is a finite- k_y , marginally stable mode, while for NCSX, t is a $k_y = 0$ zonal mode. PTSM3D was applied to HSX equilibria where the magnetic hill/well depth was altered, introducing more toroidal

curvature, and it was found that changes in τC accurately reproduce the changes in the fluxes from nonlinear gyrokinetic simulations, as τC increases when the flux decreases and vice versa. This gives confidence that PTSM3D may be used as the first nonlinearly-derived proxy for turbulent transport in stellarator optimization research.

7.2 Future Research

7.2.1 Experimental comparisons

The ability to accurately simulate turbulence in HSX makes possible a variety of new research directions. Importantly, more accurate investigations of turbulence in HSX can be performed by moving towards more realistic plasma parameters, such as a more realistic ion-electron temperature ratio, and by comparing with measurements from experimental diagnostics. The following list of possible research directions are ordered in terms of increasing complexity.

- Compare GENE density fluctuations with density fluctuations from reflectometry measurements. A synthetic diagnostic and full-wave code is necessary to ensure the correct long-wavelength, low-frequency fluctuation regime is captured in GENE. This provides a crucial test of TEM turbulence in HSX.
- Compare GENE temperature fluctuations with measurements from the correlated electron cyclotron emission (CECE) diagnostic. The dynamics of heat pulse propagation can be investigated to build on the work of Weir et al. (2015), which can possibly shed light on saturation dynamics.
- Examine zonal flow dynamics and saturation with bi-spectral analysis of potential fluctuations and compare against experimental measure-

ments. This information is readily accessible in GENE simulations and would help determine the efficacy of zonal flows in HSX.

7.2.2 Nonlinear energy transfer in stellarators

The research presented in this thesis has laid the groundwork for more in-depth studies of nonlinear energy transfer in stellarators. The improved capabilities of eigenvalue solvers to access the subdominant and stable eigenmode spectrum allows for more advanced nonlinear energy transfer analysis, such as the energy transfer between individual eigenmodes. These tools will be applied to TEM turbulence in HSX to better understand the role of the extended, marginally-stable eigenmodes in the turbulent state. A natural next step is to apply these analysis methods to other stellarator configurations, such as W7-X and LHD.

7.2.3 Turbulence optimization

The success of PTSM3D in reproducing the nonlinear gyrokinetic trends for the HSX hill and well configurations motivates the inclusion of PTSM3D in stellarator optimization frameworks, such as STELLOPT, with the goal of finding magnetic configurations where turbulent transport is reduced. PTSM3D also provides a means of assessing how changes in geometry affect turbulent transport, will be investigated in parallel with stellarator optimization.

REFERENCES

- Abel, I. G., G. G. Plunk, E. Wang, M. Barnes, S. C. Cowley, W. Dorland, and A. A. Schekochihin. 2013. Multiscale gyrokinetics for rotating tokamak plasmas: fluctuations, transport and energy flows. *Rep. Prog. Phys.* 76: 116201.
- Anderson, F.S.B., A. F. Almagri, D. T. Anderson, G. Peter, J. N. Talmadge, and J. L. Shohet. 1995. The Helically Symmetric eXperiment, (HSX), goals, design and status. *Fusion Technol.* 27(3T):273–277.
- Bañón Navarro, A., P. Morel, M. Albrecht-Marc, D. Carati, F. Merz, T. Görler, and F. Jenko. 2011. Free energy balance in gyrokinetic turbulence. *Phys. Plasmas* 18:092303.
- Baumgaertel, J. A., E. A. Belli, W. Dorland, W. Guttenfelder, G. W. Hammett, D. R. Mikkelsen, G. Rewoldt, W. M. Tang, and P. Xanthopoulos. 2011. Simulating gyrokinetic microinstabilities in stellarator geometry with GS2. *Phys. Plasmas* 18:122301.
- Baumgaertel, J. A., G. W. Hammett, D. R. Mikkelsen, M. Nunami, and P. Xanthopoulos. 2012. Gyrokinetic studies of the effect of β on drift-wave stability in the National Compact Stellarator Experiment. *Phys. Plasmas* 19:122306.
- Beer, M. A., S. C. Cowley, and G. W. Hammett. 1995. Field-aligned coordinates for nonlinear simulations of tokamak turbulence. *Phys. Plasmas* 2(7):2687–2700.
- Bellan, Paul M. 2006. *Fundamentals of plasma physics*. Cambridge: Cambridge University Press.
- Bethe, H. A. 1939. Energy production in stars. *Phys. Rev.* 55:434–456.

- Bhattacharjee, A., J. E. Sedlak, P. L. Sivilon, M. N. Rosenbluth, and D. W. Ross. 1983. Drift waves in a straight stellarator. *Phys. Fluids* 26(1983): 880–882.
- Blackford, L. S., et al. 1997. *ScaLAPACK users' guide*. Philadelphia, PA: Society for Industrial and Applied Mathematics.
- Boozer, A. H. 1981. Plasma equilibrium with rational magnetic surfaces. *Phys. Fluids* 24(11):1999–2003.
- . 1998. What is a stellarator? *Phys. Plasmas* 5(5):1647–1655.
- Brizard, A. J., and T. S. Hahm. 2007. Foundations of nonlinear gyrokinetic theory. *Rev. Mod. Phys.* 79(2):421–468.
- Burrell, K. H. 1997. Effects of $E \times B$ velocity shear and magnetic shear on turbulence and transport in magnetic confinement devices. *Phys. Plasmas* 4(5):1499.
- Candy, J., and R. E. Waltz. 2003. An Eulerian gyrokinetic-Maxwell solver. *J. Comput. Phys.* 186(2):545–581.
- Candy, J., R. E. Waltz, and M. N. Rosenbluth. 2004. Smoothness of turbulent transport across a minimum- q surface. *Phys. Plasmas* 11(5): 1879–1890.
- Canik, J. M., D. T. Anderson, F. S. B. Anderson, K. M. Likin, J. N. Talmadge, and K. Zhai. 2007. Experimental demonstration of improved neoclassical transport with quasihelical symmetry. *Phys. Rev. Lett.* 98: 085002.
- Carmody, D., M. J. Pueschel, J. K. Anderson, and P. W. Terry. 2015. Microturbulence studies of pulsed poloidal current drive discharges in the reversed field pinch. *Phys. Plasmas* 22:012504.

- Cary, J. R., and S. G. Shasharina. 1997. Omnigenity and quasihelicity in helical plasma confinement systems. *Phys. Plasmas* 4:3323.
- Chen, H., and L. Chen. 2018. On drift wave instabilities excited by strong plasma gradients in toroidal plasmas. *Phys. Plasmas* 25:014502.
- Chen, Y., S. E. Parker, W. Wan, and R. Bravenec. 2013. Benchmarking gyrokinetic simulations in a toroidal flux-tube. *Phys. Plasmas* 20(9):1–8.
- Citrin, J., C. Bourdelle, P. Cottier, D. F. Escande, O. D. Gurcan, D. R. Hatch, G. M. D. Hogewij, F. Jenko, and M. J. Pueschel. 2012. Quasilinear transport modelling at low magnetic shear. *Phys. Plasmas* 19:062305.
- Connor, J., and R. Hastie. 2004. Microstability in tokamaks with low magnetic shear. *Plasma Phys. Control. Fusion* 46(10):1501–1535.
- Connor, J. W., R. J. Hastie, and J. B. Taylor. 1978. Shear, periodicity, and plasma ballooning modes. *Phys. Rev. Lett.* 40(6):396–399.
- . 1979. High mode number stability of an axisymmetric toroidal plasma. *Proc. R. Soc. London. A.* 365(1720):1–17.
- Coppi, B., S. Migliuolo, and Y-K. Pu. 1990. Candidate mode for electron thermal energy transport in multi-keV plasmas. *Phys. Fluids B Plasma Phys.* 2(10):2322–2333.
- Cuthbert, P., and R. L. Dewar. 2000. Anderson-localized ballooning modes in general toroidal plasmas. *Phys. Plasmas* 7(6):2302–2305.
- Dannert, T., and F. Jenko. 2005. Gyrokinetic simulation of collisionless trapped-electron mode turbulence. *Phys. Plasmas* 12:072309.
- Dewar, R., and A. Glasser. 1983. Ballooning mode spectrum in general toroidal systems. *Phys. Fluids* 26(10):3038–3052.

D'haeseleer, W. D., W. N. G. Hitchon, J. D. Callen, and J. L. Shohet. 1991. *Flux Coordinates and Magnetic Field Structure*. Berlin Heidelberg: Springer-Verlag.

Diamond, P. H., S.-I. Itoh, K. Itoh, and T. S. Hahm. 2005. Zonal flows in plasma - a review. *Plasma Phys. Control. Fusion* 47:R35–R131.

Dimitis, A. M., T. J. Williams, J. A. Byers, and B. I. Cohen. 1996. Scalings of ion-temperature-gradient-driven anomalous transport in tokamaks. *Phys. Rev. Lett.* 77(1):71–74.

Dinklage, A., et al. 2018. Magnetic configuration effects on the Wendelstein 7-X stellarator. *Nat. Phys.*

Dorland, W., F. Jenko, M. Kotschenreuther, and B. N. Rogers. 2000. Electron temperature gradient turbulence. *Phys. Rev. Lett.* 85(26):5579–5582.

Ernst, D. R., P. T. Bonoli, P. J. Catto, W. Dorland, C. L. Fiore, R. S. Granetz, M. Greenwald, A. E. Hubbard, M. Porkolab, M. H. Redi, J. E. Rice, and K. Zhurovich. 2004. Role of trapped electron mode turbulence in internal transport barrier control in the Alcator C-Mod Tokamak. *Phys. Plasmas* 11(5):2637–2648.

Ernst, D. R., J. Lang, W. M. Nevins, M. Hoffman, Y. Chen, W. Dorland, and S. Parker. 2009. Role of zonal flows in trapped electron mode turbulence through nonlinear gyrokinetic particle and continuum simulation. *Phys. Plasmas* 16:055906.

Faber, B. J., M. J. Pueschel, J. H. E. Proll, P. Xanthopoulos, P. W. Terry, C. C. Hegna, G. M. Weir, K. M. Likin, and J. N. Talmadge. 2015. Gyrokinetic studies of trapped electron mode turbulence in the Helically Symmetric eXperiment stellarator. *Phys. Plasmas* 22:072305.

Faber, B. J., M. J. Pueschel, P. W. Terry, C. C. Hegna, and J. E. Roman. 2018. Stellarator microinstability and turbulence at low magnetic shear. *Submitted to J. Plasma Phys.*

Faber, B.J. 2018. <https://gitlab.com/bfaber/ptsm3d>.

Freidberg, J. P. 2007. *Plasma physics and fusion energy*. Cambridge: Cambridge University Press.

Friedman, B., and T. A. Carter. 2014. Linear technique to understand non-normal turbulence applied to a magnetized plasma. *Phys. Rev. Lett.* 113:025003.

Friedman, B., T. A. Carter, M. V. Umansky, D. Schaffner, and I. Joseph. 2013. Nonlinear instability in simulations of Large Plasma Device turbulence. *Phys. Plasmas* 20:055704.

Frisch, U. 1995. *Turbulence: The Legacy of A. N. Kolmogorov*. Cambridge: Cambridge University Press.

Fujita, T., Y. Kamada, S. Ishida, Y. Neyatani, T. Oikawa, S. Ide, S. Takeji, Y. Koide, A. Isayama, T. Fukuda, T. Hatae, Y. Ishii, T. Ozeki, H. Shirai, and JT-60 Team. 1999. High performance experiments in JT-60U reversed shear discharges. *Nuclear Fusion* 39(11Y):1627.

Fulton, D. P., Z. Lin, I. Holod, and Y. Xiao. 2014. Microturbulence in DIII-D tokamak pedestal. I. Electrostatic instabilities. *Phys. Plasmas* 21: 042110.

Garabedian, P. R. 1996. Stellarators with the magnetic symmetry of a tokamak. *Physics of Plasmas* 3(7):2483–2485.

Garren, D. A., and A. H. Boozer. 1991a. Existence of quasihelically symmetric stellarators. *Phys. Fluids B* 3:2822.

- . 1991b. Magnetic field strength of toroidal plasma equilibria. *Phys. Fluids B* 3:2805.
- Gates, D. A., et al. 2018. Stellarator Research Opportunities: A Report of the National Stellarator Coordinating Committee. *Journal of Fusion Energy* 37(1):51–94.
- Gatto, R., P. W. Terry, and D. A. Baver. 2006. Nonlinear damping of zonal modes in anisotropic weakly collisional trapped electron mode turbulence. *Phys. Plasmas* 13:022306.
- Gerhardt, S. P., J. N. Talmadge, J. M. Canik, and D. T. Anderson. 2005. Measurements and modeling of plasma flow damping in the Helically Symmetric eXperiment. *Phys. Plasmas* 12:056116.
- Goldstein, H., C. Poole, and J. Safko. 2002. *Classical mechanics*. 3rd ed. San Francisco: Addison-Wesley.
- Görler, T. 2009. Multiscale effects in plasma microturbulence. Ph.D. thesis, Universität Ulm.
- Grulke, O., and T. Klinger. 2002. Large-scale fluctuation structures in plasma turbulence. *New J. Phys* 4:67.1–67.23.
- Guttenfelder, W., J. Lore, D. T. Anderson, F. S. B. Anderson, J. M. Canik, W. Dorland, K. M. Likin, and J. N. Talmadge. 2008. Effect of Quasihelical Symmetry on Trapped-Electron Mode Transport in the HSX Stellarator. *Phys. Rev. Lett.* 101:215002.
- Hahm, T. S., M. A. Beer, Z. Lin, G. W. Hammett, W. W. Lee, and W. M. Tang. 1999. Shearing rate of time-dependent $E \times B$ flow. *Phys. Plasmas* 6(3):922–926.

- Hatch, D. R., F. Jenko, A. Bañón Navarro, V. Bratanov, P. W. Terry, and M. J. Pueschel. 2016a. Linear signatures in nonlinear gyrokinetics: Interpreting turbulence with pseudospectra. *New J. Phys.* 18:075018.
- Hatch, D. R., M. Kotschenreuther, S. Mahajan, P. Valanju, F. Jenko, D. Told, T. Görler, and S. Saarelma. 2016b. Microtearing turbulence limiting the JET-ILW pedestal. *Nucl. Fusion* 56:104003.
- Hatch, D. R., P. W. Terry, F. Jenko, F. Merz, and W. M. Nevins. 2011a. Saturation of gyrokinetic turbulence through damped eigenmodes. *Phys. Rev. Lett.* 106:115003.
- Hatch, D. R., P. W. Terry, F. Jenko, F. Merz, M. J. Pueschel, W. M. Nevins, and E. Wang. 2011b. Role of subdominant stable modes in plasma microturbulence. *Phys. Plasmas* 18:055706.
- Hatch, D. R., P. W. Terry, W. M. Nevins, and W. Dorland. 2009. Role of stable eigenmodes in gyrokinetic models of ion temperature gradient turbulence. *Phys. Plasmas* 16(2):022311.
- Hegna, C. C., and S. R. Hudson. 2001. Loss of second-ballooning stability in three-dimensional equilibria. *Phys. Rev. Lett.* 87(3):3–6.
- Hegna, C. C., P. W. Terry, and B. J. Faber. 2018. Theory of ITG turbulent saturation in stellarators : Identifying mechanisms to reduce turbulent transport. *Phys. Plasmas* 25:022511.
- Helander, P. 2014. Theory of plasma confinement in non-axisymmetric magnetic fields. *Rep. Prog. Phys.* 77:087001.
- Helander, P., J. H. E. Proll, and G. G. Plunk. 2013. Collisionless microinstabilities in stellarators. I. Analytical theory of trapped-particle modes. *Phys. Plasmas* 20:122505.

- Helander, P., and D. J. Sigmar. 2002. *Collisional transport in magnetized plasmas*. Cambridge: Cambridge University Press.
- Hernandez, V., J. E. Roman, and V. Vidal. 2005. SLEPc: A scalable and flexible toolkit for the solution of eigenvalue problems. *ACM Trans. Math. Softw.* 31(3):351–362.
- Hinton, F. 1976. Theory of plasma transport in toroidal confinement systems. *Rev. Mod. Phys.* 48(2):239.
- Hudson, S. R., C. C. Hegna, R. Torasso, and A. Ware. 2004. Ballooning modes in quasi-symmetric stellarators. *Plasma Phys. Control. Fusion* 46: 869–876.
- Jenko, F., and W. Dorland. 2002. Prediction of significant tokamak turbulence at electron gyroradius scales. *Phys. Rev. Lett.* 89:225001.
- Jenko, F., W. Dorland, M. Kotschenreuther, and B. N. Rogers. 2000. Electron temperature gradient driven turbulence. *Phys. Plasmas* 7(5): 1904–1910.
- Jenko, F., and A. Kendl. 2002. Radial and zonal modes in hyperfine-scale stellarator turbulence. *Phys. Plasmas* 9(10):4103–4106.
- Kadomtsev, B. B., and O. P. Pogutse. 1967. Plasma instability due to particle trapping in a toroidal geometry. *Sov. Phys. JETP* 24(6):1172–1179.
- Keilhacker, M., A. Gibson, C. Gormezano, and P.H. Rebut. 2001. The scientific success of JET. *Nuclear Fusion* 41(12):1925.
- Kolmogorov, A. N. 1991a. Dissipation of energy in the locally isotropic turbulence. *Proceedings of the Royal Society of London A: Mathematical, Physical and Engineering Sciences* 434(1890):15–17.

- . 1991b. The local structure of turbulence in incompressible viscous fluid for very large reynolds number. *Proceedings of the Royal Society of London A: Mathematical, Physical and Engineering Sciences* 434(1890): 9–13.
- Krall, N. A., and A. W. Trivelpiece. 1973. *Principles of plasma physics*. New York: McGraw-Hill.
- Krommes, J. 2002. Fundamental statistical descriptions of plasma turbulence in magnetic fields. *Phys. Rep.* 360:1–352.
- Landau, L. 1946. On the vibration of the electronic plasma. *JETP* 16:574.
- Landreman, M. 2011. Electric fields and transport in optimized stellarators. Ph.D. thesis, Massachusetts Institute of Technology.
- Lang, J., S. E. Parker, and Y. Chen. 2008. Nonlinear saturation of collisionless trapped electron mode turbulence: zonal flows and zonal density. *Phys. Plasmas* 15:055907.
- Liewer, P. C. 1985. Measurements of microturbulence in tokamaks and comparisons with theories of turbulence and anomalous transport. *Nuclear Fusion* 25:543–621.
- Makwana, K. D., P. W. Terry, and J.-H. Kim. 2012. Role of stable modes in zonal flow regulated turbulence. *Phys. Plasmas* 19:062310.
- Martin, M. F., M. Landremann, P. Xanthopoulos, N. R. Mandell, and W. Dorland. 2018. The parallel boundary condition for turbulence simulations in low magnetic shear devices. *arXiv prepr.*
- Merz, Florian. 2008. Gyrokinetic simulation of multimode plasma turbulence. *PhD Thesis*.
- Mynick, H. E. 2006. Transport optimization in stellarators. *Phys. Plasmas* 13:058102.

- Mynick, H. E., T. K. Chu, and A. H. Boozer. 1982. Class of model stellarator fields with enhanced confinement. *Phys. Rev. Lett.* 48(5):322–326.
- Mynick, H. E., N. Pomphrey, and P. Xanthopoulos. 2010. Optimizing Stellarators for Turbulent Transport. *Phys. Rev. Lett.* 105:095004.
- . 2011. Reducing turbulent transport in toroidal configurations via shaping. *Phys. Plasmas* 18:056101.
- Mynick, H. E., P. Xanthopoulos, and A. H. Boozer. 2009. Geometry dependence of stellarator turbulence. *Phys. Plasmas* 16:110702.
- Mynick, H. E., P. Xanthopoulos, B. J. Faber, M. Lucia, M. Rorvig, and J. N. Talmadge. 2014. Turbulent optimization of toroidal configurations. *Plasma Phys. Control. Fusion* 56:094001.
- Nadeem, M., T. Rafiq, and M. Persson. 2001. Local magnetic shear and drift waves in stellarators. *Phys. Plasmas* 8(10):4375–4385.
- Nagaoka, K., et al. 2015. Integrated discharge scenario for high-temperature helical plasma in LHD. *Nucl. Fusion* 55:113020.
- Nakata, Motoki, Masanori Nunami, Hideo Sugama, and Tomo Hiko Watanabe. 2017. Isotope effects on Trapped-Electron-Mode driven turbulence and zonal flows in helical and tokamak plasmas. *Phys. Rev. Lett.* 118:165002.
- Nevins, W. M., J. Candy, S. Cowley, T. Dannert, A. Dimits, W. Dorland, C. Estrada-Mila, G. W. Hammett, F. Jenko, M. J. Pueschel, and D. E. Shumaker. 2006. Characterizing electron temperature gradient turbulence via numerical simulation. *Phys. Plasmas* 13:122306.
- Nührenberg, J., W. Lotz, P. Merkel, C. Nührenberg, U. Schwenn, E. Strumberger, and T. Hayashi. 1995. Overview on Wendelstein 7-X theory. *Fusion Technol.* 27(3T):71–78.

- Nührenberg, J., and R. Zille. 1986. Stable stellarators at medium β and aspect ratio. *Phys. Lett. A* 114(3):129–132.
- . 1988. Quasi-helically symmetric toroidal stellarators. *Phys. Lett. A* 129:113.
- Pearlstein, L. D., and H. L. Berk. 1969. Universal eigenmode in a strongly sheared magnetic field. *Phys. Rev. Lett.* 23(5):220–222.
- Peeters, A. G., Y. Camenen, F. J. Casson, W. A. Hornsby, A. P. Snodin, D. Strintzi, and G. Szepesi. 2009. The nonlinear gyro-kinetic flux tube code GKW. *Comput. Phys. Commun.* 180(12):2650–2672.
- Plunk, G. G., P. Helander, P. Xanthopoulos, and J. W. Connor. 2014. Collisionless microinstabilities in stellarators. III. The ion-temperature-gradient mode. *Phys. Plasmas* 21:032112.
- Plunk, G. G., P. Xanthopoulos, and P. Helander. 2017. Distinct turbulence saturation regimes in stellarators. *Phys. Rev. Lett.* 118:105002.
- Proll, J. H. E., P. Helander, J. W. Connor, and G. G. Plunk. 2012a. Resilience of quasi-isodynamic stellarators against trapped-particle instabilities. *Phys. Rev. Lett.* 108:245002.
- Proll, J. H. E., P. Helander, P. Xanthopoulos, and J. W. Connor. 2012b. Gyrokinetic TEM stability calculations for quasi-isodynamic stellarators. *J. Phys. Conf. Ser.* 401:012021.
- Proll, J. H. E., H. E. Mynick, P. Xanthopoulos, S. Lazerson, and B. J. Faber. 2016. TEM turbulence optimisation in stellarators. *Plasma Phys. Control. Fusion* 58:014006.
- Proll, J. H. E., P. Xanthopoulos, and P. Helander. 2013. Collisionless microinstabilities in stellarators. II. Numerical simulations. *Phys. Plasmas* 20:122506.

- Pueschel, M. J. 2009. Electromagnetic effects in gyrokinetic simulations of plasma turbulence. Ph.D. thesis, Wilhelms-Universität Münster.
- Pueschel, M. J., T. Dannert, and F. Jenko. 2010. On the role of numerical dissipation in gyrokinetic Vlasov simulations of plasma microturbulence. *Comput. Phys. Commun.* 181:1428–1437.
- Pueschel, M. J., B. J. Faber, J. Citrin, C. C. Hegna, P. W. Terry, and D. R. Hatch. 2016. Stellarator turbulence : subdominant eigenmodes and quasilinear modeling. *Phys. Rev. Lett.* 116:085001.
- Pueschel, M. J., and F. Jenko. 2010. Transport properties of finite- β microturbulence. *Phys. Plasmas* 17:062307.
- Rafiq, T., and C. C. Hegna. 2006. Dissipative trapped-electron instability in quasihelically symmetric stellarators. *Phys. Plasmas* 13(2006):062501.
- Reiman, A., et al. 1999. Physics design of a high- β quasi-axisymmetric stellarator. *Plasma Phys. Control. Fusion* 41:B273–B283.
- Rewoldt, G., L. Ku, and W. M. Tang. 2005. Comparison of microinstability properties for stellarator magnetic geometries. *Phys. Plasmas* 12:102512.
- Rewoldt, G., and W. M. Tang. 1990. Toroidal microinstability studies of high-temperature tokamaks. *Phys. Fluids B Plasma Phys.* 2(2):318–323.
- Shafiee, Shahriar, and Erkan Topal. 2009. When will fossil fuel reserves be diminished? *Energy Policy* 37(1):181 – 189.
- Sugama, H., and T. H. Watanabe. 2006. Collisionless damping of zonal flows in helical systems. *Phys. Plasmas* 13:012501.
- Tamm, I. E. 1961. *Plasma physics and the problem of controlled thermonuclear reactions*. New York: Pergamon.

- Tang, W. M. 1978. Microinstability theory in tokamaks. *Nucl. Fusion* 18(8):1089.
- Taylor, J. B. 1964. Equilibrium and stability of plasma in arbitrary mirror fields. *Phys. Fluids* 7:767.
- Terry, P. 2000. Suppression of turbulence and transport by sheared flow. *Rev. Mod. Phys.* 72(1):109–165.
- Terry, P. W., D. A. Baver, and S. Gupta. 2006. Role of stable eigenmodes in saturated local plasma turbulence. *Phys. Plasmas* 13:022307.
- Terry, P. W., B. J. Faber, C. C. Hegna, V. V. Mirnov, M. J. Pueschel, and G. G. Whelan. 2018. Saturation scalings of toroidal ion temperature gradient turbulence. *Phys. Plasmas* 25:012308.
- Wakatani, M. 1988. *Stellarator and heliotron devices*. Oxford: Oxford University Press.
- Waltz, R. E., and A. H. Boozer. 1993. Local shear in general magnetic stellarator geometry. *Phys. Fluids B* 5(7):2201–2205.
- Weir, G. M., B. J. Faber, K. M. Likin, J. N. Talmadge, D. T. Anderson, and F. S. B. Anderson. 2015. Profile stiffness measurements in the Helically Symmetric eXperiment and comparison to nonlinear gyrokinetic calculations. *Phys. Plasmas* 22:056107.
- Wesson, J. 2003. *Tokamaks*. 4th ed. Oxford: Oxford University Press.
- Whelan, G. G., M. J. Pueschel, and P. W. Terry. 2018. Nonlinear electromagnetic stabilization of plasma microturbulence. *Phys. Rev. Lett.* 120:175002.
- White, R. B. 2001. *Theory of toroidally confined plasmas*. London: Imperial College Press.

- Wobig, H. 1993. The theoretical basis of a drift-optimized stellarator reactor. *Plasma Phys. Control. Fusion* 35:903–917.
- Xanthopoulos, P., W. Cooper, F. Jenko, Y. Turkin, A. Runov, and J. Geiger. 2009. A geometry interface for gyrokinetic microturbulence investigations in toroidal configurations. *Phys. Plasmas* 16:082303.
- Xanthopoulos, P., and F. Jenko. 2007. Gyrokinetic analysis of linear microinstabilities for the stellarator Wendelstein 7-X. *Phys. Plasmas* 14:042501.
- Xanthopoulos, P., F. Merz, T. Görler, and F. Jenko. 2007. Nonlinear gyrokinetic simulations of Ion-Temperature-Gradient turbulence for the optimized Wendelstein 7-X stellarator. *Phys. Rev. Lett.* 99:035002.
- Xanthopoulos, P., H. E. Mynick, P. Helander, Y. Turkin, G. G. Plunk, F. Jenko, T. Görler, D. Told, T. Bird, and J. H. E. Proll. 2014. Controlling turbulence in present and future stellarators. *Phys. Rev. Lett.* 113:155001.
- Xanthopoulos, P., G. G. Plunk, A. Zocco, and P. Helander. 2016. Intrinsic turbulence stabilization in a stellarator. *Phys. Rev. X* 6:021033.
- Xu, Y. 2016. A general comparison between tokamak and stellarator plasmas. *Matter and Radiation at Extremes* 1(4):192–200.
- Yoshimura, Y., et al. 2005. Achievement of one hour discharge with ECH on LHD. *J. Phys. Conf. Ser.* 25:189–197.
- Zocco, A., P. Xanthopoulos, H. Doerk, J. W. Connor, and P. Helander. 2018. Threshold for the destabilisation of the ion-temperature-gradient mode in magnetically confined toroidal plasmas. *J. Plasma Phys.* 84:715840101.